

FACILITY FORM 602

N64-29196
(ACCESSION NUMBER)

205
(PAGES)

03-58249
(NAGA CR OR TMR OR AD NUMBER)

(THRU)

1

(CODE)

27

(CATEGORY)

THE

StarGuard

CORPORATION

VAN NUYS, CALIFORNIA

OTS PRICE

STAMP

MICROFILM

NAS 7-10.3
22 JULY 1964

REPORT 6069

COPY NO. 14

(Title -- Unclassified)
FINAL REPORT
SPACECRAFT ENGINE THRUST CHAMBER COOLING
for the Period
13 May 1963 to 12 April 1964

UNCLASSIFIED

(Title -- Unclassified)
FINAL REPORT
SPACECRAFT ENGINE THRUST CHAMBER COOLING

for the Period
13 May 1963 to 12 April 1964

Contract NAS 7-103
Amendment 2

Project 278

PREPARED BY

J. G. Campbell M. D. Carey
J. G. Campbell M. D. Carey

C. F. Sanders, Jr. C. D. Coulbert
C. F. Sanders, Jr. C. D. Coulbert

CHECKED BY

C. D. Coulbert
C. D. Coulbert
Project Engineer

APPROVED BY

S. J. Minton
S. J. Minton,
Manager, Applied Research

UNCLASSIFIED

THE  **Marquardt**
CORPORATION

VAN NUYS, CALIFORNIA

UNCLASSIFIED

CONTENTS

<u>Section</u>		<u>Page</u>
I	SUMMARY	1
II	INTRODUCTION.	3
	A. Program Background.	3
	B. Program Approach.	3
	C. Cooling Techniques Studied.	5
	D. Experimental Program.	7
III	ANALYTICAL STUDIES.	9
	A. Thermochemical Equilibrium Studies.	9
	B. Thermochemical Erosion Analysis	9
	C. Ablative Cooling Studies.	26
	D. Heat Sink Design Studies.	49
	E. Film Cooling Studies.	50
IV	EXPERIMENTAL STUDIES.	53
	A. Test Program Objectives	53
	B. Test Setup and Hardware	53
	C. Description of Tests.	54
V	CONCLUSIONS AND RECOMMENDATIONS	61
VI	REFERENCES AND BIBLIOGRAPHY	63
--	APPENDIX A -- Summary of Nomenclature	171
--	APPENDIX B -- Reaction Phenomena and Kinetics of Solid- Gas Reactions	173
--	DISTRIBUTION.	196

TMC 8673

UNCLASSIFIED

ILLUSTRATIONS

<u>Figure</u>		<u>Page</u>
1.	Model for Thermochemical Erosion Analysis	83
2.	Heat Flux to Nozzle Throat with High Performance Liquid Propellants	84
3.	Heat Flux to Nozzle Throat with High Performance Liquid Propellants	85
4.	Flow Diagram for Thermochemical Erosion Analysis.	86
5.	Standard Nozzle Geometry.	87
6.	Thrust Chamber Sections Used in Analysis.	88
7.	Transpiration Cooled Graphite Nozzle Temperature and Erosion Rate for O_2/H_2	89
8.	Transpiration Cooled Graphite Nozzle Temperature and Erosion Rate for P7000.	90
9.	Transpiration Cooled Graphite Nozzle Temperature and Erosion Rate for P8500.	91
10.	Erosion Rate Profile for an Uncooled Pyrolytic Graphite Nozzle. .	92
11.	Nozzle Temperature and Erosion Rate for O_2/H_2 , H_2 Coolant	93
12.	Nozzle Temperature and Erosion Rate for P8500, H_2 Coolant	94
13.	Effect of Size on Nozzle Cooling.	95
14.	Effect of Combustion Temperature on Nozzle Cooling.	96
15.	Combustion Chamber and Expansion Nozzle Cooling, $D_* = 1.5$ ins.. .	97
16.	Combustion Chamber and Expansion Nozzle Cooling, $D_* = 6$ ins....	98
17.	Variation of Graphite Nozzle Erosion Rate for Several Cooling Gases	99
18.	Gaseous Species at Graphite Nozzle Surface, Heat Sink Cooling . .	100
19.	Gaseous Species at Graphite Nozzle Surface, Gaseous Water Transpiration Cooling	101

TMC A673

ILLUSTRATIONS (Continued)

<u>Figure</u>	<u>Page</u>
20. Gaseous Species at Graphite Nozzle Surface, Hydrogen Transpiration Cooling	102
21. Gaseous Species at Graphite Nozzle Surface, Helium Transpiration Cooling	103
22. Gaseous Species at Graphite Nozzle Surface, Methane Transpiration Cooling	104
23. Erosion Rate vs. Reaction Rate, Heat Sink Cooling	105
24. Gaseous Species at Wall vs. Reaction Rate Multiple, $T_w = 2000^\circ R$.	106
25. Gaseous Species at Wall vs. Reaction Rate Multiple, $T_w = 4000^\circ R$.	107
26. Gaseous Species at Wall vs. Reaction Rate Multiple, $T_w = 6000^\circ R$.	108
27. Gaseous Species at Wall vs. Reaction Rate Multiple, $T_w = 7000^\circ R$.	109
28. Erosion Rate vs. Mass Transfer Rate, Heat Sink Cooling.	110
29. Thermal Analyzer Circuit for Transient Temperature Analysis of NASA Experimental Silica-Phenolic Nozzles.	111
30. Analytical Temperature Distributions in Silica-Phenolic Nozzle Compared with NASA TND-1726 Experimental Data, Run Time = 30 seconds.	112
31. Analytical Temperature Distributions in Silica-Phenolic Nozzle Compared with NASA TND-1726 Experimental Data, Run Time = 30 seconds.	113
32. Analytical Temperature Distributions in Silica-Phenolic Nozzle Compared with NASA TND-1726 Experimental Data, Run Time = 40 seconds.	114
33. Analytical Temperature Distributions in Silica-Phenolic Nozzle Compared with NASA TND-1726 Experimental Data, Run Time = 40 seconds.	115
34. Analytically Determined Wall Temperature History for a Silica- Phenolic Cylinder Compared to Experimental Nozzle Test Data . . .	116

ILLUSTRATIONS (Continued)

<u>Figure</u>		<u>Page</u>
35.	Comparison of Test Data and Analytical Results for Ablative Refrasil-Phenolic, Char Depth vs. Burning Time.	117
36.	Microphotographs of Fired Silica-Phenolic Rocket Chamber. . . .	118
37.	Surface Temperature Response of Silica-Phenolic Semi-Infinite Solid as a Function of Heat Transfer Coefficient.	119
38.	Dissociation and Vaporization of Silica	120
39.	Silica Carbon Chemical Equilibria as a Function of Temperature at a Pressure of 5 psia	121
40.	Fused Silica Foam Samples from Silica-Phenolic Thrust Chamber Wall.	122
41.	Silica-Carbon Chemical Equilibria as a Function of Temperature at a Pressure of 100 psia	123
42.	Silica-Carbon Chemical Equilibria as a Function of Temperature at a Pressure of 200 psia	124
43.	Silica-Carbon Chemical Equilibria as a Function of Temperature at a Pressure of 10^{-3} mm Hg	125
44.	Wall Temperature Reduction from Transpiration Cooling Effect of Dimensionally Ablating Silica-Phenolic Thrust Chamber. . . .	126
45.	Ablative Nozzle Throat Erosion Pattern Compared to Measured Cold Wall Heat Flux Distribution.	127
46.	Experimental Surface Regression Rates for Silica-Phenolic Thrust Chamber Throat Section	128
47.	Experimental Surface Regression Rates for Silica-Phenolic Thrust Chamber Throat Section	129
48.	Experimental Surface Regression as a Function of Time for Silica-Phenolic Thrust Chamber Throat Sections.	130
49.	Analytically Determined Surface Regression Rates for a Silica-Phenolic Thrust Chamber as a Function of Heat Flux.	131

ILLUSTRATIONS (Continued)

<u>Figure</u>	<u>Page</u>
50. Analytically Determined Surface Regression Rate for a Silica-Phenolic Thrust Chamber as a Function of Heat Flux.	132
51. Endothermic and Sensible Heat Absorption of Silica-Phenolic Laminate as a Function of Temperature	133
52. Steady State Surface Temperature as a Function of Endothermic and Sensible Heat Absorbed for a Dimensionally Ablating Composite Material, $T_g = 5000^\circ\text{F}$	134
53. Steady State Surface Temperature as a Function of Endothermic and Sensible Heat Absorbed for a Dimensionally Ablating Composite Material, $T_g = 7000^\circ\text{F}$	135
54. Flow Velocity of Molten Silica Layer as a Function of Thrust Chamber Inner Surface Temperature	136
55. Inside Surface Temperature Rise Time for a Convectively Heated Cylinder	137
56. Time for Heated Inside Surface of Cylinder to Reach $(T_g - T_o) / (T_g - T_o) = 0.3$	138
57. Time for Heated Inside Surface of Cylinder to Reach $(T_g - T_o) / (T_g - T_o) = 0.5$	139
58. Time for Heated Inside Surface of Cylinder to Reach $(T_g - T_o) / (T_g - T_o) = 0.7$	140
59. Transient Temperature Response of Inner Surface of Graphite Throat Insert	141
60. Gaseous Film Cooling Requirements for Standard Nozzle with Two-Row Hole Pattern.	142
61. Gaseous Film Cooling Requirements for Standard Nozzle with Optimum Tangential Slot	143
62. Optimum Slot Width for Standard Nozzle with Optimum Tangential Slot.	144
63. Multislot, Film Cooled Pyrolytic Graphite Nozzle.	145

UNCLASSIFIED

ILLUSTRATIONS (Continued)

<u>Figure</u>		<u>Page</u>
64.	Insert Disk for Multislot, Film Cooled Pyrolytic Graphite Nozzle.	146
65.	Gaseous Film Cooling for Standard Nozzle with Multislot Cooling	147
66.	Comparison of Cooling Techniques.	148
67.	Saturn Model Engine Injector (Copper Injector).	149
68.	Schematic of Propellant Feed and Film Coolant System.	150
69.	Astrosystems Engine Installed in ATL Pad B.	151
70.	Variation of Theoretical Specific Impulse with Chamber Pressure.	152
71.	Thermocouple Installation in Graphite Nozzle.	153
72.	Film Cooled Slotted Steel Nozzle.	154
73.	Variation of Temperature with Time for Slotted Steel Nozzle with Hydrogen Film Cooling, Run 24.	155
74.	Burnout of Slotted Steel Nozzle with Hydrogen Film Cooling at 0.098 pps Hydrogen Flow Rate	156
75.	Thermocouple Locations for Runs 30 to 33, Combined Radiation/Film Cooling.	157
76.	Gaseous Film Coolant Manifold Used for Tangential Film Injection	158
77.	Thermocouple Locations for Runs 43, 44, and 58, Combined Radiation/Film Cooling.	159
78.	Variation of Temperature with Time for Uncooled Steel Nozzle, Run 51.	160
79.	Variation of Analytical and Experimental Nozzle Temperatures with Flow Rate, Radiation/Helium Film Cooling	161
80.	Variation of Analytical and Experimental Nozzle Temperatures with Flow Rate, Radiation/Hydrogen Film Cooling	162

TMC A673

UNCLASSIFIED

ILLUSTRATIONS (Continued)

<u>Figure</u>	<u>Page</u>
81. Variation of Specific Impulse Efficiency with Film Coolant Flow Rate for Helium, Hydrogen, and Methane	163
82. Graph-I-Tite G Nozzle after 203 seconds of Operation with Helium Film Cooling	164
83. Average Erosion of Helium Film Cooled Graphite Nozzle after Runs 45 and 46.	165
84. Variation of Temperature with Time for Helium Film Cooled Graph-I-Tite G Nozzle, Run 45	166
85. Graph-I-Tite G Nozzle after 240 seconds of Operation with Methane Film Cooling.	167
86. 180° Single Slot Pyrolytic Graphite Nozzle after 228 seconds of Operation with Methane Film Cooling.	168
87. Multislot Pyrolytic Graphite Nozzle after 180 seconds of Operation with Methane Film Cooling	169
88. Multislot Pyrolytic Graphite Nozzle after 274 seconds of Operation with Carbon Monoxide Cooling.	170

UNCLASSIFIED

TABLES

<u>Table</u>	<u>Page</u>
I. Coolants Inert to Graphite at 6000°R and 100 psia	69
II. Coolants which Decompose or React with Graphite at 6000°R and 100 psia.	70
III. Combustion Products for High Performance Liquid Propellant Systems	71
IV. Chemical Ablation Model, Silica Phenolic.	72
V. Evaluation of Heat Sink Capability of Materials for Nozzle Insert.	73
VI. Evaluation of Heat Sink Capability of Materials for Nozzle. . .	74
VII. Summary of Nozzle Test Data	75
VIII. Nozzle Temperatures for Runs 30 through 33.	79
IX. Nozzle Temperatures for Runs 43, 44, and 58	80
X. Nozzle Temperatures for Run 47.	81

TMC A 673

UNCLASSIFIED

I. SUMMARY

Thrust chamber cooling techniques applicable to liquid rocket engines using propellant combinations having combustion temperatures up to 8500°F have been investigated analytically and experimentally. (Two of the most promising thermal protection concepts developed during this program and demonstrated experimentally were the concept of multislot film cooled pyrolytic graphite and the concept of reducing graphite chemical erosion by injection of a gaseous hydrocarbon film to provide a favorable chemical environment in the nozzle boundary layer.)

A thermochemical erosion analysis computer program has been developed to calculate chemical erosion rates of graphite thrust chamber components based on reaction kinetics as well as heat and mass transfer phenomena occurring in cooled and uncooled rocket thrust chambers.)

Analyses based on this computer program revealed that the most effective gaseous film or transpiration coolant is hydrogen followed by helium and the other gases in the order of their molecular weight. The transpiration coolant found most effective in reducing chemical erosion of graphite was methane.) Chemical erosion could be reduced to zero, based on analysis, at a graphite temperature as high as 6000°R while, with all other coolant gases, the graphite temperature would have to be reduced to temperatures below 4000°R. This anomalous phenomenon, predicted analytically, was evaluated experimentally during small scale oxygen-hydrogen thrust chamber tests. Zero erosion of methane-cooled graphite nozzles was demonstrated at conditions where helium and carbon monoxide cooled graphite nozzles did erode.

The effective demonstration of the multislot film cooled pyrolytic graphite with both hydrogen and methane as well as other gases such as helium and carbon monoxide has provided a feasible cooling concept for application to the most severe rocket combustion environments. This concept, which approaches transpiration cooling in efficiency, takes advantage of the high temperature structural capabilities of the pyrolytic materials.

Analytical and experimental studies of the chemical mechanism of ablation in silica-phenolic ablative composites have provided evidence that the endothermic chemical reaction of silica with the carbon char in the thrust chamber environment is far more important than the transpiration cooling and heat absorption associated with the resin degradation. Thus, internal chemical reaction may very well control the performance of this type of thrust chamber material. Based on these studies, an analytical ablation model was formulated and criteria for improved ablative systems are proposed. The predicted performance of these materials with film cooling would depend more on the adiabatic wall temperature achieved than on the chemical composition of the coolant.

Analytical and experimental investigations of combined thrust chamber cooling techniques have provided additional design data and criteria for selection and application of various cooling concepts. A heat sink design optimization study has resulted in a technique for establishing optimum nozzle wall thicknesses based on combustion conditions, material properties, and engine size. Analyses show that substantial increases in run time are available with film cooling of heat sink configurations. Film cooling tests and analytical studies have been made for various gases to evaluate the effectiveness of single and multiple slot film injection compared to transpiration cooling. Experimental data were also obtained on combined film and radiation cooling using a helium cooled, molybdenum exit nozzle.

Based on the results of this program, it is recommended that the thermochemical erosion studies be extended to include new nozzle materials, additional combustion product species, and the effects of transient heat conduction. Studies should also be undertaken to provide additional reaction kinetics data, especially for the high energy propellant systems which include fluorine.

Theoretical and experimental studies should be pursued to apply these advanced cooling concepts and materials to the more severe higher temperature rocket systems in order to evaluate the design problems associated with using new propellants for long runs, with throttling, or for intermittent operation.

II. INTRODUCTION

A. Program Background

A program to evaluate liquid rocket thrust chamber cooling techniques applicable to spacecraft engines was conducted under NASA Contract NAS 7-103 during the year 1962. Studies were directed toward determining the limitations of the various cooling techniques and developing a procedure for selecting the most suitable design concepts for spacecraft engine application. The results of these studies were reported in Marquardt Report 5981, Volumes I and II (References 1 and 2).

Based on the results of these studies, it was concluded that improved cooling concepts would be required for the advanced high energy propellants. One of the more promising approaches appeared to be the development of combined cooling techniques to attain long operating life with a minimum engine performance penalty.

B. Program Approach

The studies undertaken during this follow-on contract (NAS 7-103, Amendment 2) were directed toward development of combinations of thrust chamber cooling techniques and materials which would be suitable for the most severe liquid propulsion systems presently envisioned, with combustion temperatures up to 8500°F and combustion pressures ranging from 100 to 3000 psia. It is generally recognized that cooling methods and materials in current use are marginal or inadequate to meet the high heat fluxes and temperatures existing in such combustion environments.

The two types of cooling which are theoretically unlimited in their capability for cooling are film and transpiration cooling. Therefore, this study has been organized so as to evaluate film and transpiration cooling, both in conventional methods of application, and also in more novel methods of application which combine film or transpiration cooling with other cooling methods such as radiation, ablation, heat sink, and regenerative cooling. Since the primary challenge to thrust chamber design for the advanced liquid propellants is the high heat flux and temperature near the nozzle throat, combined cooling methods were studied primarily for application in the throat region, but all of the concepts investigated would also be applicable in the combustion chamber and expansion nozzle. Combinations which use one cooling method in one portion of the thrust chamber and another cooling method in another portion of the chamber might be advantageous for some applications, but they were not evaluated in detail during this study.

The possibility of using a coolant other than the fuel or oxidizer was introduced into the study. The use of a "third component" coolant has been ruled out in the past, but it was thought advisable to evaluate the advantages of

using a third component, realizing that system complexity and reliability penalties might result. The study of film and transpiration cooling was also extended to encompass the thermochemical effects of various coolants due to their chemical reaction with the wall and the combustion gases.

An important aspect of film and transpiration cooling is the associated loss in combustion performance. The available experimental data regarding this are very inadequate. However, for several coolant and propellant combinations for which test data are available, the performance penalty is approximately that which would occur if the coolants were completely inert. No data are available for the effects of film and transpiration cooling on the performance of advanced liquid propellants. It is recognized that the performance penalty will probably depend on the particular coolants and propellants used and also on the location of the injection. For example, coolant which is injected through the injector face and combustion chamber walls, if reactive with the propellants, or if it were one of the propellants, might produce little or no performance loss. Coolant injected near or downstream from the throat, however, might produce a greater performance penalty. It was planned that the thrust penalty due to film and transpiration cooling near the nozzle throat be measured for some of the coolants of current interest, particularly the low molecular weight gases.

It was also recognized that many advanced propulsion systems must perform satisfactorily for only a short period of time, so that transient effects on thrust chambers, such as erosion or ablation, may be permissible in order to avoid making unreasonable and expensive demands on cooling systems and materials. Therefore, emphasis has been placed on understanding the effects of the chemistry of the propulsion environment on the transient behavior of thrust chamber materials.

Before an intelligent evaluation of combined cooling methods could be made, a better understanding of the phenomena governing behavior of some of the individual cooling methods was necessary since combinations of these cooling methods at the same locations in the thrust chamber introduced new conditions more complex, in most cases, than those which arise when the cooling methods are used singly. Therefore, analytical studies of heat sinks, ablation phenomena, and surface reaction kinetics were conducted with the expectation that the results of these studies of single systems would provide guidelines to optimum combinations of methods.

An incomplete list of cooling combinations of interest is as follows:

1. Film/heat sink
2. Transpiration/heat sink
3. Film/radiation

4. Transpiration/radiation
5. Film/ablation
6. Transpiration/ablation
7. Film/regenerative
8. Transpiration/regenerative
9. Radiation/heat sink

Zoned combustion might be considered a variety of film cooling, but this method has not been evaluated. Some of the major questions regarding individual cooling systems will now be discussed. Detailed results of the program are presented in Section III, Analytical Studies.

C. Cooling Techniques Studied

1. Inert Film Protection

A major portion of the analysis program has been devoted to the study of a gaseous transpiration cooling method, also termed "inert film protection". The original concept was that, if enough inert gas were introduced into the boundary layer, either by transpiration or film injection, the rate of chemical attack of the wall could be reduced or eliminated entirely. To establish the feasibility and attractiveness of this concept, a computer program was formulated for analysis of steady state chemical erosion and surface temperature of a graphite thrust chamber with transpiration of coolant gases through the wall using the propellant combination, O_2 and H_2 . This choice of wall material and propellants was made because of the relative simplicity of the resultant chemical environment in the boundary layer, because graphite is an outstanding high temperature material, and in order to permit test correlation with a relatively simple propellant system. Similar computer programs could theoretically be formulated for other wall materials and propellant combinations although reaction kinetics data would probably have to be generated by laboratory tests for most other materials and propellants.

The computer program developed was designed to include the effect of any arbitrary steady state heat flux into the wall and thus be easily adaptable to the analysis of the combined effect of transpiration and radiation cooling for thin wall graphite motors which reach a steady state wall temperature rapidly. However, program modifications would be necessary to analyze combined transpiration/heat sink systems.

The reference to inert films is not meant to imply that only noble gases are to be considered as coolants. Other gases may also be inert to graphite and/or the combustion gases up to very high temperatures. In fact, a number of such gases have already been identified, including carbon monoxide and carbon suboxide (C_3O_2). A second category of gases are those that may react with graphite but at such a low rate as to be acceptable. An example is hydrogen which is such an excellent coolant that its reaction with graphite can be tolerated. A third category of gases are those which produce a favorable chemical reaction in the boundary layer with a net result of reducing the erosion rate of the wall. An example is methane, which pyrolyzes in the boundary layer, producing carbon, which it is theorized, may react with water vapor from the free stream, preventing or reducing the reaction of the water and graphite.

The computer program was to be formulated for transpiration injection only, with no attempt to analyze the inert film protection concept for discrete film injection because of the extremely difficult nature of the analysis of the turbulent boundary with pressure and chemical composition gradients in the flow direction. This difficulty is due to mass and heat transfer processes taking place at the wall and at the edge of the boundary layer. A comparison of the difference between film and transpiration injection of inert films would best be obtained experimentally.

2. Ablation

Despite a considerable effort to understand ablation phenomena (restricted here to reinforced plastics and similar materials), current descriptions have consisted primarily of attempts to correlate test data for a wide variety of test conditions, sometimes using oversimplified parameters such as "effective heat of ablation". The behavior of ablation materials in re-entry conditions has also rather arbitrarily been assumed to be representative of ablation in rocket motor conditions, which have been studied much less than the ablation phenomena in re-entry. It was apparent that a better understanding of the chemical and heat transfer processes taking place in rocket chamber ablation was necessary before the advantages of combining film cooling with ablation or controlling film chemistry (using "inert film protection") over ablatives could be evaluated. Studies of chemical and heat transfer processes at ablative surfaces have therefore been pursued.

3. Heat Sink

Heat sinks have been used successfully in rocket nozzle applications in the past, but design optimization has been done for only a limited number of design conditions. Therefore, some attempt to parameterize nozzle heat sink characteristics has been made.

4. Film Cooling

Almost all film cooling studies in the past have been done for gas flows over adiabatic walls in cylindrical sections or over flat plates. All film cooling "analyses" really consist primarily of empirical curves which have correction factors introduced to assist correlation with test data. Since pure analysis has been found so inadequate for film cooling in cylinders or over flat plates, it was desirable that test data be obtained for an evaluation of film cooling when applied to converging-diverging nozzles which have non-adiabatic walls due to radiation or heat sink cooling.

D. Experimental Program

A small scale experimental program was undertaken to explore, in a hydrogen-oxygen rocket engine environment, some of the more promising cooling concepts which evolved during the analytical portion of the program. These tests also supplied experimental data on material erosion rates and film cooling effectiveness not available in the literature. Specific cooling concepts to be evaluated were as follows:

1. Multislit cooling of a pyrolytic graphite nozzle
2. Transpiration cooling of a porous graphite nozzle, using inert or reactive coolant gases
3. Combined film and radiation cooling

Future experimental investigations envisioned as a logical extension of this work are the application of these cooling concepts to the higher energy propellant systems such as $\text{OF}_2/\text{B}_2\text{H}_6$. Marquardt is currently completing the construction of a remote rocket test site in Magic Mountain, California, to be used for testing with exotic cryogenic and high impulse liquid propellants.

UNCLASSIFIED

This page intentionally left blank.

MAC A673

UNCLASSIFIED

III. ANALYTICAL STUDIES

A. Thermochemical Equilibrium Studies

Thermodynamic equilibrium studies were made of the possible reactions of various coolants with graphite, using the IBM 704 thermodynamic sub-routine. The equilibrium studies amount to a screening process, in that complete inertness of the coolant in contact with the graphite can be established. However, if some finite amount of reaction occurs between coolant and graphite, the usefulness of the coolant can be evaluated only if kinetics data are available for all important reactions. These reactions include not only the reaction between the coolant and the wall, but also reactions between all product species and combustion species with the wall.

Thirteen gases (Tables I and II) were chosen for thermochemical equilibrium studies, based on their suitability for cryogenic storage and their possible inertness to carbon at elevated temperatures. The reactions were evaluated at a pressure of 100 psia and over the temperature range from 2500° to 7500°R. The initial graphite-to-coolant weight ratio was 2.0.

Four coolants which were found not to react with the graphite at 6000°R are shown in Table I. Two of those gases, CO and C₃O₂, actually release carbon at intermediate temperatures of 1000° to 3000°R producing CO and CO₂, although the kinetics of such reactions are not known.

It should be remembered that calculations based on thermodynamic equilibrium assume that products of all forward and reverse reactions remain available for further reactions, which may not be the case in application since either solid or gaseous products may be carried away.

Nine coolants which react with graphite at 6000°R and 100 psia are listed in Table II along with the major compounds formed with graphite.

It has been assumed during this study that all of the noble gases will be nonreactive with the graphite wall and the combustion products. Recent work has shown that xenon can react with fluorine to form several types of molecules such as XeF₄, but these compounds are stable only at low temperatures and can be ignored in the current application. Lighter noble gases are even more difficult to compound and would be even more unstable even at room temperature (Reference 3).

B. Thermochemical Erosion Analysis

1. Analysis Objectives

The principal objective of the thermochemical erosion analysis was to determine how much the rate of chemical erosion of a thrust chamber wall could be reduced by injection of various coolant gases into the boundary layer. The coolants would alter the chemical composition of the boundary layer so as to provide a more favorable environment as well as producing a cooling effect.

A more favorable chemical environment for the thrust chamber wall could be achieved by several categories of coolants, as follows:

1. Inert gases, meaning the noble gases such as helium, neon, etc., and also gases which on the basis of equilibrium thermodynamics should not react with the wall. An example of the latter would be the use of carbon monoxide for cooling of graphite.
2. Reacting gases which, although reactive with the wall, react at a slower rate than some of the combustion gas species which they displace in the boundary layer. An example of this category of coolant was found during the present study to be hydrogen when used in cooling a graphite thrust chamber for O_2/H_2 propellant.
3. Reacting gases which either decompose or react with the combustion gas to produce a gas composition at the wall which either reduces or eliminates chemical erosion of the wall. An example of this category of coolant was found during the present study to be methane, which pyrolyzes and either eliminates erosion of a graphite chamber or may even deposit additional graphite on the wall.

No previous investigation of this concept was known, and the complexity of the problem indicated the advisability of restricting the initial analysis to a specific thrust chamber material, pyrolytic graphite, and a specific propellant combination, O_2 and H_2 .

Pyrolytic graphite had previously been found to be one of the most outstanding high temperature materials available for thrust chamber construction, due not only to its exceptional high temperature strength but also to its low reaction rates in the combustion products of such diverse propellant combinations as O_2/H_2 and F_2/H_2 . It was hoped that very small amounts of injected gases would be sufficient, considering both their cooling and chemical effects in the boundary layer, to provide protection and permit the utilization of the high temperature structural capability of pyrolytic graphite. Implicit in the basic objective of the concept was the supposition that it would be advantageous to reduce the amount of required coolant. Most of the previous work with film and transpiration cooling had been done by providing enough coolant to permit use of conventional materials such as steel. There was some limited data indicating that film cooling of combustion chambers could be accomplished without a loss of performance, but that film cooling of the contraction region and throat did cause a significant loss in performance in proportion to the amount of coolant used. Therefore, the potential advantages of the concept being studied would be: (1) minimization of performance loss due to cooling; and (2) greater reliability of a pyrolytic graphite structure as compared to lower melting point materials such as steel.

Only gaseous injection of coolants was considered since it was thought that uniform injection of very small amounts of liquid coolant would be quite difficult to achieve.

After choosing the thrust chamber material and propellant combination to be studied, it was necessary to choose a method of injecting the coolant. It is well established that transpiration is the most efficient form of cooling. This method can be approached in efficiency by films injected at closely spaced intervals. It was evident also that the analysis could more easily be made for a transpiring coolant, despite the fact that the practicability of using a true porous transpiration structure is questionable for materials like graphite.

Therefore, the model chosen (Figure 1) for analysis was that of a porous pyrolytic graphite wall transpiring various cooling gases into the boundary layer. The only difference in the analysis between pyrolytic graphite and commercial graphite would be in densities, surface reaction rates, and heat conduction into the interior of the wall. Provision for the conduction effect was included on a steady state basis, but nearly all the numerical results obtained to date were for an adiabatic wall.

The cooling techniques being investigated were directed ultimately toward use with advanced liquid propellants which produce much higher combustion temperatures than O_2/H_2 . However, as the analysis evolved, it became evident that no meaningful analysis of the chemical erosion by the advanced propellants was possible at the time, due to the lack of kinetics data for reactions of the combustion products of advanced propellants such as F_2/H_2 with candidate thrust chamber materials such as tungsten or graphite. However, it was thought that the advantage of controlling the chemical composition of the boundary could be studied by considering some combination of combustion products and wall material for which kinetics data were available. Also, the high heat flux effects of the advanced propellants were simulated by specifying several hypothetical propellants as discussed in the next section.

2. Advanced Propellants

Some liquid propellant combinations which give high performance are listed in Table III, which also lists their combustion products, performance, and combustion temperature at selected mixture ratios. The mixture ratios chosen are those that give approximately maximum performance. It is known that greater percentages of oxidizer will often yield a more optimum overall system, at the expense of I_{sp} , but consideration of the optimum mixture ratio is beyond the scope of this study. It might be noted, however, that the combustion temperature will ordinarily increase with mixture ratio, in several cases reaching $8500^\circ F$, which is the maximum temperature being considered in this study.

Two hypothetical propellant combinations, designated P7000 and P8500, to indicate combustion temperatures of 7000° and 8500°F, are also listed in Table III. The combustion products of P7000 and P8500 were arbitrarily assumed to be the same as those of O_2/H_2 , which were assumed for the calculations to be 62.5 percent H_2O and 37.5 percent H_2 .

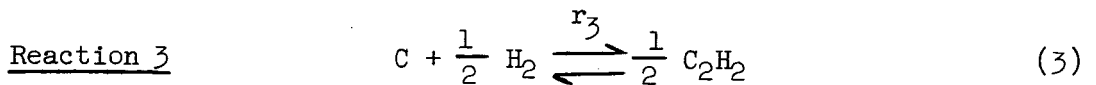
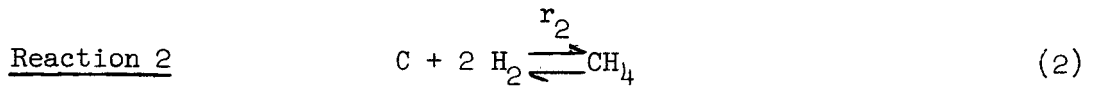
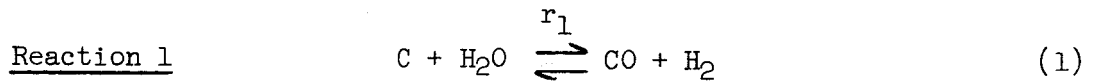
It is shown in Table III that the combustion products of O_2/H_2 include not only H_2O and H_2 but also small amounts of H , OH , O and O_2 . However, the mathematical difficulties which might be encountered in analyzing the problem were unknown, and it was thought advisable to maintain a reasonably simple analysis model for the first computer program. The sublimation of graphite was excluded from the computer program for the same reason. Justification for the use of the simple model lies, in addition to expediency, in the fact that the objective was primarily to evaluate trends in nozzle erosion using various coolants, which could be done although the absolute values of the erosion rates are only approximate using presently inadequate kinetics data. The results of the present analysis are not expected to be highly accurate, especially at wall temperatures where sublimation of graphite occurs, but they do show the way to go in future analyses of nozzle cooling methods.

The computer program which resulted from the analysis is limited to systems composed of graphite, water, hydrogen, methane, acetylene, carbon monoxide and inert gases. Examination of Table III shows that knowledge of the reaction rates of a number of other gases with graphite would be required for analysis of the chemical erosion of graphite for all of the advanced liquid propellant combinations. The reaction rates of oxygen and graphite could be obtained, but it is doubtful whether a literature survey at the present time would yield any kinetics data for the boron and fluorine compounds listed in Table III. In any case, it was thought that most of the implications of inert or other chemical films for very high temperature combustion gases could be obtained by specifying some arbitrary chemical composition adaptable to the computer program together with a high combustion temperature. Therefore, propellants P7000 and P8500 were specified. A comparison of the calculated heat flux to the nozzle from the various advanced propellants is shown in Figures 2 and 3, and it is seen that P7000 and P8500 represent the heat fluxes expected from the advanced propellants, which greatly exceed the heat flux from O_2/H_2 . The heat flux comparisons in Figures 2 and 3 are for ideal combustion. However, all other calculations in this study were based on 95 percent C^* efficiency.

3. Analysis Procedure

A model of the problem to be analyzed is shown in Figure 1. The principal combustion gases of interest are H_2O and H_2 . Reactions of H_2O and H_2 with graphite were compared on the basis of free energy changes, and the following reactions were chosen to be of greatest importance:

UNCLASSIFIED



a. Reaction Rate Equations

The reaction rates of the above equations were studied in terms of various models, as described in Appendix B. The rate equations which were chosen for the analysis are as follows:

$$r_1 = c_1 e^{-\frac{E_1}{RT_w}} \left[P_{\text{H}_2\text{O}} - \frac{P_{\text{CO}} P_{\text{H}_2}}{K_{e1}} \right] \quad (4)$$

$$r_2 = c_2 e^{-\frac{E_2}{RT_w}} \left[P_{\text{H}_2} - \frac{P_{\text{CH}_4}^{.5}}{K_{e2}^{.5}} \right] \quad (5)$$

$$r_3 = c_3 e^{-\frac{E_3}{RT_w}} \left[P_{\text{H}_2} - \frac{P_{\text{C}_2\text{H}_2}}{K_{e3}^2} \right] \quad (6)$$

The equilibrium constants K_{e1} , K_{e2} , and K_{e3} are defined as follows:

$$K_{e1} = \frac{(P_{CO}) (P_{H_2})}{(P_{H_2O})} \quad (7)$$

$$K_{e2} = \frac{P_{CH_4}}{(P_{H_2})^2} \quad (8)$$

$$K_{e3} = \left(\frac{P_{C_2H_2}}{P_{H_2}} \right)^{1/2} \quad (9)$$

The equilibrium constants can also be described as follows:

$$K_{e1} = e^{(A_1 - \frac{\Delta H_1}{RT_w})} \quad (10)$$

$$K_{e2} = e^{(A_2 - \frac{\Delta H_2}{RT_w})} \quad (11)$$

$$K_{e3} = e^{(A_3 - \frac{\Delta H_3}{RT_w})} \quad (12)$$

The partial pressures of the species were obtained from Dalton's Law:

$$P_i = (x_i)_w P \quad (12a)$$

The rate equations are based on first order reactions. Review of available kinetics data did not reveal an adequate basis for any other assumption since practically all kinetics data which report partial pressure exponents from $1/2$ to $3/2$ were gathered in low mass transfer conditions, so that the true kinetics behavior was obscured by diffusion effects. However, other than first order reactions can be used in the program if found necessary.

b. Mass Transfer Equations

Calculation of the rate of mass transfer of gaseous species across the boundary layer was done using simplified engineering relationships derived from the analogy between convective heat transfer and mass transfer rates across a boundary layer.

The physical problem being studied consists of a multi-component mixture of gases with different physical properties and molecular weights. Simplification was made in describing the problem along the lines suggested in Reference 4.

The mass transfer rate of each species from the wall to the free stream is described as follows:

$$(N_i)_w = (x_i)_w F + k_i \left[(x_i)_w - (x_i)_g \right] \quad (13)$$

The first term on the right side of Equation (13) represents the transfer of species 'i' due to the bulk movement of the gas mixture away from the wall. In some special cases, the bulk motion of the mixture may be toward the wall, in which case F is negative. The numerical evaluation of F is obtained from the following expression:

$$F = (N_{H_2O})_w + (N_{CO})_w + (N_{CH_4})_w + (N_{C_2H_2})_w + (N_{H_2})_w + (N_{inerts})_w \quad (13a)$$

The rate of mass transfer of CO from the wall to the stream is given by:

$$(N_{CO})_w = r_1 + G_c (x_{CO})_c \quad (13b)$$

Similarly, the mass transfer of inert gases from the wall to the stream is given by:

$$(N_{\text{inerts}})_w = G_c (x_{\text{inerts}})_c \quad (13c)$$

In this fashion, Equation (13a) can be evaluated, leading to the following:

$$F = r_1 - r_2 + G_c \sum (x_i)_c \quad (13d)$$

But:

$$\sum (x_i)_c = 1 \quad (13e)$$

Therefore:

$$F = r_1 - r_2 + G_c \quad (13f)$$

The second term on the right side of Equation (13) represents the transfer of species 'i' due to molecular diffusion caused by a concentration gradient of species 'i'.

The diffusion coefficient, k_i^\bullet , carries a black dot exponent to indicate that it includes a correction for the effect of the mass transfer rate on the uncorrected mass transfer coefficient, k_i . For simplicity the mass transfer coefficients for all species were assumed to be the same, so the subscript "i" can be dropped. The correction factor for k^\bullet was obtained from Reference 4, page 663, from film theory and is defined as follows:

$$\theta = \frac{k^\bullet}{k} \quad (14)$$

and is evaluated from:

$$\theta = \frac{\phi}{e^\phi - 1} \quad (15)$$

$$\phi = \frac{F}{k} \quad (16)$$

The mass transfer coefficient, k , can be obtained from the analogy between heat and mass transfer, and for equal Prandtl and Schmidt numbers it can be shown that:

$$k = \frac{h_g}{\bar{c}_p} \quad (17)$$

Where:

h_g = Convective heat transfer coefficient, uncorrected for mass transfer effects

\bar{c}_p = Mean specific heat in boundary layer

$$= \sum_i \frac{(x_i)_w + (x_i)_g}{2} c_{p_i}$$

The rate of the transfer of each species from the wall to the free stream (i.e., combustion gas) must equal its net rate of production at the wall by chemical reaction plus its rate of transpiration at the wall as a cooling gas.

As an illustration, consider the mass balance for the species, H_2 .

$$\text{Rate of generation at wall} = r_1 \quad (18)$$

$$\text{Rate of consumption at wall} = 2 r_2 + 0.5 r_3 \quad (19)$$

$$\text{Rate of transpiration at wall} = (x_{H_2})_c G_c \quad (20)$$

Rate of transfer from wall to stream =

$$(x_{H_2})_w F + k \cdot \left[(x_{H_2})_w - (x_{H_2})_g \right] \quad (21)$$

The mass balance at the wall for H_2 is then as follows:

$$(x_{H_2})_w F + k^* \left[(x_{H_2})_w - (x_{H_2})_g \right] = r_1 - 2 r_2 - 0.5 r_3 + (x_{H_2})_c G_c \quad (22)$$

Solution of Equation(22) for $(x_{H_2})_w$ leads to the following equation for the mole fraction of H_2 at the wall:

$$(x_{H_2})_w = \frac{k^* (x_{H_2})_g + r_1 - 2 r_2 - 0.5 r_3 + G_c (x_{H_2})_c}{k^* + F} \quad (23)$$

By the same procedure, similar equations were obtained for the species, H_2O , CO , CH_4 , C_2H_2 , and inert gases as follows:

$$(x_{H_2O})_w = \frac{k^* (x_{H_2O})_g - r_1 + G_c (x_{H_2O})_c}{k^* + F} \quad (24)$$

$$(x_{CO})_w = \frac{k^* (x_{CO})_g + r_1 + G_c (x_{CO})_c}{k^* + F} \quad (25)$$

$$(x_{CH_4})_w = \frac{k^* (x_{CH_4})_g + r_2 + G_c (x_{CH_4})_c}{k^* + F} \quad (26)$$

$$(x_{C_2H_2})_w = \frac{k^* (x_{C_2H_2})_g + 0.5 r_3 + G_c (x_{C_2H_2})_c}{k^* + F} \quad (27)$$

$$(x_{inert})_w = \frac{k^* (x_{inert})_g + G_c (x_{inert})_c}{k^* + F} \quad (28)$$

The preceding equations for the reaction rates and mole fractions at the wall of the various species are solved using the IBM 7040 computer for simultaneous solutions at a constant wall temperature, as shown in Figure 4. A heat balance equation is then solved to determine whether the wall temperature used for simultaneous solution of the reaction rate and wall composition equations is satisfactory.

Iterations on the wall temperature, reaction rates and gas composition at the wall are made as shown in Figure 4 until all equations are satisfied. The IBM computer program makes provision for as many as three inert gases in the coolant and combustion gas. The program also provides for a multiplication factor, C_m , to arbitrarily increase the mass transfer coefficient.

c. Erosion Rate Equation

The rate of chemical erosion of the graphite wall can be shown to be described as follows:

$$\dot{y} = \frac{12,012 (r_1 + r_2 + r_3)}{\rho} \quad (29)$$

Where:

\dot{y} = Erosion rate, mils/sec

r_1, r_2, r_3 = Reaction rates, $\frac{\text{lb-moles of carbon}}{\text{in}^2 \text{sec}}$

ρ = Wall density, lb/in³

12,012 = Molecular weight of carbon x 1000

d. Wall Temperature Equation

The wall temperature is affected by the rate of heat transfer to the wall (restricted to convection for this study), heat transfer into the wall by conduction, heat absorbed or evolved at the wall by chemical reactions, and heat absorbed at the wall by transpiring coolant. A heat balance on the total projected area of the wall leads to the following equation for the equilibrium wall temperature:

$$T_w = \frac{hT_g + G_c L (\bar{c}_p)_c T_c - r_1 \Delta H_1 - r_2 \Delta H_2 - r_3 \Delta H_3 - Q_k}{h + G_c L (\bar{c}_p)_c} \quad (30)$$

The convection coefficient, h , is corrected for the effects of mass transfer by Equation (31), which gives a fairly good correlation with test data for the effect of transpiration on convection heat transfer coefficients:

$$h = h_g e^{\left[-0.5 \left(\frac{1}{\bar{M}} \right)^{0.43} \frac{F}{G_g St_g} \right]} \quad (31)$$

Where:

h_g = Uncorrected convective heat transfer coefficient

\bar{M} = Molecular weight of stream \div molecular weight at wall

Values of h_g were calculated from the modified Bartz equation as presented in Reference 5.

4. Parameter Study of Nozzle Erosion

The analysis program was used to calculate the chemical erosion of pyrolytic graphite for a range of combustion chamber sizes, pressures and temperatures. A standard nozzle geometry (Figure 5) used for most of the studies had a throat diameter of 1.25 inches, a convergence angle of 30°, a divergence angle of 15°, a radius of curvature of 1.25 inches, and extended from a contraction ratio of 4 to an expansion ratio of 1.5.

The nozzle was divided into 5 sections. The calculations were made at the midpoint of each section, and then the flow rates were totaled to give the total nozzle coolant flow rate. The method of division of the nozzle into five sections is shown in Figure 6, where Sections 1, 2, 3, 4, and 5 comprise the standard nozzle for the analysis. Also shown in Figure 6 are Section 0, representing a cylindrical 4:1 combustion chamber, and Section 6, representing a portion of a Rao expansion nozzle.

During the iterative computation procedure, shown in Figure 4, the coolant mass flow rate G_c and propellant mass flow rate G_g at each section were held constant while the wall temperature and gas composition at the wall were calculated from the mass and heat balance equations. The value of G_g was determined from the propellant flow rate Z_g by the following equation:

$$Z_g = G_g M_g A_g \quad (32)$$

Where

Z_g = Propellant flow rate, lb/sec

G_g = Propellant flow rate, lb-mole/in²sec

M_g = Molecular weight of propellant gas

A_g = Cross-sectional area of combustion chamber section at average area ratio of section

The midpoint of each section was determined at the average area ratio; for example, the average area ratio of Section 1 is 3.25. All stream properties such as the heat transfer coefficient, h_g , and the static pressure, P , were evaluated at the average area ratio of each section, with the exception of the stream recovery temperature, which was approximated by the combustion chamber temperature, T_g , at all stations. The coolant inlet temperature was 70°F.

The coolant flow was calculated from the following equation:

$$Z_c = G_c M_c A_c \quad (33)$$

The coolant area, A_c , is simply the cooled wall surface area of the section.

The wall temperature, erosion, etc., are different at every station because of changing stream conditions, but the propellant flow rate Z_g is constant everywhere. Therefore, the cooling requirements are plotted as a coolant/propellant flow ratio, Z_c/Z_g . The flow ratio for the nozzle is the total of Z_c/Z_g for Sections 1, 2, 3, 4, and 5 for any given wall temperature. The coolant/propellant area ratio, A_c/A_g , of each section is shown in Figure 6 for throat diameters of 0.6, 1.25, 3.0, and 6.0 inches.

a. Erosion Rates

The effect of transpiration cooling on wall temperatures and throat erosion rates is shown for O₂/H₂, P7000, and P8500, all at 100 psia, in Figures 7 through 9. The coolant-propellant flow ratio, Z_c/Z_g , is the amount of coolant required to cool the entire nozzle (4:1 contraction to 1.5 expansion) to the same temperature. Only the erosion rates at the throat are shown since this region is usually where control of erosion is most important. The first conclusion to be drawn from Figures 7 through 9 is that the low molecular weight coolants are favored because of their excellent cooling capability. In particular, hydrogen, although reactive with carbon, is such a good coolant that its overall effect is to eliminate nozzle erosion with less weight flow than any other

UNCLASSIFIED

REPORT 6069

coolant except, in some cases, CH_4 . This fact is due not only to the relatively slow reaction rates of H_2 and carbon as compared to H_2O and carbon, but also due to the fact that the mass transfer rates are so high that it takes a large amount of transpired gas flow to cause a large change in the gas composition at the wall. However, a cooling effect proportional to the coolant flow rate reduces the wall temperature with a rapid decrease in reaction rate.

Another interesting result is that a negative erosion rate was predicted for intermediate wall temperatures when cooling with CH_4 , implying that pyrolysis of the methane produces carbon in the boundary layer which deposits graphite in a manner analogous to the production of pyrolytic graphite. Even if other factors such as fluid dynamic effects might prevent actual deposition of carbon on the nozzle wall, the presence of free carbon would act as a buffer between the combustion gas and the graphite wall, reacting with erosive combustion gas species before they can diffuse to the wall. The behavior of methane is of interest for propellants such as OF_2/CH_4 and might also be considered as an auxiliary coolant for propellants which in themselves are not good coolants.

The erosion rate in other portions of a thrust chamber can be either greater or less than the throat erosion rate, depending on the combined effects of local heat and mass transfer rates, static pressures and combustion temperature. An illustration of the variation of erosion rate is shown in Figure 10 for an uncooled pyrolytic graphite thrust chamber at 100 psia chamber pressure. The wall temperature is always less than the combustion temperature because reactions 1 and 3 are endothermic. Several of the most important points illustrated in Figure 10 are as follows:

1. The erosion rate of O_2/H_2 is less in the throat than in the converging section of the nozzle.
2. The erosion rates for P7000 and P8500 are greatest in the throat.
3. The erosion rates drop more rapidly in the diverging section of the nozzle than would be predicted using the assumption of mass transfer control since the first order reaction rates are directly proportional to static pressure. For example, the mass transfer coefficients are about the same at equal expansion or contraction ratios, but the static pressures are not, hence the much lower erosion rates in the expansion nozzle. Again, it should be remembered that the analysis does not pretend to be accurate for very high wall temperatures but is only adequate to indicate trends and relative protection of various coolants.

UNCLASSIFIED

b. Thrust Chamber Pressure Effect

The percent of propellant required for cooling decreases slowly with increasing chamber pressure, as shown in Figures 11 and 12 for hydrogen cooling of the nozzle. Also shown are the enormous erosion rates of uncooled nozzles at higher chamber pressures due to the static pressure influence on reaction kinetics.

c. Thrust Chamber Size Effect

The percent of propellant required for cooling the nozzle is quite insensitive to size, as shown for throat diameters of 1.25, 3.0, and 6.0 inches in Figure 13 for a hydrogen cooled nozzle.

d. Combustion Temperature Effect

Coolant requirements increase with increasing combustion temperature, as shown in Figure 14 for hydrogen cooling. The extremely large erosion rates of uncooled pyrolytic graphite nozzles exposed to 7000° to 8500°F propellants are also shown. These erosion rates emphasize the necessity for some form of cooling or chemical film protection for nozzles using the advanced propellants.

e. Combustion Chamber and Expansion Nozzle Cooling

Cooling of the combustion chamber and expansion nozzle has been treated separately since there is a strong possibility that cooling of the combustion chamber can be accomplished without any performance loss, and cooling of the expansion nozzle may be unnecessary because of the very low erosion rates of an uncooled nozzle. However, a few calculations were made for a 4:1 chamber, using an empirically derived typical dependence of L^* with D^* . Calculations were also made for a section of a Rao expansion nozzle between 1.5:1 and 5:1. The ratios of cooled surface area to cross sectional flow area for the combustion chamber, nozzle, and bell sections are tabulated in Figure 6.

The results are shown in Figures 15 and 16 for D^* of 1.25 inches and 6.0 inches, respectively, cooling with hydrogen at 100 psia for P8500. The cooling requirements for the nozzle and chamber for the particular geometries evaluated are about the same for a D^* of 1.25 but are quite different for a D^* of 6.0 inches.

f. Chemical Effects of Coolant

Previous investigations of chemical erosion of graphite nozzles have been made using the assumption that the kinetics of the reactions of the erosive species with the graphite wall were so fast that thermodynamic equilibrium was achieved at the interface between the graphite wall and the gaseous

reactants and products. By that assumption, the rate of graphite erosion was limited by the rate of mass transfer of the reacting species through the boundary layer. However, it is now recognized that erosion rates calculated on this basis are higher than measured values by from one to two orders of magnitude.

The two principal innovations of the present analysis were: (1) consideration of both kinetics and mass transfer effects on graphite erosion; and (2) consideration of the chemical effects of various coolants on the erosion and cooling of the nozzle.

It is interesting to investigate the extent to which the coolants reduce graphite erosion because of their effect on chemical reactions, and to compare that reduction with the reduction of erosion due to lowering the wall temperature with a resultant reduction of the heterogeneous reaction rates. The variation of throat erosion with wall temperature is shown in Figure 17 for several cooling gases. Of course, different coolant flow rates would be required to achieve the same wall temperature, as shown in Figure 9, for the assumed condition of a pyrolytic graphite nozzle, D^* of 1.25 inches, a chamber pressure of 100 psia and the combustion temperature of 8500°F.

The erosion rates for the curve labeled "heat sink cooling" are the rates which would occur during the transient heating of a pyrolytic graphite heat sink without benefit of any film or transpiration cooling. The local gas composition at the wall for this condition is shown in Figure 18. The decreased water content at higher wall temperatures reflects the increased reaction rate of water and carbon as the temperature is raised.

Gaseous water is an effective coolant but reacts with carbon. However, it is shown in Figure 17 that the erosion rates when cooling with water would be only slightly greater (at the same wall temperature) than if no coolant were used. The gas composition at the wall using gaseous H_2O coolant is shown in Figure 19. However, it must be realized that some oxidizers, such as O_2 , will most likely react with carbon at a much faster rate than H_2O and might thus incur much greater erosion if used as coolants with the erosion rate perhaps being controlled by mass transfer rather than kinetics. This possibility emphasizes the importance of knowing the reaction kinetics if chemical erosion is to be predicted.

Hydrogen reduces the reaction rate, at a fixed wall temperature, by replacing some of the H_2O by the slower reacting H_2 , see Figure 20. Helium achieves the same effect, tending to replace both H_2O and H_2 with an inert, as shown in Figure 21.

Methane produces an unusual effect, and its cooling can be considered secondary to its chemical effect, which causes zero or negative erosion for wall temperatures as high as 6000°R. Gas composition at the wall with methane coolant is shown in Figure 22. Acetylene was also studied as a coolant

and was found to produce an effect similar to that of CH_4 although not as pronounced. It is possible that other reacting coolants would also produce favorable chemical reactions in the boundary layer.

The principal conclusion to be drawn from the foregoing comparisons is that the cooling effect of most of the coolants considered is far more important than their chemical effects. The principal exceptions are gases such as CH_4 and C_2H_2 which react to produce a more favorable chemical environment or gases which might be highly reactive, such as O_2 or OF_2 . For example, at a wall temperature of 5000°R , in the example of Figure 17, the erosion rate without any coolant is twice that for cooling with helium. However, a 400°F reduction of wall temperature, even using a reactive coolant such as H_2O , would achieve the same erosion rate as predicted for the inert helium. The 400°F drop in wall temperature would require a 21 percent increase in H_2O coolant flow rate, but the absolute magnitude of the coolant flow rates for transpiration cooling is so small that the increase is probably insignificant.

g. Reaction Rate Effects

As previously discussed, the heterogeneous reaction rates in a rocket motor are generally so slow that thermodynamic equilibrium between the wall and adjacent gaseous species is not achieved. A study of the effect of arbitrarily increased reaction rates was made for the throat of a 100 psia chamber using P8500. No cooling gas was used. The reaction rates for all three reactions were increased by factors of 10, 100, 1000, and 10,000. The throat erosion rate for various multiples of the nominal reaction rates is shown in Figure 23. It is apparent that a reaction rate multiple of at least 1000 would be required to approach the condition of mass transfer control. This fact is further illustrated in Figures 24 through 27 which plot the gaseous species at the wall versus reaction rate multiples for constant wall temperatures of 2000° , 4000° , 6000° , and 7000°R . Also shown as dotted lines, are the gaseous species calculated for thermodynamic equilibrium between combustion gases and the graphite wall.

Some species included in the equilibrium composition are not considered in the erosion program, but it is evident that the gaseous composition at the wall approaches thermodynamic equilibrium as the heterogeneous reaction rates are increased. The departure from thermodynamic equilibrium for the nominal reaction rate multiple of 1.0 is vividly shown in Figures 24 through 27.

Figure 27 for a wall temperature of 7000°R , illustrates the limitations of the present IBM computer program at very high graphite wall temperatures where sublimation of graphite becomes appreciable, producing many equilibrium species which are not included explicitly in the present analysis. However, the major species, CO , H_2 , and C_2H_2 , still show fairly good agreement with the erosion program wall compositions for large reaction rate multiples.

UNCLASSIFIED

REPORT 6069

Thermodynamic equilibrium is almost impossible to reach at the low wall temperature of 2000°R, as shown in Figure 24, but intermediate temperatures of 4000°R and 6000°R would permit thermodynamic equilibrium with reaction rate multiples of about 1000 to 10,000.

h. Mass Transfer Rate Effects

The insensitivity of erosion rates to increased mass transfer coefficients is illustrated in Figure 28 which shows the throat erosion of an uncooled nozzle using various multiples of the mass transfer coefficient.

C. Ablative Cooling Studies

1. Introduction

In the quest for improved ablative rocket thrust chamber materials, it is possible to establish some specific material characteristics required of any new materials considered if significant improvements in performance are to be achieved.

Ablative materials presently used in liquid rocket thrust chambers with propellants such as $N_2O_4/0.5 N_2H_4-0.5 UDMH$ or O_2/H_2 have shown promise of providing a simple, reliable thrust chamber cooling technique. In practice, however, these materials have proven to be marginal in their capability to cope with throat erosion, long run times, and propellant injector performance variations. If chamber pressure is increased, the performance of these ablative materials is even more restricted.

Improved materials are necessary to meet the above requirements as well as the more severe operating conditions imposed in the thrust chambers of liquid rocket engines using the higher energy propellant systems such as OF_2/B_2H_6 or F_2/H_2 . Although it is to be expected that continued improvements and refinements will be made in the two basic ablative systems, silica-phenolic and carbon cloth phenolic, a major advance in the state of the art is required to really meet the demands of the hotter propellants.

The silica-phenolic ablative composite has consistently shown superior performance over similar ablatives for use as the combustion chamber liner of liquid engines using $N_2O_4/0.5 N_2H_4-0.5 UDMH$. Run times of over 10 minutes have been reported (Reference 6) at chamber pressures up to 150 psia. For rocket engines in the thrust range of 2000 pounds and above, silica-phenolic appears to be practical as a throat material. However, throat erosion rates of 1 or 2 mils per second appear to be typical for this application. Of course, in all of these applications, the basic silica-phenolic has been optimized in composition and configuration by variation of such parameters as resin content, use of resin modifiers and additives, fiber type and orientation, and in the fabrication and curing techniques.

TMC 673

UNCLASSIFIED

UNCLASSIFIED

REPORT 6069

The carbon cloth-phenolic ablative composite has shown good performance in the exit nozzles of solid propellant rocket motors. However, the performance of this same material in a liquid rocket thrust chamber has been very poor. This performance has been attributed to the highly oxidizing nature of liquid propellant exhaust products which contain water vapor or carbon dioxide. In the very hot propellant gases such as H_2/F_2 or OF_2/B_2H_6 , the carbon phenolics have outperformed the silica phenolics because the exhaust products containing such species as HF are less reactive with the carbon matrix than with the SiO_2 of the silica-phenolic system. The surface temperature of the carbon phenolic can exceed $5000^\circ F$ and the material not fail through melting or vaporizing while molten silica would flow readily at temperatures above $4500^\circ F$.

Three basic approaches appear as logical avenues of research for improved ablatives. The first is to discover the ideal thrust chamber material which (1) would be capable of stable structural operation at the combustion gas temperature, (2) would be inert to the combustion gases and (3) would provide adequate insulation of the surrounding structure. Materials which approach the structural requirement, but so far have fallen short of the other requirements, are the graphites, refractory oxides, and carbides, as well as the more refractory metals such as tungsten and tantalum.

The second approach is to provide a composite material which is composed of a stable high temperature matrix material which is impregnated with a filler or resin which will decompose as the material absorbs heat and by outgassing of the decomposition products will provide cooling of the surface of the thrust chamber walls during the life of the engine. In some cases, the cooling provided may be sufficient to reduce the erosion rate to an acceptable value during the engine life. Outgassing appears to be the predominant cooling mechanism in the performance of carbon phenolics in nonoxidizing environments.

The third approach is to develop a composite material in which a highly endothermic reaction occurs between the major constituents of the composite at such a rate and at such a temperature that the surface of the composite will be cooled to a temperature where structural integrity is maintained at some minimum or acceptable erosion rate. It would be desirable that the products of the endothermic reaction be a solid plus a gas, so that a solid matrix remains and the product gas would also act as a transpiration coolant. Examination of silica-phenolic ablation in a liquid rocket environment reveals that the endothermic reaction between the silica and carbon char may well be the predominant erosion-controlling mechanism.

2. Preliminary Analytical and Experimental Studies

Several analytical and experimental tasks were undertaken to provide an understanding of the thermodynamic and chemical phenomena which were controlling the ablative char and erosion rates in silica phenolics.

TMC A673

UNCLASSIFIED

UNCLASSIFIED

a. Thermochemical Equilibrium Studies

A preliminary evaluation of the probability of a number of endothermic reactions occurring within the ablative composite was undertaken using the IBM 7040 Thermodynamic Subroutine to calculate the equilibrium composition of the mixture of reactants and products as a function of temperature. The enthalpy changes associated with these reactions were also calculated as a function of temperature.

Three important factors, in addition to enthalpy changes, were also considered as affecting the occurrence of the reactions indicated by the analyses. One important factor would be the reaction kinetics involved, which would affect the rate of these reactions in the time allowed by the situation in the combustion chamber. Also affecting the occurrence of these reactions would be the physical form of the reactants (liquid, fibers, gases, powder, etc.). A third consideration would be the physical phenomena associated with the indicated reactions. If one of the reaction products is a gas which is immediately driven off while a solid residue remains in the matrix, the reactions would tend to go to completion. If the reaction products resulted in complete loss of structural integrity of the chamber walls at an intermediate temperature (i.e., below 3500°F), the result of the reaction would probably be rapid erosion.

b. Heat Transfer Analysis

For specified ablative decomposition rates or char rates or erosion rates, the equilibrium transpiration cooled wall temperatures were calculated. These temperatures were then compared with the structural capability of the ablative matrix surface. In the case of glass forming oxides for which viscosity versus temperature is known, the flow of molten material along the nozzle walls can be estimated.

Of course, there must also be a heat balance between the heat absorbing capability of the ablative composite (due to conduction, reaction, vaporization, etc.) and the heat flux to the transpiration cooled wall by convection and radiation. It is desirable to operate at the highest wall temperature possible to minimize the heat input to the various heat absorbing phenomena, in order to attain maximum operating time with minimum mass addition.

c. Laboratory Evaluation

The probability of the analytically derived endothermic reactions being completed in the time available in the thrust chamber depends upon kinetic considerations. Several simple laboratory analysis techniques were used to obtain clues to the actual chemical reactions occurring within the ablative matrix. These techniques included, among others:

TMC 673

UNCLASSIFIED

1. The Differential Thermal Analyzer, which was used to detect the occurrence of endothermic and exothermic reactions within a resin, filler, matrix composite between room temperature and 2800°F.
2. Qualitative and quantitative analysis of the composition of various reaction products in the degraded silica-phenolic char structure.
3. Heating an ablative composite in an inert atmosphere to temperatures above 2000°F and analyzing the products by spectrography and X-ray diffraction to obtain data on the formation of stable reaction products at temperatures near the operating wall temperatures. Heating to different temperature levels and for different times provided qualitative kinetic data.

3. Char Rate and Transient Temperature Analysis

One of the more important parameters to be determined in the ablative process is the surface temperature of the ablating material which is the driving force for heat flow to the substrate. Since it is difficult to measure thrust chamber wall temperatures under operating conditions, other means must be used to estimate the surface temperatures analytically or experimentally. It was thought that the viscosity of the molten silica as a function of temperature could be used to bracket the feasible temperatures since viscosity could be correlated with the surface removal rate and the shear forces needed to accomplish the surface removal. A viscous shear flow model, described later, indicated that surface temperatures of 4000° to 4500°F appeared reasonable for an ablating silica-phenolic surface subjected to the dynamic shear stresses in the throat of a liquid propellant thrust chamber. Therefore, a preliminary charring ablation analysis was made assuming a constant surface temperature of 4300°F.

Three charring rate analyses were made using the IBM 704 Thermal Analyzer program.

The first analysis was conducted for a 1-inch silica-phenolic slab with an adiabatic back wall and a constant surface temperature of 4300°F. No allowance was made for transpiration cooling effects or for heat absorbed in the resin system degradation or phase change of the silica reinforcement. Excellent correlation was achieved when the analytically determined temperature distributions for the heating period were compared with experimental data obtained from NASA-Lewis Research Center for silica-phenolic nozzles attached to a 100 psia chamber pressure H₂/O₂ rocket engine. Somewhat poorer correlation was achieved in the cooling period, which was partly attributed to the choice of a slab configuration.

UNCLASSIFIED

REPORT 6069

The second analysis was made of wall sections of a 1750-pound thrust Saturn S-IVB ullage engine prototype. This analysis utilized a convective heat flux which was calculated to be consistent with the combustion chamber environment at the given location. The surface temperature of the analytical model was allowed to respond to this heat flux and the thermal diffusion properties of the material. The back faces of the cylindrical sections were assumed to radiate to a simulated test cell environment and, as before, no allowance was made for other than sensible heat absorption by the material. The surface temperature of the analytical model rose rapidly in 10 seconds to 4400°F and climbed gradually to 4600°F. The temperature distributions in the wall checked reasonably well with engine experimental data and very well with NASA-Lewis data.

A third transient thermal analysis was made for a cylindrical wall section equivalent to the experimental nozzles tested by NASA-Lewis (Reference 7). A schematic of the wall section is shown in Figure 29 with the equivalent thermal circuit. The boundary conditions and material properties were identical to the first analysis ($T_s = 4300^\circ\text{F}$, adiabatic outside wall, $\alpha = 3 \times 10^{-4} \text{ in.}^2/\text{sec}$). Again, excellent correlation was achieved with experimental data on the initial 30-second heating period, and also satisfactory correlation was achieved in the cooling period due to consideration of the radial heat conduction. The results are shown in Figures 30 through 33.

The two NASA-Lewis test nozzles were initially run for 30 seconds with 5 subsequent runs of 40 seconds each and complete cooling between runs. The temperature data were obtained at 3 axial planes in the nozzle with 4 thermocouples at various depths set 90 degrees apart. Figure 34 compares the analytically determined temperature history at a point in the nozzle with the temperature history for a single thermocouple at the same depth for the initial 30-second run and cool-down of one chamber. It is noted from Figure 34 that the experimental data rise faster than the calculated temperature curve. It is likely that the value of thermal conductivity is higher than the published value. The faster cooling rate after shut-down can be accounted for if radiation heat transfer from the hot surface is considered during the cooling period. Figures 30 and 31 show temperature distributions at various times during the initial run for both chambers and for all 3 planes plotted together as a function of distance from the inner surface. Figures 32 and 33 show temperature distributions for one chamber and one axial plane only but contain composite temperature history data for all six runs on the same plot.

Several important conclusions of this thermal analysis program are given as follows:

1. Surface temperature assumptions in excess of 4000°F for ablating silica-phenolic materials may be considered reasonable, both from the standpoint of resulting temperature histories in the material during heating, and from the viscous shear flow analogy described later in this text.

TMC A673

UNCLASSIFIED

UNCLASSIFIED

REPORT 6069

2. The fact that excellent correlation of analytically determined temperature distributions with the experimental data was achieved precludes the possibility of any great reduction in heat transfer by the transpiration cooling and heat absorption by chemical reactions in the charring ablation of silica-phenolic materials. When dimensional ablation occurs and phase change and chemical reactions have to be taken into account, endothermic absorption is important, as discussed later.

There are several precautions that must be observed when applying the simple thermal diffusion charring ablation model to future analyses. This model is for transient ablation where no surface recession is taking place. In general, radiation heat transfer inside the combustion chamber need not be accounted for but should be taken into account in the throat and exit areas. The temperature history of the outside of the ablative wall appears to be somewhat insensitive to the inside surface temperature for the range of material properties and combustion conditions encountered in current ablative thrust chambers. It may also be said that, for the initial steady state run, the thermal properties of the virgin materials are adequate to define the movement of the char line (800°F isothermal line) since the heat diffusion into the virgin material is a function of its prerun properties rather than the properties of the char structure formed behind this 800°F line. The changed thermal properties of the char structure must be considered, however, on a restart firing where the time required for the char progression to resume is definitely a function of the thermal diffusivity of the char. The change in thermal properties must also be considered in the cooling of the chamber.

Inasmuch as conventional charring ablation systems (i.e., silica-phenolics) demonstrate no particular reduction in surface temperature or charring rate attributable to heat absorbed in degradation of the resin, the consideration of precharred reinforced resin systems looks reasonable. The precharred systems are processed by undergoing controlled pyrolytic degradation, and the resulting product has greater structural integrity and dimensional stability than a virgin resin system which is pyrolyzed in the combustion chamber environment.

The analytical parameter which several agencies have used to calculate char depth as a function of time, when no dimensional ablation is present, is $\sqrt{\alpha t}$ (α = Thermal diffusivity) which appears in the general Fourier solution for transient heat conduction into a solid. All agencies have used this parameter either directly as char depth = Constant $\times \sqrt{\alpha t}$ or have used an effective diffusivity to account for the changing thermal properties of the material. Figure 35 presents char depth test data from several agencies compared to analytically determined progression of an 800°F isothermal line into the substrate. The 800°F isotherm transient for a cylinder produces a history which is dependent upon time to less than the 0.50 power (0.47 power for the case shown in Figure 35) with the actual exponent dependent upon the inside radius and the radius ratio. Calculations can be made to determine the range of cylinder proportions over which time to the 0.5 power may be used as a good approximation in char progression analysis.

TMC 4673

UNCLASSIFIED

UNCLASSIFIED

REPORT 6069

4. Analytical and Laboratory Studies

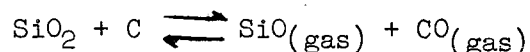
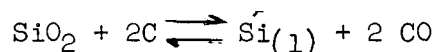
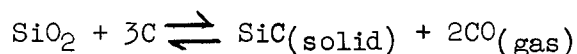
a. General Considerations

The chemical reaction potential between silica and a carbonaceous residue, though recognized, has not been directly related to ablative material performance in general. Several such $\text{SiO}_2\text{-C}$ reactions may take place in the range from about 2000° to 4500°F yielding SiC and CO initially and ultimately SiO and CO . The reactions may, in fact, completely consume the carbon in the char layer before any reaction occurs between the propellant combustion products and the carbon residue.

Both theoretical and experimental studies have been conducted to evaluate the kinetic nature of these chemical reactions and their possible effect on the ablation rate of silica-phenolic materials. A microphotograph of a wall section of a fired silica-phenolic thrust chamber (Figure 36) shows a carbon depleted layer to illustrate the region of interest in the carbon-silica reaction study.

An analysis of the transient thrust chamber surface temperature rise that would be predicted on the basis of only convective heat transfer in the chamber and heat conduction in the silica-phenolic wall material is shown graphically in Figure 37. These curves show that for a gas temperature of 5000°F and values of heat transfer coefficient above $100 \text{ Btu/hr-ft}^2\text{-}^\circ\text{F}$ the melting temperature of the silica (3100°F) is reached within 5 seconds. For the run times in excess of 50 seconds, the temperature of the silica surface without cooling would be within 650°F of the gas temperature. Therefore, all of the possible Si-C-O reactions that could occur at temperatures up to the flame temperature are of interest.

The region of carbon depletion beneath the molten layer is a region wherein SiO_2 may be ablated internally due to chemical reaction with the amorphous carbon residue of the charring process. The possible chemical reactions are as defined below:



UNCLASSIFIED

In all cases, there is an amount of SiO_2 in excess of that required to complete the reactions with the available carbon. Because of the silica-carbon depletion in the form of gaseous products, the melt layer assumes a foamy, low density consistency rather than becoming a uniform layer of molten silica. The techniques used to analyze the above mechanisms have included the following:

1. Heating of charred samples of silica-phenolic thrust chamber sections in a laboratory furnace in both inert and partial vacuum atmospheres
2. Heating of sandwich sections of alternate quartz glass and graphite slabs in a laboratory furnace
3. Heating of a virgin sample of silica-phenolic laminate in a Differential Thermal Analyzer
4. Flash exposure of a fired thrust chamber slag coated surface to an oxy-acetylene torch
5. Spectrographic analysis to examine elemental composition of ablative residues
6. X-ray diffraction analysis to determine the presence of crystalline structures (such as SiC) in the heated thrust chamber char sections and surface slag
7. Microphotographic study of the char structure
8. A computer analysis program to determine the chemical equilibrium composition of the silica-carbon reactions as a function of temperature and pressure.

b. Laboratory Experimental Analyses

(1). Experiment No. 1

Three char samples of a silica-phenolic thrust chamber wall were induction heated in a carbon crucible under controlled environmental conditions. The results are described as follows:

Speciman No. a:

Atmosphere: Argon at a pressure of 5 to
8 inches of mercury

Run time: 2 minutes

Maximum temperature: 2300°F

UNCLASSIFIED

REPORT 6069

The sample was reduced to a small fraction of its original size as a result of the experiment, with a large loss in weight. The curves of Figure 38 show that vaporization or dissociation of the silica alone would not occur at this temperature and pressure. It must be concluded that the silica was lost through reaction with the carbon to form $\text{SiO}_{(\text{gas})}$. The possibility of this reaction can be shown in Figure 39 which gives the chemical equilibrium composition for this reaction as a function of temperature and pressure.

Specimen No. b:

Pressure: 1 atmosphere (Argon)

Maximum temperature: 2850°F

Test Procedure:

Specimen heated 5 times to a temperature of 2650°F or less. The sixth run produced a temperature of 2850°F for a 1 minute run.

Little mass loss resulted compared to the previous experiment and as noted from rounding of the edges only. Sectioning of the sample revealed a light gray surface layer contrasting with the deeper gray-black color of the substrate. From inspection of the char under a 45 power microscope, it was noted that there were silvery-gray deposits throughout the surface layer. It was suspected that these could be formations of silicon carbide. A subsequent quantitative chemical analysis revealed a carbon content of the order of 5 percent near the sample surface and 15 percent in the substrate material. This, of course, did not indicate the form of the carbon. Samples of both sections were subsequently sent to Sloan Research Industries for X-ray diffraction analysis to determine the presence of SiC. The results revealed a concentration of approximately 15 percent SiC in the surface layers (carbon depletion area) and about 5 percent SiC in the substrate. It is stressed that these percentages are only approximate, since exacting quantitative measurements cannot be made with this technique. It is likely that a mass loss occurred in the form of CO from the following reactions:



The 15 percent carbon content in the sample interior is about the amount expected for the residue from the original depolymerization of the phenolic resin. During the experiment, the temperature in the interior was apparently too low to give a high yield of SiC. At the surface, where the temperature reached 2850°F, it appears that the reaction went to completion in the presence of the excess of SiO_2 . The carbon concentrations found from this experiment were subsequently used for a computer analysis program to evaluate the silica-carbon equilibrium reactions as a function of temperature and pressure as reported in a following section.

TMC A673

UNCLASSIFIED

UNCLASSIFIED

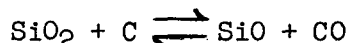
REPORT 6069

Specimen No. c:

Pressure: Initially 1 atmosphere (Argon) for 5 minutes, then vacuum pull down for 1 minute.

Maximum temperature: 3070°F

Extreme outgassing of the sample occurred to the extent that there was virtually nothing left of the sample. It was apparent from this result that the SiC reaction alone could not account for the great degree of mass loss and that the silica itself was lost as a consequence of the chemical reaction. In all probability, the predominate reaction was the following:



The products of this reaction are, of course, gaseous, leaving no solid residue for the reaction quantities involved.

(2). Experiment No. 2

In this test, eight slabs of graphite approximately 1 by 1 by 0.25 inch and four slabs of quartz glass nominally 1 by 1 by 0.050 inch were stacked alternately and heated in the carbon crucible for 12 minutes. The pressure was 1 atmosphere, an argon purge was used, and the temperature ranged from 2600° to 3300°F. At the end of this period, all of the SiO₂ had reacted and the loss of material was approximately equal to the original concentration of the silica (15 percent by weight). Examination of the graphite crucible after the test run revealed that a heavy crust had formed on its surface. This crust could have been SiC from the reaction. It seems likely that both the SiO and SiC reactions were taking place simultaneously. It can be seen from analytical studies that the SiC reaction will predominate over the SiO reaction at the lower temperatures. However, it was necessary at some stage of the reaction for SiO(gas) or SiO₂ vapor to be formed in order that the material could be transported to react with the wall of the crucible.

(3). Experiment No. 3

A test was run to follow up Experiment No. 2 to determine if SiO or SiO₂ vapors had to be formed initially for the silica-carbon reaction to take place under the temperature and pressure conditions of the experiment. In this test, a single slab of quartz was supported by a slab of zirconia (ZrO₂) under which was placed a graphite slab. The test conditions were

TMC 4673

UNCLASSIFIED

UNCLASSIFIED

similar to those of the preceding test. The silica melted under heating and reacted only slightly with the surface of the ZrO_2 . The results would thus indicate that liquid phase contact of silica with carbon is adequate to bring about reaction. A silicon carbide rod had also been placed in the crucible during the same test, and it was unaffected by the conditions of the experiment.

(4). Experiment No. 4--Differential Thermal Analysis (DTA)

A sample of resin-bonded, high silica cloth was submitted to the Differential Thermal Analyzer (DTA) to explore the possibility that endothermic silica-carbon reactions could occur during the ablation of the material at temperatures of 1800°F or greater.

Specimens were machined for testing from stock samples of C100-48 cloth W/SC 1008 resin. The nominal dimensions were 0.25 by 0.50 inch. The initial weight was 0.937 gram. The specimen was wrapped in 0.001-inch platinum foil. The reference material was alumina powder similarly wrapped in platinum foil. The differential thermocouples of chromel-alumel were inserted in the specimens and the assembly was placed in the furnace. The furnace was heated at a rate of 8.6°F/min until a temperature of 2500°F was attained. The differential thermocouple output was used to position the chart, and the output of the furnace control thermocouple was used to drive the pen upscale. After cooling, the final specimen weight was 0.820 gram.

As the resin-bonded, high-silica cloth was heated, it appeared that sufficient heat was generated by combustion of the gases given off to mask any heat absorption caused by charring, water evolution, etc. Above 1700°F, the endothermic absorptions were observable.

The quantity of heat evolved per unit was not determined because no calibrating DTA runs were made.

(5). Experiment No. 5--Microscopic Observations of the Char Structure of Silica Reinforced Phenolic

Initial microscopic observations were made on samples of Refrasil reinforced phenolic sections cut from thrust chambers that had been run with N_2O_4 /Aerozone 50 at 100 psia chamber pressure. The Marquardt Materials and Processes Laboratory cut and mounted sections of the virgin material and also a section through the char surface adjacent to the flame. Samples were taken of excessive bubble formation and also of thin bubble formation.

Photomicrographs, taken at 10, 50, and 100 power magnification, pointed out the following:

1. Fiber diameters were 10 to 12 μ with several hundred strands per bundle.

TACA 673

UNCLASSIFIED

UNCLASSIFIED

2. There were small gas pockets or voids in some of the virgin phenolic samples.
3. By looking at the char surface interface through the 45 power binocular microscope, the various surface zones could be clearly observed. The following characteristics were noted:
 - a. Deep continuous cracks or delaminations in the char structure
 - b. Origination of the surface bubbles from within the fiber bundles as they were heated and fused
 - c. Metallic appearance of coating on silica fibers near cracks and delaminations
 - d. Metallic appearance of coating in the larger silica bubbles not yet exposed to combustion gas
 - e. Whiteness of small bubbles within the melt layer
 - f. Depletion of carbon in the substrate below the molten silica layer (See Figure 36).

(6). Experiment No. 6--X-Ray Diffraction Analysis of Fused Surface Slag of Fired Silica-Phenolic Thrust Chambers

To determine the composition of the fused surface layer of fired silica-phenolic thrust chambers for comparison with theoretical predictions, four samples were taken from characteristic areas in three Saturn S-IVB ullage engine test chambers (See Figure 40). The samples were chosen from different appearing residues from the chamber liners, i.e., one sample appeared to be predominately pure fused silica, other samples of the fused material appeared to be metallic coated, and another sample appeared to be of carbonaceous composition. In all cases, these residues proved to be almost pure silica with minor traces of SiC and other constituents which caused the differences in appearance. The black appearing residue, for instance, was caused by iron deposits from a burnout of an injector attachment ring. One thrust chamber had a tantalum liner insert which melted and traces of this material appeared in the fused residue. The metallic looking coating of SiC on the fused silica foam was microscopically thin and constituted a very small percentage of the sample. A subsequent oxy-acetylene torch

TWCA 673

UNCLASSIFIED

UNCLASSIFIED

REPORT 6069

test flashing of the thrust chamber, which was completely coated, demonstrated that the coating could be instantaneously removed in an oxidizing atmosphere at moderately high temperatures. This result leads to the belief that the SiC at the surface resulted as a flash coating caused by the reducing nature of a fuel purge during shutdown.

In short, no fundamental difference could be found in the samples that detracts from the basic theory that the fused silica in the surface layer becomes depleted of carbon from internal chemical reaction.

c. Analytical Determination of Silica-Carbon Reactions

From the chemical analysis of a charred thrust chamber section which had been heated in the laboratory furnace in an inert environment of 1 atmosphere pressure to 2850°F, it was found that there were two general regions of carbon depletion in the char specimen. The outer layer, which was light gray in color, contained 5 percent carbon and the inner layer, which was a darker char, contained about 15 percent carbon, the remaining constituents being silica and a 3 to 5 percent concentration of glass-forming impurities. From this information, a computer analysis was made of the equilibrium composition of a silica and carbon mixture as a function of temperature and pressure for carbon concentration of 5 to 15 percent. The results for 15 percent carbon are shown in Figures 39, 41, 42, and 43. It is of note that the silicon carbide reaction preferential is limited to temperatures of less than 3000°F and is apparently independent of pressure, except that the suppression of the SiO reaction at higher pressures will extend the range of SiC formation at 350 psia to about 3100°F. At temperatures above this point, the silica that reacts with the carbon becomes an equilibrium mixture of metallic silicon and SiO gas with the latter product becoming predominant at temperatures ranging from 3700° to 4300°F, depending on the chamber pressure. Above these temperatures, the reaction products for the 5 percent carbon specimen are SiO gas, CO, and unreacted SiO₂, with the SiO concentration reaching a maximum of 17 to 18 percent of the products by weight. This amount of SiO evolution would substantially add to the dimensional ablation rate along with altering the viscosity and density properties of the molten boundary layer. The analytical results demonstrate that the heat absorbed by the silica-carbon reactants could be as high as 2000 to 4500 Btu/lb in the temperature span from 2000° to 4300°F, whereas an increase of about 750 Btu/lb would have been absorbed by sensible heat storage effects for a nonreacting silica-carbon matrix.

This quantity of heat absorbed is of significant importance to be used in a heat balance to formulate a dimensional ablation model. It must be emphasized that these quantities of heat would be absorbed only if the reactions had sufficient time to go to completion. A chemical model is shown in Table IV for the silica-carbon matrix reaction which may be equivalent to an ablating silica-phenolic thrust chamber wall. It is theoretically possible to lose 90 percent of the silica content of the charred material and all of the carbon by formation of gaseous products if chemical equilibrium is attained at the predicted high

TMC A 673

UNCLASSIFIED

UNCLASSIFIED

REPORT 6069

surface temperatures of 4000° to 4500°F. This may explain the deep grooving of silica-phenolic thrust chambers in areas wherein the shear forces on the molten layer of silica would be relatively low but subject to high gas temperatures caused by local variation of O/F ratio.

Another serious consideration of the carbon-silica reaction is for the space shutdown postrun condition. Along with chemical reaction, simple dissociation and vaporizing of the silica may occur under these conditions of high vacuum and heat soaking. The chemical equilibrium of silica and carbon reacting under these conditions as shown in Figure 44 indicates that the entire char substrate could gasify if allowed to remain very long at temperatures as low as 2700° to 2900°F. Again, it must be emphasized that this would occur only if the reaction had sufficient time at these temperatures to go to completion.

Figure 38 gives the vapor pressure and dissociation pressure of molten silica as a function of temperature. At vacuum pressures in the range of 10^{-3} mm Hg, which might prevail in the thrust chamber in space under conditions of postrun charring of the resin system and the diffusion of SiO_2 vapor products, the loss of SiO_2 could be critical in view of the time required for the surface to cool below the reaction temperature at this pressure. A sample calculation is given below to illustrate this possibility for the vaporization of SiO_2 .

Assume, for example, a surface temperature of 4300°F, which appears reasonable from analyses described in this text. A molten layer thickness of 0.050 inch with an inner boundary at 3100°F is also consistent with this analysis. This provides an average temperature difference of 600°F above 3100°F.

Average specific heat of silica layer, $C_p = 0.36$ Btu/lb-°F

Heat of vaporization, $H_R = 3700$ Btu/lb

$$\frac{\text{Sensible heat stored in material above } 3100^\circ\text{F}}{\text{Heat of vaporization}} = \frac{C_p \Delta T}{H_R}$$

$$\frac{C_p \Delta T}{H_R} = \frac{0.36 (600)}{3700} = 0.0585$$

This would mean that 5.85 percent of the SiO_2 in the 0.050-inch thick molten layer could vaporize at a pressure of 10^{-3} mm Hg if the heat content were thus absorbed before it could be dissipated by radiation and conduction heat transfer effects. If this percentage of the molten layer were removed at the surface, a loss of 3 mils of silica would occur at each shutdown interval. The cumulative effect on multipulse duty cycles could be a serious consideration.

TMC A673

UNCLASSIFIED

UNCLASSIFIED

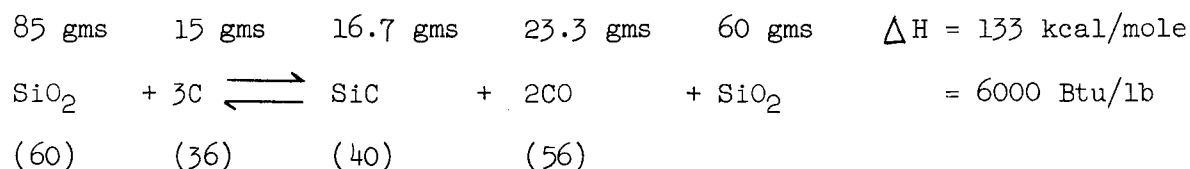
REPORT 6069

It would be desirable to conduct laboratory experiments to determine the actual silica-carbon reaction and vaporization rates as a function of the temperature and pressure conditions that would be encountered by a space-craft engine throughout its operating life.

The sample calculations given below present a chemical mass and energy balance for the reactions possible within the charred silica-phenolic thrust chamber walls.

Sample Calculations

Chemical Mass Balance for Reaction Zone No. 1--Initial Composition: 15%C, 85% SiO₂



Consider 100 gms charred material

Weight of SiO₂ to react = 60/36 x 15 = 25 gms

Unreacted SiO₂ = 85 - 25 = 60 gms

Weight of SiC formed = 40/36 x 15 = 16.7 gms

Weight of CO lost = 40 - 16.7 = 23.3 gms

Weight of solid residue = 100 - 23.3 = 76.7 gms

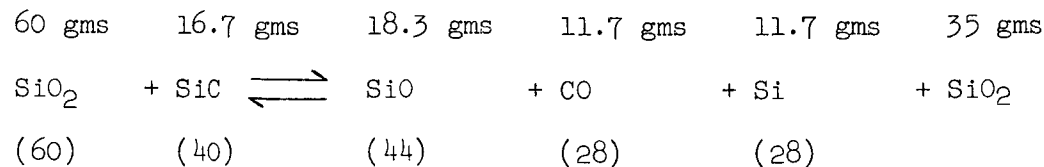
Weight % SiC formed = 16.7/76.7 = 21.8%

Weight % of C = 12/40(0.218) = 6.5%

ΔH = 0.218(6000) = 1308 Btu/lb initial char

Reaction Zone No. 2 - Initial Composition: 6.5% C, 93.5% SiO₂

76.7 gms remaining (60 gms SiO₂, 16.7 gms SiC)



TMC A673

UNCLASSIFIED

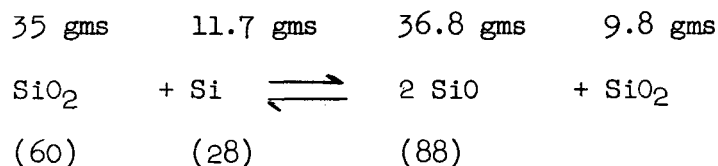
UNCLASSIFIED

REPORT 6069

Weight of SiO₂ to react = 60/40 (16.7) = 25 gms
 Unreacted SiO₂ = 60 - 25 = 35 gms
 Weight of CO lost = 16.7/40 x 28 = 11.7 gms
 Weight of SiO lost = 16.7/40 x 44 = 18.3 gms
 Weight of Si formed = 16.7/40 x 28 = 11.7 gms
 Weight lost = 11.7 + 18.3 = 30.0 gms
 Residue = 35 + 11.7 = 46.7 gms

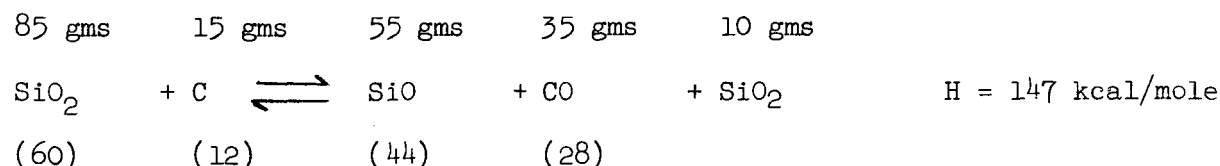
Reaction Zone No. 3 - Initial Composition: 100% SiO₂ + Si

46.7 gms remaining (35 gms SiO₂, 11.7 gms Si)



Weight of SiO₂ to react = 60/28 (11.7) = 25.2 gms
 Weight of SiO gas = 11.7/28 x 88 = 36.8 gms
 Weight of SiO₂ remaining = 35 - 25.2 = 9.8 gms

If all of the initial 15 gms of C were to react directly with the 85 gms SiO₂, the following reaction would prevail if allowed to go to completion:



Weight of SiO₂ to react = 15/12 (60) = 75 gms
 Residue = 85 - 75 = 10 gms (Checks with above)

TMC A673

UNCLASSIFIED

UNCLASSIFIED

The indications from an analytically derived 15 percent carbon/85 percent silica equilibrium reaction are that this condition is possible in the range from 4300° to 4600°F.

5. Dimensional Ablation Models

The theoretical thermochemical and heat transfer analyses together with laboratory studies of the chemical mechanisms of ablation have shed new light on the relative importance of these phenomena in controlling ablation rates within rocket thrust chambers. From the results of this investigation, a simplified ablation model was formulated to predict dimensional ablation rates of a silica-phenolic composite in a thrust chamber environment. The agreement of these predictions with full scale experimental data supports the conclusion that erosion rates may be controlled by the chemical kinetics of the silica-carbon reaction within the chamber.

The analytical and laboratory studies described in this text provide a basis for the simplified ablation model based on the following assumptions:

1. Charring rates and transient temperature distributions may be predicted on the basis of thermal conduction only. The heat absorbed and gases evolved in thermal degradation of the resin are insufficient to control surface temperature or erosion rate.
2. The viscous character of the molten silica is such that comparatively high dynamic shear stresses can be sustained at surface temperatures well above its melting point.
3. The highly endothermic reactions possible between the silica and the carbon char residue in the chamber wall can take place under thrust chamber firing conditions with the evolution of gaseous CO and SiO (as confirmed by laboratory and test firing data).
4. Reactions between the propellant combustion products and the ablative wall materials is a minor effect in the silica-phenolic ablation, as evidenced by the depletion of carbon in the composite while completely shielded from combustion products by the molten silica film formed during firing.

TMC A673

UNCLASSIFIED

UNCLASSIFIED

REPORT 6069

Results formulated from the above criteria compared to experimental results explain the sensitivity of localized erosion rates to heat transfer and gas temperature distribution on the basis of the kinetics of the above phenomena. This effect is illustrated in Figure 45 which compares the throat erosion pattern of a silica phenolic thrust chamber with the measured cold wall heat flux utilizing the same injector (Reference 8). Local heat fluxes are shown to vary only by a factor of two compared to throat erosion rates varying from zero to 5 mils/sec.

a. Chemical Ablation Model

The ablation model involves a simplified heat balance between that convected to the ablating surface, that absorbed chemically and sensibly in the reaction zones, and that conducted to the material substrate through an arbitrary isothermal line beyond which no highly endothermic reactions are assumed to occur. The chemical model used is that shown in Table IV for an initial resin content of 30 percent. The ablation model used for illustration purposes is one wherein the entire region of carbon depletion is assumed to occur between 2500°F and the surface temperature of approximately 4000° to 4200°F. The heat absorbed in this region by chemical reaction and enthalpy change of the products was calculated to be about 4200 Btu/lb. These values assume completion of all reactions, leaving a 10 percent SiO₂ residue from the original charred material. (It is considered later that this reaction may not go to completion.)

The transpiration cooling ("blowing" parameter) effect has been evaluated and found to be negligible for the purposes of this model. A surface regression rate of 2 mils/sec, assuming all gaseous products given off, would lower the adiabatic wall temperature less than 200°F for a gas temperature of 4750°F and a chamber pressure of 100 psia (See Figure 44).

Throat erosion rates as a function of time were calculated from steady state sea level experimental test data for the Saturn S-IVB ullage engine. This information is shown in Figures 46, 47, and 48 and is used for comparison with analytical results (See Figure 49). Some amount of trial and error was used to arrive at surface temperatures which were compatible with both results. Typical calculations follow.

b. Ablation Model Calculations

A heat balance calculation had been made to examine heat balance criteria for an ablating silica-phenolic thrust chamber when only heat conduction and surface melting is considered. The following assumptions were made:

1. Heat transfer coefficient = 500 Btu/hr-ft²-°F
2. Gas temperature = 4900°F
3. Surface temperature = 4300°F
4. Dimensional ablation rate = 2 mils/sec

TWCA 673

UNCLASSIFIED

UNCLASSIFIED

Under these conditions of heat transfer at time $t = 100$ sec, the material could only absorb about 25 percent of the convected heat flux through phase change and sensible heat storage effects. The unaccounted for heat flux, if divided by the mass removal rate, would indicate that about 4000 Btu/lb would have to be absorbed in another manner. This value is very close to that predicted by the silica-carbon chemical equilibrium studies. The only other alternative would be for the surface temperature to rise in order to balance the heat transfer across the surface boundary. For this case, the surface temperature would have to rise to 4750°F or within 150°F of the gas temperature. This would appear unlikely since the viscosity would be lowered by a factor of almost 20 over that at 4300°F and a factor of 100 over that at 4000°F which may indicate a more rapid flow rate than is actually the case. If high ablation rates on the order of 5 mils/sec are assumed, the surface temperature would have to stabilize at 4650°F in order to effect a heat balance. These high surface temperatures appear very unlikely, both from the standpoint of the lowered silica viscosity and also from the fact that the internal chemical reaction which is known to be taking place has an equilibrium temperature of several hundred degrees below these values (around 4000°F for 15 percent C/85 percent SiO₂ at 100 psia).

It has been calculated that gas temperatures as low as 4500°F have existed in the early S-IVB sea level steady state thrust chamber firings which are used for comparative purposes. The erosion rates for these chambers have been on the order of 1.5 to 2.0 mils/sec.

The Q/A absorbed chemically might be as follows:

$$Q/A_{\text{convection}} = h_c \Delta T = 500 \frac{(4500 - 4000)}{144 (3600)} = 0.483 \text{ Btu/in.}^2\text{-sec}$$

$$Q/A \text{ conducted through } 3100^\circ\text{F isothermal} = 0.1 \text{ Btu/in.}^2\text{-sec at } t = 100 \text{ sec}$$

$$\text{Weight of silica char} = 5.3 \times 10^{-5} \text{ lb/mil-in.}^2$$

$$\frac{0.383 \text{ Btu}}{\text{in.}^2\text{-sec} \times \frac{1.75 \text{ mil}}{\text{sec}} \times \frac{5.3 \times 10^{-5} \text{ lb}}{\text{mil-in.}^2}} = 4130 \text{ Btu/lb}$$

TMC 4673

UNCLASSIFIED

UNCLASSIFIED

REPORT 6069

Consider now higher flame temperatures where erosion rates have risen to 5 mils/sec at gas temperatures of the order of 4900°F. It may also be reasonable to assume that the surface temperature has risen a few hundred degrees higher to perhaps 4200°F.

$$Q/A \text{ convection} = \frac{500 (4900 - 4200)}{144 (3600)} = 0.675 \text{ Btu/in.}^2\text{-sec}$$

$$Q/A \text{ conducted} = 0.1 \text{ Btu/in.}^2\text{-sec}$$

$$Q/A \text{ absorbed } (3100^\circ - 4200^\circ\text{F}) = 0.575 \text{ Btu/in.}^2\text{-sec}$$

$$\frac{0.575 \text{ Btu}}{\text{in.}^2\text{-sec} \times \frac{5 \text{ mil}}{\text{sec}} \times \frac{5.3 \times 10^{-5}}{\text{mil-in.}^2}} = 2170 \text{ Btu/lb}$$

If the surface temperature had remained at 4000°F, the heat absorbed per pound would have been 2900 Btu/lb.

It appears from this experimental evidence that this material may ablate less efficiently when the gas temperatures are raised to more than a few hundred degrees higher than its normal chemical equilibrium temperature and that the silica-carbon reaction may not have time to go to completion before the initial reaction products are lost. This may suggest an exponential variation of ablation rate with gas temperature rather than the approximately linear one shown in Figure 50 at high heat transfer rates. (The analysis for these curves had assumed a constant heat absorbed of 4200 Btu/lb)

It is likely that when high rates of dimensional ablation are taking place (in excess of 2 mils/sec), in the throat region, that some combination of chemical and physical erosion may be taking place with the chemical reaction still predominating. In actual practice, there may be a build-up of silica at the throat exit indicating silica flow. However, the ever present depletion of carbon in the fused surface layer would indicate that at least Reaction No. 2 in the chemical ablation model had gone to completion (See Table IV and Figure 51). If Reaction No. 3 were not allowed to occur, the solid residue would be in the range of 50 to 60 percent instead of the 10 percent postulated by the theoretical model. This would also be at the expense of about 1600 Btu/lb of endothermic heat absorption capacity. The loss of this quantity of heat absorption ability would be very close to the reduction in ablative efficiency which is predicted by the "high ablation rate" heat balance previously shown.

TMC A673

UNCLASSIFIED

UNCLASSIFIED

A brief analysis was made of the effect of effective endothermic heat absorption on wall temperature and erosion rate for two different combustion gas temperatures, 5000° and 7000°F. The curves of Figures 52 and 53 show that a thrust chamber material surface absorbing 5000 Btu/lb at a temperature of 4300°F in a 5000°F gas would recede at a rate of 0.5 mil/sec and under similar conditions in a 7000°F gas would recede at a rate of 2.0 mil/sec.

To simplify the ablation model presented, the temperature distribution which determines heat conduction to the substrate is referenced to the original surface. At erosion rates of 2 mils/sec or less, this appears to be a reasonable approximation since after 20 seconds the heat conducted to the substrate is only on the order of 10 percent of the convected heat flux. The assumption of a boundary moving at 2 mils/sec would only vary this flux by a few percent. In the case of higher erosion rates (5 mils/sec), the conducted heat flux could remain as high as 50 percent of the convected flux for some period of time, and consequently the moving boundary would have to be considered.

c. Viscous Shear Flow Ablation Model

Prior to the establishment of criteria to formulate a chemical ablation model, a simple viscous shear flow model was made for a molten silica surface in a typical liquid propellant thrust chamber environment. The purpose was to examine this mode of ablation and to establish surface temperature criteria for the transient heat conduction analysis previously described.

The feasibility of a 4000° to 4500°F surface temperature was verified through the criteria of the thermal conductivity of the molten silica and the viscosity of the silica at temperatures above its melting point. An initial approximation for the thickness of the molten layer was arrived at with the following criteria:

1. The thermal conductivity of pure silica at its melting point of 3100°F is given as 2.97×10^{-5} Btu/in.-sec.-°F. Indications are that it is reasonably constant at values above this point.
2. The hot wall heat flux to a 4300°F surface for conventional hypergolic propellants at $P_c = 150$ psi, a gas temperature of 4950°F, and a throat diameter of approximately 3 inches would be about 0.9 Btu/in.²-sec.

Therefore

$$\begin{aligned} \delta_{(\text{melt layer})} &= \frac{k [T_{\text{surface}} - T_{\text{wall(melting point)}}]}{q_w} \\ &= \frac{2.97 \times 10^{-5} (4300 - 3100)}{0.9} = 0.043 \text{ in.} \end{aligned}$$

TMC A673

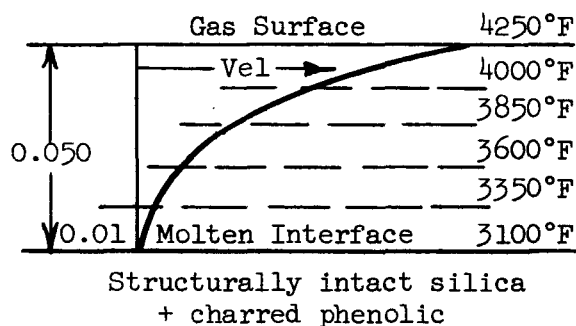
UNCLASSIFIED

UNCLASSIFIED

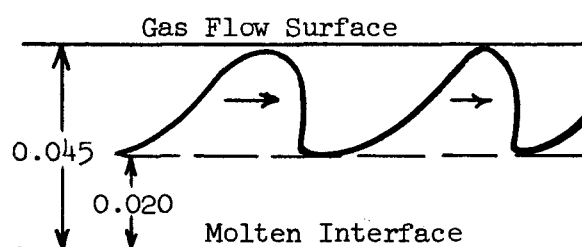
REPORT 6069

From this approximate value, a molten boundary layer thickness of 0.050 inch was assumed for an idealized flow model. For the purpose of simplification, the 0.050-inch molten layer was divided into equal layers of 0.010-inch thickness with a linear temperature increment from the melting point to 4250°F. The simplified model is shown below along with a model scaled from microphotographs of fired silica reinforced phenolic thrust chamber sections.

Idealized Model



Realistic Model



It is interesting to note at this point that the molten layer thickness of the chamber section is roughly the same as that calculated from heat transfer criteria. Equating the dynamic gas friction shear stress to the viscous shear stress required to continuously deform a viscous fluid in one-dimensional flow, yields

$$f \frac{\rho v^2}{2} = \tau = \mu \frac{dv}{dx}$$

Where

v = Combustion gas velocity

ρ = Combustion gas density

f = Dimensionless friction factor which is largely independent of surface condition and Reynolds number when operating at high Reynolds numbers (above 10^5) in turbulent flow. (A value of 0.015 is used.)

μ = Viscosity of molten silica as a function of temperature

$\frac{dv}{dx}$ = One-dimensional velocity gradient in molten layer

τ = Shear stress

TMC 673

UNCLASSIFIED

UNCLASSIFIED

REPORT 6069

First computing the dynamic gas shear stress, values of 0.06 psi in the chamber section and 0.9 psi in the throat section are obtained. Using these values and the temperature dependent viscosity value taken at increments of 0.010 inch in the flow model, a velocity gradient can be solved for each point. The relative velocities at each point integrated through simple summations are totaled to give the velocity of flow of the silica at the surface with respect to the substrate material. Using this method, the movement of a particle of molten silica at the surface assumed a velocity of 0.041 inch per second at the throat and a value of 0.02 inch per second in the chamber. A slightly different flow model is shown in Figure 54. It must be pointed out at this time that the above values are to be considered only to examine the feasibility of the initial surface temperature assumption and as such would indicate that the assumption was reasonable. Together with the correlation achieved with the heat sink analysis with experimental data, it appears that surface temperature assumptions of 4000° to 4500°F with silica reinforced ablative materials can be amply justified.

In order to use the viscous shear analogy to predict the dimensional ablation rate of the molten layer, there is much yet to be learned about the mode of removal of the silica melt. It has been observed in a laboratory experiment that very minute gas bubbles from the resin degradation process effuse continually through the molten layer during pyrolysis of the sample. This would indicate that the molten layer may be highly porous during the ablation process. Postrun microphotographs also generally substantiate this factor. It is not known whether the silica melt is lost to the gas stream when the minute bubbles break or whether dimensional loss is caused by simple shear flow of the molten media. The postrun liner condition might indicate, that because of surface tension effects, the silica is able to lump into a node and flow through the chamber much as a raindrop runs down a window pane. It may be generalized that the surface removal rate is a function of both the viscosity and surface tension of the silica melt, which are in turn temperature dependent. The viscous effect, as described, may also be affected by porosity caused by gas evolution. The melt layer thickness and surface temperature of the melt appear to be functions of gas enthalpy and, of course, the dynamic shear forces are dependent upon the velocity and density of the combustion gases.

The contribution offered by this simple shear flow analysis was to establish upper temperature limits for the ablating silica-phenolic as controlled by dynamic shear force-viscous property interaction. (The internal chemical kinetics, if in control, may limit the surface to a lower temperature.) The shortcomings of this model are that a heat balance cannot be affected at the molten flow line-char base boundary using liquid phase ablation criteria only. This is described in more depth for the chemical ablation model presented earlier.

TMC A673

UNCLASSIFIED

UNCLASSIFIED

REPORT 6069

D. Heat Sink Design Studies

Combustion chamber and exit nozzle component temperatures may be held below structural limits while heat is being conducted away from the surface and absorbed in the chamber and nozzle walls. Promising heat sink materials are those which have high heat capacity, high thermal conductivity, high structural temperature limits, and compatibility with combustion gases. Possible candidates would be pyrolytic graphite, isotropic graphite, tungsten, and beryllia.

The effect of heat sink geometry is shown graphically in Figure 55. The effects of the wall thickness and nozzle radius on the surface temperature rise of a typical graphite nozzle are shown in this plot which also shows two striking facts:

1. For large radius nozzles, run times are not extended by increasing the wall thickness beyond a certain value (approximately 2 inches for the case shown).
2. For small radius nozzles with the same heat transfer coefficients, run times are not only longer for the same wall thickness, but the allowable run times continue to increase with increasing wall thickness to an optimum well beyond the optimum for the larger nozzle.

Figures 56, 57, and 58 have been plotted to present graphically the effect of heat transfer coefficient on the rate of surface temperature rise of a given rocket nozzle heat sink configuration. For thin walled (Re near 1.0) nozzle inserts, the time to reach a given temperature is inversely proportional to the heat transfer coefficient. But for thick walls (large values of Re approaching 10), the heating time is inversely proportional to the heat transfer coefficient to a power greater than 2.0, thus making run time more sensitive to a reduction in the heat transfer coefficient. This reduction in heat transfer rate may possibly be achieved through the use of film cooling.

The effect of increasing the thermal conductivity of a heat sink, as determined by Figures 56, 57, and 58, is to increase the optimum wall thickness and at the same time to increase the allowable run time. Tables V and VI provide specific examples to illustrate the effect of variation of heat sink thermal properties.

Figure 59 shows the effect of axial heat conduction and increasing wall thickness on the transient temperature response of a graphite throat insert. For this particular example, a 50 percent increase in run time is gained by increasing the graphite wall thickness by 0.54 inch. Consideration of the effect of axial heat conduction results in a 7 percent increase in run time to reach the specified surface temperature.

TMC A673

UNCLASSIFIED

UNCLASSIFIED

REPORT 6069

E. Film Cooling Studies

Film cooling calculations were made for several coolants and nozzle configurations in order to provide a comparison of conventional film cooling analysis with the test program results. The analysis used the methods of References 9 and 10 with modifications in some cases to account for multiple slot film injection. The analysis is based on the conventional assumptions that the wall is adiabatic, that all effects of film cooling can be interpreted in terms of an "adiabatic" wall temperature (T'_{ad}) assumed identical to the local wall temperature, while the heat transfer coefficient is assumed to be unaffected by the film cooling. Furthermore, the correlations used in the analysis were obtained from tests of film cooling in cylinders, and the validity of their use in converging-diverging nozzles is unknown. Several recent reports (References 11 and 12) describe gaseous film cooling of rocket nozzles, but no improved equation for film cooling correlation has yet resulted. Nearly all film cooling calculations were made for O_2/H_2 at 100 psia, an O/F ratio of 5, and a C^* efficiency of 95 percent. Coolant inlet temperature was always 70°F.

1. Two-Row Hole Pattern at $C_r = 4:1$

Two circumferential rows of holes near a contraction ratio of 4:1 were assumed to be drilled radially in the standard nozzle (Figure 5). In one case, the total hole area used was that which gave optimum injection velocity when cooling the exit station at $A_e/A_* = 1.5:1$ to 1000°F, and then the coolant requirements for other exit station temperatures were calculated using that fixed area. The exit station is the hottest station according to the assumptions of the analysis. Later, additional calculations were made assuming that the hole area was optimized at all flow rates. A comparison of film coolant requirements for fixed or optimized hole areas for H_2 , He, CH_4 , and N_2 is shown in Figure 60. The exceptional cooling capability of the low molecular weight gases (H_2 and He) is evident. The optimization of hole area (i.e., compatibility of film exit velocity vector with local stream velocity) is also important. Since the propellant flow rate for the assumed nozzle is 0.53 pps, it is obvious that very large coolant flow rates are indicated in order to use a conventional material such as steel.

2. Tangential Slot at $C_r = 5.38:1$

The nozzle contour used in the test program was identical to that used in the film cooling and erosion program analyses except that the contraction side of the test nozzle contour was extended to a contraction ratio of 5.38. A second film cooling configuration, used extensively in the test program, consisted of a circumferential slot injecting coolant tangentially to the nozzle wall at $C_r = 5.38:1$. An analysis of hydrogen cooling requirements for tangential slot areas optimized at each flow rate for cooling the exit station gave very close to the same results for $C_r = 5.38:1$ as for the optimized radial holes at 4:1. The

TMCA 673

UNCLASSIFIED

UNCLASSIFIED

REPORT 6069

slightly increased length of nozzle to be cooled was evidently balanced by the increased cooling effectiveness of the tangential injection. The flow rate is shown in Figure 61, and the variation of the optimum slot width for tangential injection at $C_r = 5.38:1$ is shown in Figure 62. The slot width used in the test program was 0.035 ± 0.003 inch.

3. Multislot Cooling

Film cooling calculations were made for radial injection of hydrogen in the multislot configuration on Figure 63. Two multislot nozzles were tested using the design shown in Figure 63. Each nozzle was made of eleven $1/4$ -inch thick edge oriented pyrolytic graphite disks which had coolant slots machined on one face. A typical disk with coolant slots is shown in Figure 64. The coolant slots were staggered in a checkerboard fashion, so that the slots along any nozzle flow path were separated by two disks (0.5 inch). This design provided cooling efficiency intermediate between single slot cooling and transpiration cooling. The transpiration condition could be more closely approached by closer axial spacing of slots, first by having consecutive slots in every disk for a 0.25-inch spacing, and then by using thinner pyrolytic graphite disks. The pyrolytic graphite has a high thermal expansion during heating and may also shrink in permanent "growth". The disks were successfully contained during motor tests by a Belleville spring as shown in Figure 63.

The dimensions of the coolant slots were determined using an analysis of compressible flow with friction and required optimizing the related requirements of injection efficiency, fabricability, and coolant manifold pressure.

The analysis procedure for film cooling was modified to account for the effect of upstream film cooling by using an "adiabatic wall temperature" (T'_{ad}) at any location which was the same as the wall (i.e., recovery) temperature which would have been predicted at that location from the upstream cooling alone, as discussed by Sellers in Reference 13. The maximum wall temperature anywhere in the nozzle is at a point furthest downstream from a slot and just upstream from the next slot. The hydrogen cooling requirements for various values of the maximum wall temperature are shown for each of the injection stations in Figure 65. The numbering system for the slots is shown in Figure 63. Again, the motor condition was for O_2/H_2 at 100 psia, an O/F ratio of 2.0, and a C^* efficiency of 95 percent.

The total coolant for all of the slots is plotted in Figure 66, where it is compared with the hydrogen cooling requirement for tangential injection at 5.38:1 and for transpiration cooling. No coolant was used at Slots 7 and 8.

TMCA 673

UNCLASSIFIED

UNCLASSIFIED

REPORT 6069

This page intentionally left blank.

TMC A673

UNCLASSIFIED

IV. EXPERIMENTAL STUDIES

A. Test Program Objectives

The test program was conducted using gaseous oxygen/hydrogen propellants to provide test data in support of the following objectives:

1. Combined Film and Radiation Cooling

No experimental data were available for combined film and radiation cooling of rocket nozzles. In fact, at the beginning of the program no data were available for conventional gaseous film cooling of nozzles, all previous data having been obtained for cylindrical combustion chamber sections. Therefore, test data were required to evaluate combined film and radiation cooling of nozzles and the effects of a converging-diverging nozzle. Another important objective was to determine the performance losses attributable to film cooling of a rocket nozzle.

2. Inert and Reactive Gas Cooling of Graphite Nozzles

An experimental program was required to evaluate some of the most promising cooling concepts which had evolved during the analytical portion of the program. In particular, the following ideas were to be evaluated:

1. Multislot cooling of pyrolytic graphite nozzle
2. Transpiration cooling of porous graphite nozzle, using inert and reactive coolant gases
3. Negative erosion (i.e., deposition) of graphite nozzle cooled by methane
4. Single slot film cooling of graphite nozzle, using inert and reactive coolants

B. Test Setup and Hardware

The tests were originally planned for use of an off the shelf injector and combustion chamber purchased from Astrosystems, Inc., together with various cooled and uncooled exit nozzle designs produced by Marquardt. The nominal throat diameter for the tests was 1.25 inches. The nominal propellant flow was 0.539 pps using gaseous O_2/H_2 at an O/F ratio of 5.0, and a nominal chamber pressure of 100 psia. The Astrosystems water cooled combustion chamber sections were assembled in building block fashion, and four chamber sections were used, thus providing a total L^* of about 64 inches.

UNCLASSIFIED

REPORT 6069

During preliminary performance evaluation, the Astrosystems propellant injector burned out. A new, interim, water cooled, single triplet injector was made which had two hydrogen streams impinging on a center oxygen stream. This injector did not overheat and it gave good performance. However, it produced uneven heating in uncooled steel nozzles during short transient runs. A copper injector design which had been successful on earlier Marquardt programs was then fabricated. The copper injector, shown in Figure 67, is cooled by the propellant gases and it gives good performance. However, a hot streak did occur due to a poor oxygen inlet manifold design. The copper injector was used for the test program however, due to the short time remaining.

A propellant flow diagram for the test setup is shown in Figure 68. When inert gaseous film coolants were used, the film coolant flow was limited to about a one second lead before ignition in order to avoid hard starts. The engine was mounted with the axis in the horizontal plane (See Figure 69) hung on two flexures. Thrust measurement required calibration to eliminate the effects of water cooling lines, etc. The effect of film cooling on thrust efficiency was indicated by the following relationship:

$$I_{sp} \text{ efficiency} = \frac{(I_{sp})_{\text{test}}}{(I_{sp})_{\text{theo}}} \times (100)$$

where

$(I_{sp})_{\text{test}}$ = Actual I_{sp} based on measured thrust and total of coolant and propellant flow rates

$(I_{sp})_{\text{theo}}$ = Theoretical I_{sp} at measured chamber pressure assuming total test flow is O_2/H_2 at $O/F = 5.0$

A curve of theoretical I_{sp} versus chamber pressure is given in Figure 70.

The above definition of I_{sp} efficiency obviously is not adequate to precisely predict film cooling effects on large expansion ratio operation in space, but it is useful for a quick approximation of the thrust penalties associated with film cooling.

C. Description of Tests

A total of 59 test runs were made during the program. Test data for the most important runs are summarized in Table VII.

TMC A673

UNCLASSIFIED

UNCLASSIFIED

REPORT 6069

During the first 13 test runs, the Astrosystems injector burned out and was replaced by a water cooled triplet injector, which was found to cause hot streaks. A coating of Rokide Z had been put on the water cooled combustion chamber sections to try to avoid a precooled boundary layer at the approach to the film cooled and uncooled nozzles. No analysis was made of the problem and it was not considered mandatory to avoid the boundary layer cooling effect. It was also planned to measure nozzle throat surface temperature by a pyrometer directed through the motor exhaust toward the inside surface of the throat. This would have been possible for the test nozzles which had an expansion ratio of 1.5, since it was thought that the combustion products of O_2/H_2 would not interfere with the pyrometer reading. However, the early test runs showed that the Rokide Z was slowly flaking off and produced a bright orange flame which would prevent pyrometer readings. Therefore, the Rokide Z coating was removed from the chamber sections prior to Run 14.

1. Uncooled Graphite Nozzles

Runs 14 through 19 were made with uncooled graphite nozzles. Three nozzles were made of ATJ graphite and three were made of Graph-I-Tite G. One nozzle of each type was instrumented with thermocouples as shown in Figure 71. The thermocouples were installed to provide a check on the pyrometer readings of inner wall temperature at the throat. The purpose of testing the graphite nozzles was to determine the rate of erosion in the test nozzle, to provide a base for comparison with film cooled nozzles, and also to determine whether convergent portions of later cooled designs could be made of the molded graphites or whether a more oxidation resistant material might be required.

The tests produced greater erosion rates than had been expected, reaching about 4.0 mils/sec after 1 minute. Especially severe erosion occurred in several hot spots in the convergent section. The erosion at the throat was so severe that the thermocouples nearest the inner wall burned out within 20 seconds, and no further attempt was made to correlate thermocouple data with pyrometer readings. The tests of the uncooled graphite nozzles showed that neither ATJ graphite nor Graph-I-Tite G were suitable for use in the O_2/H_2 motor.

2. Film Cooled, Thick Steel Nozzle

Runs 20 through 23 were made with nitrogen and hydrogen film cooling of a single injection slot steel nozzle (See Figure 72). The nozzle wall was 0.15 inch thick and a coolant manifold was located at the nozzle entrance. The coolant passed from the coolant manifold through 50 holes (visible in the photograph) and it then was injected radially through a 0.040-inch slot between the nozzle section and the adjacent water cooled chamber section, at a contraction ratio of 5.38:1. The inner contour of this and all other test nozzles was as shown in Figure 5. A leak in the coolant system was not discovered until Run 23 with gaseous hydrogen, during which escaping hydrogen caused a fire around the test stand.

TMC A 673

UNCLASSIFIED

Run 24 was made with the single slot nozzle cooled with a hydrogen coolant flow of 0.098 pps and a propellant flow of 0.534 pps. Melting of the steel nozzle surface occurred along hot spots in the contraction region. Transient wall temperatures and thermocouple locations on the steel nozzle are shown in Figure 73. The hot spots were evidently between the thermocouples because the highest recorded temperature was only about 1100°F. The melt patterns shown in Figure 74 indicate some unexplained heating pattern causing melting at the injection slot where the lowest wall temperatures would be predicted. Possible explanations include burning of excess oxygen, or delayed start of film cooling of about 1.6 seconds. In any case, no further single slot film cooling with hydrogen was attempted during the program in order to assure that the test hardware would not be burned out by a repetition of this unexplained phenomenon. It is interesting to note that the I_{sp} efficiency during Run 24 was increased from 95 percent to 100 percent (See Figure 81), possibly due to burning of oxygen with the hydrogen film.

The copper injector (Figure 67) became available after Run 24, and Runs 24 to 29 were short runs with an uncooled steel nozzle (wall thickness of 0.15 inch) to determine the heating rate distribution with the copper injector. The I_{sp} efficiency during these runs averaged about 94 percent. The nozzle was rotated one bolt hole after each run. The heating rate was found to be more uniform than when using the single triplet injector, but hot spots still existed. No time remained for injector rework, so the copper injector was used for the rest of the test program.

Runs 30 through 33 were made using the single slot steel nozzle with helium film cooling, which was varied for each run. Nozzle burn out at the throat occurred during Run 33 with a helium flow rate of 0.06 pps. The recorded nozzle temperatures are tabulated in Table VIII, and the locations of the thermocouples are shown in Figure 75. It may be noted from the tabulated data that a hot spot existed near Thermocouple No. 6 at the throat.

Runs 34 through 39 were made with a thick (0.15-inch) wall steel nozzle cooled by tangential helium injection (the film injection section is shown in Figure 76) of about 0.1 pps. The nozzle was rotated one bolt hole after Runs 35 through 37. After run 38 the tangential film coolant injector was rotated 180°. The purpose of these tests was to obtain the temperature distribution with film cooling, and it was concluded that the uneven distribution was due to the main injector rather than to the film cooling injector.

3. Film Cooled, Thin Steel Nozzle

A thin wall (0.060-inch) 347 stainless steel nozzle of the standard test nozzle contour was used for the final film cooling tests. The surface was oxidized to produce a coating with an estimated emissivity of 0.9. The film was injected tangentially at $C_r = 5.38:1$ through the film cooling manifold shown in Figure 76.

Runs 43 and 44 were made using helium coolant at various flow rates. The steel nozzle burned out during Run 44 using 0.0393 pps of helium flow. The recorded temperatures are tabulated in Table IX and the locations of the thermocouples are shown in Figure 77. Again several hot spots were evident.

Methane was used as a tangentially injected film with another thin steel nozzle during Run 58, using 0.209 pps of coolant. The tangential film cooling injector burned out after 6 seconds because the water cooling was not turned on, but some useful data were obtained. These are tabulated in Table IX.

4. Film Cooled Molybdenum Nozzle

A molybdenum nozzle with a wall thickness of 0.10 inch was made using the standard test nozzle contour. The molybdenum was coated with molybdenum disilicide by the Chromizing Corporation.

Run 47 was made with various amounts of helium cooling using tangential injection (as shown in Figure 76) and the maximum temperature (near the Thermocouple No. 2 location) was about 2900°F using a helium flow rate of 0.0241 pps. The maximum nozzle temperature as indicated by pyrometer readings after a correction for an emissivity of 0.65 for various coolant flow rates is shown in Table X. One combustion chamber section burned out at the cutoff point. It is believed that the burnout was caused by poor water distribution as a result of unequal water discharge pressure. The high engine performance, approaching 100 percent, may have been caused by addition of leaking water to the combustion chamber through a gradually enlarging burnout spot, although this does not appear likely after a detailed study of all test data. On the other hand, the very high performance with small helium flow must be considered questionable.

Two more combustion chamber sections were burned out during the following run due to cooling water distribution problems.

5. Uncooled Thin Steel Nozzle

An uncooled thin steel nozzle was tested during Run 51 to obtain data on heating rates at various locations in the nozzle which were then used to predict a radiation cooled steady state temperature of 3940°F at the hottest spot (Thermocouple No. 2) and an average nozzle temperature of 3740°F. Some of the transient temperature histories are shown in Figure 78.

6. Summary of Radiation/Film Cooling Tests

The variation of analytical and experimental nozzle temperatures with coolant flow rate is plotted in Figure 79 for helium cooling and in Figure 80 for hydrogen cooling. It is seen that a large decrease of equilibrium nozzle temperatures can be achieved by a rather small amount of film cooling. However, the

UNCLASSIFIED

REPORT 6069

limited film cooling data shown indicate that helium is about as good as hydrogen as a film coolant on an equal weight flow basis, instead of being inferior by a 3:1 weight flow ratio as was predicted analytically. This again raises the possibility of burning oxygen in the hydrogen film.

The effect on thrust of film cooling with H_2 , He, and CH_4 is summarized in Figure 81. The data show that methane cooling may incur a rather large loss in performance, whereas small amounts of helium can be used with no loss of performance. In fact, some of the data for helium show an increase above the performance without cooling. Only one data point for hydrogen cooling is available from Run 24, and it shows a rather surprising result in that no loss in I_{sp} was indicated.

7. Film Cooled Graphite Nozzles

Two Graph-I-Tite G nozzles of the same design as those tested earlier (Figure 71) were cooled by tangentially injected gaseous film, at the beginning of the 5.38:1 contraction.

Runs 45 and 46 were made with the same nozzle using helium. The duration of Run 45 was 60 seconds and no erosion was evident. The helium flow rate was 0.0449 pps. The duration of Run 46 was 143 seconds and the helium flow rate was 0.0361 pps. The throat erosion is shown in Figure 82. The erosion performance data are shown in Figure 83. The temperature data for Run 45 (Figure 84) show that the throat temperature was only about 2000°F after 60 seconds. Steady state temperatures of about 3300°F at the throat were reached after about 100 seconds during Run 46. The high erosion rate of Graph-I-Tite G is again evident, even at intermediate temperatures with inert film cooling.

The second Graph-I-Tite G nozzle was cooled with about 0.021 pps of methane during Run 49 (60 seconds) and Run 50 (180 seconds). Only slight throat erosion was measured after Run 49, but severe local erosion was observed after Run 50 in the hot spots and zero erosion was measured in other parts of the nozzle where the film did not break down (See Figure 85).

Methane is clearly superior to helium in reducing graphite erosion, since the erosion during Run 50 was less than during Run 46, although the methane flow rate was only about 60 percent of the helium flow rate, and the run time with methane was 180 seconds, as compared to only 143 seconds with helium. However, the loss in specific impulse is much greater with methane, as shown in Figure 81.

8. Single Slot Cooling of Pyrolytic Graphite Nozzles

An edge oriented pyrolytic graphite nozzle (shown in Figure 63) was tested with injection of methane through slots machined on one face of one pyrolytic graphite disk at Slot 3, about 3/8 inch upstream from the throat. The

TMC A673

UNCLASSIFIED

UNCLASSIFIED

REPORT 6069

single slot was a somewhat different design from that used for the later multislot tests. It extended continuously around half the circumference of the nozzle, so that half of the nozzle throat was cooled and the opposite half was uncooled. The initial methane flow during Run 40 started at a rate of 0.00864 pps and gradually decreased to 0.003 pps after 60 seconds, due probably to clogging of the single slot inlet by pyrolysis of methane in the coolant manifold. There was zero erosion in the cooled side of the throat and slight erosion on the uncooled side near one of the hot spots after Run 40. The steel retaining ring of the multislot design disrupted the exhaust expansion and caused anomalous thrust readings.

The single slot cooled nozzle was again tested during Run 42, with methane coolant flow varying from 0.00475 pps at the start to 0.00133 pps at the end of the 168 second run. Again, the decreased flow was due to slot restriction. Slight amounts of methane seeped between the forward pyrolytic graphite disks during these runs and resulted in what appeared to be deposits of pyrolytic graphite on the contraction region of the nozzle as shown in Figure 86. No erosion occurred on the upper half of the nozzle which was film cooled. However, noticeable erosion occurred on the uncooled half.

Run 41 was made to confirm that the very low thrust during the previous test of the multislot nozzle was due to the effect of the spring loaded backup ring which disrupted the gas expansion, rather than to any coolant effect. However, it is not thought that the performance effect of coolants in the multislot nozzle is correctly assessed even by comparison with the uncooled performance from Run 41.

9. Multislot Cooled Pyrolytic Graphite Nozzle

a. Methane Cooling

A multislot pyrolytic graphite nozzle (shown in Figure 63) was tested using 0.0209 pps of methane cooling injected through all of the slots (no slots at 7 and 8). Run 52 was terminated after 15 seconds because of inadequate hydrogen propellant flow. Run 53 was 180 seconds in duration. Only a slight amount of localized erosion was observed at the nozzle inlet. There was no erosion at the throat. The contraction region had carbon deposits on it which appeared to be pyrolytic graphite as shown in Figure 87. Much less clogging of the slots by carbon occurred during Run 53 than had occurred during the single slot Runs 40 and 42, indicating that clogging of the coolant slots can probably be controlled by minimizing the stay time of the methane in the coolant manifold.

b. Hydrogen Cooling

A second multislot pyrolytic graphite nozzle was tested during Run 56 for 170 seconds with a hydrogen cooling flow rate of 0.00635 pps, which is only 1.18 percent of propellant flow. No erosion was evident and in fact the nozzle looked as though it had not been tested at all. The throat diameter after the run was measured as 1.240 inches, indicating a decrease from the original 1.248 nominal diameter, possible due to annealing effects on the pyrolytic graphite.

TMC A673

UNCLASSIFIED

UNCLASSIFIED

c. Carbon Monoxide Cooling

The same multislotted pyrolytic graphite nozzle that had been tested with hydrogen cooling (Run 56) was later tested for 270 seconds using 0.0211 pps of carbon monoxide as coolant. The throat erosion was 0.006 inch. The contraction region had a polished surface (See Figure 88) which was perhaps due to flame polishing or, less probably, deposition of carbon. However, the appearance of the surface was different than the surface after cooling with CH₄.

10. Transpiration Cooled Porous Graphite Nozzle Insert

One test was made using 0.00029 pps of helium transpiring through a nozzle insert of Spear 3499S porous graphite. This flow rate was more than sufficient to cool the inside graphite surface to 3000°F according to the theoretical analysis of thermochemical erosion. The nozzle throat insert replaced three of the pyrolytic graphite disks, centered about the throat, and the insert radial thickness was about 0.5 inch. At the end of the 67 second run, the porous insert had eroded well below the adjacent uncooled pyrolytic graphite disks, showing that the inherently poor oxidation resistance of the porous graphite more than offset the helium cooling. It was concluded that in nozzles in which the erosion is limited by surface reaction rates, it is very important to use pyrolytic graphite rather than commercial graphites, and that the difference between the two graphites cannot easily be overcome by film or transpiration cooling.

TMC A673

UNCLASSIFIED

UNCLASSIFIED

V. CONCLUSIONS AND RECOMMENDATIONS

A most promising thrust chamber cooling concept for rocket engines using high energy propellants is the use of multislot film cooled pyrolytic graphite. This concept, which can approach pure transpiration cooling in efficiency, also takes advantage of all of the high temperature capability of the pyrolytic materials.

The analytical chemical erosion studies have revealed several important thermodynamic concepts which should affect all future analyses of the performance of refractory materials in a rocket engine combustion environment. These include: (1) the fact that chemical erosion rates for many cases are controlled by the kinetics of the reactions involved, (2) the fact that reactive combustion gas species concentrations at the nozzle wall are not altered greatly by the introduction of inert coolants in amounts required for cooling, and (3) a favorable chemical environment at the wall can be maintained over carbon by the introduction of a hydrocarbon gas such as methane.

The most effective gaseous film coolant is hydrogen followed by helium and the other gases approximately in order of their molecular weight.

Analytical and experimental silica-phenolic ablation studies have provided evidence that internal endothermic chemical reactions between silica and carbon may well control the ablation performance of this type of material in a liquid rocket thrust chamber.

An analytical technique for optimizing the design of rocket nozzle heat sink geometries has been developed.

The analytical chemical erosion program developed under this contract has provided a rational approach to further studies of the performance of cooled and uncooled refractory materials in the rocket combustion environment.

Based on the results of this program, it is recommended that the thermochemical erosion studies be extended to include new nozzle materials, additional combustion product species, and the effects of transient heat conduction. Studies should also be undertaken to provide additional reaction kinetics data, especially for the high energy propellant systems which include fluorine.

Theoretical and experimental studies should be pursued to apply these advanced cooling concepts and materials to the more severe, higher temperature rocket systems in order to evaluate the design problems associated with using new propellants for long runs, with throttling, or for intermittent operation.

TMCA 673

UNCLASSIFIED

UNCLASSIFIED

This page intentionally left blank.

VI. REFERENCES AND BIBLIOGRAPHY

1. Marquardt Report 5981, "(U) Final Report, Thrust Chamber Cooling Techniques for Spacecraft Engines for the Period 13 February 1962 to 12 February 1963. Volume I: Evaluation Procedure and Analysis", 12 March 1963. UNCLASSIFIED.
2. Marquardt Report 5981, "(U) Final Report, Thrust Chamber Cooling Techniques for Spacecraft Engines for the Period 13 February 1962 to 12 February 1963. Volume II: Design Procedure and Data", 12 March 1963. UNCLASSIFIED.
3. Selig, H., J. G. Malm, and H. H. Claassen, "The Chemistry of the Noble Gases", Scientific American, May 1964, Vol. 210, No. 5, pp 66-77.
4. Bird, R. B., W. E. Steward, and E. N. Lightfoot, "Transport Phenomena", John Wiley & Sons, Inc., 1962.
5. Jet Propulsion Lab., T. R. No. 32-43, "A Comparison of Analytical and Experimental Local Heat Fluxes in Liquid--Propellant Rocket Thrust Chambers", W. E. Welsh, Jr., and A. B. Witte, 1 February 1961.
6. Fio Rito, R. J., "Engine Design Aspects for Ablatively Cooled Hypergolic Pulse Rockets", Chemical Propulsion Information Agency, 5th Liquid Propulsion Symposium Bulletin Vol. II, pp 565-620, November 1963.
7. NASA TN D-1726, "Experimental Investigation of Rocket-Engine Ablative Material Performance after Postrun Cooling at Altitude Pressures", R. J. Rollbuhler, Lewis Research Center, June 1963.
8. Jet Propulsion Laboratory Report TR 32-561, "An Experimental Investigation of Uncooled Thrust Chamber Materials for Use in Storeable Liquid Propellant Rocket Engines", R. W. Rowley, February 1964.
9. NASA TN D-130, "Use of a Theoretical Flow Model to Correlate Data for Film Cooling or Heating an Adiabatic Wall by Tangential Injection of Gases of Different Fluid Properties", J. E. Hatch and S. S. Papell, 1959.
10. NASA TN D-299, "Effect on Gaseous Film Cooling of Coolant Injection Through Angled Slots and Normal Holes", S. S. Papell, 1960.
11. NASA TN D-1988, "An Experimental Investigation of Gaseous Film Cooling of a Rocket Motor", J. G. Lucas and R. L. Golloday, October 1963.
12. Alsos, D. F., "An Experimental Investigation of Nozzle Cooling for a Small Rocket Engine", Thesis Air Force Institute of Technology, GAE/ME/63-1, August 1963.

UNCLASSIFIED

13. Sellers, J. P., Jr., "Gaseous Film Cooling with Multiple Injection Stations", AIAA Journal, September 1963, Vol. 1, No. 9, pp 2154-56.
14. ASD-TDR-62-260, Air Force Materials Laboratory, Research and Technology Division, Part I: "Refractory Reinforcements for Ablative Plastics", Part II: "Synthesis of Zirconium Nitride and Zirconium Oxide Flakes", R. L. Hough, October 1963.
15. RTD-TDR-63-4102, Battelle Memorial Institute, "Refractory Ceramics of Interest in Aerospace Structural Applications - A Materials Selection Handbook", Contract AF 33(657)-8326, J. R. Hague, J. F. Lynch and A. Rudnick, October 1963.
16. Georgia Institute of Technology Report AD 326-432, "Fused Silicon Rocket Nozzles", by Poules and Murphy, August 1961, CONFIDENTIAL.
17. Allegany Ballistics Laboratory Report ABL/X-94, "Fundamentals of Ablative Rocket Insulation", G. Sutherland and P. Hunt, April 1963.
18. General Electroc Corporation Report R63SD20, (AD404742), "Response of Charring Ablators to Hyperthermal Environment", Contract AF 04 (647)-617, February 1963.
19. NAVWEPS Report 8022, U. S. Naval Propellant Plant, (AD298343), "Temperature Measurements and Heat Transfer Calculations in Rocket Nozzle Throats and Exit Cones", J. Nanigan, December 1962.
20. Defense Documentation Center Report AD 337129, "Ablating and Thermal Insulating Materials", 1953 to May 1963. CONFIDENTIAL.
21. Union Carbide Corp. Report AD 409923, "Research on Physical and Chemical Principles Affecting High Temperature Materials for Rocket Nozzles", Contract DA-30-0 69-RD-2787, Robert Lowrie, June 1963.
22. Aerojet-General Corp., Solid Rocket Plant Report AD 401788, "Fiber Reinforced Carbide Rocket Nozzle Liners", Contract AF 33(657)-8890, April 1963.
23. Aerojet-General Corp., Report 652/SA4-2.2-F-1, (AD 408999), "Ablative Thrust Chamber Feasibility", Contract AF 04 (647)-652/SA4, June 1963.
24. NASA TN D-2024, "The Effect of Resin Composition and Fillers on the Performance of a Molded Charring Ablator", R. W. Peters and K. L. Wadlin, December 1963.
25. U. S. Navy Ordnance Test Station, NAVWEPS Report 7918, (AD 403360), "Thermal Studies of Reinforced Plastic Materials. Part I: Diffusivity of Five Reinforced-Plastic Heat Barriers", W. E. Donaldson and T. T. Castonquay, February 1963.

TMC A673

UNCLASSIFIED

UNCLASSIFIED

26. Atomics International Report AD 281110, Third Quarterly Report, "Study of Thermal Properties of Refractories", Contract AF 33(657)-7136, R. E. Taylor and M. M. Nakata, April 1962.
27. Aerospace Research Laboratories Report ARL-63-170, "Research on the Thermal Properties of Zirconia", Contract AF 33(616)-8208, R. B. Burdick and W. R. Hoskyna.
28. Bell Aerosystems Company Report 63-13(m), (AD 401 854), "Modulus of Rupture, Thermal Conductivity, and Thermal Exposure Tests on Foamed Aluminum Oxide and Foamed Zirconium Oxide", Contract AF 33(657)-8555, March 1963.
29. ASD-TDR-62-939, Aeronautical Systems Division, Dir/Materials and Processes, Physics Lab., Wright-Patterson Air Force Base, "Analysis of Thermal Degradation of Glass Reinforced Phenolic and Epoxy Laminates, Final Report", July 1963.
30. Munson, T. R., and R. J. Spindler, "Transient Thermal Behavior of Decomposing Materials. Part I: General Theory and Application to Convective Heating", Institute of Aerospace Sciences Paper 62-30, January 1962.
31. Cordo Chemical Corp., Project No. CLX 42, "Report of Investigation of Ablative Properties of Materials Molded at Extremely Low Pressure", March 1963.
32. Aerojet-General Corp. Report BSD-TDR-63-118, "Ablative Thrust Chamber Feasibility", Contract No. AF 04(647)-652/SA4, T. A. Hughes.
33. ASD-TDR-63-254, Aeronautical Systems Division, AF Materials Laboratory, Non-metallic Materials Division, Wright-Patterson Air Force Base, Part II, "Thermal Erosion of Ablative Materials", July 1963.
34. Air Force Systems Command Report TM-63-16, "Thermophysical Properties of Some Candidate Superorbital Heat Shield and Insulation Materials", J. H. Charlesworth, June 1963.
35. Cordo Chemical Cor. Report CLX 67, "Ablative Materials: Molding Compounds", July 1963.
36. ASD-TDR-62-635, Aeronautical Systems Division, Dir/Materials and Processes, Nonmetallic Materials Laboratory, Wright-Patterson Air Force Base, "Carbon-Base Fiber Reinforced Plastics", August 1962.
37. Northrop Corp., Norair Division Report NOR-60-257, (AD 270 419), "Evaluation of Graphite Cloth Reinforced Modified Phenolic Resin Laminate", D. H. Wykes, August 1960.

TMCA 673

UNCLASSIFIED

38. Avco Corp. Report RAD-SR-62-251, (AD 292 318), "Thermodynamics of Certain Refractory Compounds. Part II: Continued Theoretical and Experimental Studies on an Extended List", H. L. Schick and D. F. Anthrop, December 1962.
39. Beecher, N. and R. E. Rosensweig, "Ablation Mechanisms in Plastics With Inorganic Reinforcement", ARS Journal, Vol. 31, No. 4, pp 532-539, April 1961.
40. WADD-TR-60-646, Aeronautical Systems Division, Dir/Materials and Processes, Physics Lab., Wright-Patterson Air Force Base, Part II: "Carbonization of Plastics and Refractory Materials Research", January 1963.
41. ASD-TDR-63-403, Aeronautical Systems Division, Dir/Materials and Processes, Nonmetallic Materials Lab., Wright-Patterson Air Force Base, "Pyrolytic Reinforcing Agents for Ablative Erosion Resistant Composites", May 1963.
42. ASD-TDR-62-629, Aeronautical Systems Division, Dir/Materials and Processes, Applications Lab., Wright-Patterson Air Force Base, "Effect of Elevated Temperatures on Strength Properties of Reinforced Plastic Laminates", October 1962.
43. ASD-TR-61-439, Aeronautical Systems Division, Dir/Materials and Processes, Nonmetallic Materials Lab., Wright-Patterson Air Force Base, Part I: "Research on Criteria for Plastic Ablation Materials as Functions of Environmental Parameters", May 1962.
44. ASD-TDR-61-439, Aeronautical Systems Division, Dir/Materials and Processes, Nonmetallic Materials Lab., Wright-Patterson Air Force Base, Part II: "Research on Criteria for Plastic Ablation Materials as Functions of Environmental Parameters", Ablation Abstracts, May 1962.
45. ASD-TDR-62-746, Aeronautical Systems Division, Dir/Materials and Processes, Nonmetallic Materials Lab., Wright-Patterson Air Force Base, "Characterization of Carbonized Plastic Composites in Hyperthermal Environments", August 1962.
46. Naval Ordnance Laboratory Report NOL TR 63-100, "An Approach to Ablation Materials Study", April 1963.
47. Aerojet-General Corp. Report AD 295682, "A Survey of Insulation Materials", Contract AF 33(657)-8890, January 1963.
48. Aerojet-General Corp. Report AD 286 219, "A Preliminary Evaluation of the Mechanical, Physical, and Thermal Properties of Thirteen Reinforced Plastic Materials", Contract AF 33(657)-8890, October 1962.

UNCLASSIFIED

REPORT 6069

49. National Aeronautics and Space Administration, Langley Research Center Report TN D-1335, "Experimental Investigation of the Effect of Convective and Radiative Heat Loads on the Performance of Subliming and Charring Ablators", March 1962.
50. Simkin, D., "Applications of Plastic Materials in Aerospace", AIChE Chemical Engineering Progress Symposium, Series, Vol. 59, No. 40, 1963.
51. General Electric, Second Quarterly Report, Contract NAS3-2566, "Analytical Comparisons of Ablative Nozzle Materials", F. E. Schultz, September to December 1963.
52. Aerospace Engineering, Vol. 22, No. 1, "High Temperature Materials Issue", January 1963.
53. Atlantic Research Corp. Report AD 412455, Mod. No. 22, "Chemical Reactions Between Propellant Gases and Nozzle Materials", Contract NOrd 15536, R. S. Scheffee and W. E. West, July 1963.
54. The Dow Chemical Company Publication, "JANAF Thermochemical Tables", Midland, Michigan, 31 December 1960. UNCLASSIFIED.
55. Aeronutronic Division of Ford Motor Co. Report C-1010, "Study of Metal Additives for Solid Propellants, 12th Quarterly Report", 15 October 1960. CONFIDENTIAL.
56. Los Alamos Scientific Laboratory Report LAMS-2896, "Graphite-Hydrogen-Methane Kinetics Above 1600°K", August 1962. UNCLASSIFIED.
57. Marquardt Report 278-2-5, "Monthly Letter Progress Report, 13 September Through 12 October 1963, Contract NAS7-103". UNCLASSIFIED.
58. Marquardt Report 278-2-4, "Monthly Letter Progress Report, 13 August Through 12 September 1963, Contract NAS7-103". UNCLASSIFIED.
59. Medford, J. E., "Transient Radial Heat Transfer in Uncooled Rocket Nozzles", Aerospace Engineering, October 1962.
60. NASA TR R-56, "Graphical Presentation of Difference Solutions for Transient Radial Heat Conduction in Hollow Cylinders with Heat Transfer at the Inner Radius and Finite Slabs with Heat Transfer at One Boundary", J. E. Hatch, et al, 1960. UNCLASSIFIED.

TMC 8673

UNCLASSIFIED

UNCLASSIFIED

REPORT 6069

This page intentionally left blank.

TMC A 673

UNCLASSIFIED

TABLE ICOOLANTS INERT TO GRAPHITE AT 6000°R AND 100 psia

(Reactant Products < 1% Mole Fraction)

Coolant	Major Compounds Formed with Graphite
N ₂	CN, C ₂ N ₂
CO	--
C ₃ O ₂	--
CO Cl ₂	--

TABLE II

COOLANTS WHICH DECOMPOSE OR REACT WITH GRAPHITE AT 6000°R AND 100 psia

Coolant	Temperature at Which Products Exceed 1% (°R)	Major Compounds Formed with Graphite
HCl	5800	C ₂ H ₂
HF	5160	C ₂ F ₂ , C ₂ H ₂ , C ₂ H
HI	5000	C ₂ H ₂ , C ₂ H
H ₂	Almost all	CH ₄ , C ₂ H ₂ , C ₂ H
CS ₂	2600	CS
C ₂ H ₂	5200	C ₂ H
CH ₄	3500	C ₂ H ₂ , C ₂ H ₄ , CH ₃ , C ₂ H
CF ₄	2600	C ₂ F ₂ , CF ₃ , CF ₂
H ₂ O *	--	CO, C ₂ H ₂ , CO ₂ , C ₂ H, CH ₄

* Not cryogenically storable

UNCLASSIFIED

TABLE III
 COMBUSTION PRODUCTS FOR HIGH PERFORMANCE LIQUID PROPELLANT SYSTEMS

Propellant Combination	O/F (1)	T _c (°F)	I _{sp} (seconds)				Combustion Products (2) (Mole Fractions)																
			40:1 100 psia	100:1 100 psia	500:1 100 psia	500:1 1000 psia	H ₂ O	H ₂	H	OH	O	O ₂	CO	CO ₂	HF	F	N ₂	NO	BOF	BO	BF	BOH	
O ₂ /H ₂	5.0	5128	455	470	485	487	0.568	0.350	0.049	0.030	0.002	0.001	--	--	--	--	--	--	--	--	--	--	--
F ₂ /H ₂	12.0	6833	473	488	504	506	--	0.104	0.216	--	--	--	--	--	0.642	0.037	--	--	--	--	--	--	--
(4) OF ₂ /CH ₄	5.0	6748	416	432	450	453	0.012	0.037	0.118	0.023	0.041	0.005	0.185	0.007	0.530	0.041	--	--	--	--	--	--	--
OF ₂ /MMH	2.6	6690	409	426	447	451	0.015	0.030	0.100	0.031	0.057	0.011	0.110	0.006	0.479	0.038	0.111	0.010	--	--	--	--	--
OF ₂ /H ₂	7.0	5788	476	490	505	507	0.154	0.312	0.117	0.028	0.006	0.001	--	--	0.379	0.002	--	--	--	--	--	--	--
OF ₂ /B ₂ H ₆	4.0	7035	433	454	482	489	0.013	0.097	0.250	0.022	0.031	0.002	--	--	0.294	0.023	--	--	0.160	0.030	0.067	0.005	0.005
(3) P7000	--	7000	--	--	--	--	0.625	0.375	--	--	--	--	--	--	--	--	--	--	--	--	--	--	--
(3) P8500	--	8500	--	--	--	--	0.625	0.375	--	--	--	--	--	--	--	--	--	--	--	--	--	--	--

(1) Approximate mixture ratio for maximum I_{sp} at 100 psia.

(2) Ideal combustion. Combustion products do not vary significantly with chamber pressure.

(3) Hypothetical propellant combination.

(4) Heat of formation of OF₂ taken as 3.6 kcal/mole

UNCLASSIFIED

UNCLASSIFIED

REPORT 6069

TABLE IV
CHEMICAL ABLATION MODEL, SILICA PHENOLIC

CHARACTERISTIC REACTION REGIONS				
VIRGIN MATERIAL	CHAR OR DEPOLYMERIZATION REGION	① INITIAL CARBON DEPLETION REGION	② FINAL CARBON DEPLETION REGION	③ OXIDATION OF SILICON REGION
30% RESIN 70% SiO ₂	15% C RESIDUE 85% SiO ₂	<p>SIC FORMATION</p> <p>15% C → 5% C</p> <p>0% SiC → 22% SiC</p>	<p>OXIDATION OF SiC</p> <p>REDUCTION OF SiO₂</p> <p>5% C → 0% C</p> <p>0% Si → 25% Si</p>	<p>REDUCTION OF SiO₂ BY Si</p>
	500° F	2000° F	3100° F	4000° F
		① (EXCESS) SiO ₂ + 3 C ⇌ SiC + 2 CO (+ SiO ₂)	② (EXCESS) SiO ₂ + SiC ⇌ SiO + CO + Si (+ SiO ₂)	③ (EXCESS) SiO ₂ + Si ⇌ 2 SiO (+ SiO ₂)

TMC A 673

UNCLASSIFIED

UNCLASSIFIED

REPORT 6069

TABLE V

EVALUATION OF HEAT SINK CAPABILITY OF MATERIALS FOR NOZZLE INSERT
WITH INNER RADIUS (r_i) OF 0.345 inches
AND HEAT TRANSFER COEFFICIENT (h) OF 800 Btu/ft² hr°F
AT THE INNER SURFACE

Material	Thermal Conductivity, k (Btu/hr ft°F)	Thermal Diffusivity, α (ft ² /hr)	$\frac{h r_i}{k}$
Graphite	40.	1.039	0.575
Pyrolytic Graphite	140.	2.555	0.164
Tungsten	60.	1.547	0.383
Beryllia	24.2	0.2682	0.95

Time (t) for inner surface to reach $\frac{(T_s - T_o)}{(T_g - T_o)} = 0.5$

With $R_e = \frac{\text{Exterior radius}}{\text{Inner radius}} = \frac{1.185}{0.345}$ (From Figure 59) = 3.44

Material	$\alpha t / r_i^2$ (From Figure 57)	t (seconds)
Graphite	4.6	13.7
Pyrolytic Graphite	20.5	24.
Tungsten	8.	15.
Beryllia	1.7	18.9

Time for inner surface to reach $\frac{(T_s - T_o)}{(T_g - T_o)} = 0.5$

With optimum R_e or $R_e = 10$ if optimum not reached

Material	$\alpha t / r_i^2$	t (seconds)	Optimum R_e
Graphite	10.	29.	Approximately 10.
Pyrolytic Graphite	195.	227.	Greater than 10.
Tungsten	42.	81.	Greater than 10.
Beryllia	1.75	19.4	4.

TMCA 673

UNCLASSIFIED

UNCLASSIFIED

REPORT 6069

TABLE VI

EVALUATION OF HEAT SINK CAPABILITY OF MATERIALS FOR NOZZLE
WITH INNER RADIUS (r_i) OF 2 inches
AND HEAT TRANSFER COEFFICIENT (h) OF 800 Btu/ft² hr°F
AT THE INNER SURFACE

Time (t) for inner surface to reach $\frac{(T_s - T_o)}{(T_g - T_o)} = 0.5$

With optimum R_e ($R_e = \frac{\text{Exterior radius}}{\text{Inner radius}}$)

Material	K (Btu/hr ft°F)	α (ft ² /hr)	$\frac{h r_i}{K}$	$\frac{\alpha t}{r_i^2}$ (From Figure 57)	t (seconds)	Optimum R_e
Graphite	40.	1.039	3.33	0.07	7.	1.67
Pyrolytic Graphite	140.	2.555	0.952	1.75	68.	4.
Tungsten	60.	1.547	2.22	0.19	12.	2.
Beryllia	24.2	0.2682	5.51	0.024	9.	1.43

TMC A 673

UNCLASSIFIED

UNCLASSIFIED

TABLE VII
 SUMMARY OF TEST DATA
 Propellants - Gaseous Oxygen and Hydrogen

Nozzle Configuration	Run No.	Run Duration (sec)	O/F	Prop. Flow (pps)	P _o (psia)	F (lbs)	Coolant	Coolant Flow Rate (pps)	T _{sp} (sec)	Remarks
Water cooled nozzle	1 to 13	1.0 to 120	5.0	0.53	100		None			Preliminary check out
Graph-I-Tite G	14	45	5.05	0.4750	87.5	118	None		89.0	
ATJ Graphite	15	44.3	4.88 5.00	0.518 0.529	99.0 79.5	138 32.0	None		93.0	Data at 2 sec Data at 44 sec
Graph-I-Tite G	16	59.4	4.98 4.98	0.535 0.535	103.0 78.5	140.0 131.5	None		90.0	Data at 5 sec Data at 59 sec
ATJ Graphite	17	60.5	4.95 4.95	0.534 0.534	100.0 66.0	139.5 124.0	None		91.5	Data at 4 sec Data at 60 sec
Graph-I-Tite G	18	60	4.60	0.535	103.5	145.0	None		94.0	Data at 17 sec osc. jammed
ATJ Graphite	19	60.9	4.99 4.99	0.529 0.529	98.3 71.0	138.8 132.0	None		92.0	Data at 4 sec Data at 60 sec
Film Cooled Thick Steel (Radial Injection)	20 21 22	4.0 14.5 8.5	5.23 4.88 5.50	0.521 0.512 0.574	172.0 169.0 154.0	225.0 250.0 226.0	Nitrogen	?		Film coolant flow data is not valid because of leakage
	23	Aborted run because of hydrogen leak in film coolant manifold								
	24	29.5	5.14	0.534	130.0	191.0	Hydrogen	0.098	100	Nozzle erosion at beginning of contraction area
Thick Steel (0.15 wall)	25 26 27 28 29	3.5 2.98 3.56 3.50 3.30	5.35 5.6 4.72 4.66 5.05	0.483 0.557 0.511 0.528 0.537	90.0 101.0 98.2 100.0 99.2	130.0 148.0 136.0 141.0 145.5	None		96.0 93.0 93.0 93.0 95.0	Injector evaluation-- nozzle was rotated one bolt hole after each run to obtain temperature distribution

UNCLASSIFIED

UNCLASSIFIED

TABLE VII (Continued)

Nozzle Configuration	Run No.	Run Duration (sec)	O/F	Prop. Flow (pps)	P _o (psia)	F (lbs)	Coolant	Coolant Flow Rate (pps)	I _{sp} (sec)	Remarks
Film Cooled Thick Steel (Radial Injection)	30	17.4	4.85	0.510	133.0	200.0	Helium	0.28	84.0	Nozzle erosion at the throat
	31	15.7	4.86	0.512	125.0	184.8		0.192	88.0	
	32	15.3	4.90	0.526	122.0	179.0		0.141	90.0	
	33	9.5	5.40	0.507	102.0	150.0		0.06	92.0	
Film Cooled Thick Steel (Tangential injection)	34	8.6	5.46	0.539	115.5	171.5	Helium	0.102	90.5	Nozzle rotated one bolt hole after each run to determine temperature distribution
	35	7.8	5.60	0.570	117.0	174.5		0.0982	88.0	
	36	8.3	5.17	0.534	113.5	169.0		0.0976	91.0	
	37	8.0	4.93	0.516	112.0	163.0		0.0982	91.0	
	38	8.2	5.29	0.538	110.0	163.0		0.0957	88.5	Film injector rotated 180°
	39	8.6	5.20	0.530	112.0	162.0		0.100	88.0	
Single 180° Slot, Edge Oriented Pyrolytic Graphite	40	60.6	5.0	0.535	99.5	111.0	Methane	0.00864		Data at 4 sec
			5.0	0.535	101.5	118.0		0.0030		Data at 60 sec
	41	21.7	5.03	0.531	99.5	116.0		None		Data at 20 sec
			5.03	0.531	97.8	115.0		0.00475		Data at 8 sec
Film Cooled Thin Steel (Tangential injection)	42	167.7	5.03	0.531	97.5	119.5		0.00475		Data at 20 sec
			5.03	0.531	97.5	120.5		?		Data at 88 sec
			5.03	0.531	93.0	118.0		0.00133		Data at 167 sec
	43	83.0	5.04	0.533	110.5	166.0	Helium	0.105	89.0	Data at 12 sec
			5.04	0.533	108.5	163.5		0.095	89.5	Data at 40 sec
			5.04	0.533	107.5	162.5		0.0879	90.0	Data at 48 sec
			5.04	0.533	104.6	159.0		0.0736	90.5	Data at 64 sec
			5.04	0.533	104.0	156.0		0.0594	91.0	Data at 83 sec
	44	7.3	4.98	0.522	97.8	151.5		0.0393	94.0	Nozzle burn out at throat

UNCLASSIFIED

UNCLASSIFIED

TABLE VII (Continued)

Nozzle Configuration	Run No.	Run Duration (sec)	O/F	Prop. Flow (pps)	P _o (psia)	F (lbs)	Coolant	Coolant Flow Rate (pps)	I _{sp} (sec)	Remarks
Film Cooled Graph-I-Tite G (Tangential injection)	45	60.0	4.99	0.518	110.5	151.0	Helium	0.0449		Data at 8 sec
			4.99	0.518	105.5	154.5		0.0449		Data at 60 sec, no erosion noted
	46	143.0	4.99	0.518	105.5	154.0		0.0361		Data at 12 sec
			4.99	0.518	64.0	124.0		0.0361		Data at 143 sec, severe throat erosion
Coated Molybdenum (Tangential injection)	47	190.8	5.01	0.521	108.5	162.2	Helium	0.039	95.0 to 100	Data at 12 sec
			5.01	0.521	107.5	164.5		0.0241		Data at 190 sec, helium flow reduced in steps. Combustion chamber cooling jacket failed during or after run
	48	16.3	5.01	0.521	101.5	149.5	Methane	0.0648		Two comb. chamber sections burned out. Run was with three comb. chamber sections
Graph-I-Tite G	49	60.0	4.94	0.535	104.8	144.0	Methane	0.0208	90.0	Slight erosion at one spot on throat
	50	180.0	4.93	0.530	99.8 68.0	143.0 132.0		0.0211	90.0	Data at 20 sec Data at 160 sec severe throat erosion at hot spots
Thin Steel (0.06 wall)	51	1.5	5.01	0.531	110.0	137.0	None	None	88	Heat transfer study-- nozzle burned out
Pyrolytic Graphite	52	14.7	4.97	0.538	104.5	118.0	Methane	0.0209		Depleted H ₂ because supply valve not open
	53	180.0	4.93	0.535	102.5	123.0		0.0209		Only slight amount of throat erosion 0.003 in.

UNCLASSIFIED

UNCLASSIFIED

TABLE VII (Continued)

Nozzle Configuration	Run No.	Run Duration (sec)	O/F	Prop. Flow (pps)	P _o (psia)	F (lbs)	Coolant	Coolant Flow Rate (pps)	I _{sp} (sec)	Remarks
Thick Steel (0.15 wall)	54	0.82	4.94	1.125	199.0	320	None	None		Engine operation at 200 psi chamber pressure
	55	1.15	4.94	1.125	205.0	320	None	None		Hard start
Multislotted Pyrolytic Graphite	56	170.0	4.93	0.536	104.0	116.0	Hydrogen	0.00635		No erosion
	57	270.0	4.98	0.532	105.0	110.0	Carbon Monoxide	0.0211		Uniform erosion in contraction area
Film Cooled Thin Steel (Tangential injection)	58	6.0	4.70	0.506	116.5	166.5	Methane	0.209	79.0	Film injector burned out because of no coolant water
Porous Graphite Throat	59	67.0	5.07	0.530	100.0	107.5	Helium	0.00029		Porous insert was severely eroded.

UNCLASSIFIED

UNCLASSIFIED

TABLE VIII
NOZZLE TEMPERATURES FOR RUNS 30 THROUGH 33
 (Helium Film Cooling)

		Temperature (°F)													
Station		I		II		III (Throat)						IV (Exit)			
Thermocouple No.		1	2	3	4	5	6	7	8	--	9	10	11	12	--
Run No.	τ (sec)									Throat Avg.					Exit Avg.
30	15.1	640	650	--	750	880	860	870	890	875	840	820	820	830	828
31	15.1	700	710	--	850	970	1050	990	1000	1002	920	990	930	920	940
32	15.1	760	850	--	1000	1120	1350	1190	1160	1205	1060	1240	1090	1090	1120
33	--	1000	1240	--	1450	1470	2340	1590	1680	1770	1220	1890	1260	1340	1427

UNCLASSIFIED

UNCLASSIFIED

TABLE IX
 NOZZLE TEMPERATURES FOR RUNS 43, 44, AND 58

		Temperature (°F)													
Station		B	D		F (Throat)							G			
Thermocouple No.		1	2	3	11	4	5	6	7	8	9	10	--	12	Coolant
Run No.	Time (sec)												Throat Avg.		
43a	16	798	1300	1430	1225	1575	1650	1360	1085	1640	1160	1450	1393	1665	He
43c	42	860	1390	1520	1290	1670	1730	1403	1180	1730	1255	1498	1469	1747	He
43d	70	998	1615	1725	1535	1913	1850	1520	1400	1905	1475	1615	1651	1930	He
43e	83	1095	1730	1835	1650	2035	1985	1590	1515	2025	1590	1675	1759	2015	He
44	--	1680	2305	2380	2280	2500	--	1830	2130	2400	2220	2050	2201	2270	He
58	6	550	925	820	1270	--	1116	1240	1850	1222	1420	1080	1314	1600	CH ₄

UNCLASSIFIED

TABLE X

NOZZLE TEMPERATURES FOR RUN 47
HELIUM COOLED MOLYBDENUM NOZZLE
TEMPERATURE NEAR THROAT, PYROMETER RECORDED

Run No.	Maximum Nozzle Temperature (°F)	Helium Flow Rate (pps)
47a	2210	0.039
47b	2385	0.0345
47c	2555	0.0293
47d	2780	0.0267
47e	2905	0.0241

UNCLASSIFIED

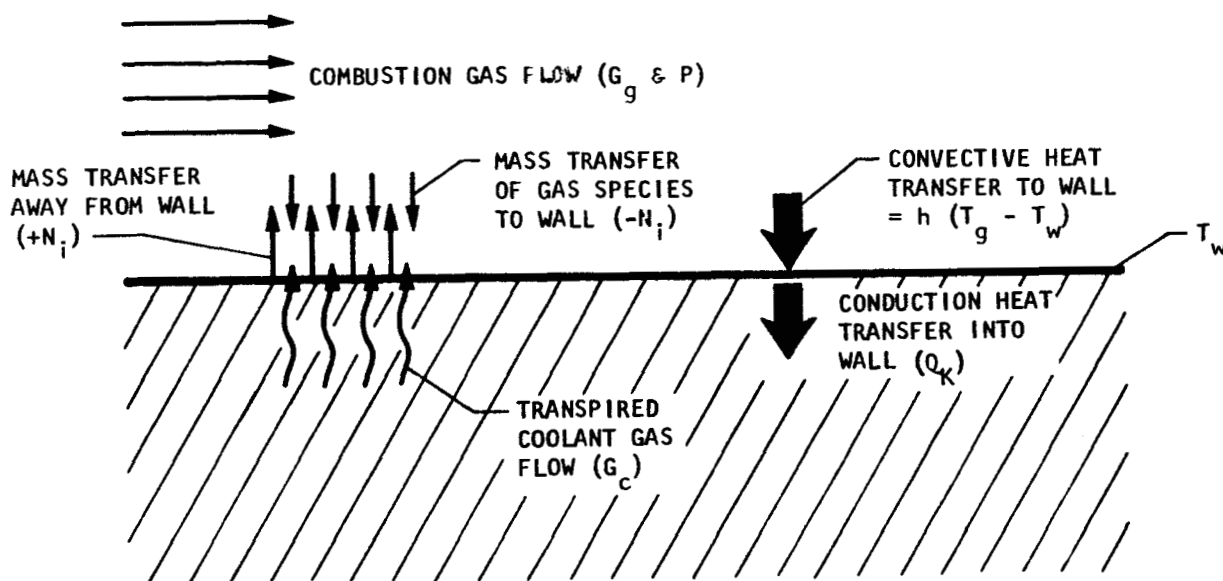
REPORT 6069

This page intentionally left blank.

TMC A 673

UNCLASSIFIED

MODEL FOR THERMOCHEMICAL EROSION ANALYSIS

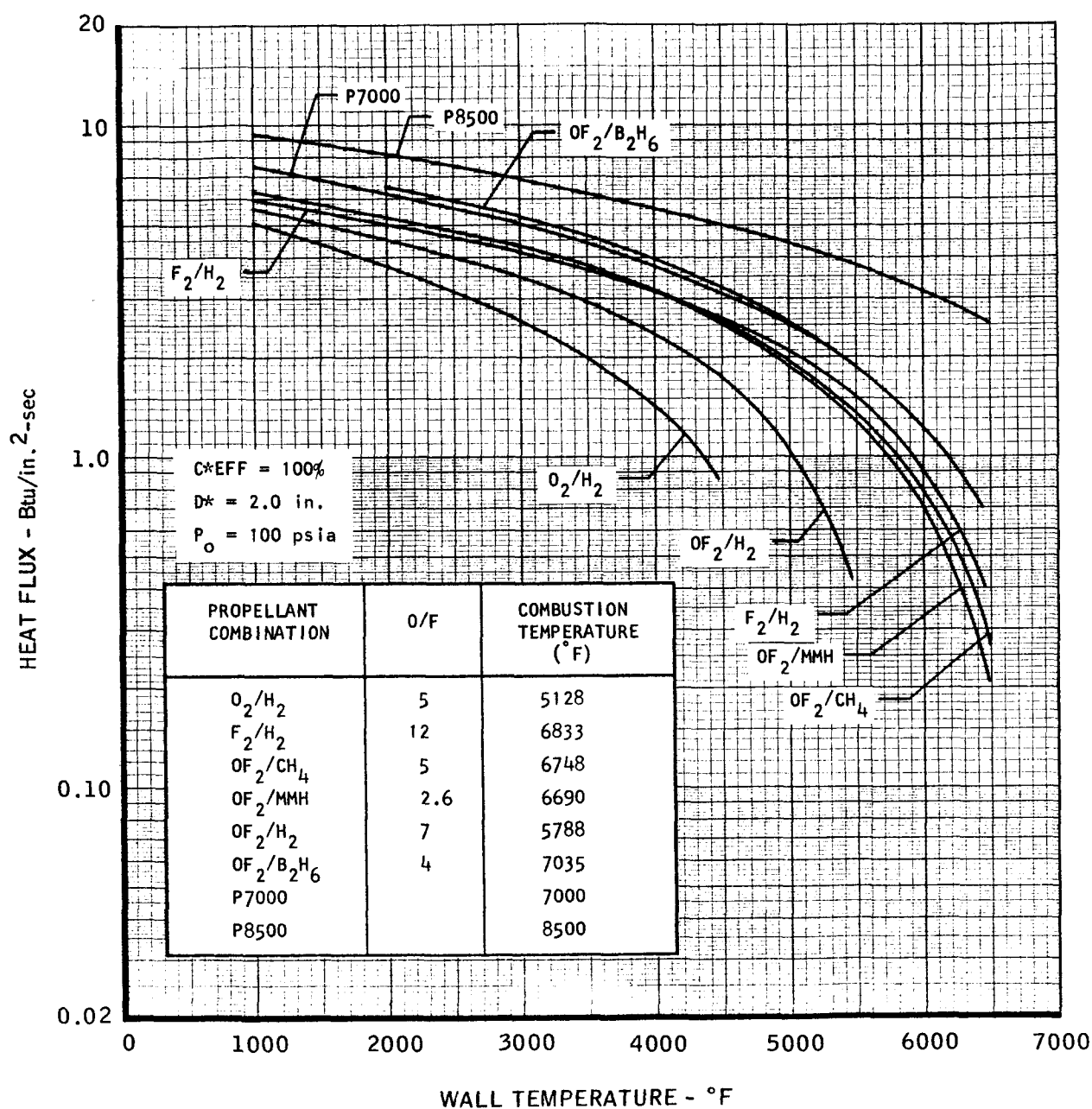
ASSUMPTIONS:

1. MATERIAL IS UNIFORMLY POROUS GRAPHITE WALL
2. ALL CHEMICAL REACTIONS OCCUR AT GAS-SOLID INTERFACE
3. CONDUCTION HEAT TRANSFER IS ZERO OR CONSTANT VALUE

UNCLASSIFIED

REPORT 6069

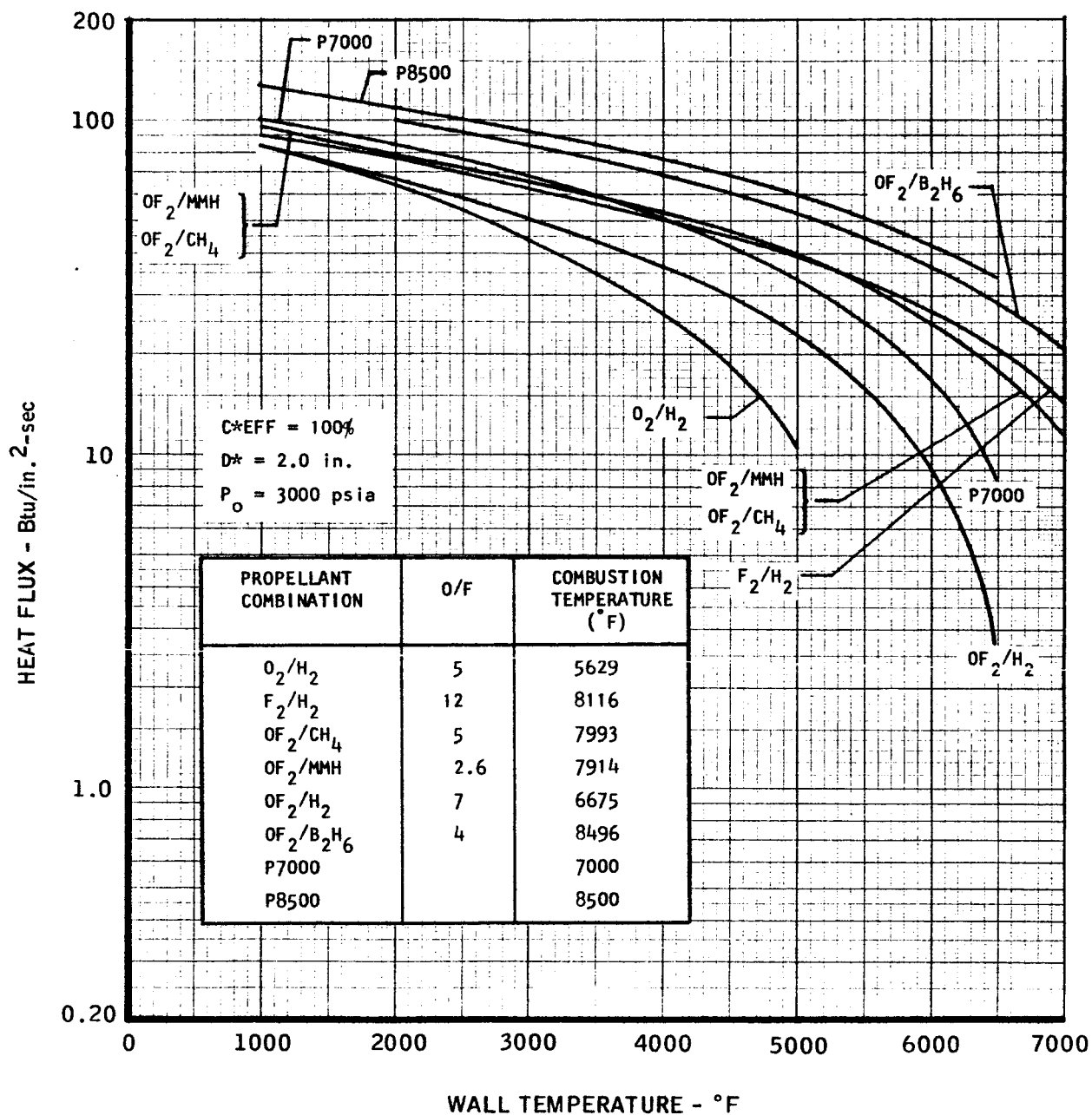
HEAT FLUX TO NOZZLE THROAT WITH HIGH PERFORMANCE LIQUID PROPELLANTS



TMC A 673

UNCLASSIFIED

HEAT FLUX TO NOZZLE THROAT WITH HIGH PERFORMANCE LIQUID PROPELLANTS



TMCA 673

FLOW DIAGRAM FOR THERMOCHEMICAL EROSION ANALYSIS

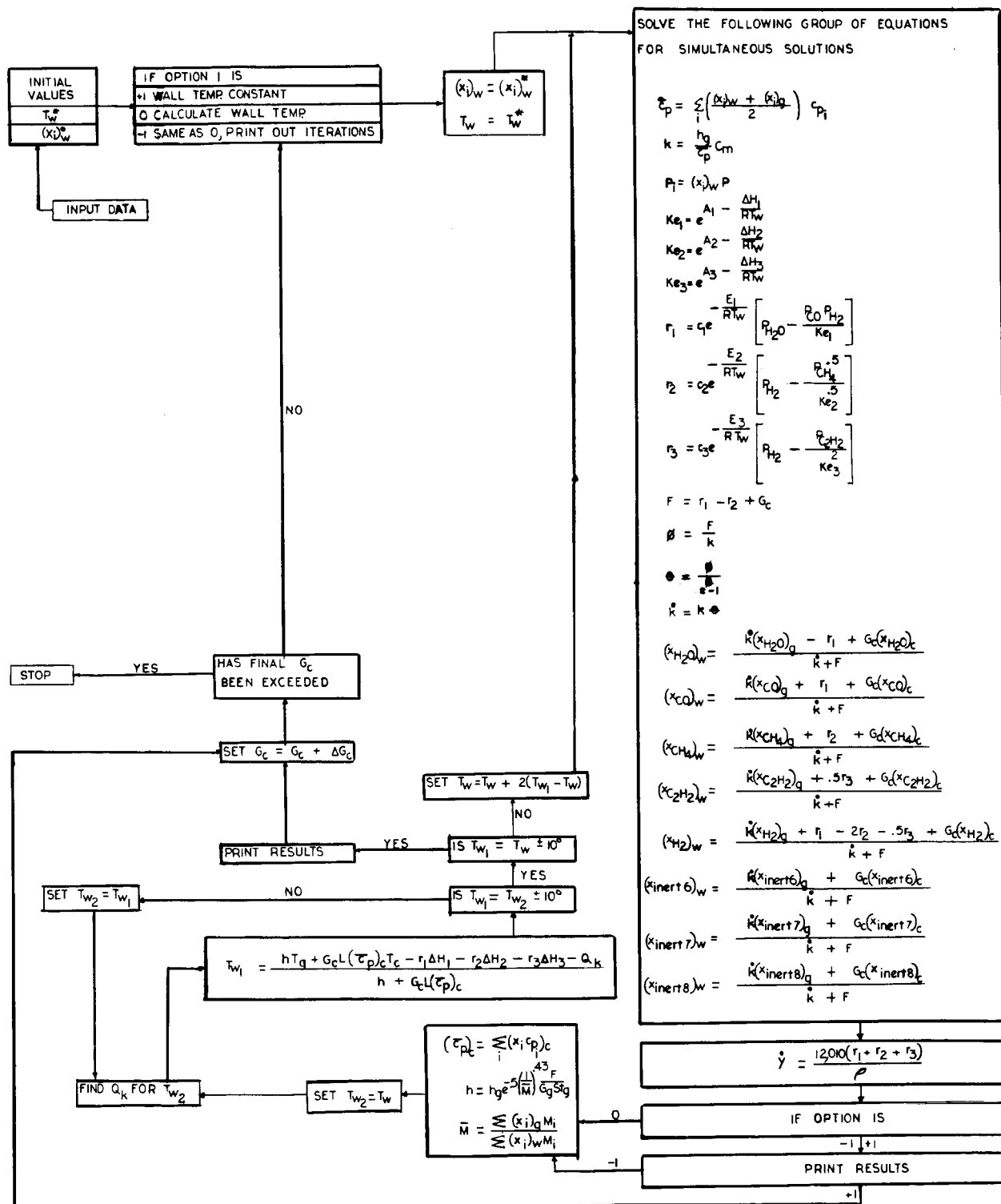
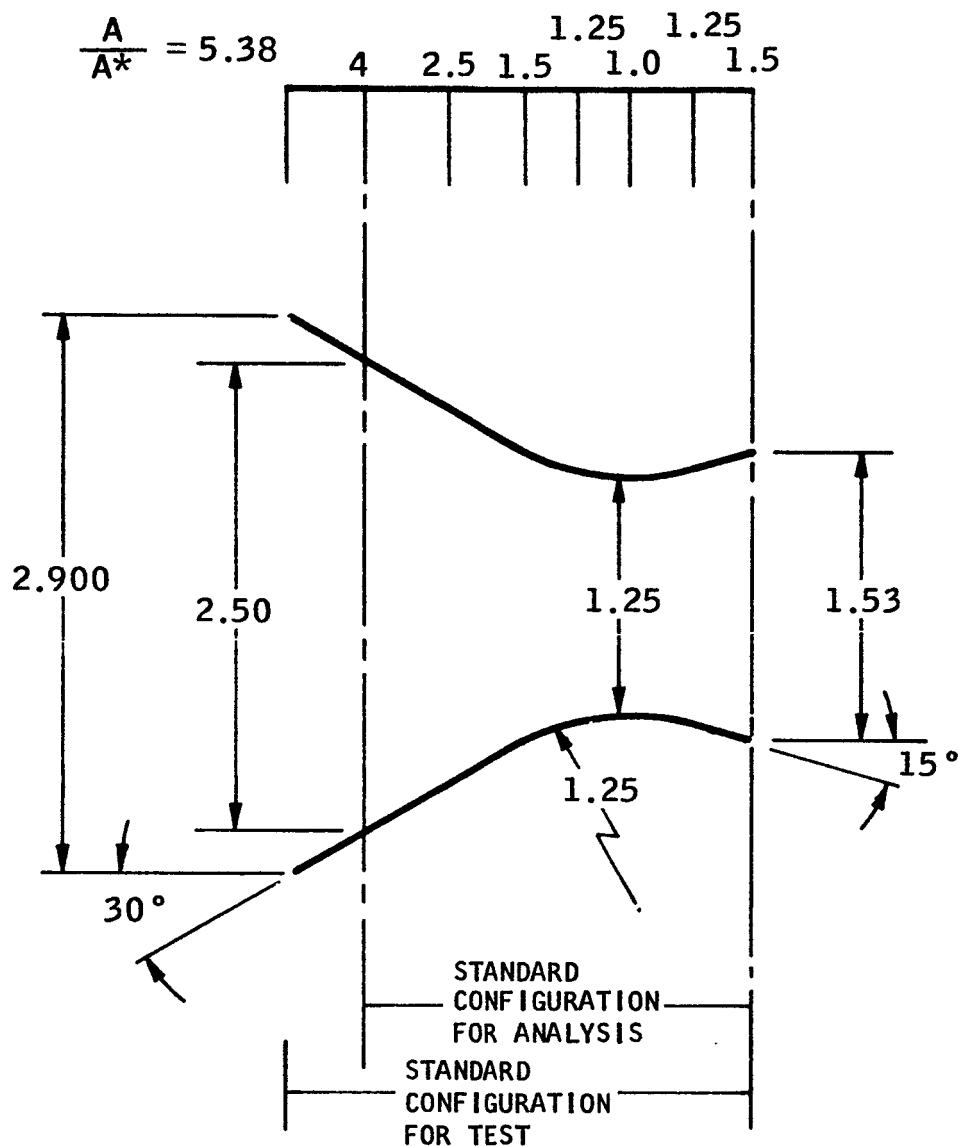


FIGURE 4

UNCLASSIFIED

REPORT 6069

STANDARD NOZZLE GEOMETRY - 1.25-inch THROAT DIAMETER



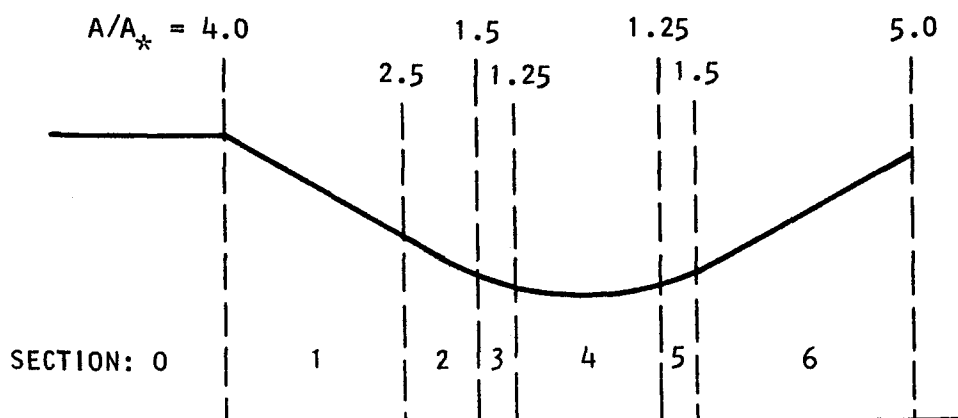
TMC A673

UNCLASSIFIED

REPORT 6069

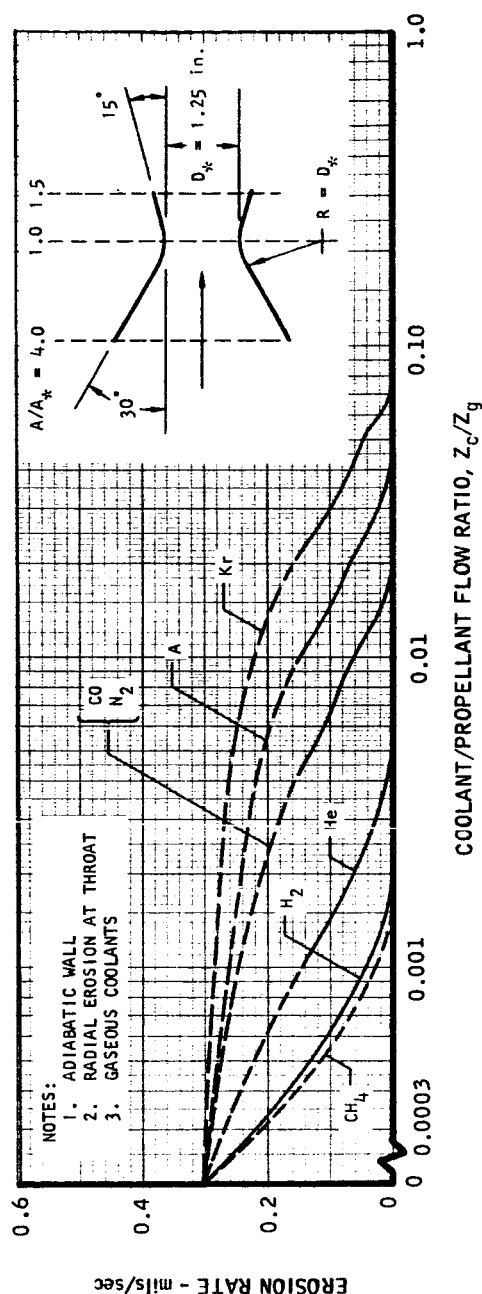
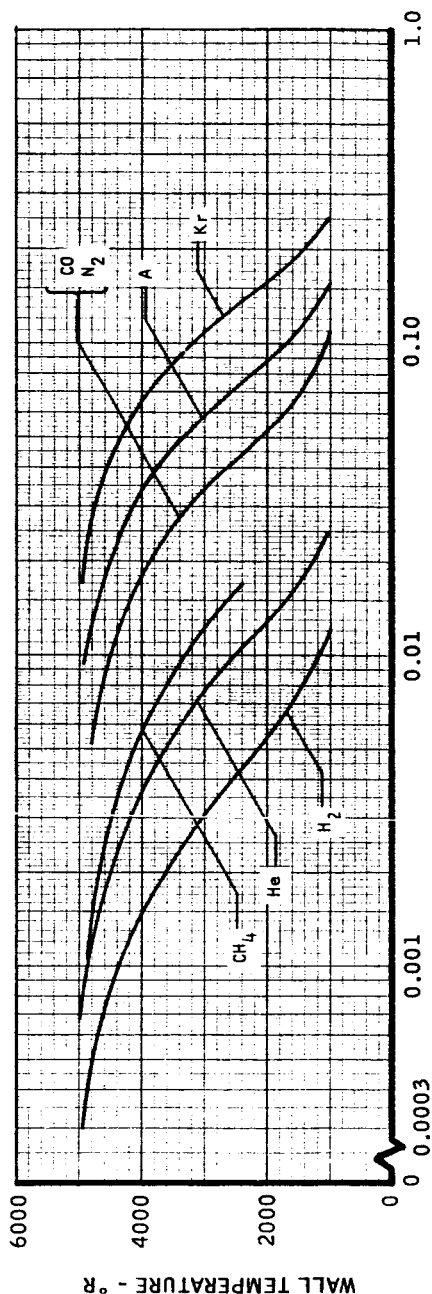
THRUST CHAMBER SECTIONS USED IN ANALYSIS

LOCATION	SECTION	A_c/A_g			
		$D_* = 0.6$	$D_* = 1.25$	$D_* = 3.0$	$D_* = 6.0$
COMBUSTION CHAMBER	0	9.0	5.1	2.83	1.33
↑	1	0.92	0.92	0.92	0.92
	2	1.01	1.01	1.01	1.01
NOZZLE	3	0.36	0.36	0.36	0.36
↓	4	3.02	3.02	3.02	3.02
	5	0.68	0.68	0.68	0.68
BELL	6	1.95	2.5	2.06	2.5



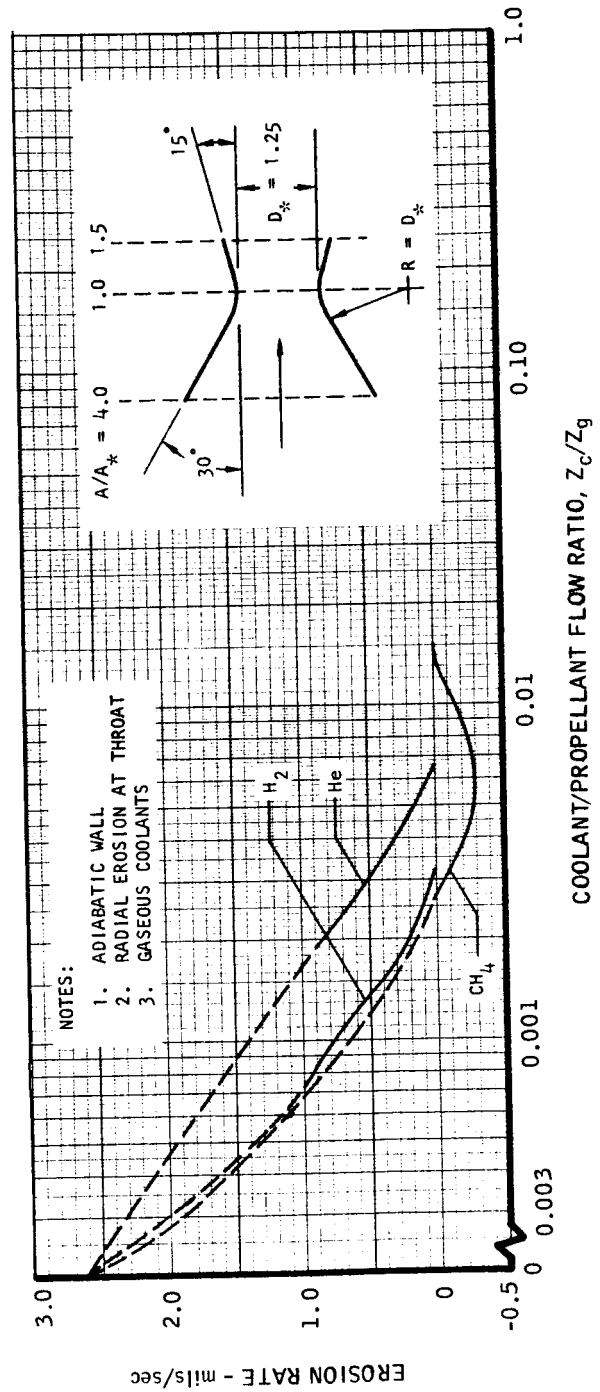
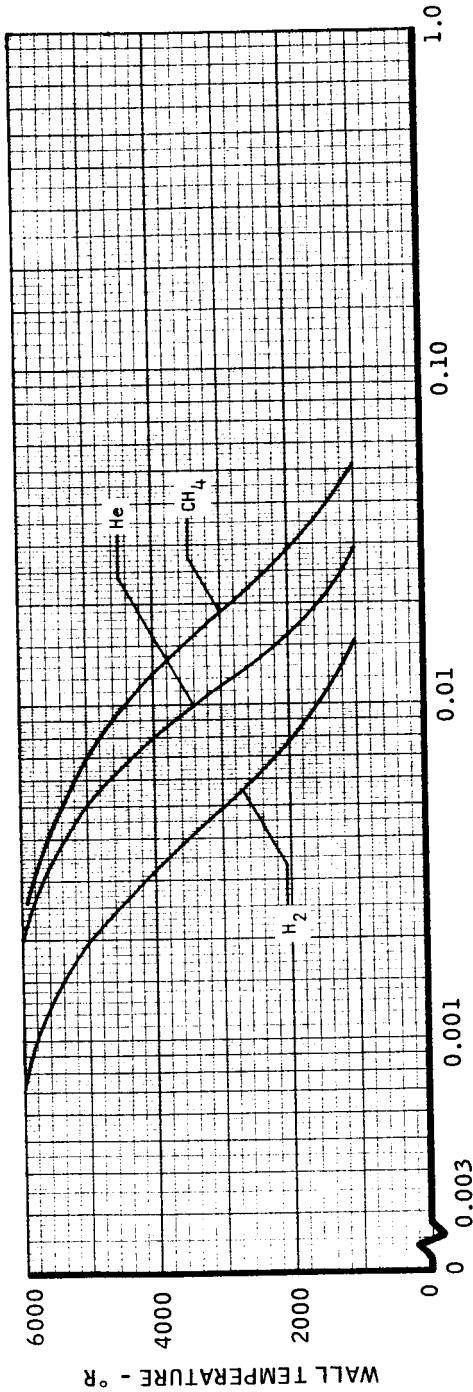
TRANSPARATION COOLED GRAPHITE NOZZLE TEMPERATURE AND EROSION RATE FOR O₂/H₂

$D_* = 1.25$ in.; $P_0 = 100$ psia; $T_g = 5210^\circ R$



TRANSPARATION COOLED GRAPHITE NOZZLE TEMPERATURE AND EROSION RATE FOR P7000

$D_* = 1.25$ in.; $P_0 = 100$ psia; $T_g = 7460^\circ R$

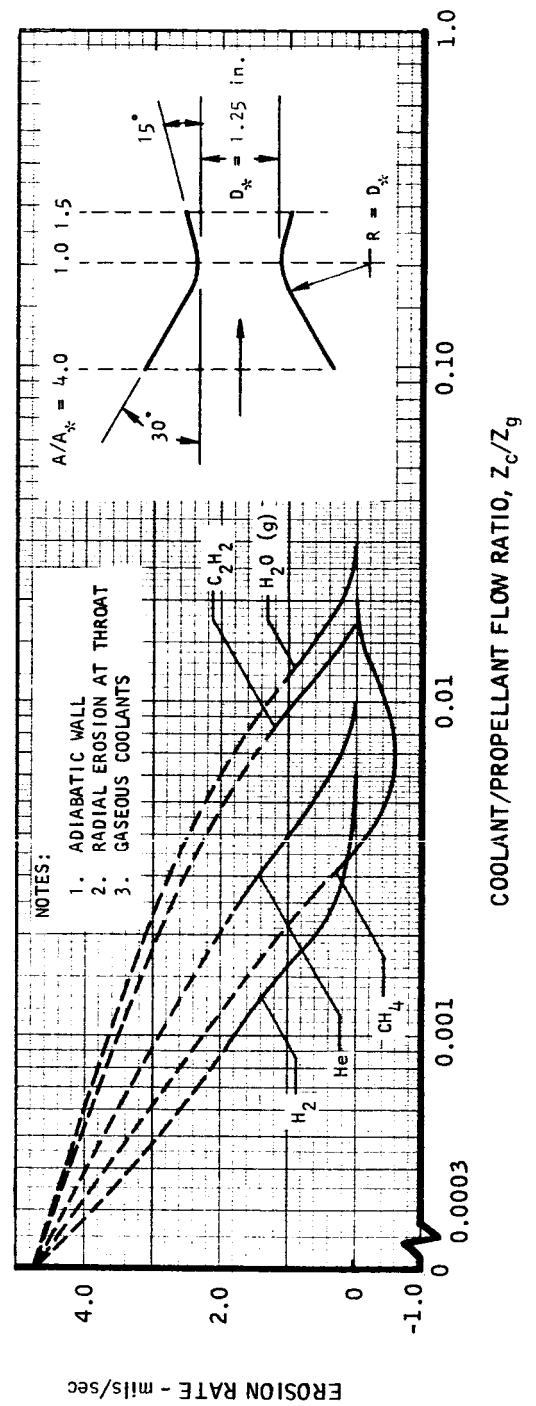
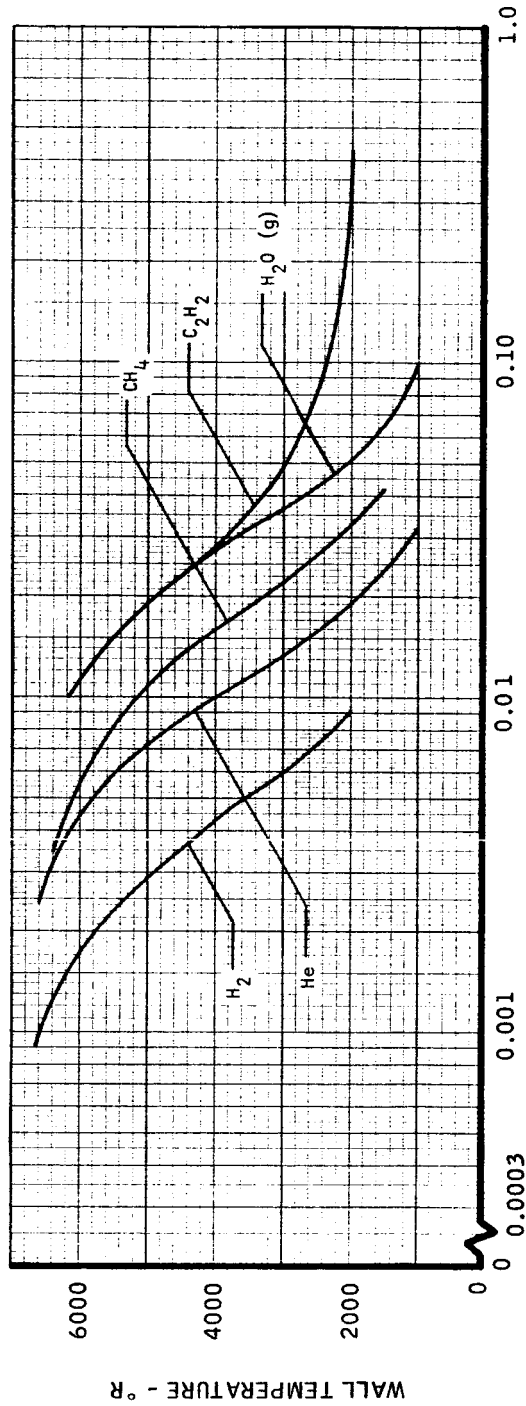


UNCLASSIFIED

REPORT 6069

TRANSPARATION COOLED GRAPHITE NOZZLE TEMPERATURE AND EROSION RATE FOR P8500

$D_* = 1.25$ in.; $P_0 = 100$ psia; $T_g = 8960^\circ\text{R}$

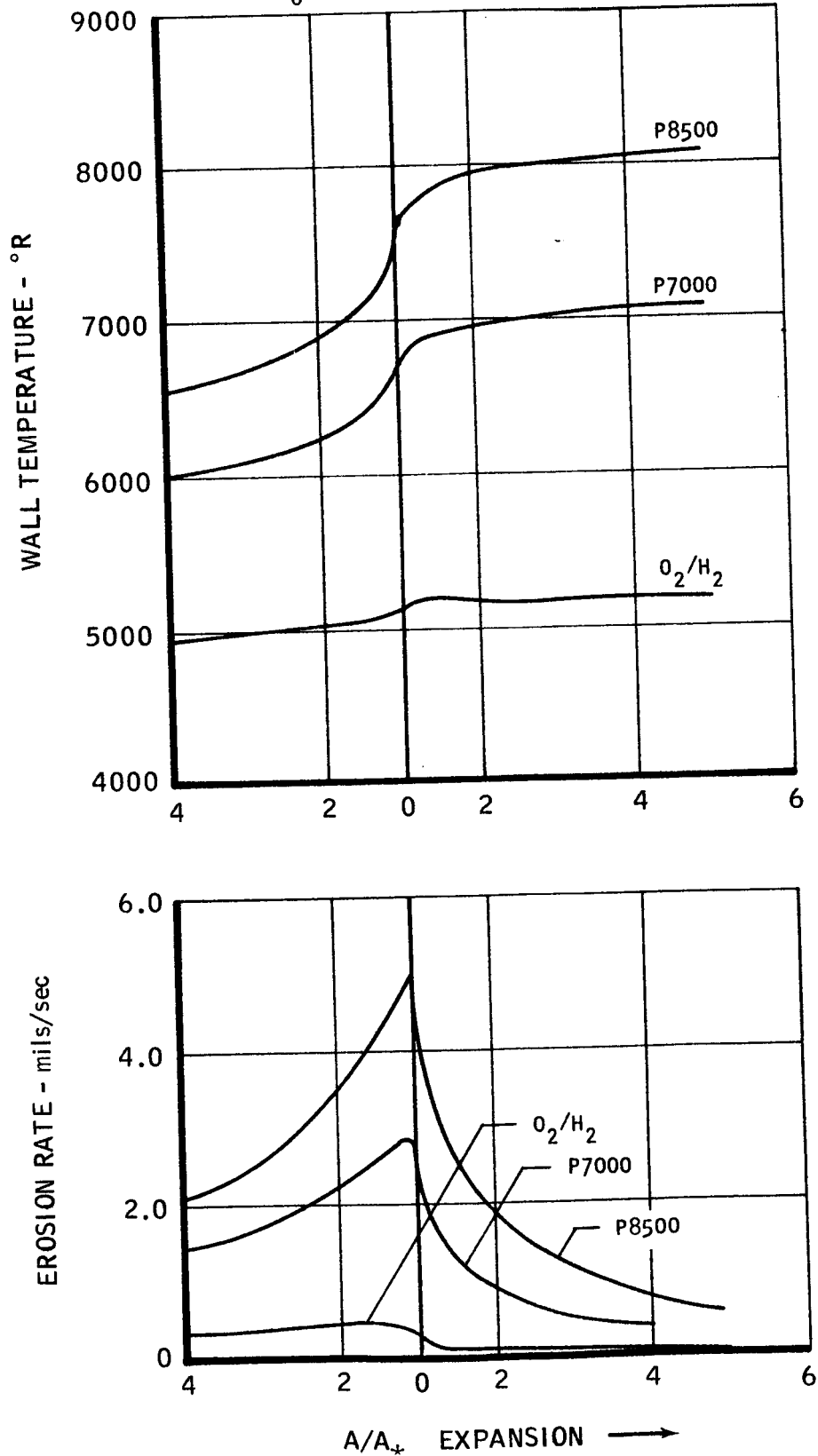


TMC A673

UNCLASSIFIED

EROSION RATE PROFILE FOR AN UNCOOLED PYROLYTIC GRAPHITE NOZZLE

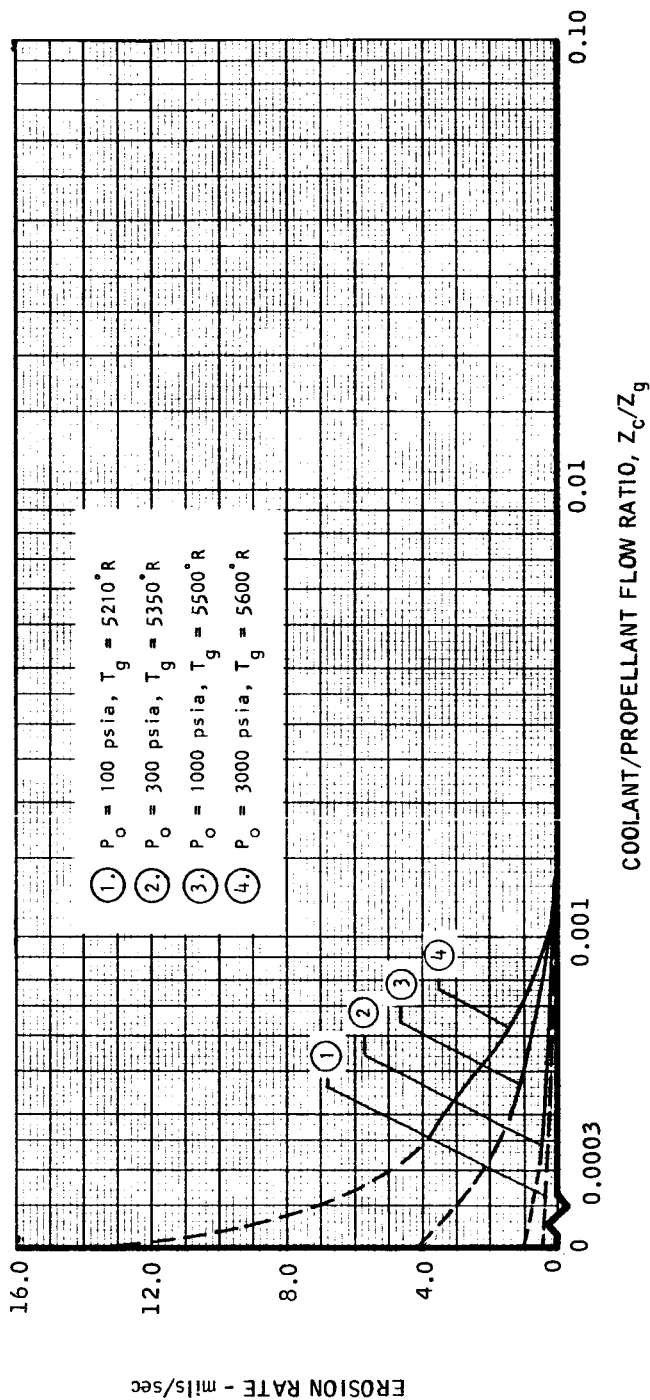
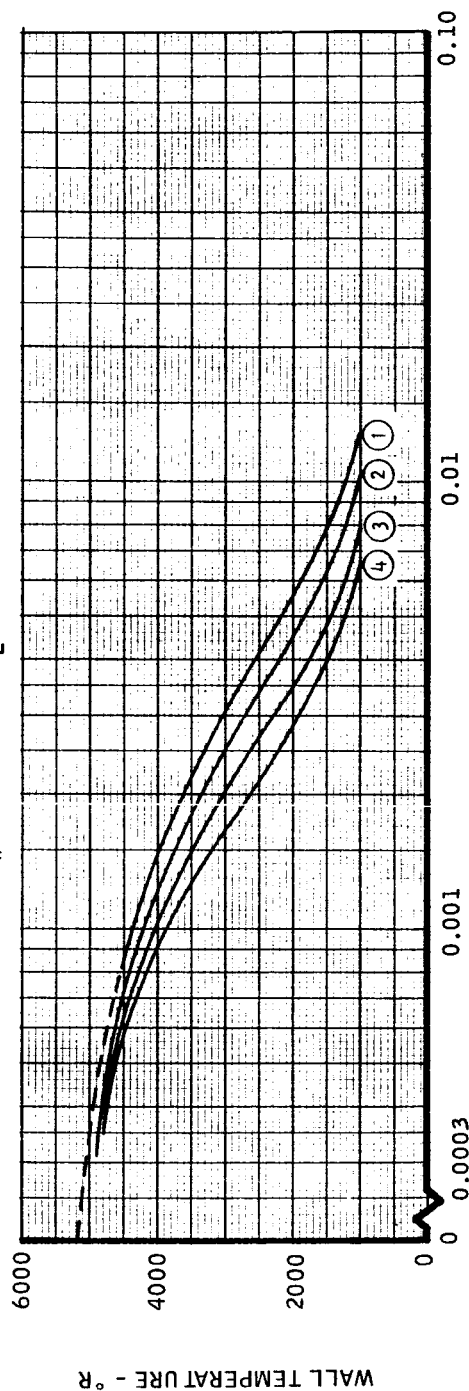
$P_0 = 100$ psia



TMC A 673

NOZZLE TEMPERATURE AND EROSION RATE FOR O_2/H_2

$D_n = 1.25$ in. H_2 COOLANT



NOZZLE TEMPERATURE AND EROSION RATE FOR P8500 H₂ COOLANT

$D_n = 1.25$ in.; $T_g = 8960^\circ\text{R}$

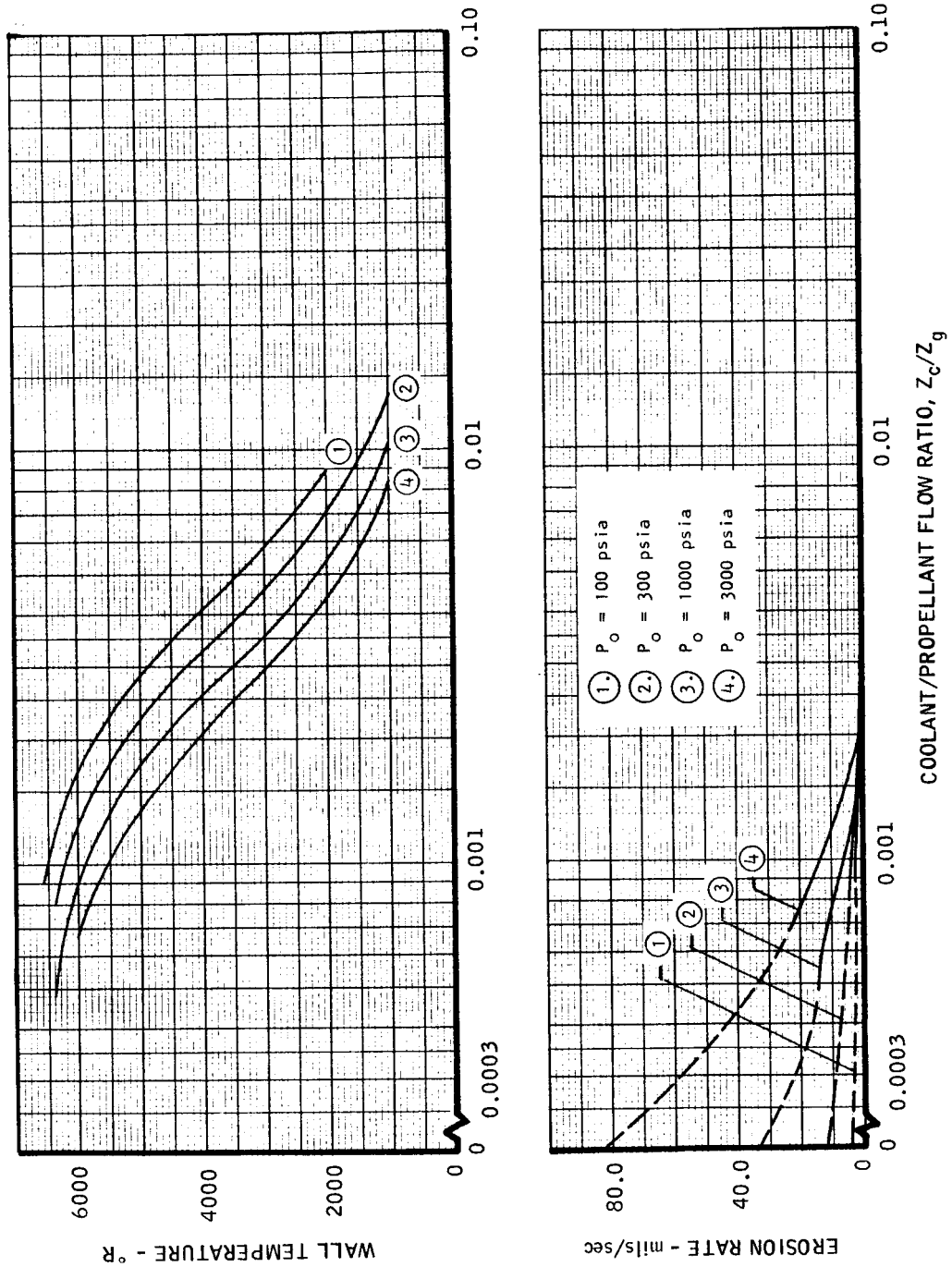


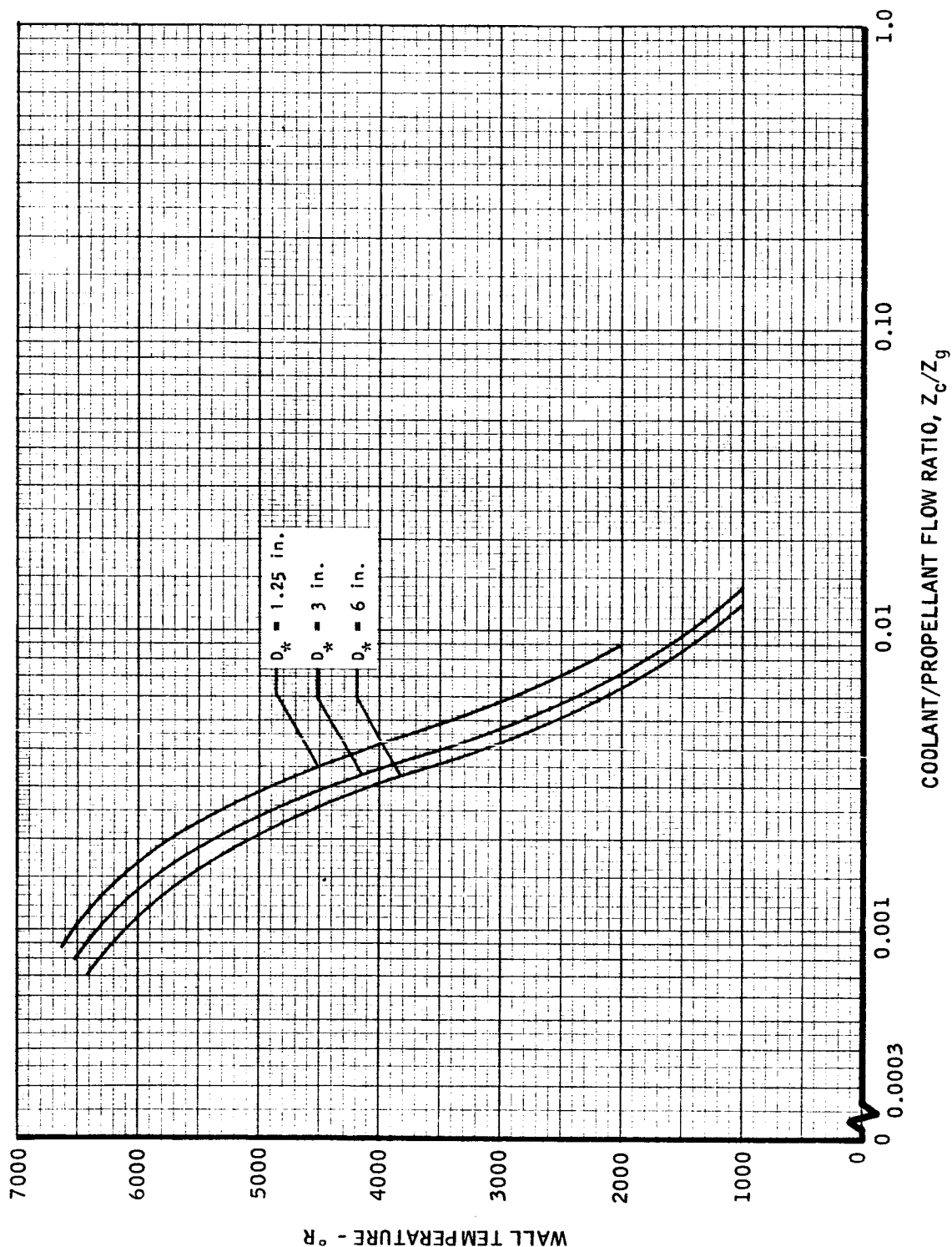
FIGURE 12

UNCLASSIFIED

REPORT 6069

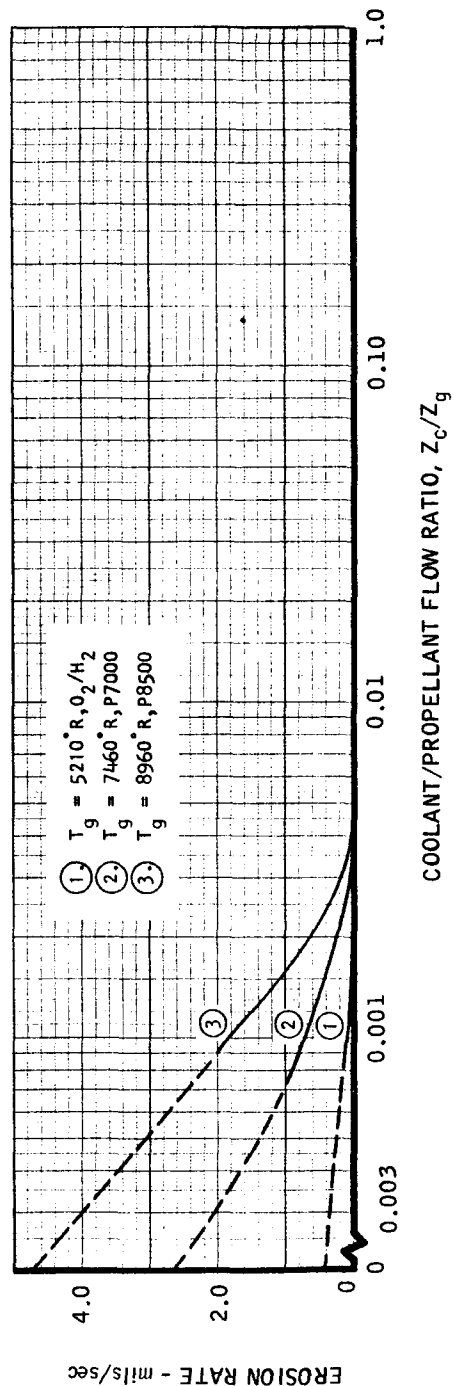
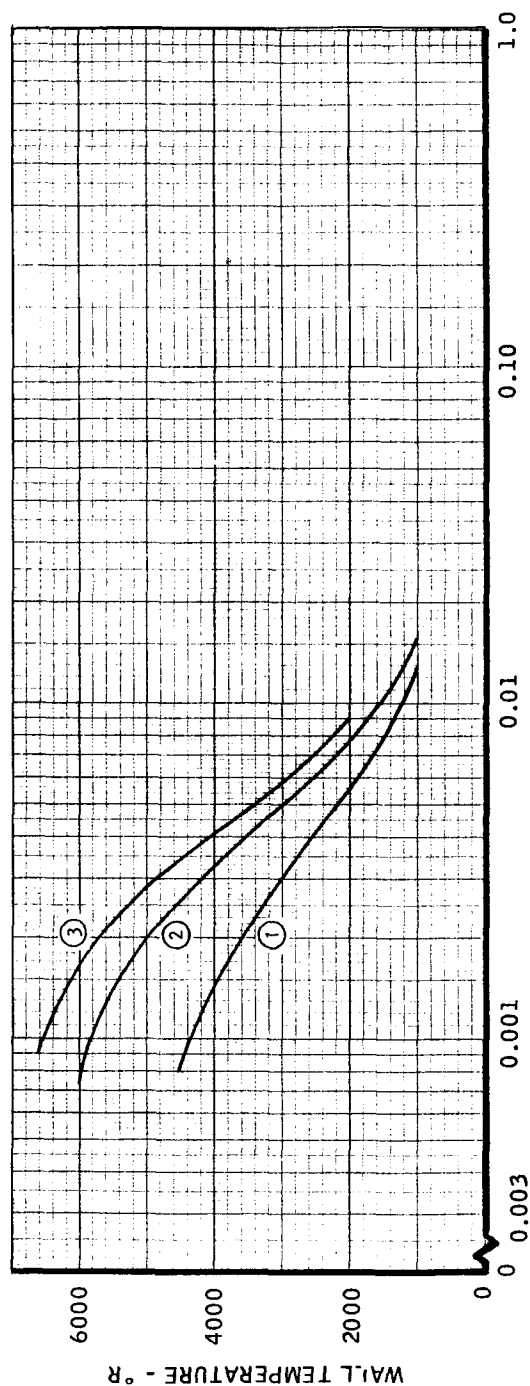
EFFECT OF SIZE ON NOZZLE COOLING

P8500; $P_0 = 100$ psia; H_2 COOLANT



TMC A673

EFFECT OF COMBUSTION TEMPERATURE ON NOZZLE COOLING

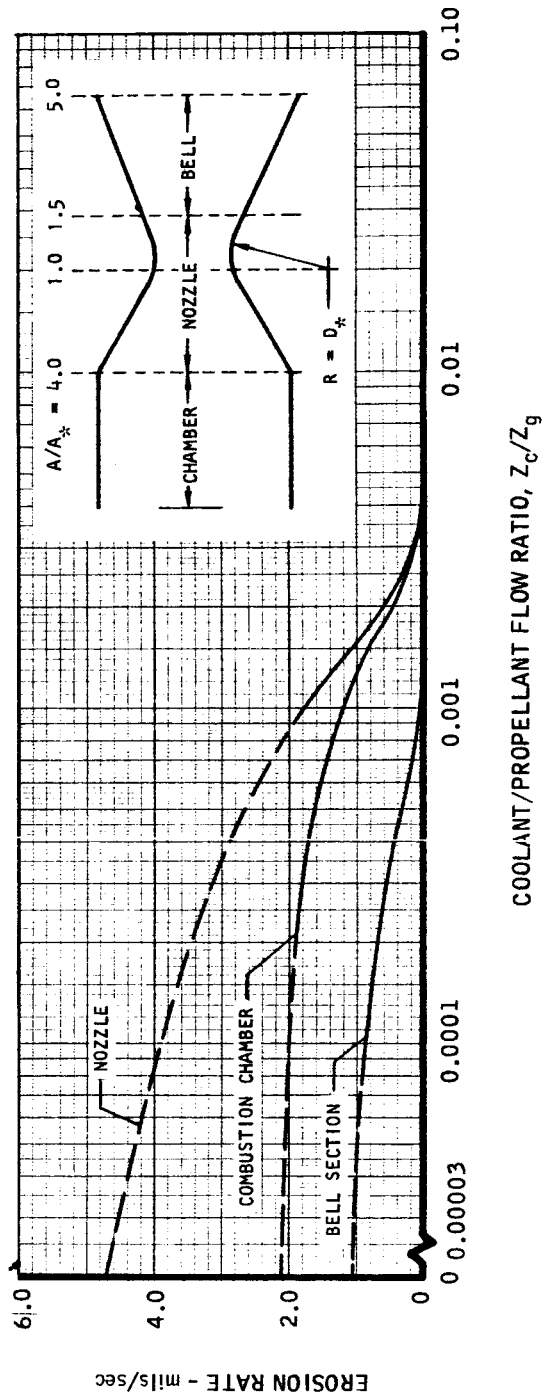
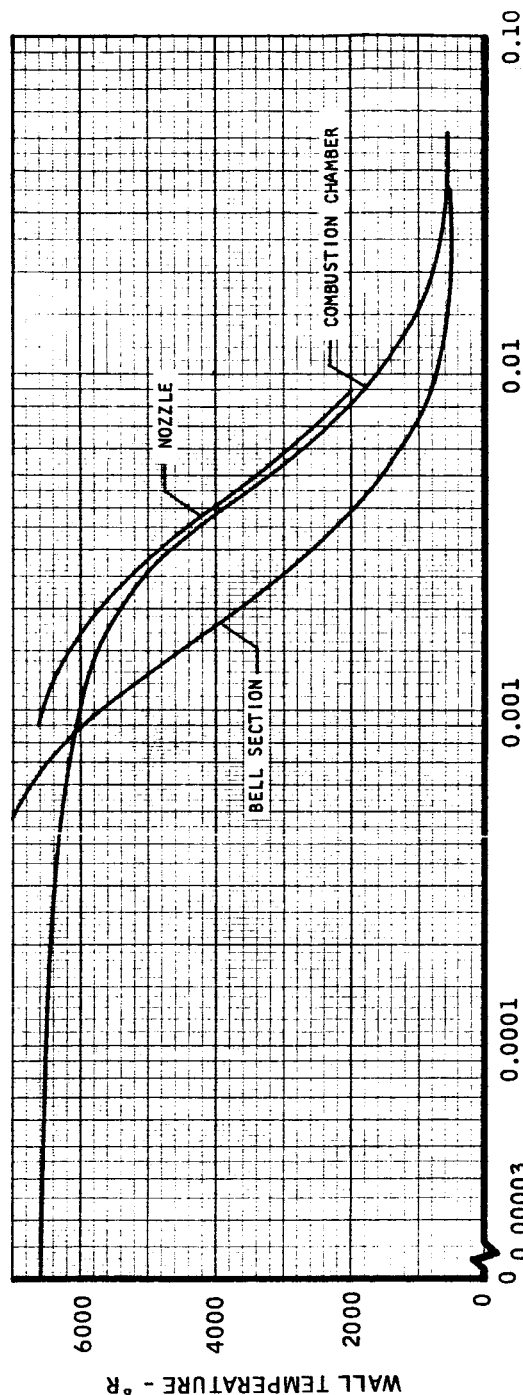
 $D_* = 1.25 \text{ in.}; P_0 = 100 \text{ psia}; \text{H}_2 \text{ COOLANT}$


UNCLASSIFIED

REPORT 6069

COMBUSTION CHAMBER AND EXPANSION NOZZLE COOLING

P8500 $D_{*} = 1.25$ in.; $P_o = 100$ psia; H_2 COOLANT; $T_g = 8960^{\circ}R$

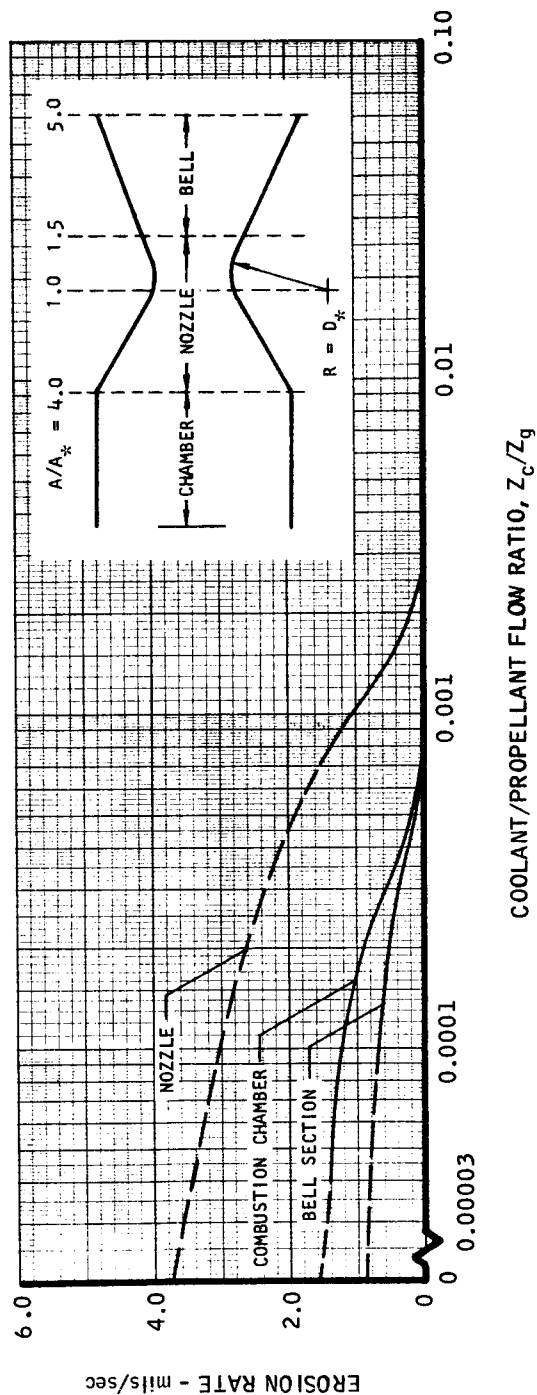
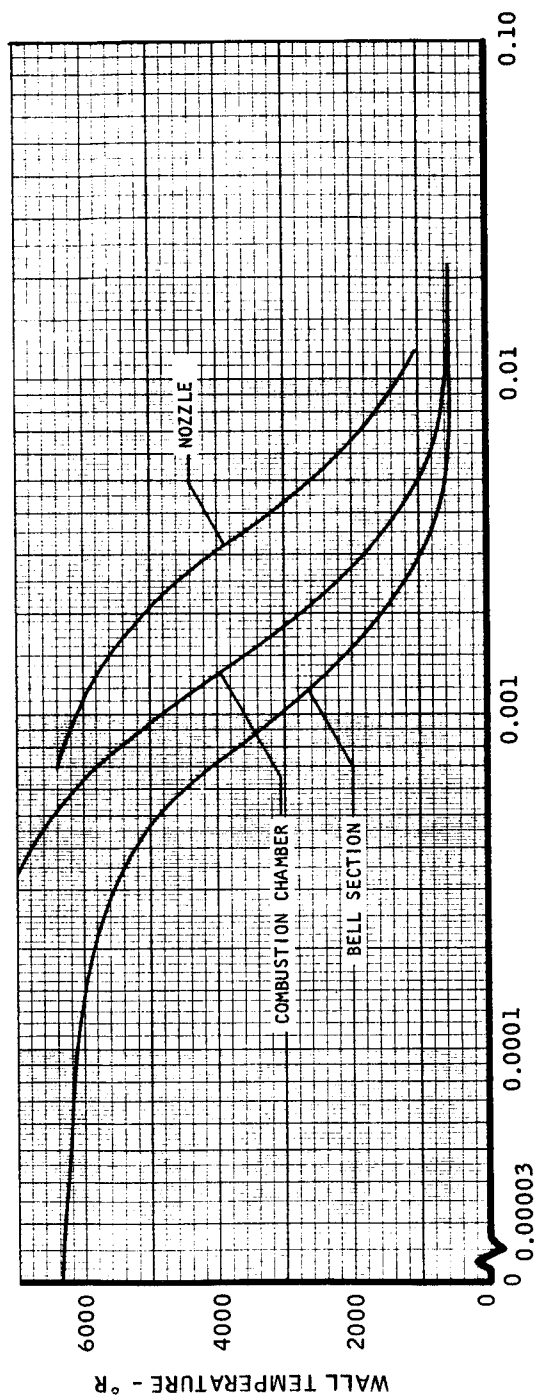


TMC A673

UNCLASSIFIED

COMBUSTION CHAMBER AND EXPANSION NOZZLE COOLING

P8500, $D_* = 6$ in.; $P_0 = 100$ psia; $T_g = 8960^\circ R$; H_2 COOLANT

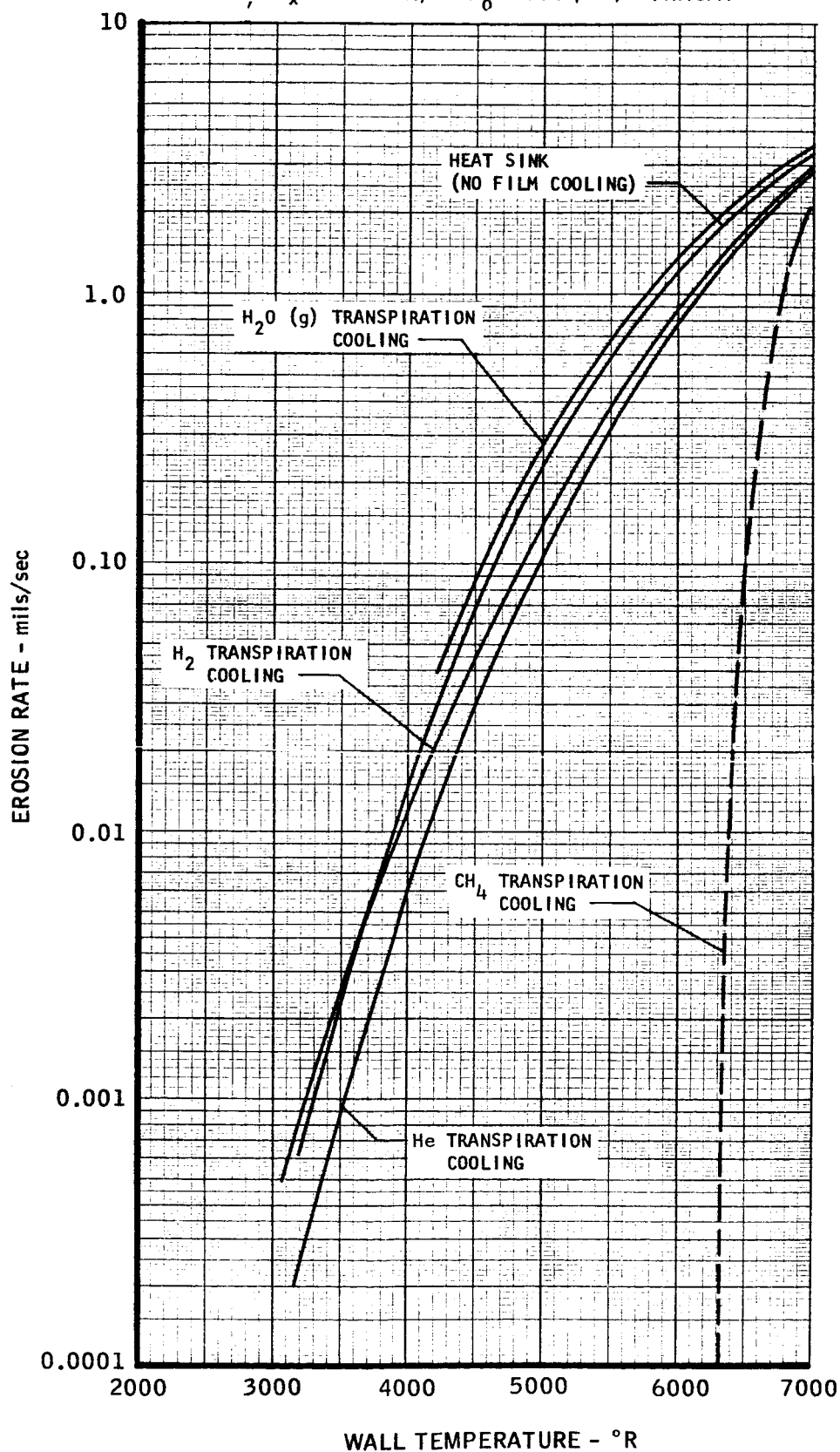


UNCLASSIFIED

REPORT 6069

VARIATION OF GRAPHITE NOZZLE EROSION RATE FOR SEVERAL COOLING GASES

P8500 ; $D_* = 1.25$ in.; $P_0 = 100$ psia; THROAT



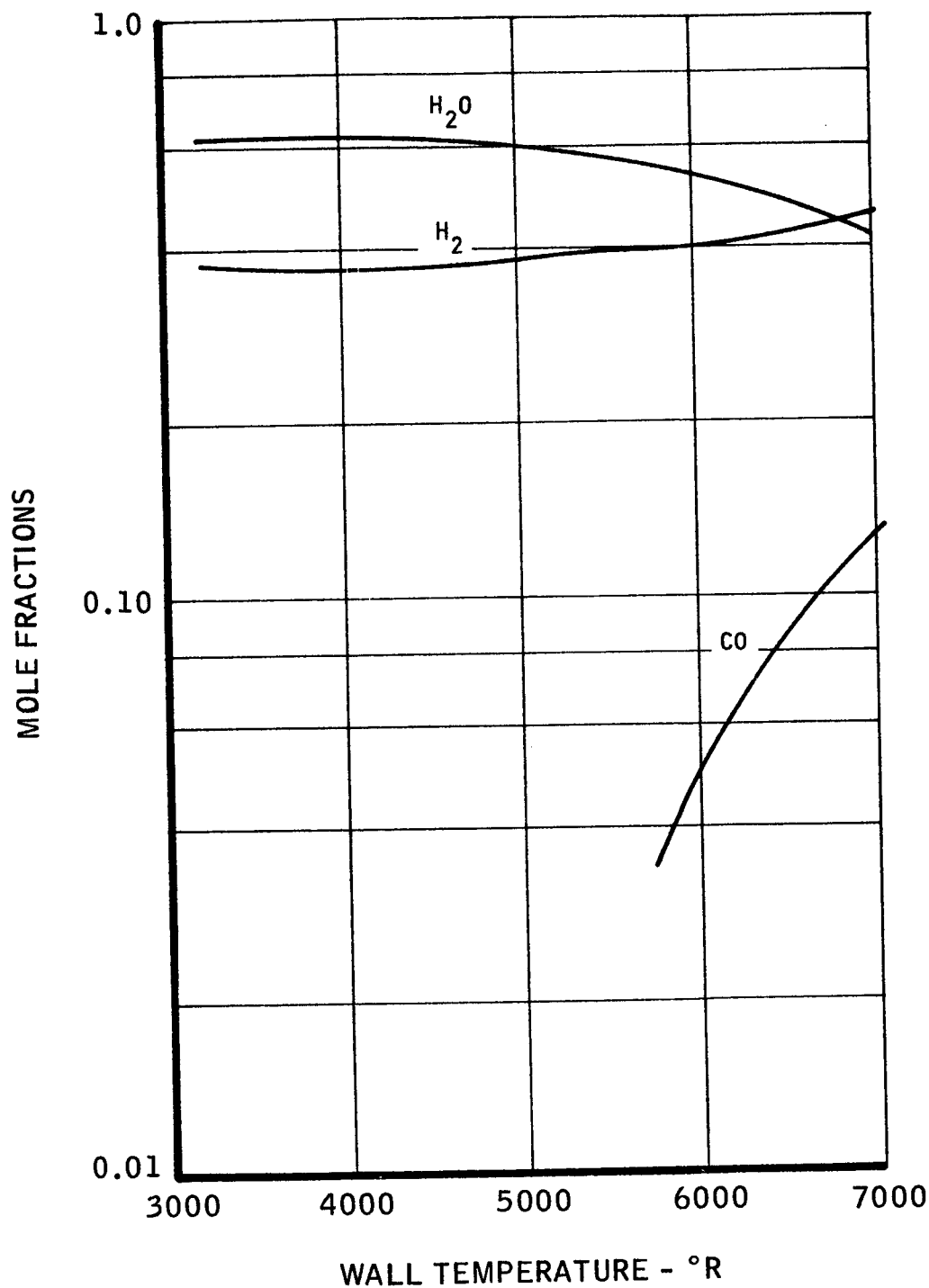
TAC 4673

UNCLASSIFIED

REPORT 6069

GASEOUS SPECIES AT GRAPHITE NOZZLE SURFACE HEAT SINK (NO FILM COOLING)

P8500; $D_* = 1.25$ in.; $P_0 = 100$ psia; THROAT



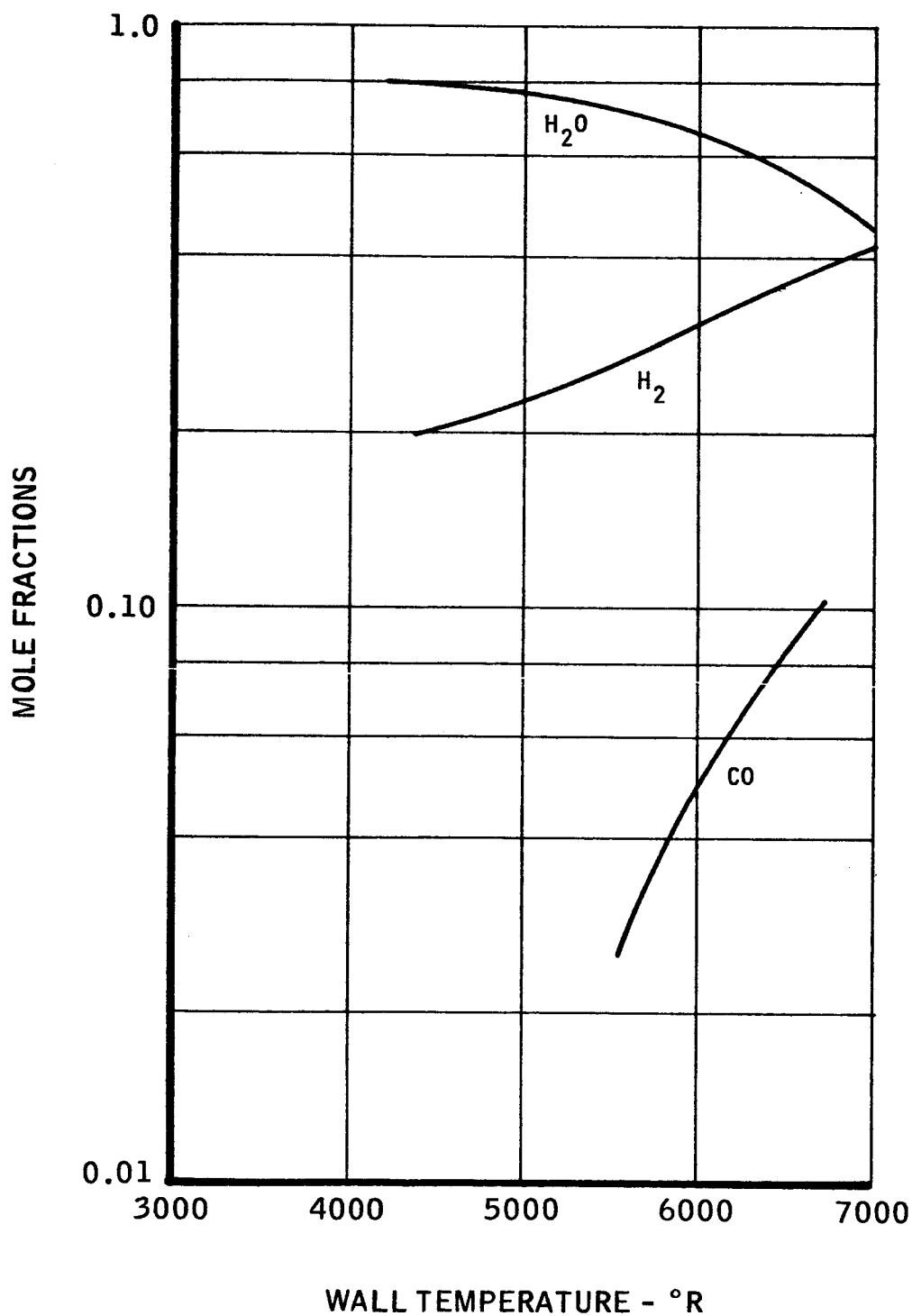
TMC A 673

UNCLASSIFIED

REPORT 6069

GASEOUS SPECIES AT GRAPHITE NOZZLE SURFACE GASEOUS WATER TRANSPIRATION COOLING

P8500 ; $D_* = 1.25$ in. ; $P_o = 100$ psia ; THROAT

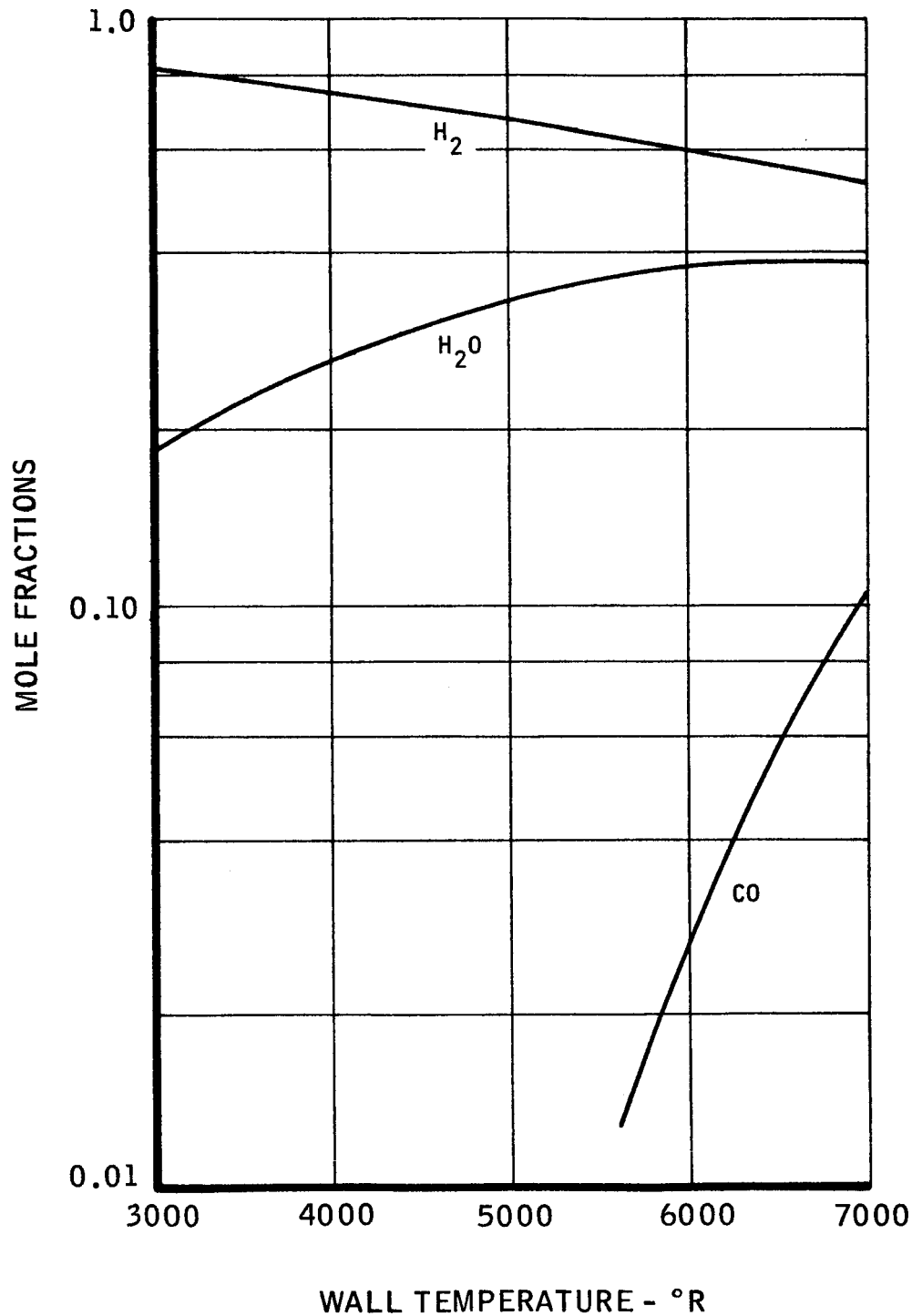


TMC 4673

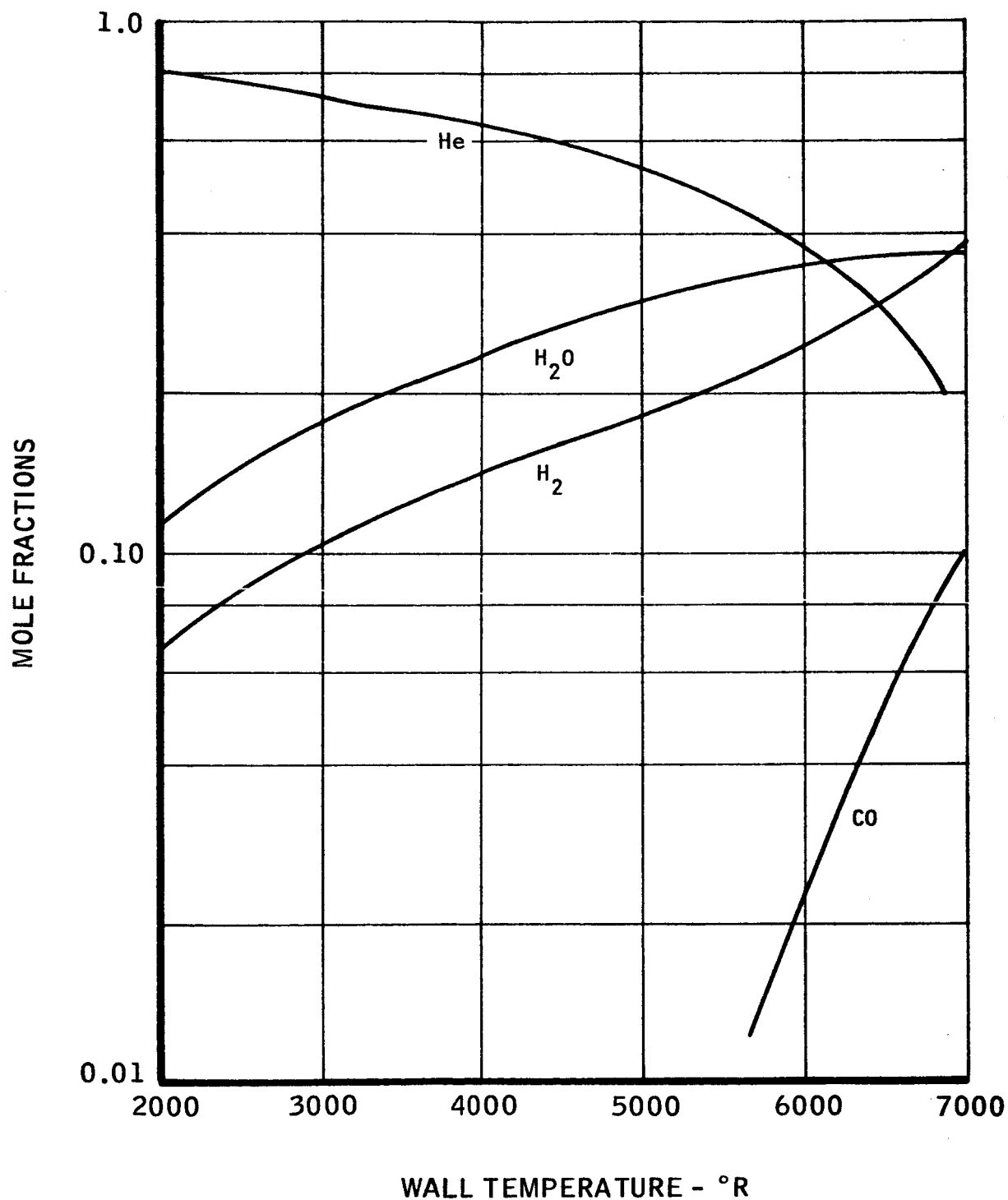
UNCLASSIFIED

GASEOUS SPECIES AT GRAPHITE NOZZLE SURFACE HYDROGEN TRANSPIRATION COOLING

P8500, $D_* = 1.25$ in., $P_o = 100$ psia, THROAT



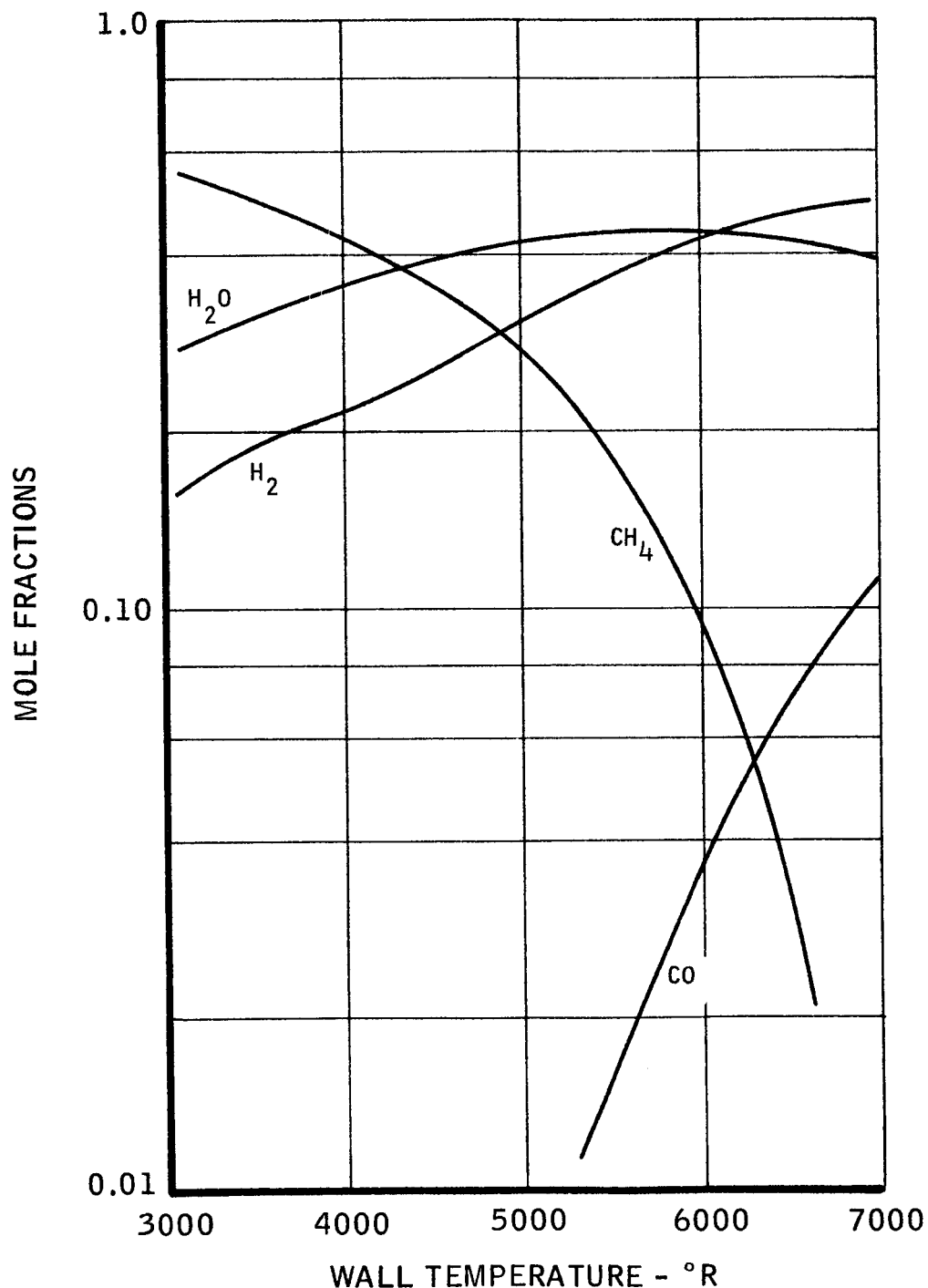
TMC A 673

GASEOUS SPECIES AT GRAPHITE NOZZLE SURFACE
HELIUM TRANSPIRATION COOLINGP8500 ; $D_* = 1.25$ in., $P_0 = 100$ psia ; THROAT

TMC A673

GASEOUS SPECIES AT GRAPHITE NOZZLE SURFACE METHANE TRANSPIRATION COOLING

P8500, $D_x = 1.25$ in.; $P_0 = 100$ psia; THROAT

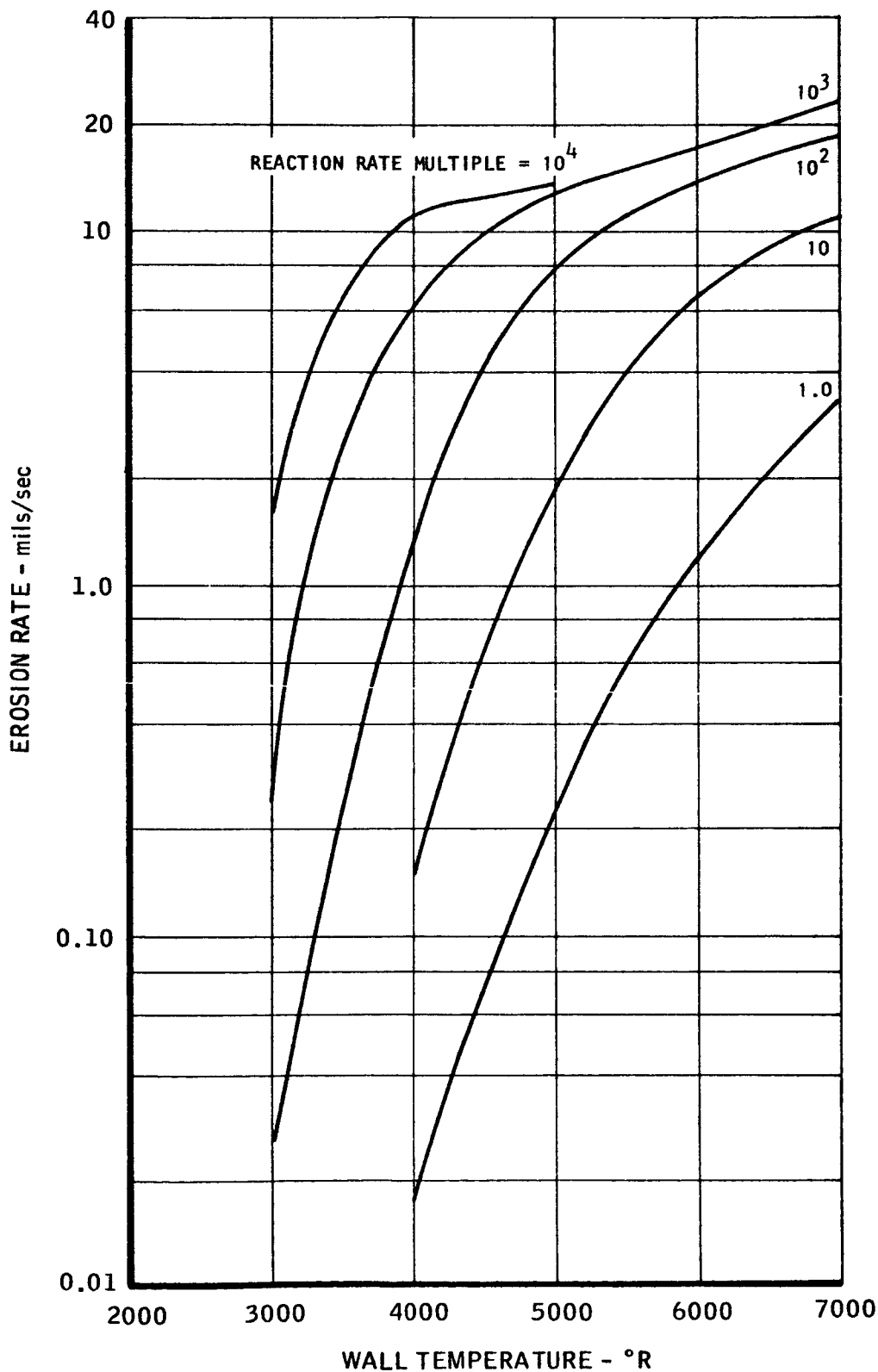


UNCLASSIFIED

REPORT 6069

EROSION RATE vs. REACTION RATE HEAT SINK (NO FILM COOLING)

P8500, $D_{*} = 1.25$ in.; $P_0 = 100$ psia; THROAT;



TMC A673

GASEOUS SPECIES AT WALL vs. REACTION RATE MULTIPLE

P8500, HEAT SINK; $D_* = 1.25$ in.; THROAT; $T_w = 2000^\circ\text{R}$; $P_o = 100$ psia

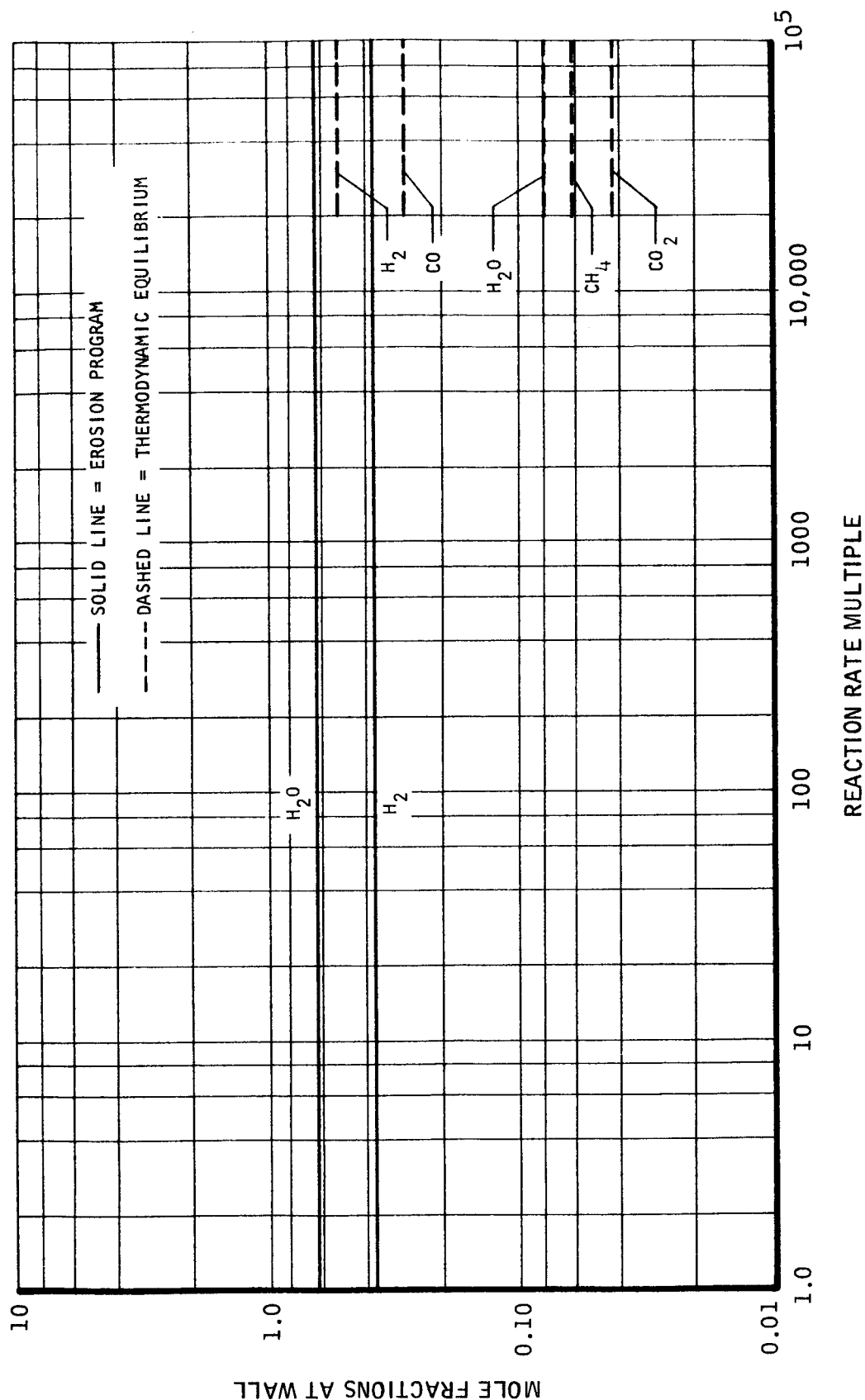
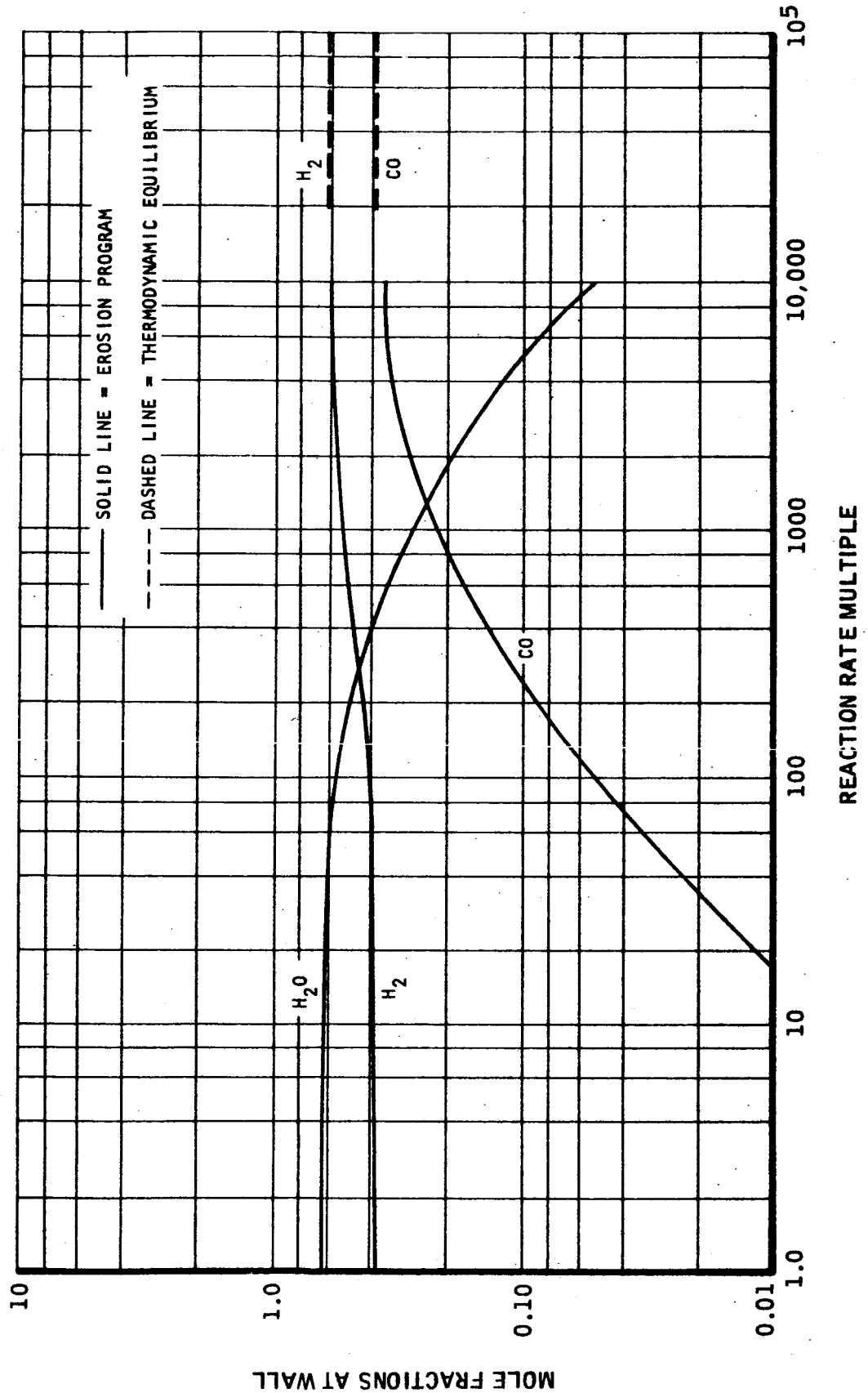


FIGURE 24

UNCLASSIFIED

GASEOUS SPECIES AT WALL VS. REACTION RATE MULTIPLE

P8500, HEAT SINK; $D^* = 1.25$ in.; THROAT; $T_w = 4000^\circ R$; $P_0 = 100$ psia



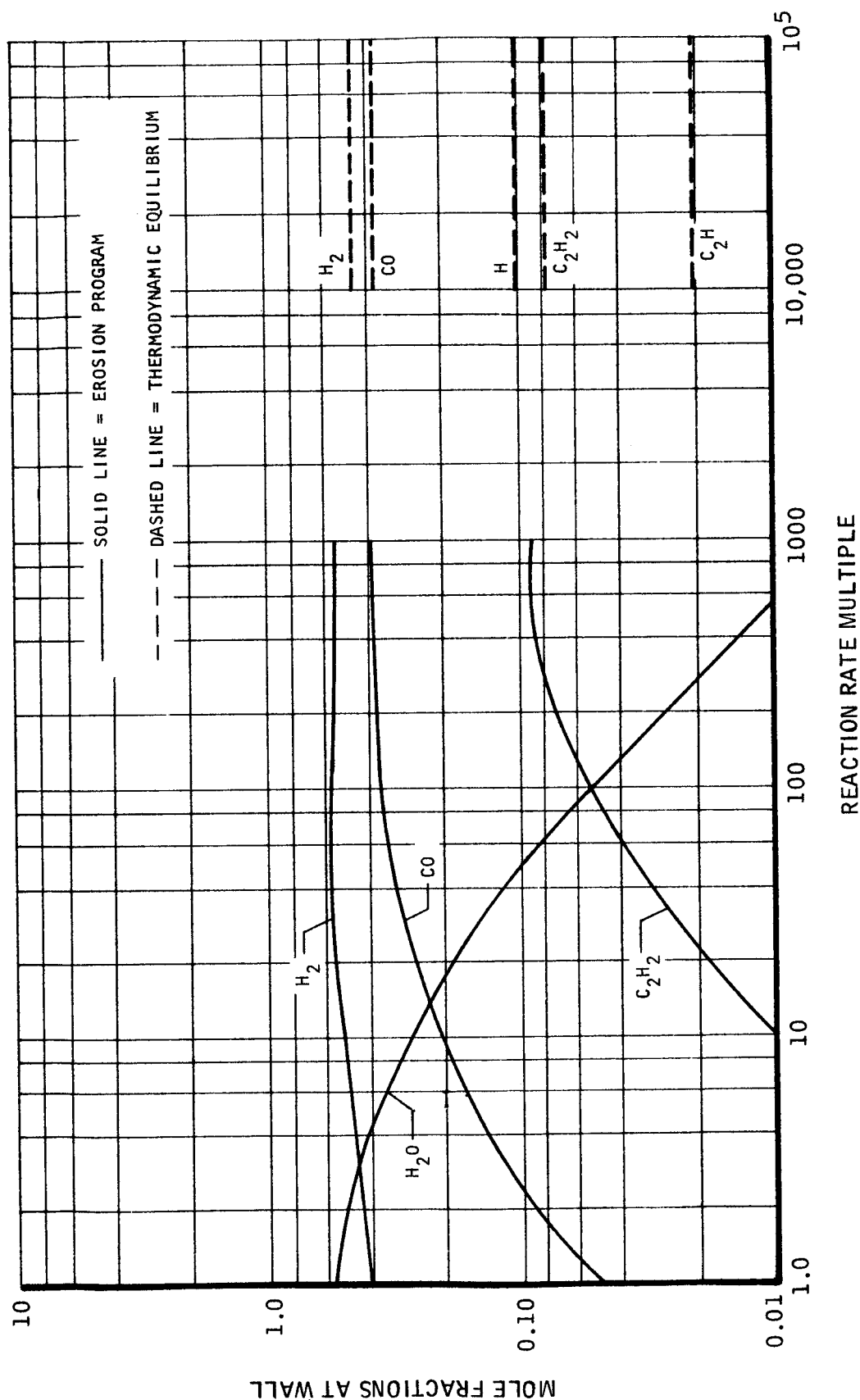
TMC A673

UNCLASSIFIED

REPORT 6069

GASEOUS SPECIES AT WALL VS. REACTION RATE MULTIPLE

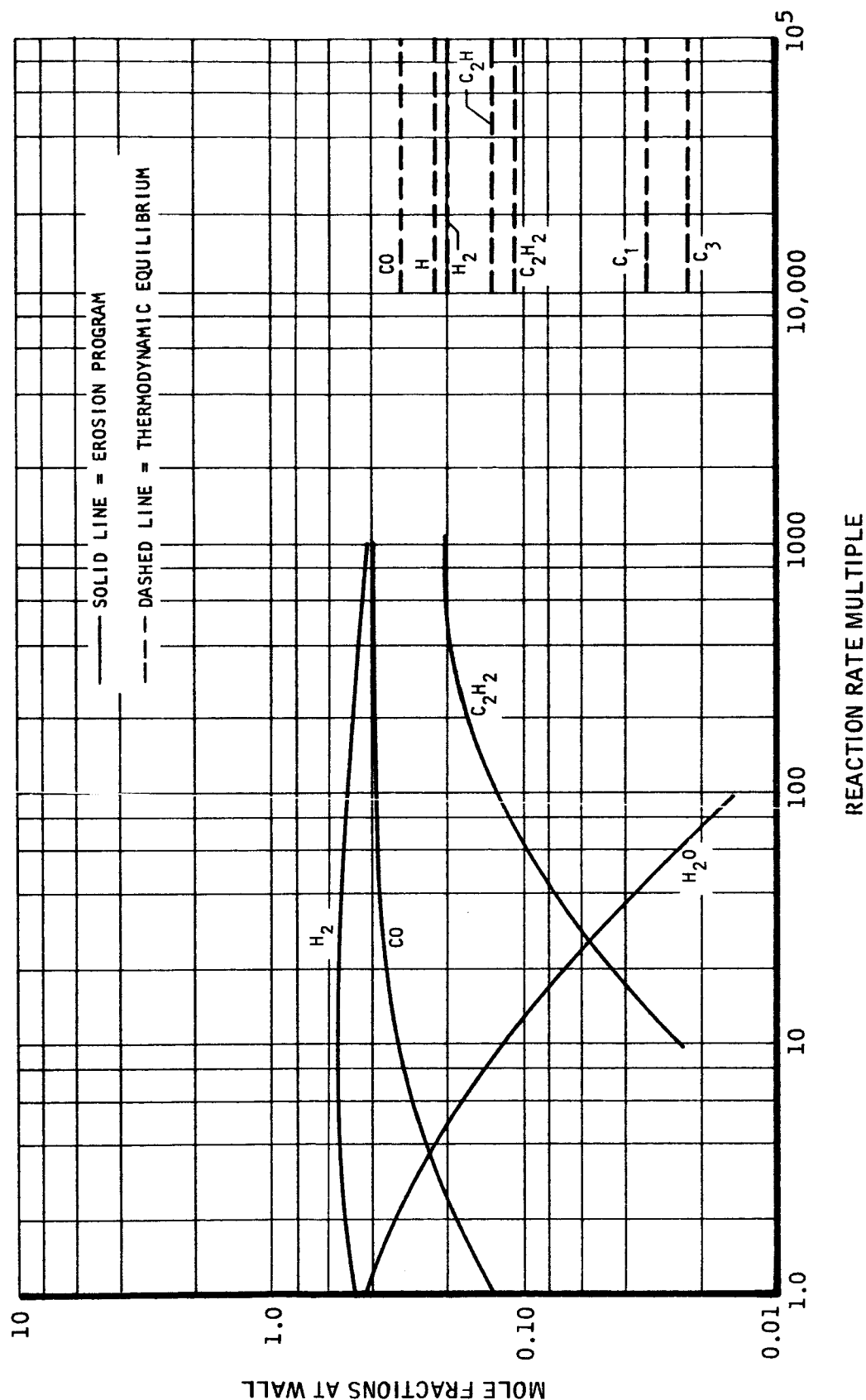
P8500, HEAT SINK; $D_* = 1.25$ in.; THROAT; $T_w = 6000^\circ\text{R}$; $P_0 = 100$ psia

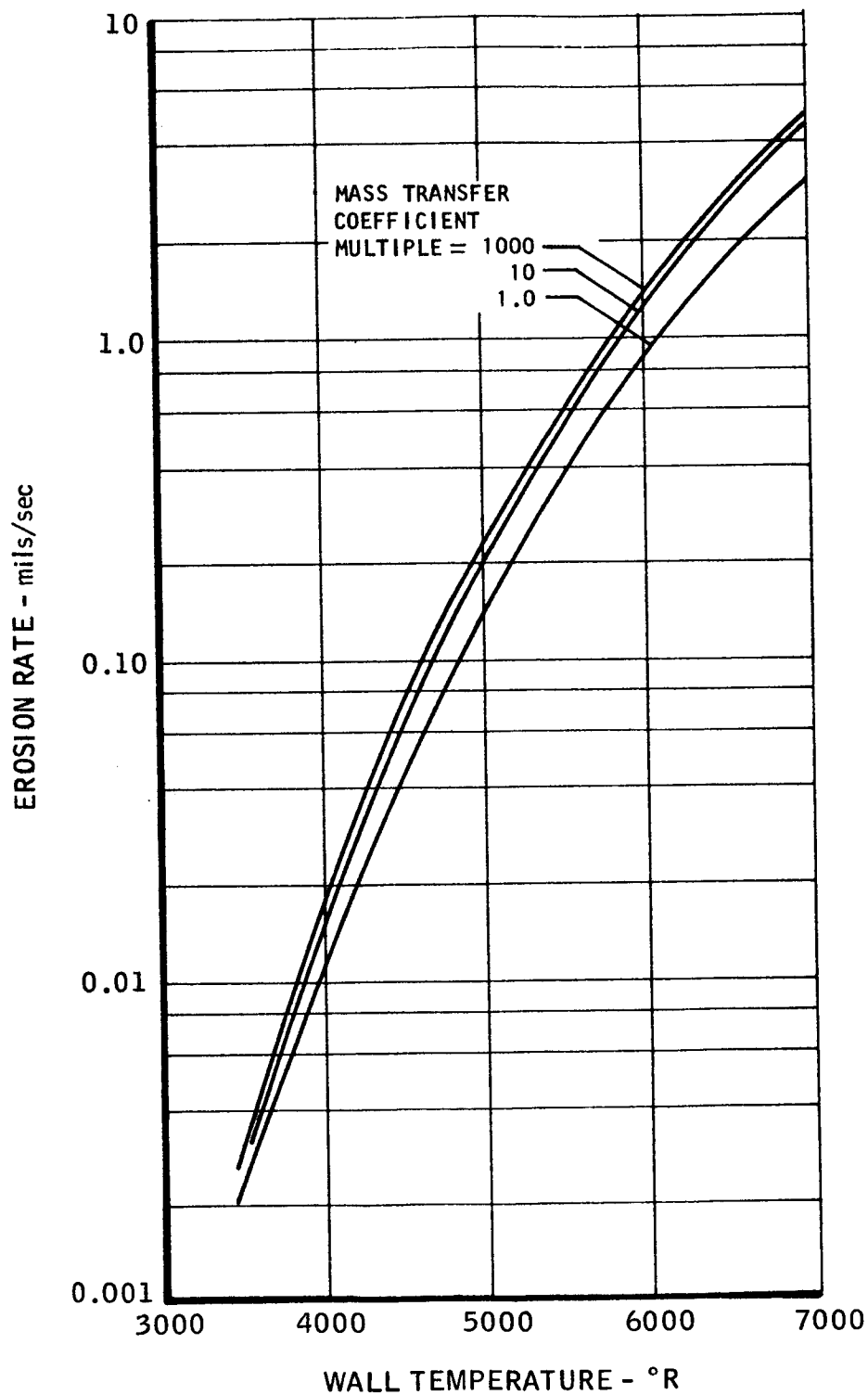


TMC A673

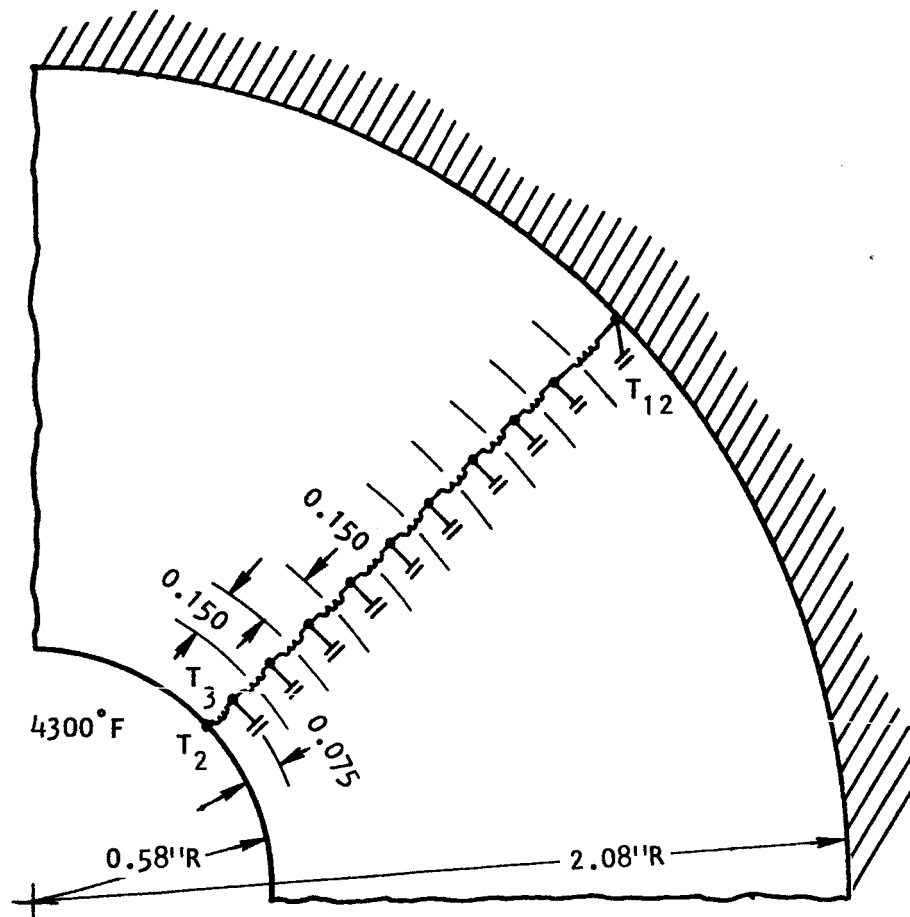
GASEOUS SPECIES AT WALL VS. REACTION RATE MULTIPLE

P8500, HEAT SINK, $D_* = 1.25$ in.; THROAT; $T_w = 7000^\circ\text{R}$; $P_o = 100$ psia



EROSION RATE vs. MASS TRANSFER RATE
HEAT SINK (NO FILM COOLING)P8500, $D_* = 1.25$ in.; $P_0 = 100$ psia, THROAT

THERMAL ANALYZER CIRCUIT FOR TRANSIENT TEMPERATURE ANALYSIS OF NASA EXPERIMENTAL SILICA-PHENOLIC NOZZLES



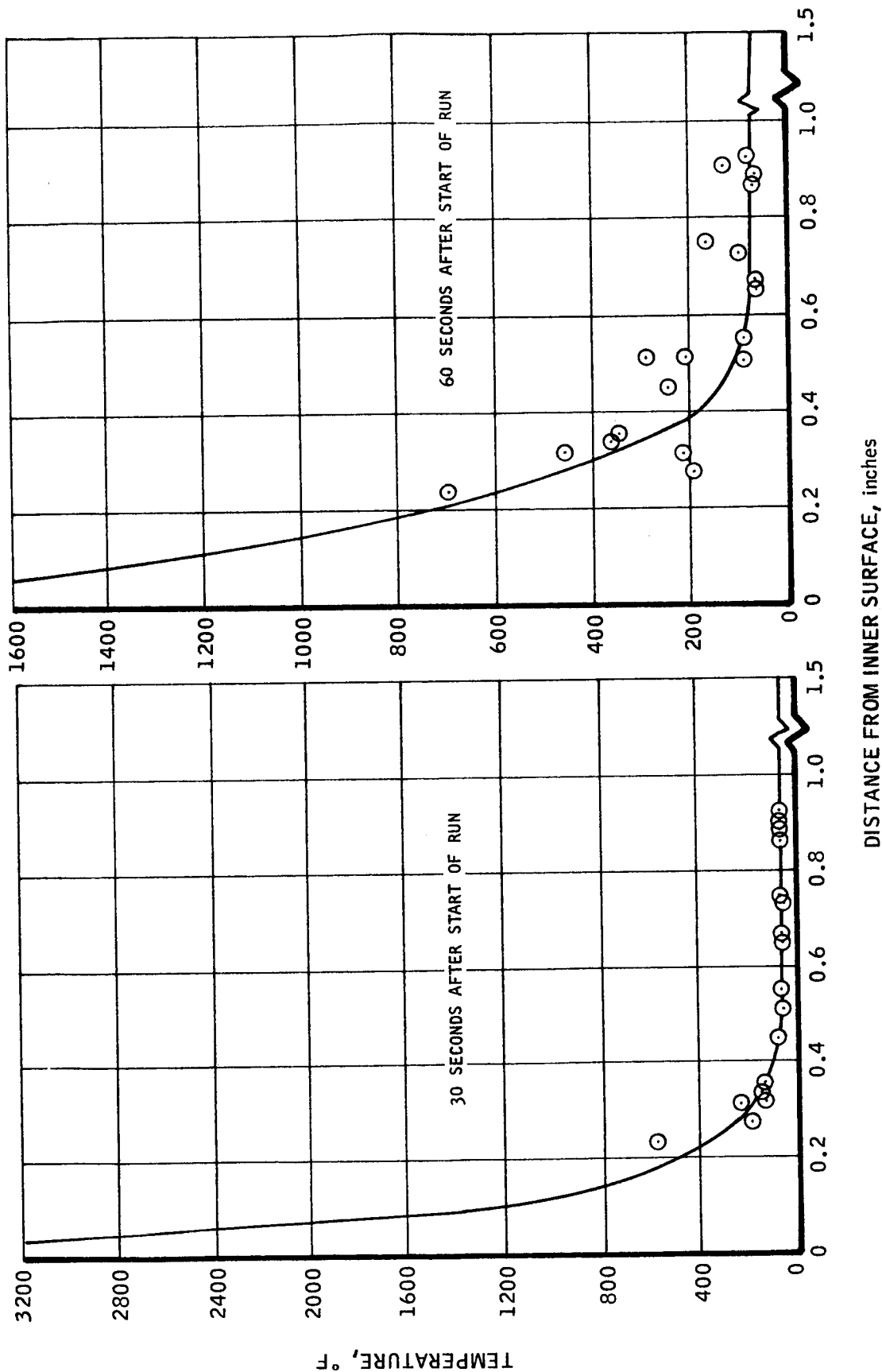
THERMAL CONDUCTIVITY = 3.0 Btu-in./hr ft² °F

SPECIFIC HEAT = 0.3 Btu/lb °F

DENSITY = 0.0625 lb/cu in.

UNCLASSIFIED

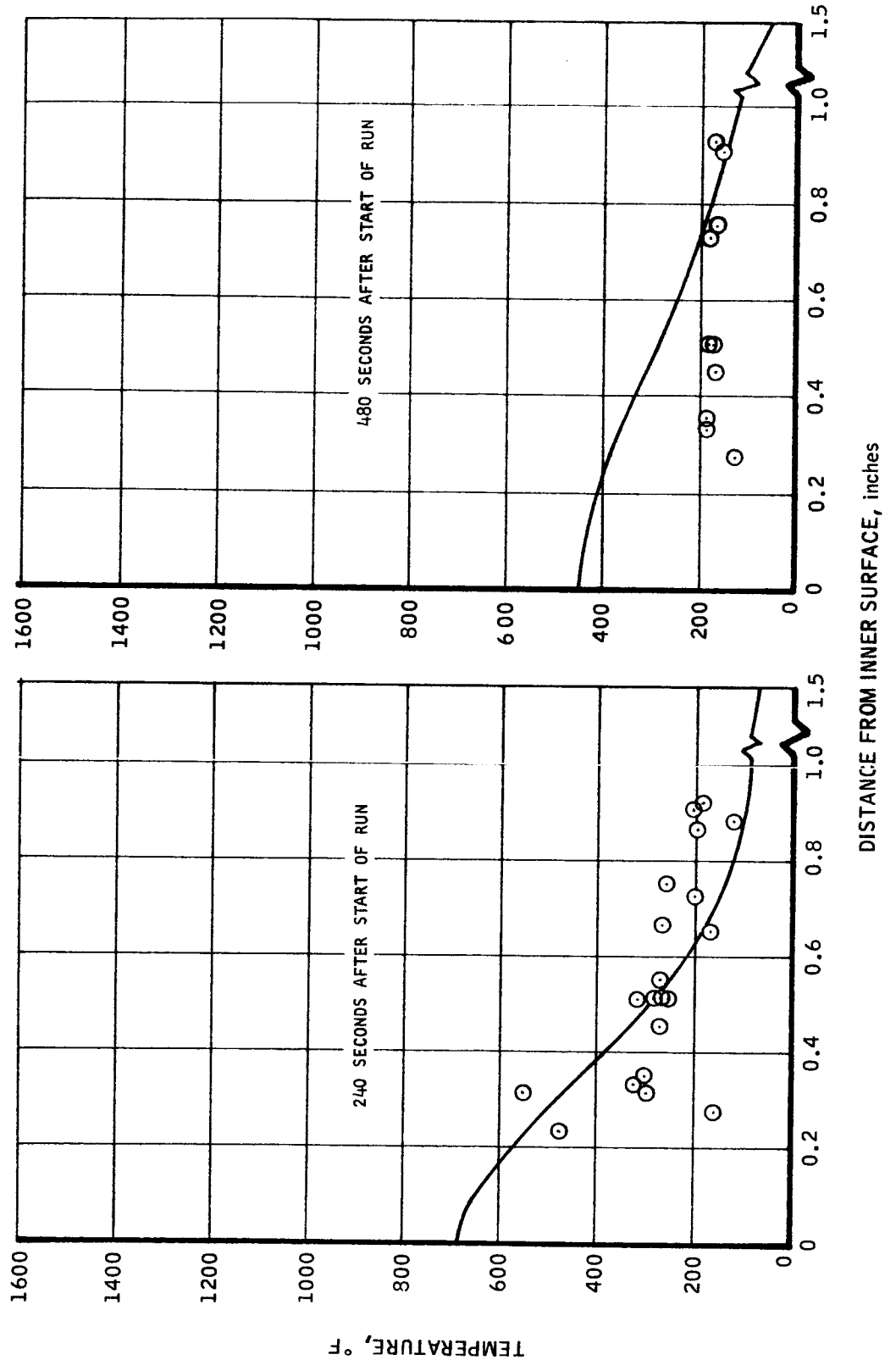
ANALYTICAL TEMPERATURE DISTRIBUTIONS IN SILICA-PHENOLIC NOZZLE
COMPARED WITH NASA TND-1726 EXPERIMENTAL DATA
RUN TIME 30 SECONDS



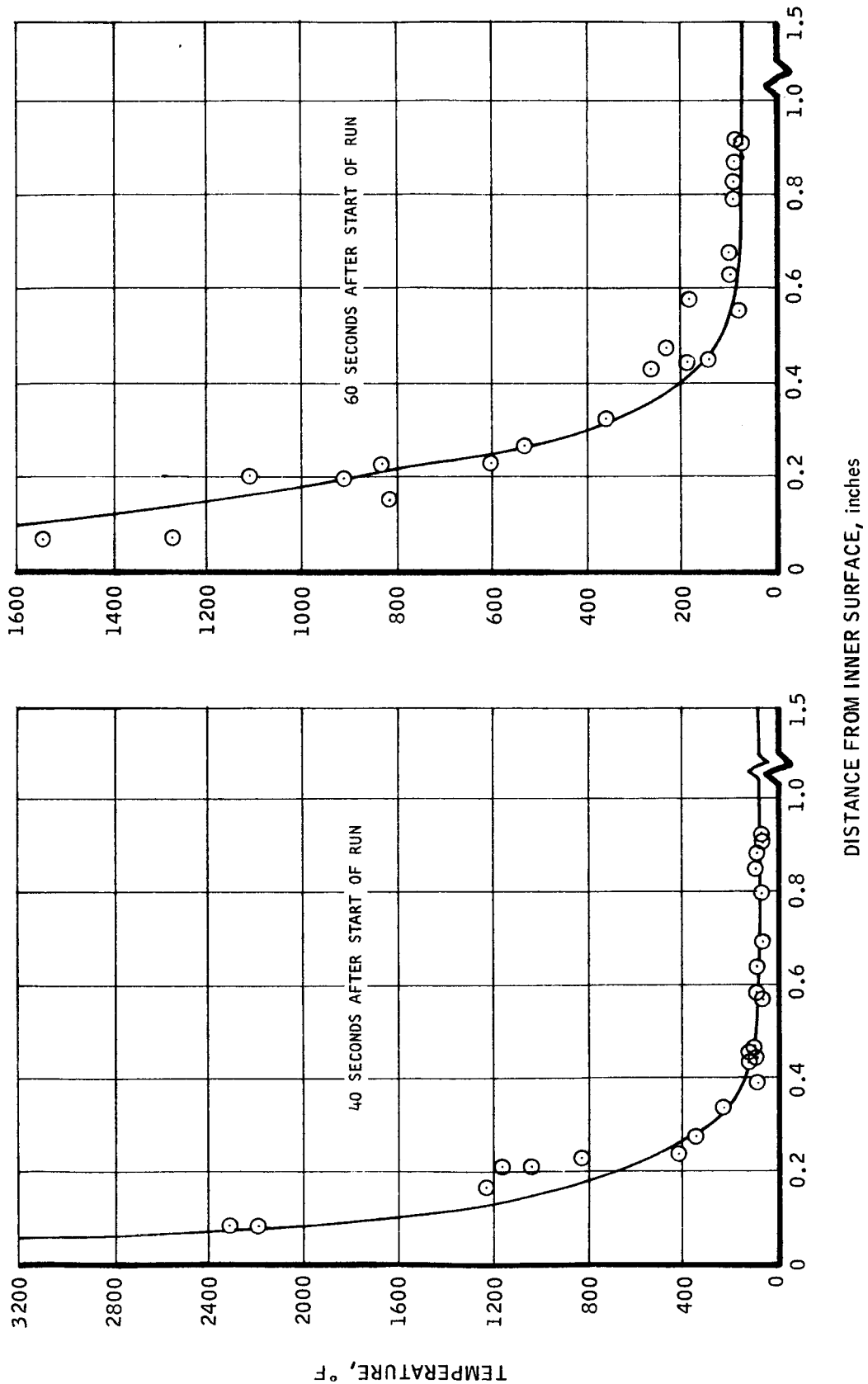
TMC A 673

UNCLASSIFIED

ANALYTICAL TEMPERATURE DISTRIBUTIONS IN SILICA-PHENOLIC NOZZLE
COMPARED WITH NASA TND-1726 EXPERIMENTAL DATA
RUN TIME 30 SECONDS



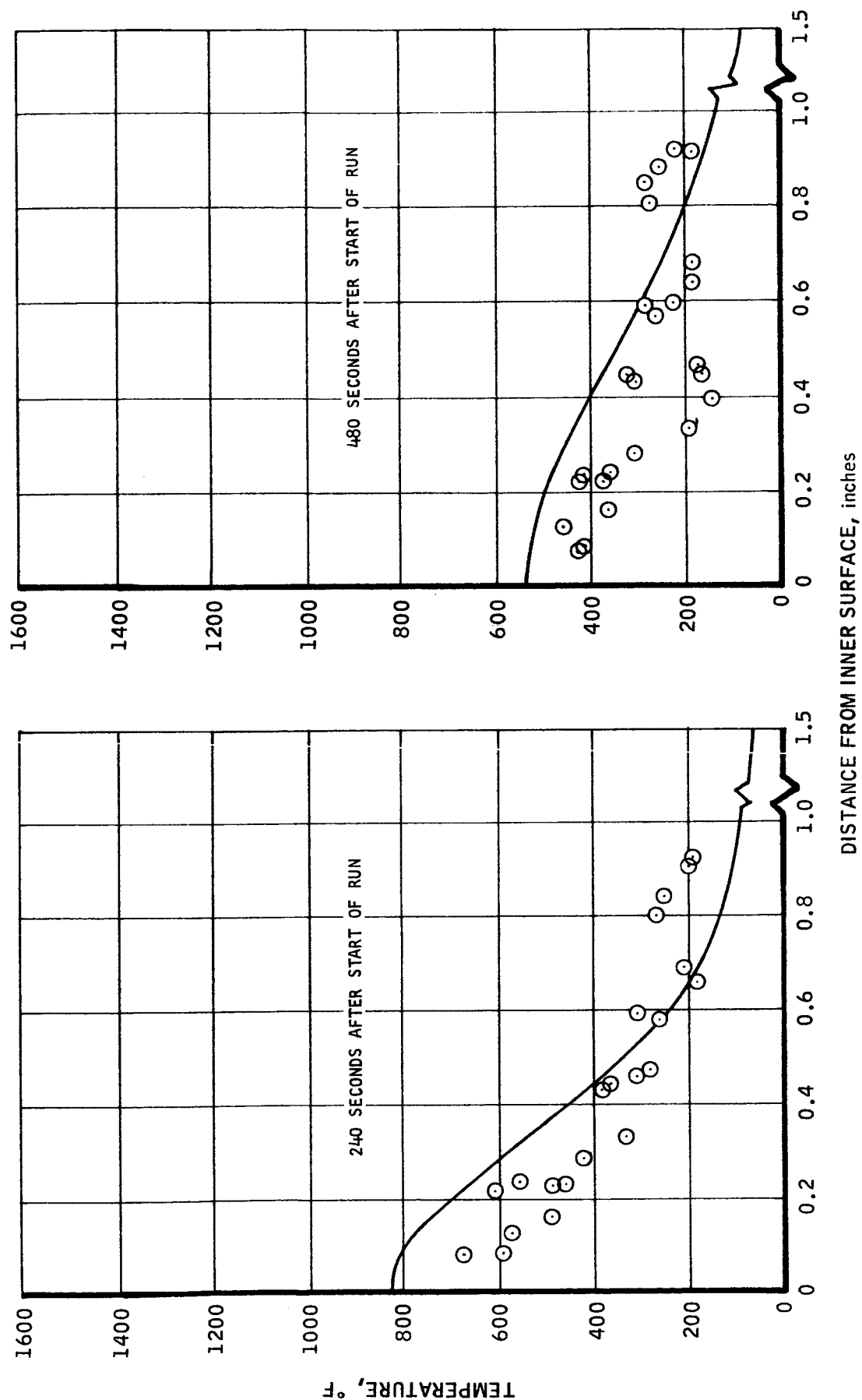
TMC A673

ANALYTICAL TEMPERATURE DISTRIBUTIONS IN SILICA-PHENOLIC NOZZLE
COMPARED WITH NASA TND-1726 EXPERIMENTAL DATA
RUN TIME 40 SECONDS

UNCLASSIFIED

REPORT 6069

ANALYTICAL TEMPERATURE DISTRIBUTIONS IN SILICA-PHENOLIC NOZZLE
COMPARED WITH NASA TND-1726 EXPERIMENTAL DATA
RUN TIME 40 SECONDS

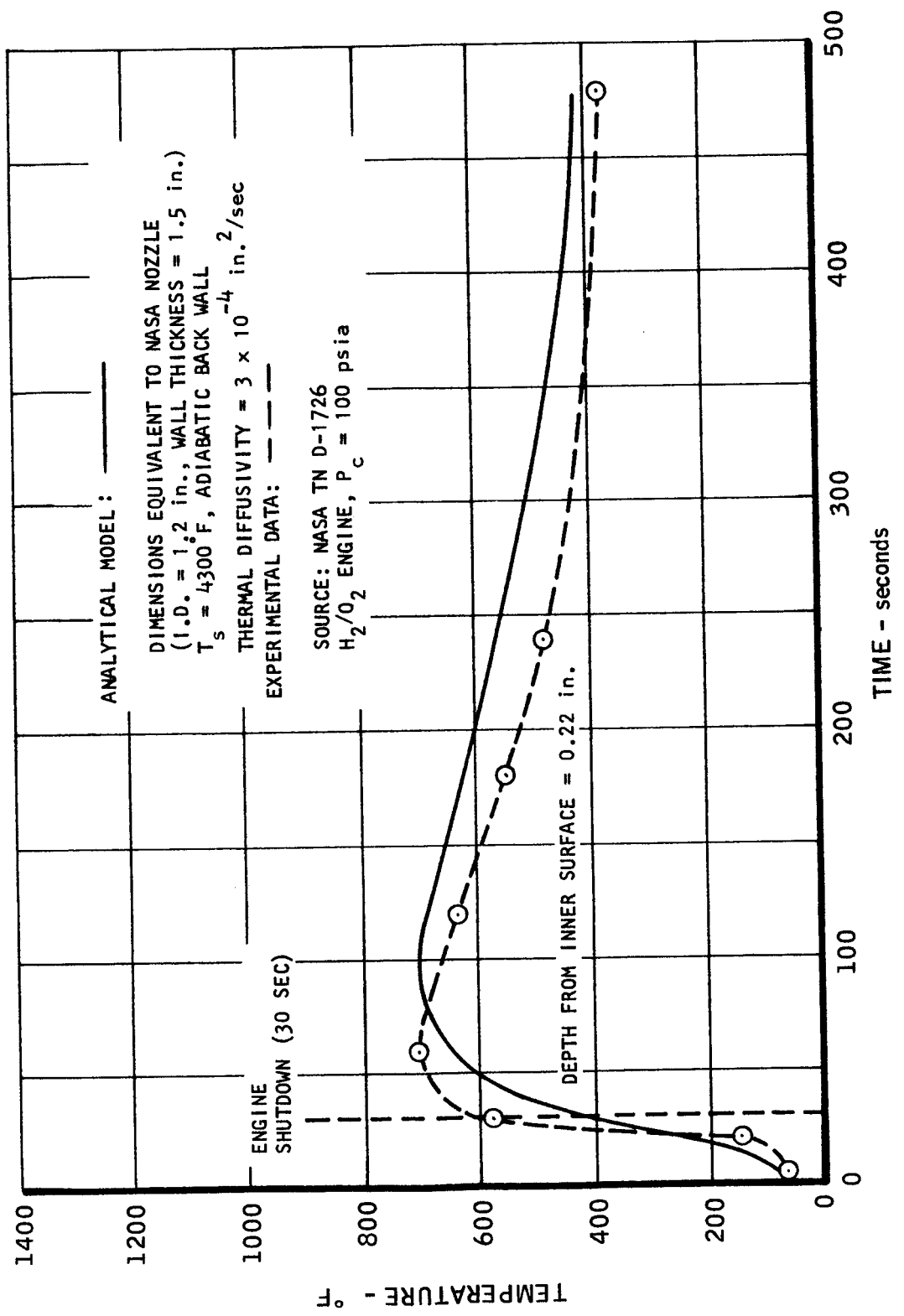


TMC A673

278-97 UNCLASSIFIED

FIGURE 33

ANALYTICALLY DETERMINED WALL TEMPERATURE HISTORY FOR A SILICA-PHENOLIC CYLINDER
COMPARED TO EXPERIMENTAL NOZZLE TEST DATA

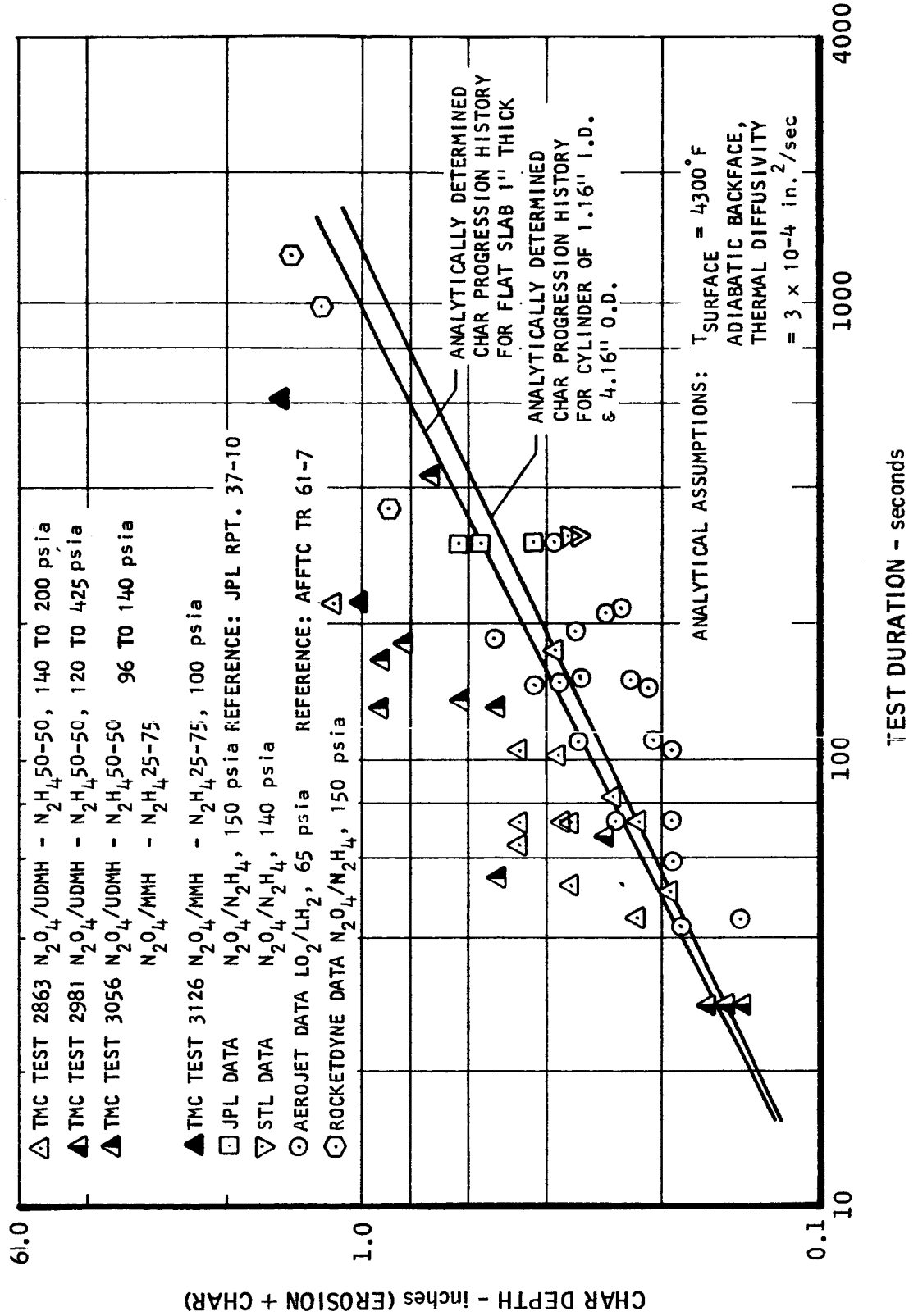


TMC A 673

UNCLASSIFIED

REPORT 6069

COMPARISON OF TEST DATA AND ANALYTICAL RESULTS FOR ABLATIVE REFRASIL-PHENOLIC CHAR DEPTH vs. BURNING TIME



TMC 673

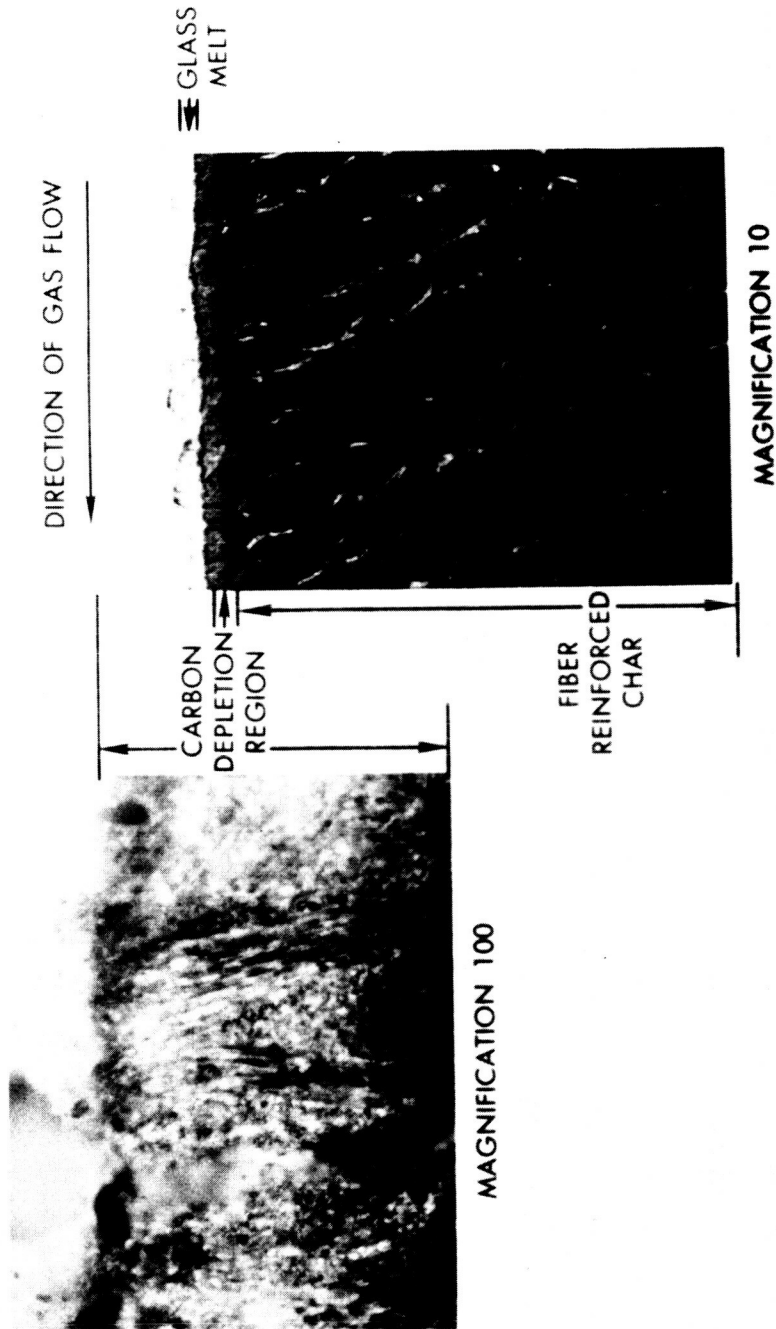


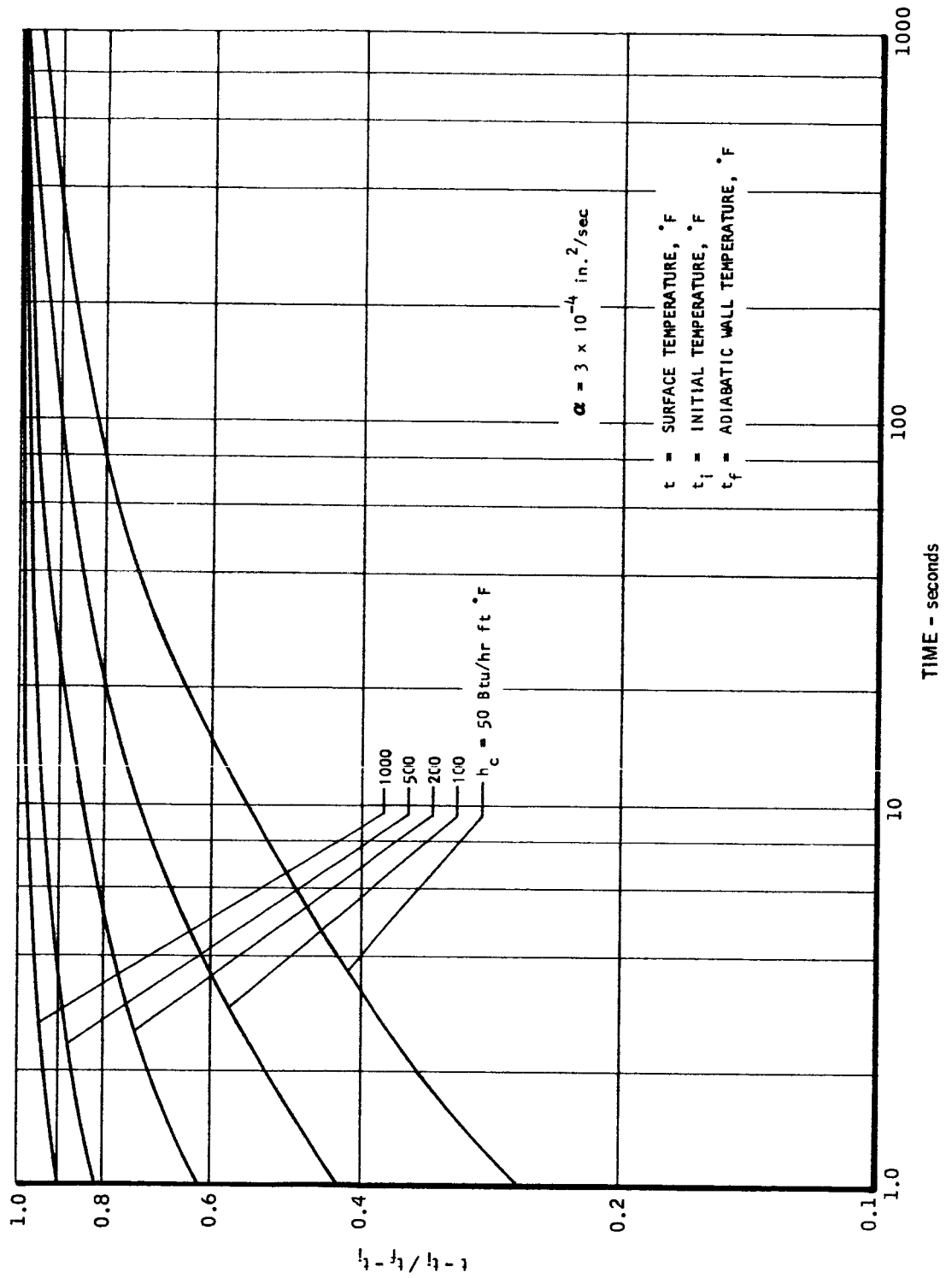
FIGURE 36. Microphotographs of Fired Silica-Phenolic Rocket Chamber

C6295-1

UNCLASSIFIED

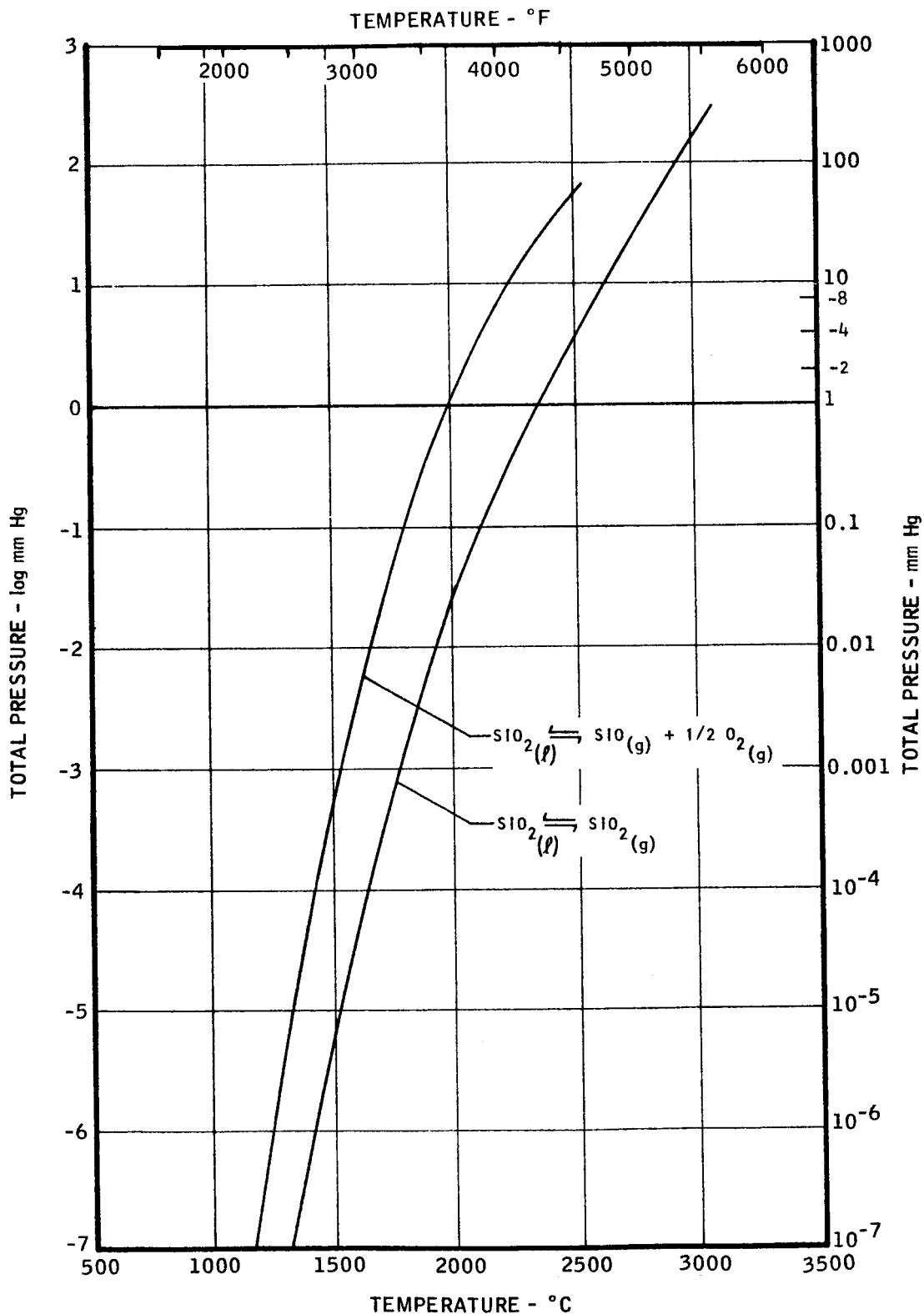
REPORT 6069

SURFACE TEMPERATURE RESPONSE OF SILICA-PHENOLIC SEMI-INFINITE SOLID
AS A FUNCTION OF HEAT TRANSFER COEFFICIENT



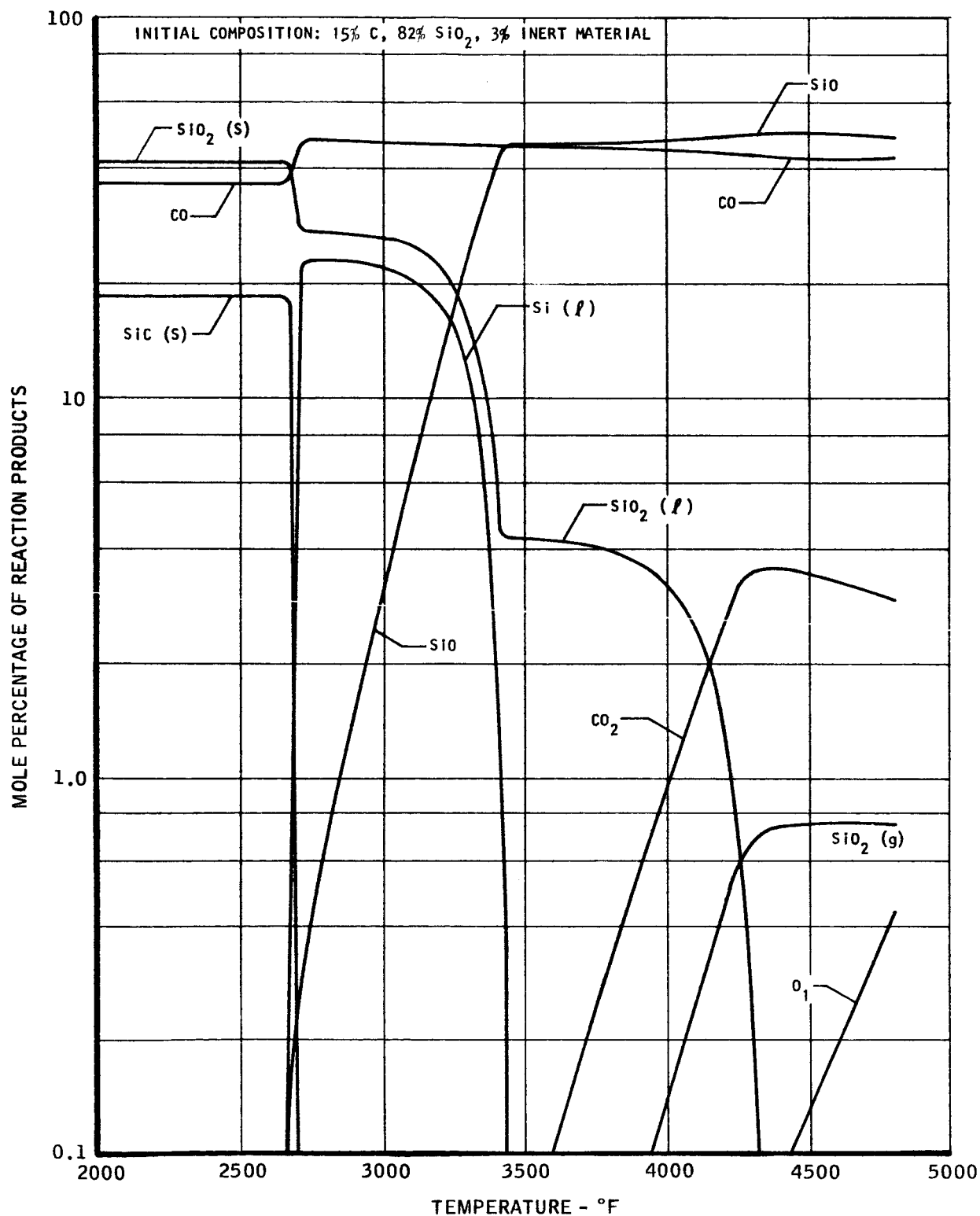
TMC A673

DISSOCIATION AND VAPORIZATION OF SILICA

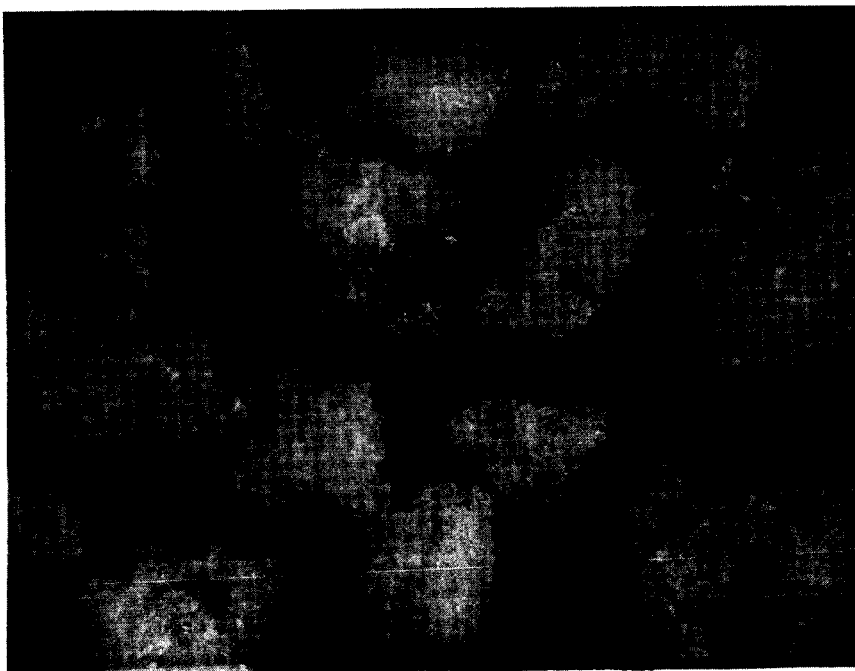
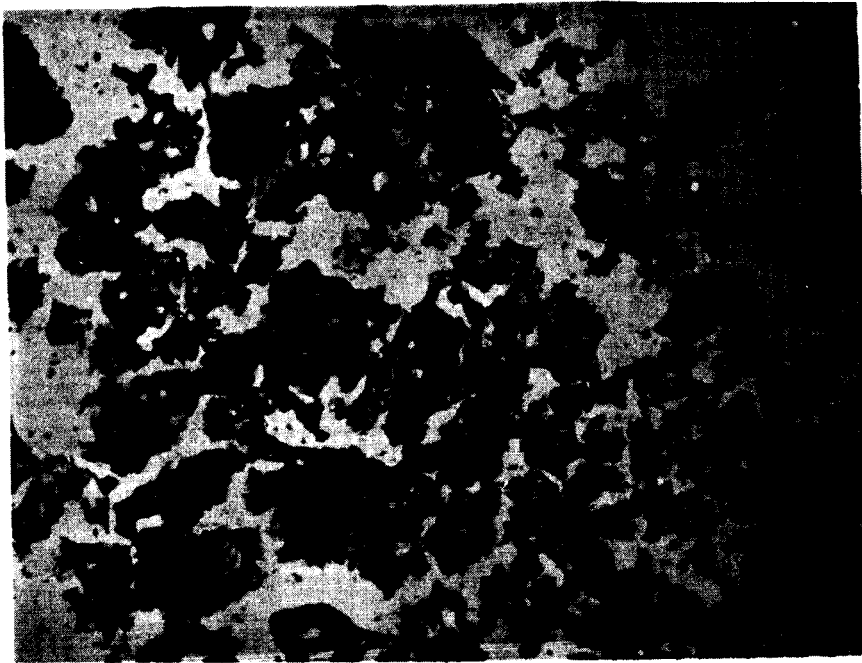


UNCLASSIFIED

SILICA-CARBON CHEMICAL EQUILIBRIA AS A FUNCTION OF TEMPERATURE
AT A PRESSURE OF 5 PSIA



TMC 4673



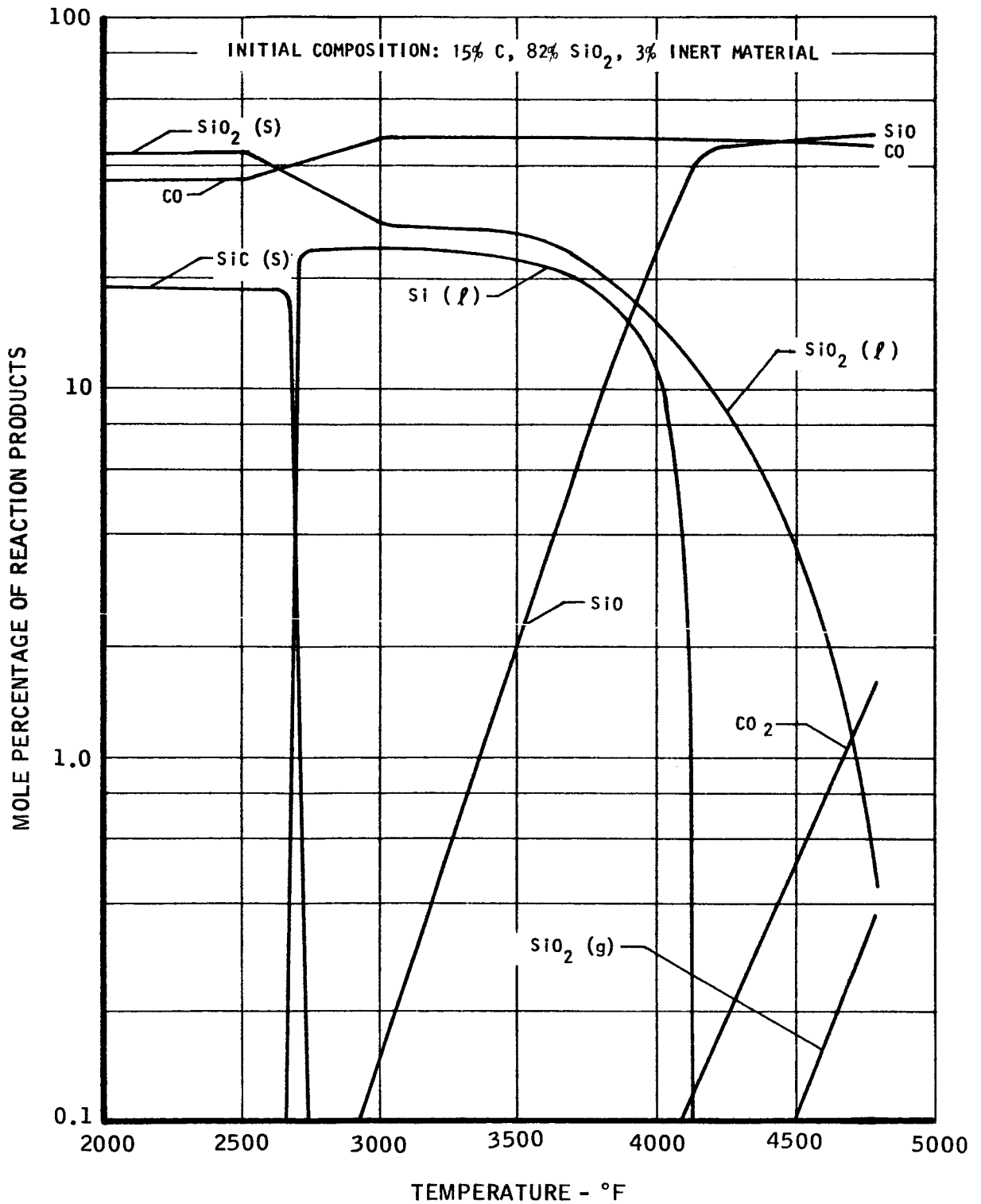
C5025-1

FIGURE 40. Fused Silica Foam Samples from Silica-Phenolic Thrust Chamber Wall

UNCLASSIFIED

REPORT 6069

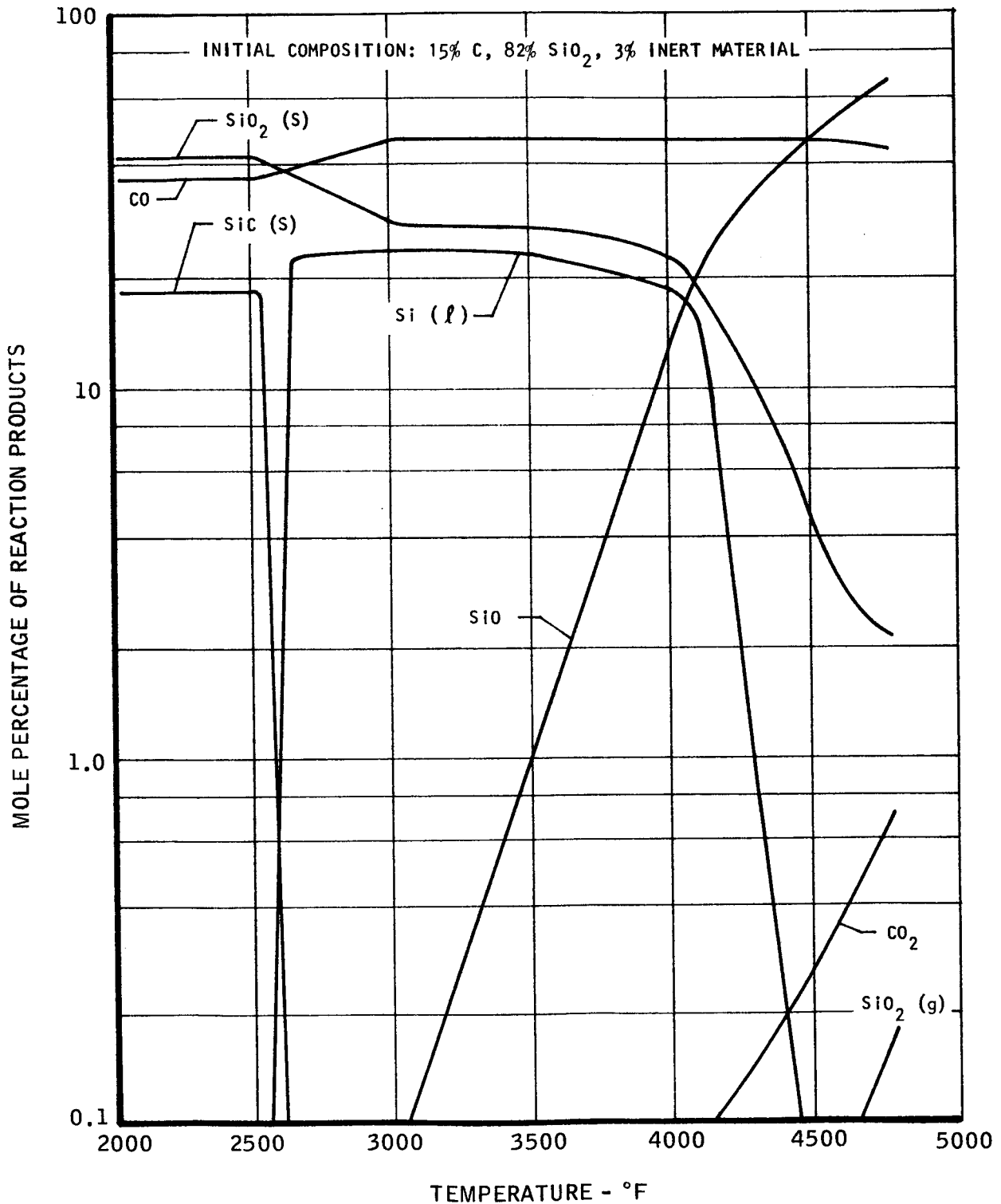
SILICA-CARBON CHEMICAL EQUILIBRIA AS A FUNCTION OF TEMPERATURE AT A PRESSURE OF 100 PSIA



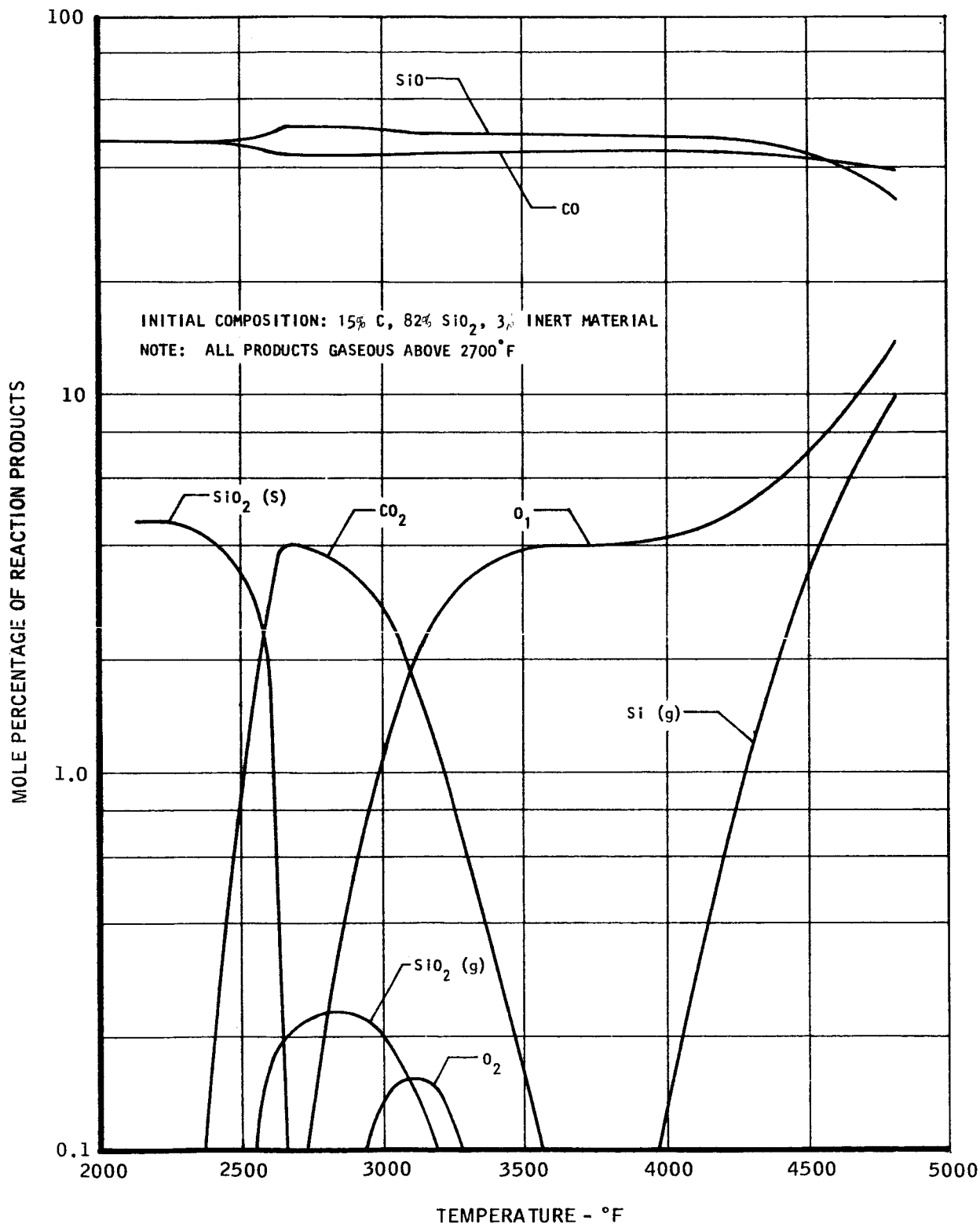
TAC 8673

UNCLASSIFIED

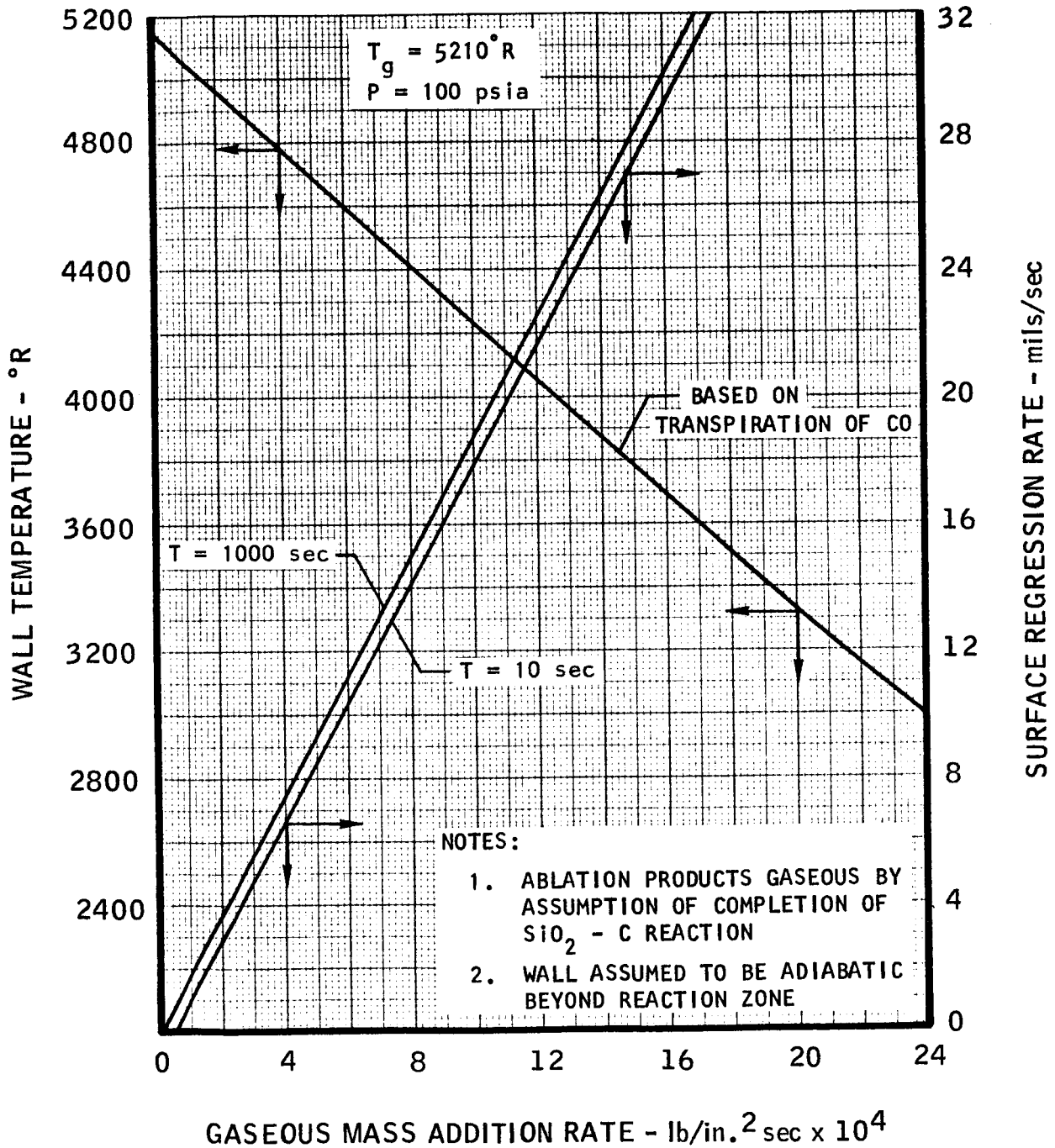
SILICA-CARBON CHEMICAL EQUILIBRIA AS A FUNCTION OF TEMPERATURE AT A PRESSURE OF 200 PSIA



TMC A 673

SILICA-CARBON CHEMICAL EQUILIBRIA AS A FUNCTION OF TEMPERATURE
AT A PRESSURE OF 10^{-3} mm Hg

WALL TEMPERATURE REDUCTION FROM TRANSPIRATION COOLING EFFECT OF DIMENSIONALLY ABLATING SILICA-PHENOLIC THRUST CHAMBER

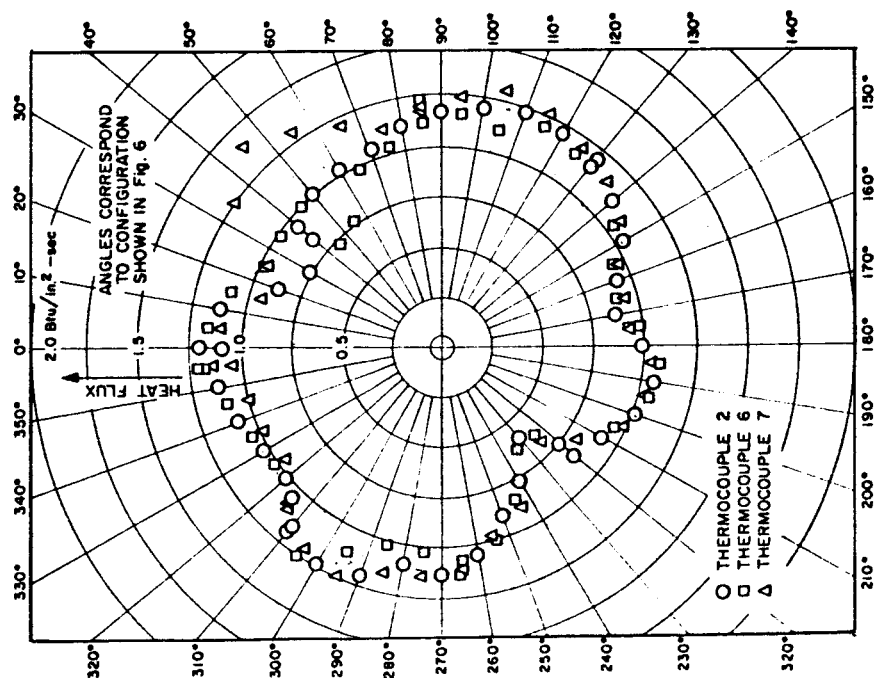


UNCLASSIFIED

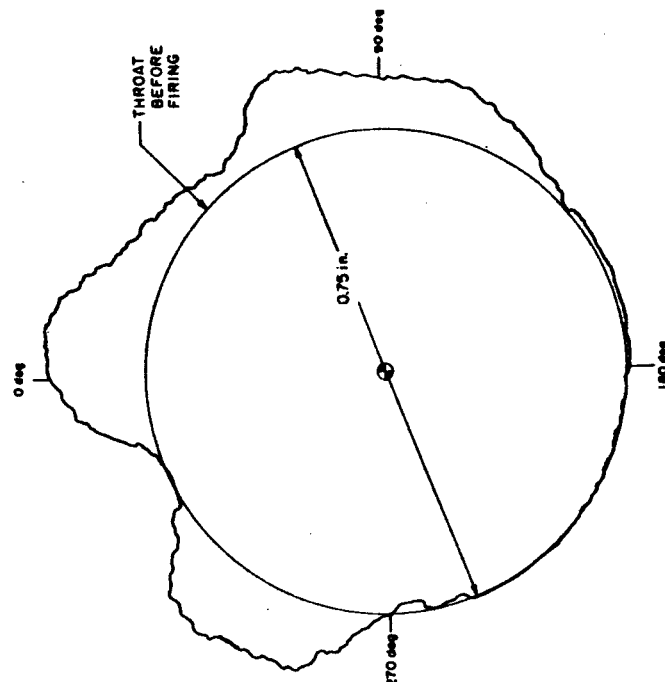
THE
Marquardt
CORPORATION
VAN NUYS, CALIFORNIA

REPORT 6069

ABLATIVE NOZZLE THROAT EROSION PATTERN COMPARED TO MEASURED COLD WALL HEAT FLUX DISTRIBUTION



A. CIRCUMFERENTIAL DISTRIBUTION OF
HEAT FLUX PRODUCED BY MOD. 11 INJECTOR



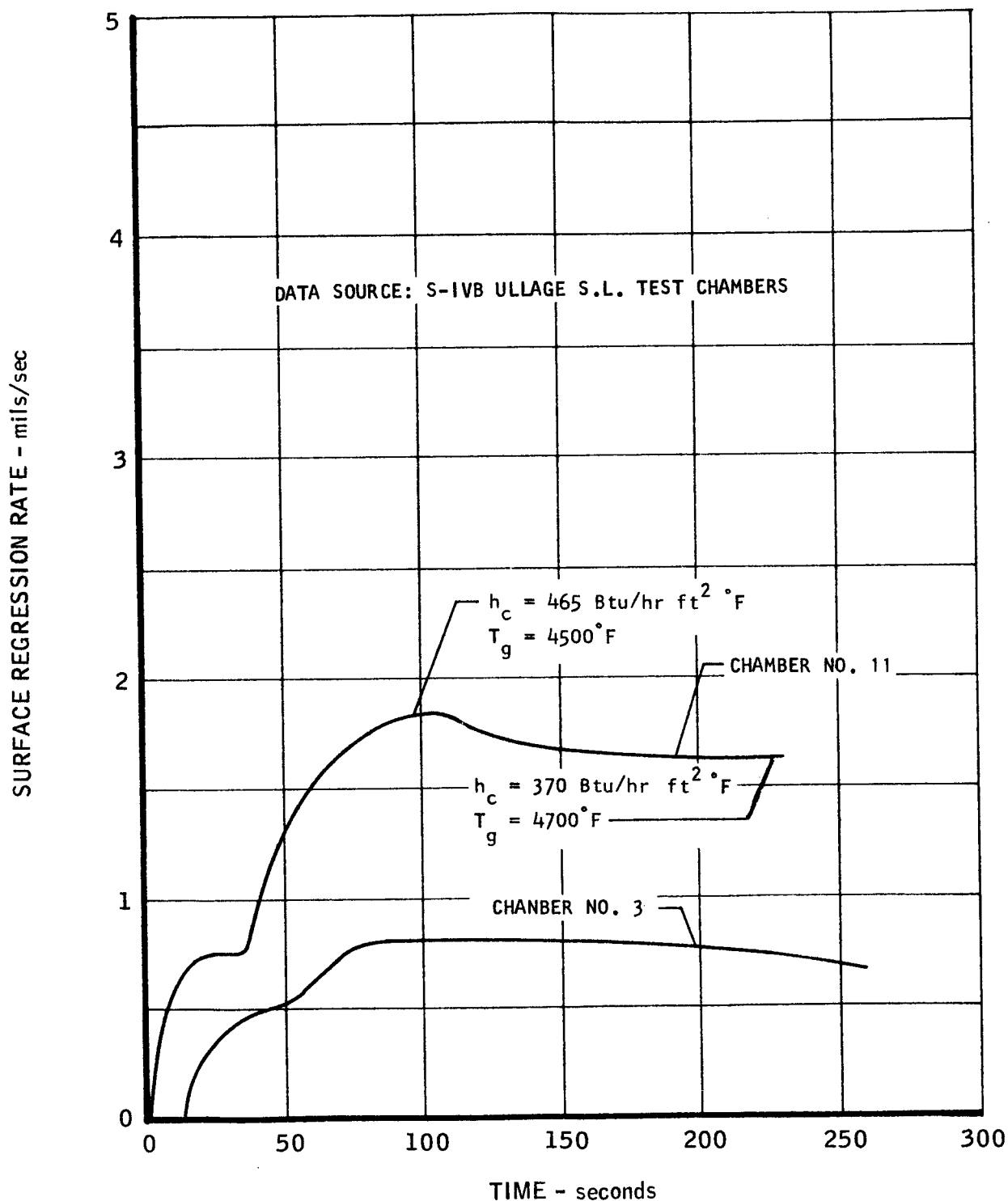
B. CROSS SECTION OF NOZZLE THROAT
OF REFRASIL-PHENOLIC ABLATIVE
THRUST CHAMBER AFTER TESTING
WITH MOD. 11 INJECTOR

REFERENCE: JPL TR 32-561

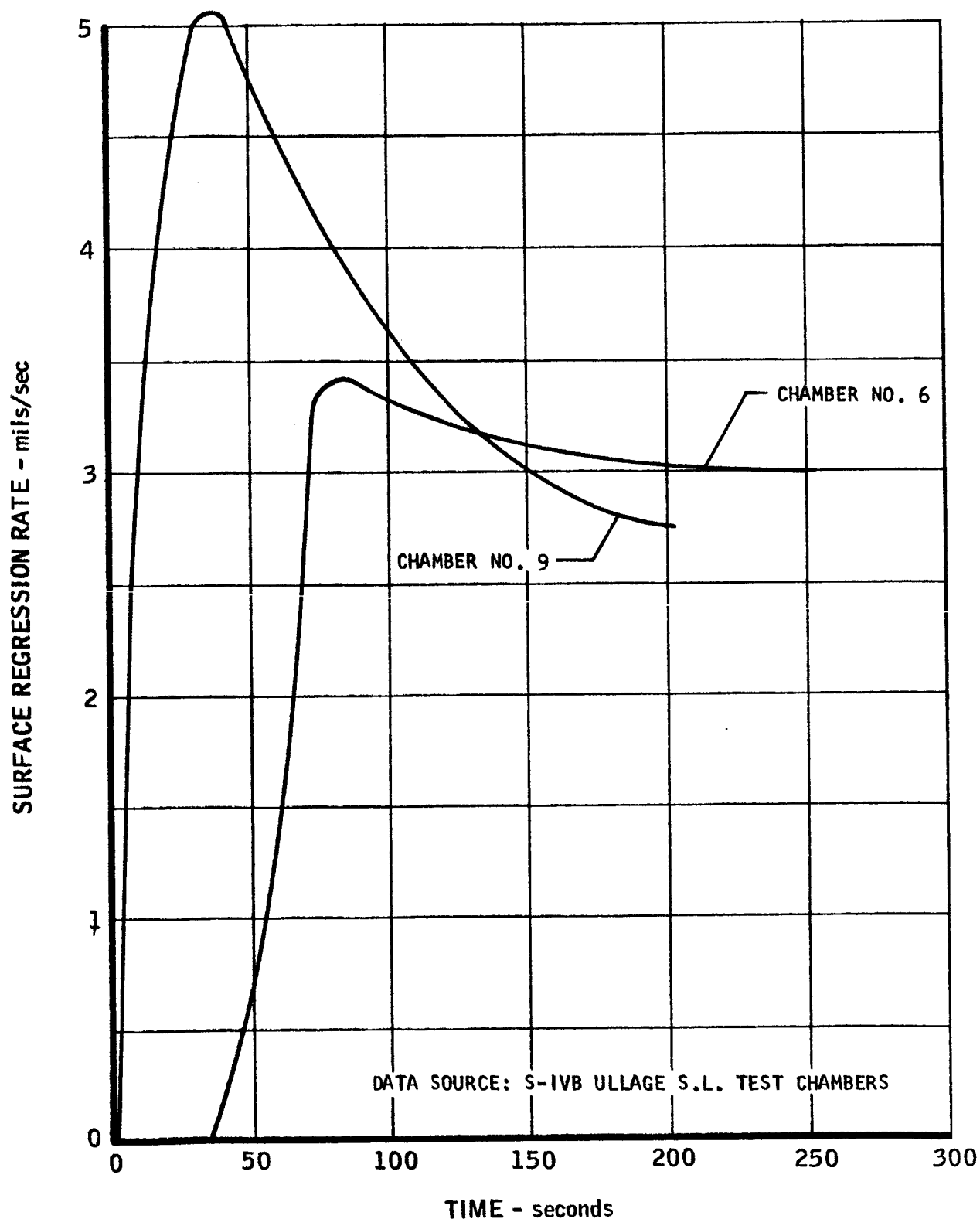
UNCLASSIFIED

REPORT 6069

EXPERIMENTAL SURFACE REGRESSION RATES FOR SILICA-PHENOLIC THRUST CHAMBER THROAT SECTION

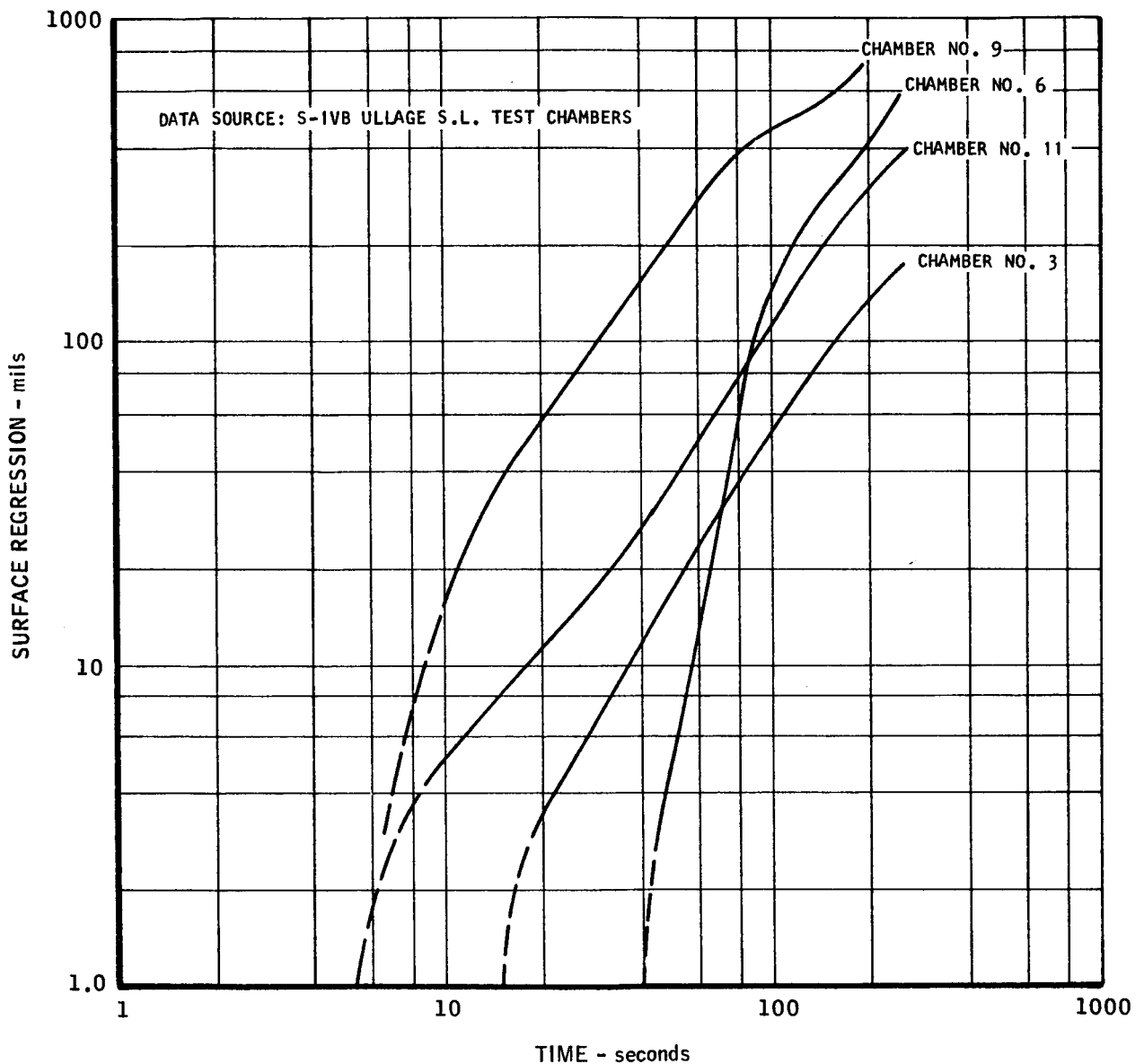


TMC A 673

EXPERIMENTAL SURFACE REGRESSION RATES
FOR SILICA-PHENOLIC THRUST CHAMBER THROAT SECTION

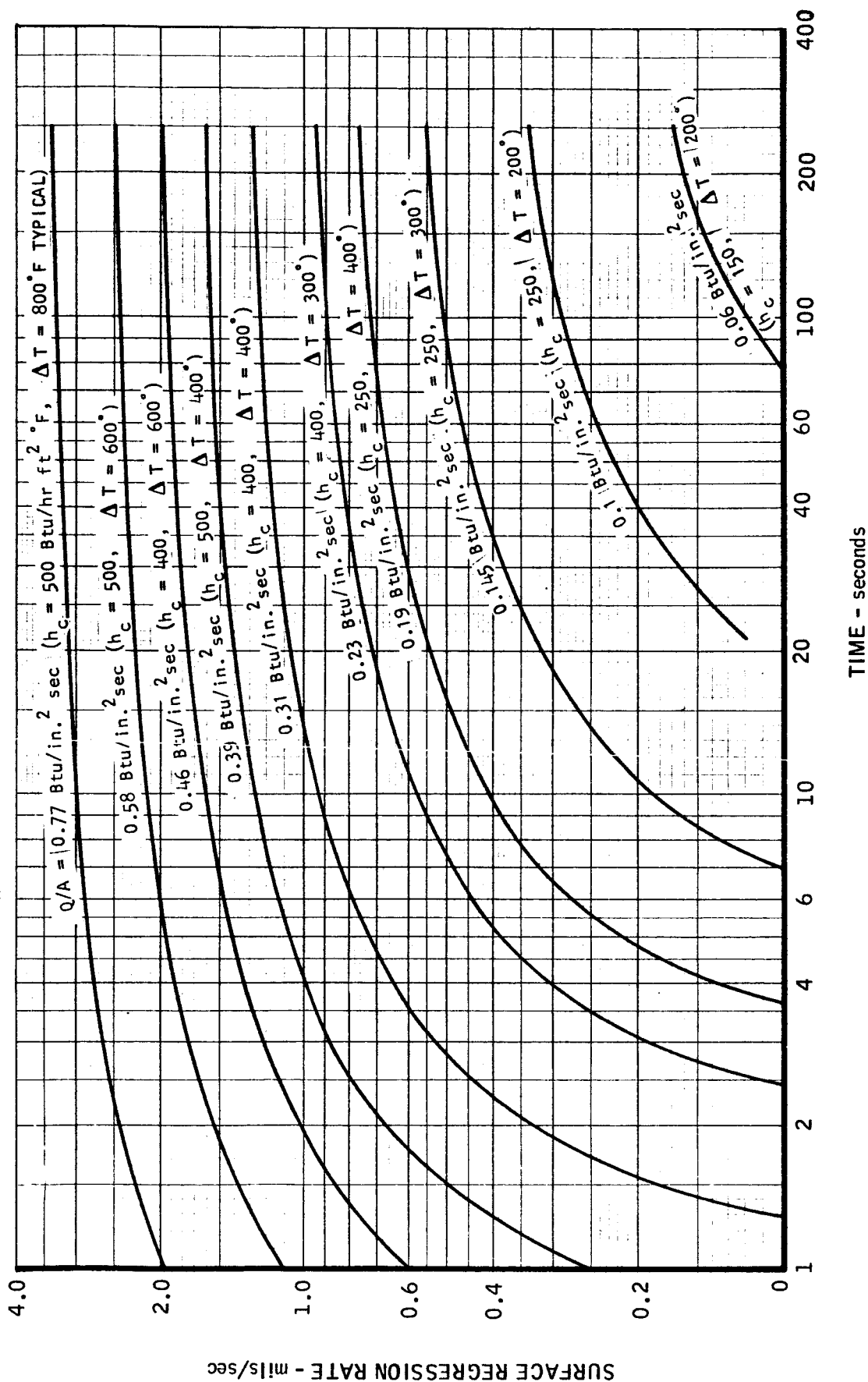
TMC A673

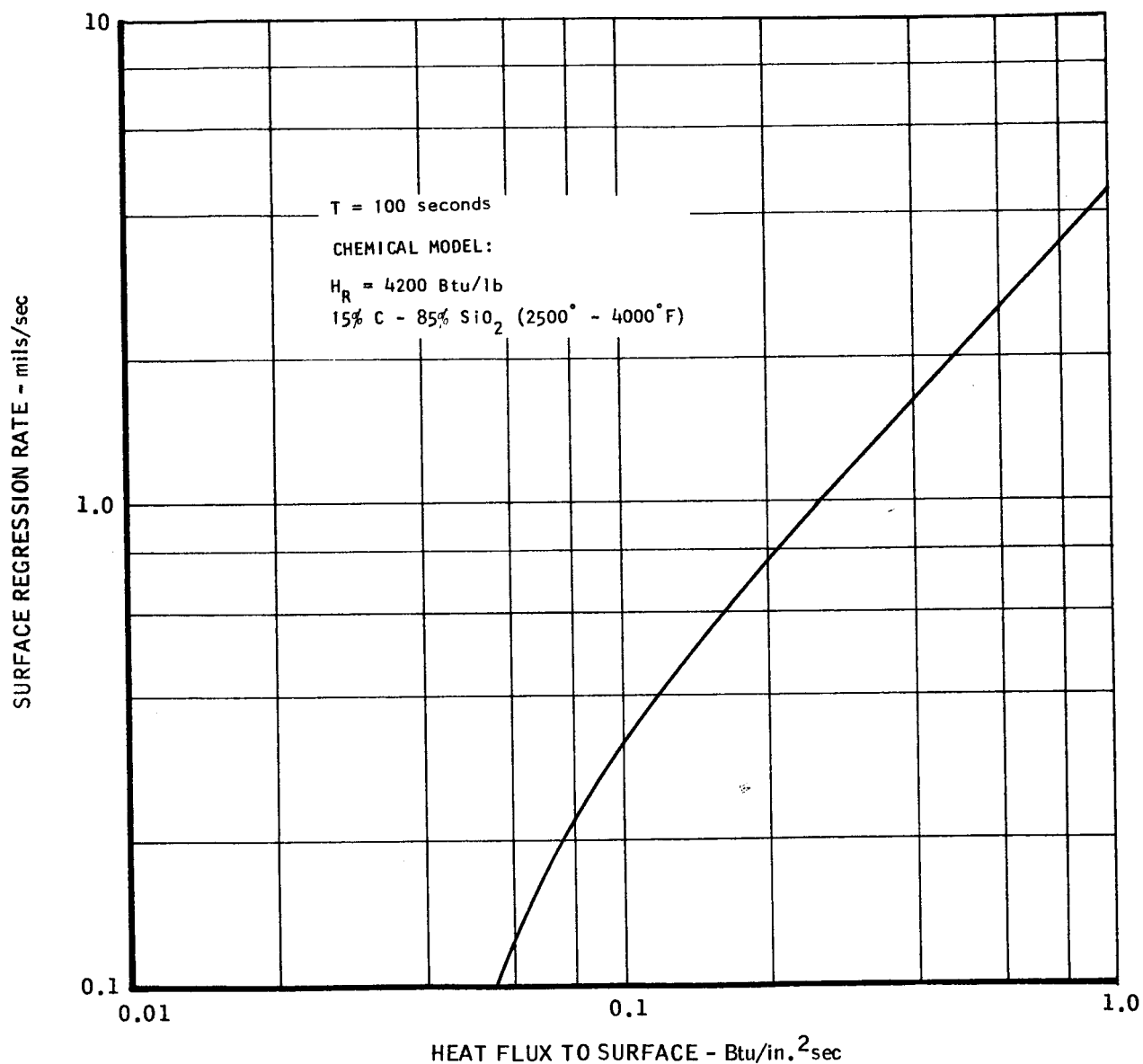
EXPERIMENTAL SURFACE REGRESSION AS A FUNCTION OF TIME
FOR SILICA-PHENOLIC THRUST CHAMBER THROAT SECTIONS



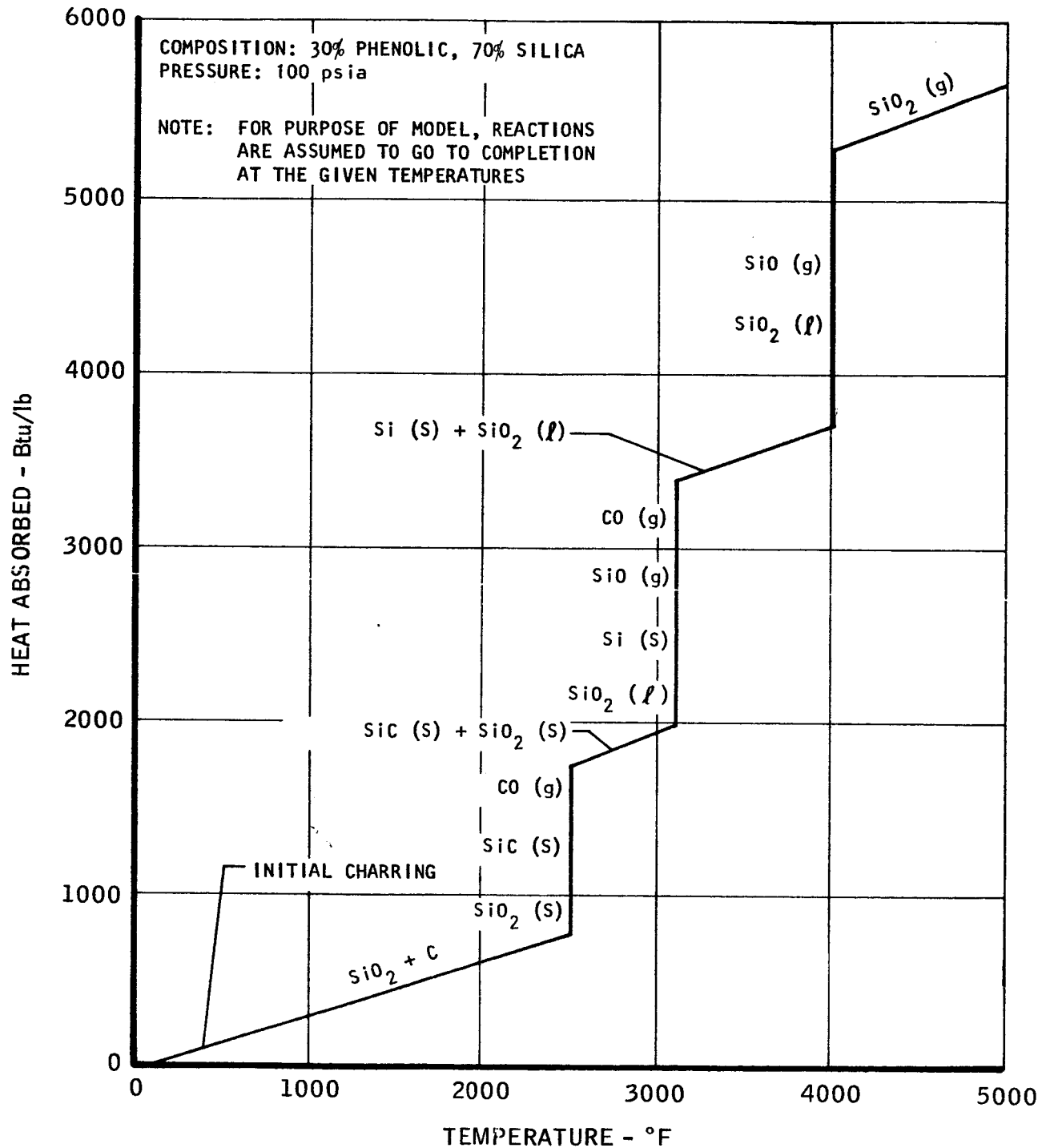
ANALYTICALLY DETERMINED SURFACE REGRESSION RATES FOR A SILICA-PHENOLIC THRUST CHAMBER AS A FUNCTION OF HEAT FLUX

CHEMICAL MODEL: $H_R = 4200 \text{ Btu/lb}$ for 15% C - 85% SiO_2 ($2500^\circ - 4000^\circ \text{F}$)



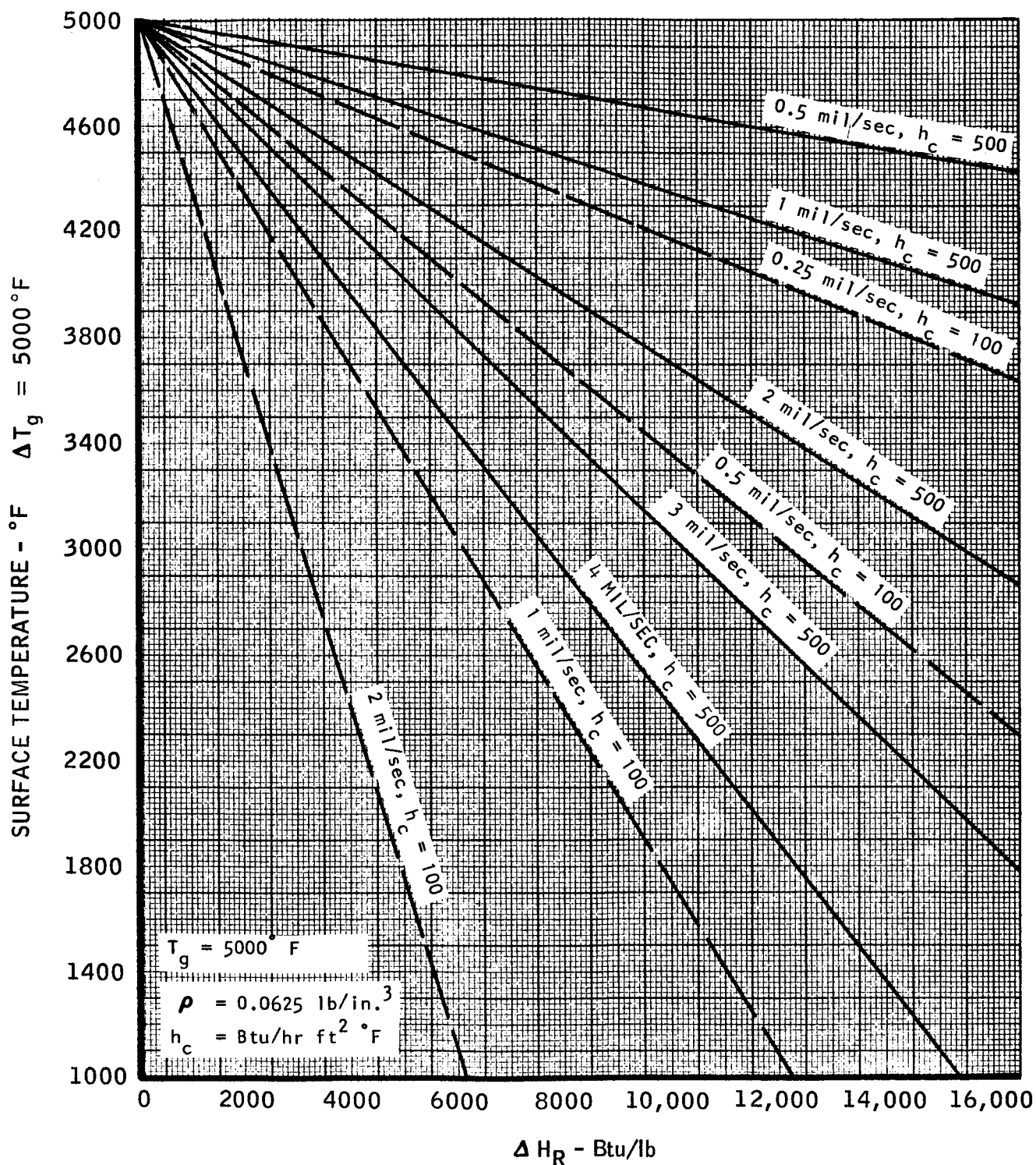
ANALYTICALLY DETERMINED SURFACE REGRESSION RATE
FOR A SILICA-PHENOLIC THRUST CHAMBER AS A FUNCTION OF HEAT FLUX

ENDOTHERMIC AND SENSIBLE HEAT ABSORPTION OF SILICA-PHENOLIC LAMINATE AS A FUNCTION OF TEMPERATURE

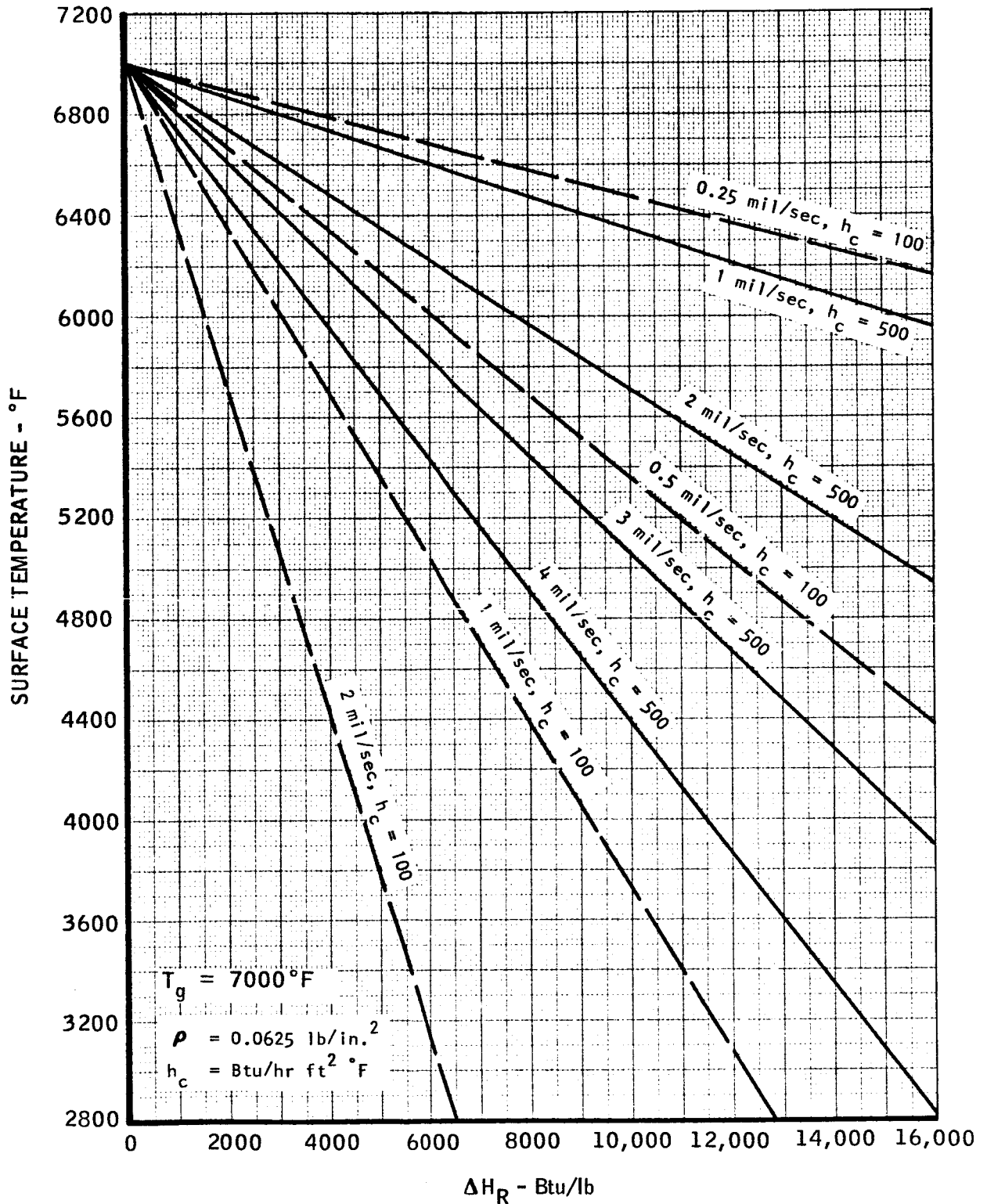


TMCA 673

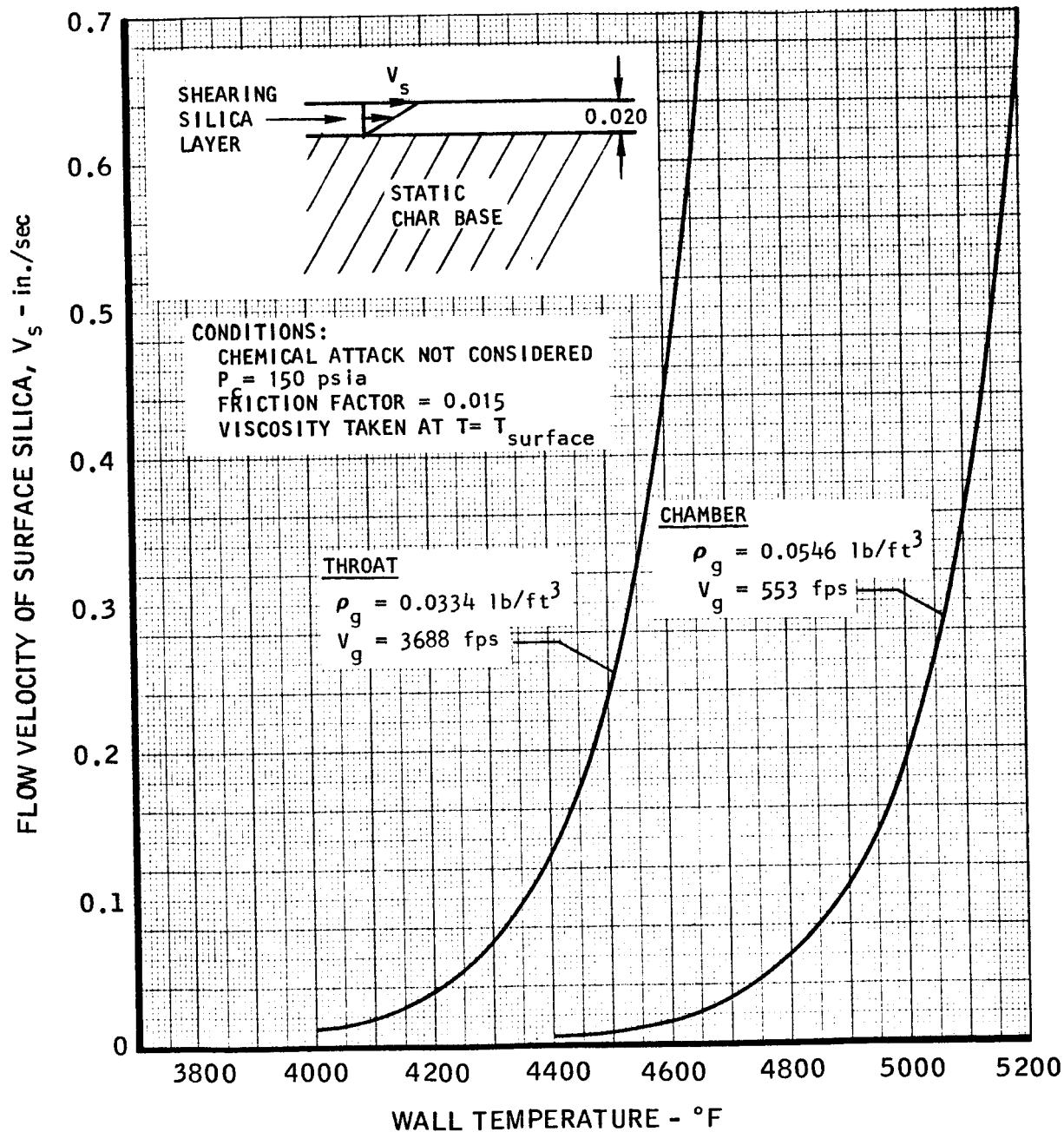
STEADY STATE SURFACE TEMPERATURE AS A FUNCTION OF ENDOTHERMIC
AND SENSIBLE HEAT ABSORBED
FOR A DIMENSIONALLY ABLATING COMPOSITE MATERIAL



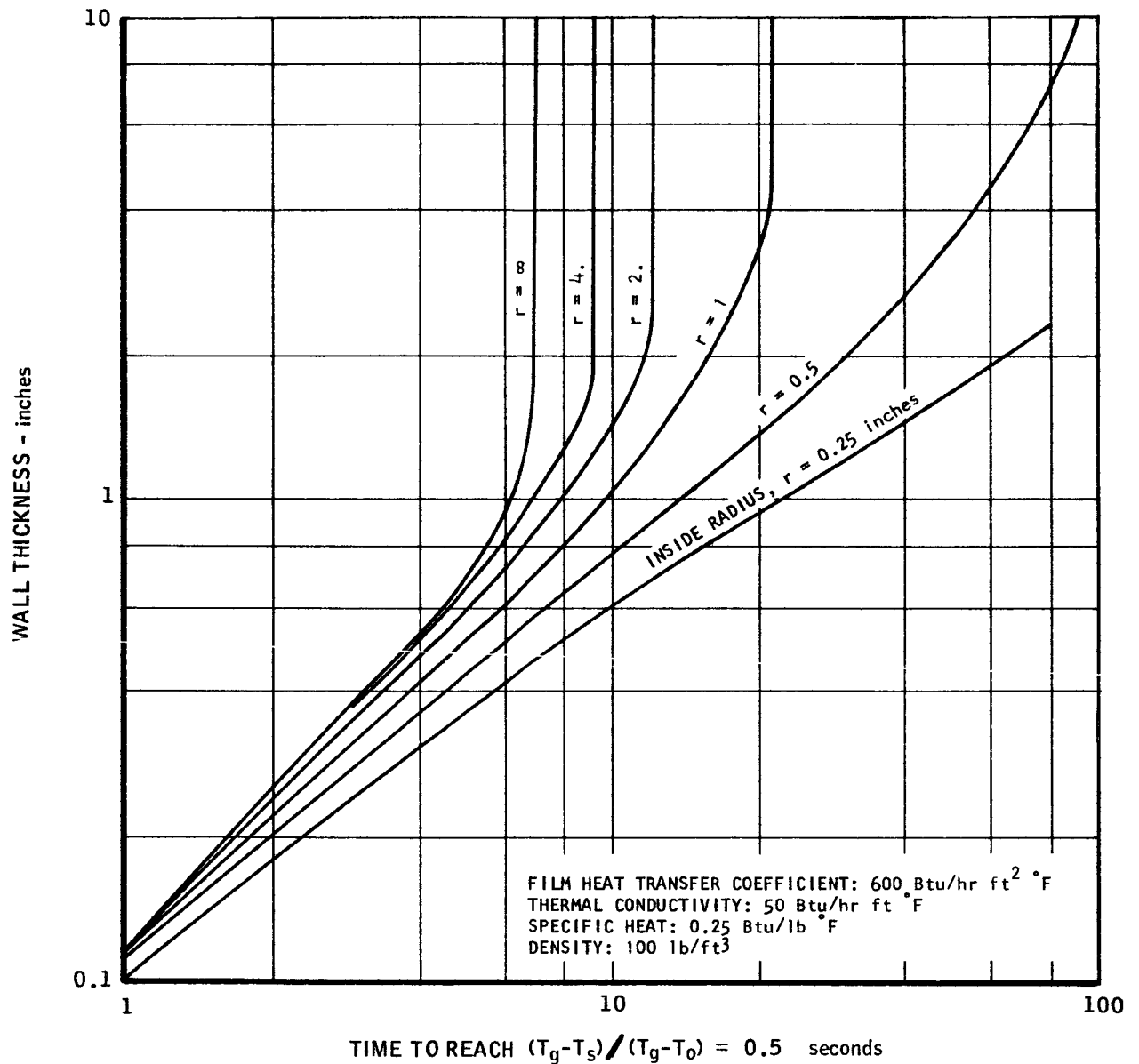
STEADY STATE SURFACE TEMPERATURE AS A FUNCTION OF ENDOTHERMIC
AND SENSIBLE HEAT ABSORBED FOR DIMENSIONALLY
ABLATING COMPOSITE MATERIAL



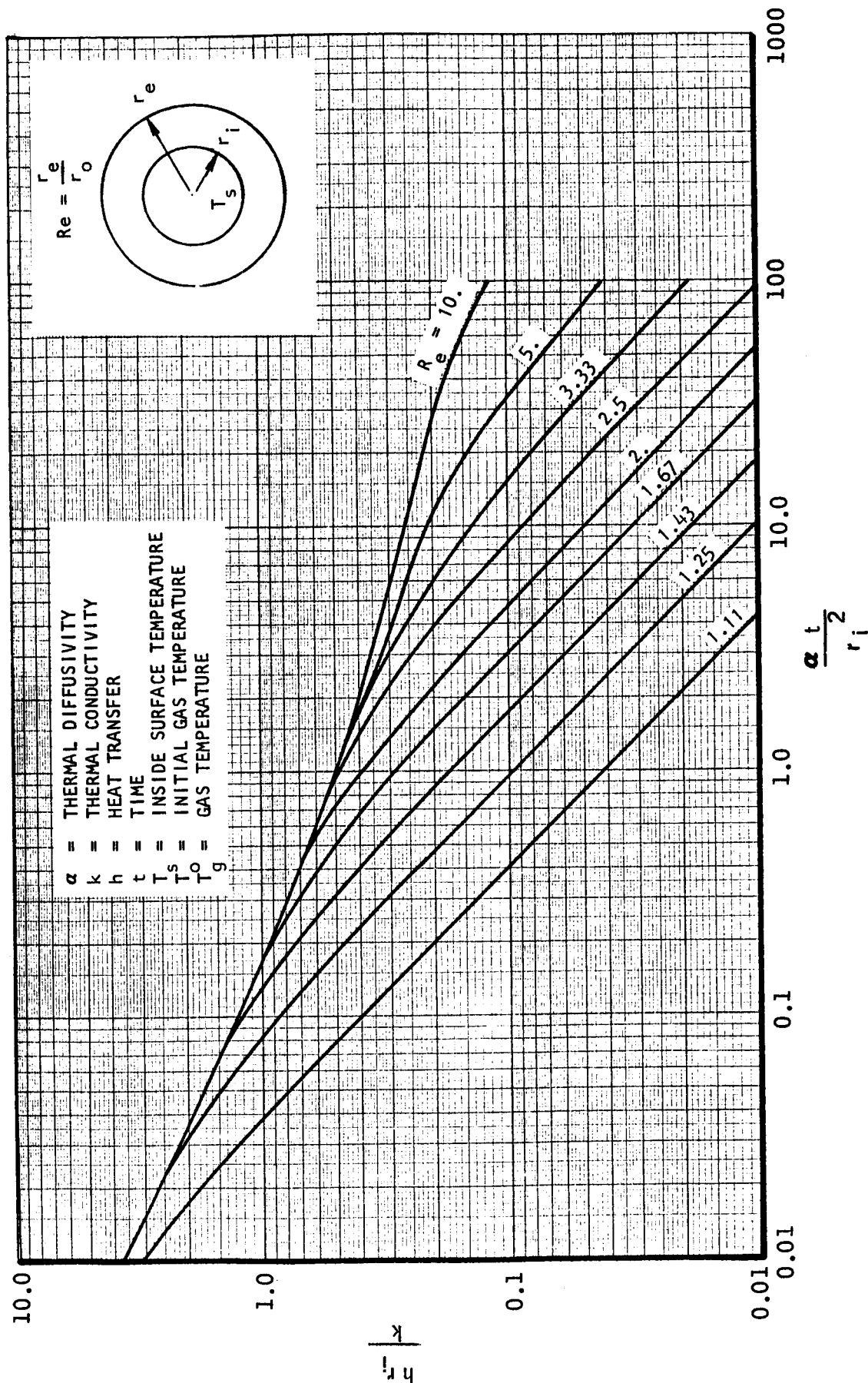
FLOW VELOCITY OF ERODING MOLTEN SILICA LAYER AS A FUNCTION OF THRUST CHAMBER INNER SURFACE TEMPERATURE



INSIDE SURFACE TEMPERATURE RISE TIME FOR A CONVECTIVELY HEATED CYLINDER



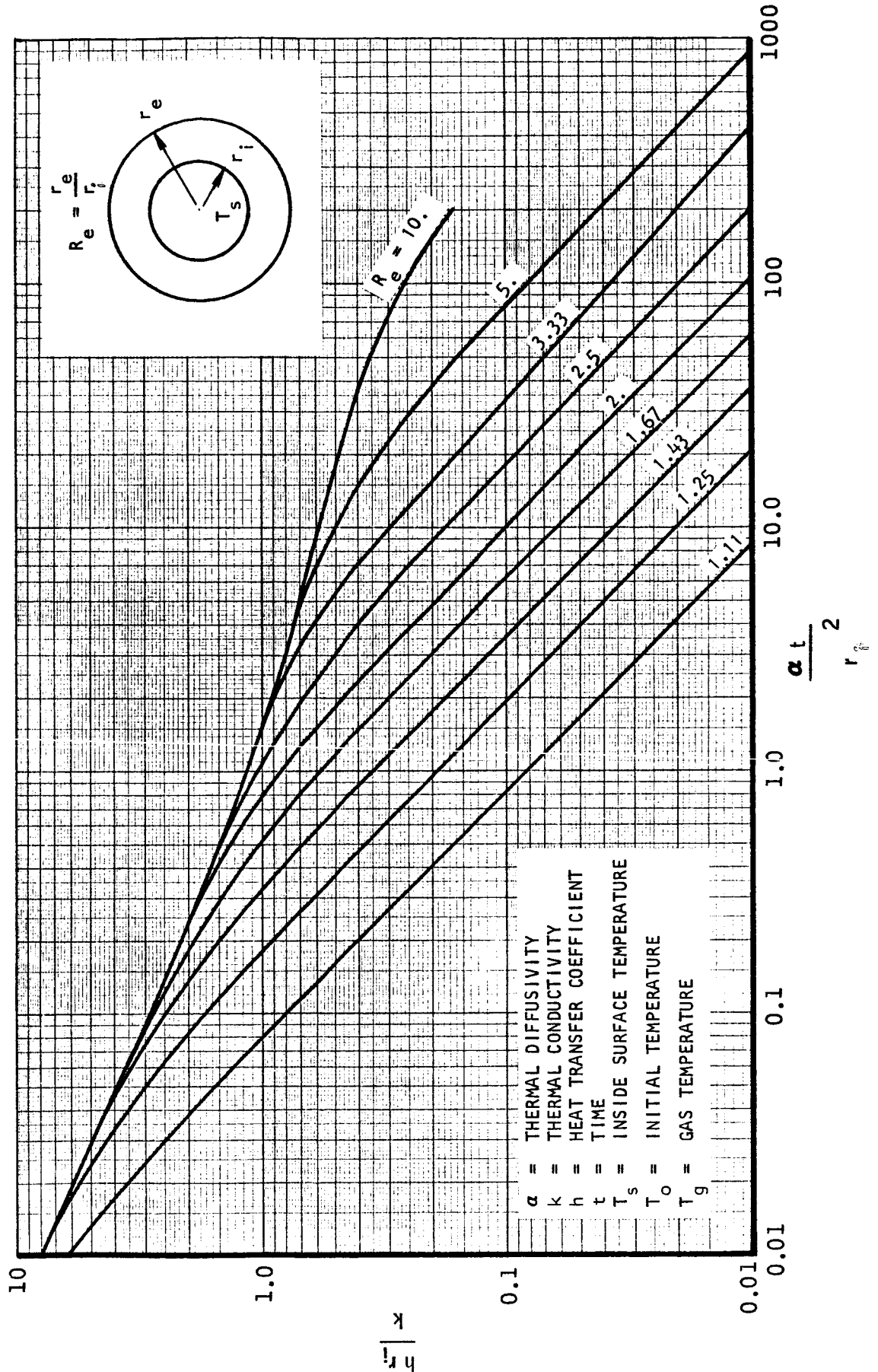
TIME FOR HEATED INSIDE SURFACE OF CYLINDER TO REACH $(T_s - T_o) / (T_g - T_o) = 0.3$



UNCLASSIFIED

REPORT 6069

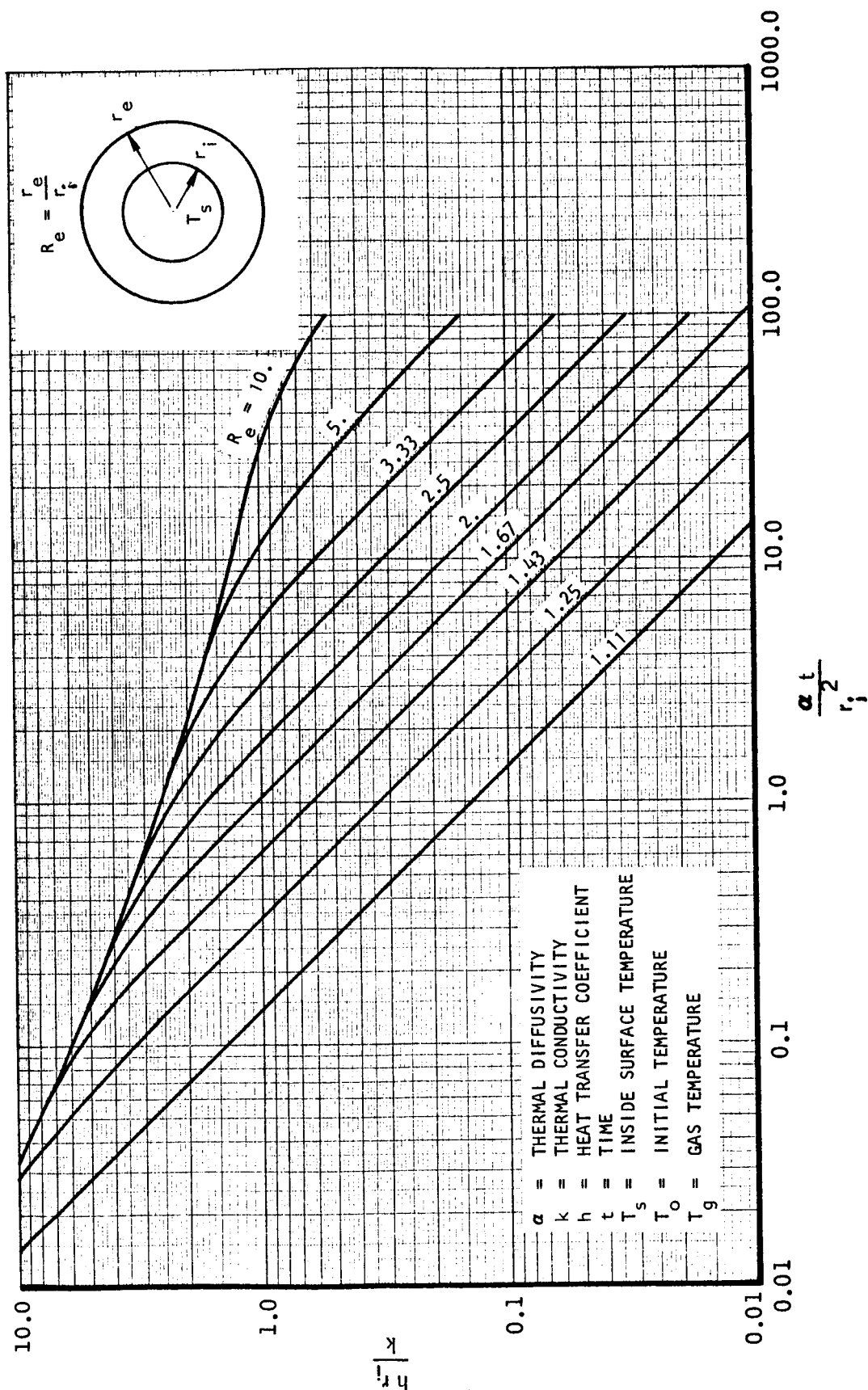
TIME FOR HEATED INSIDE SURFACE OF CYLINDER TO REACH $(T_s - T_o) / (T_g - T_o) = 0.5$



10M141 UNCLASSIFIED

FIGURE 57

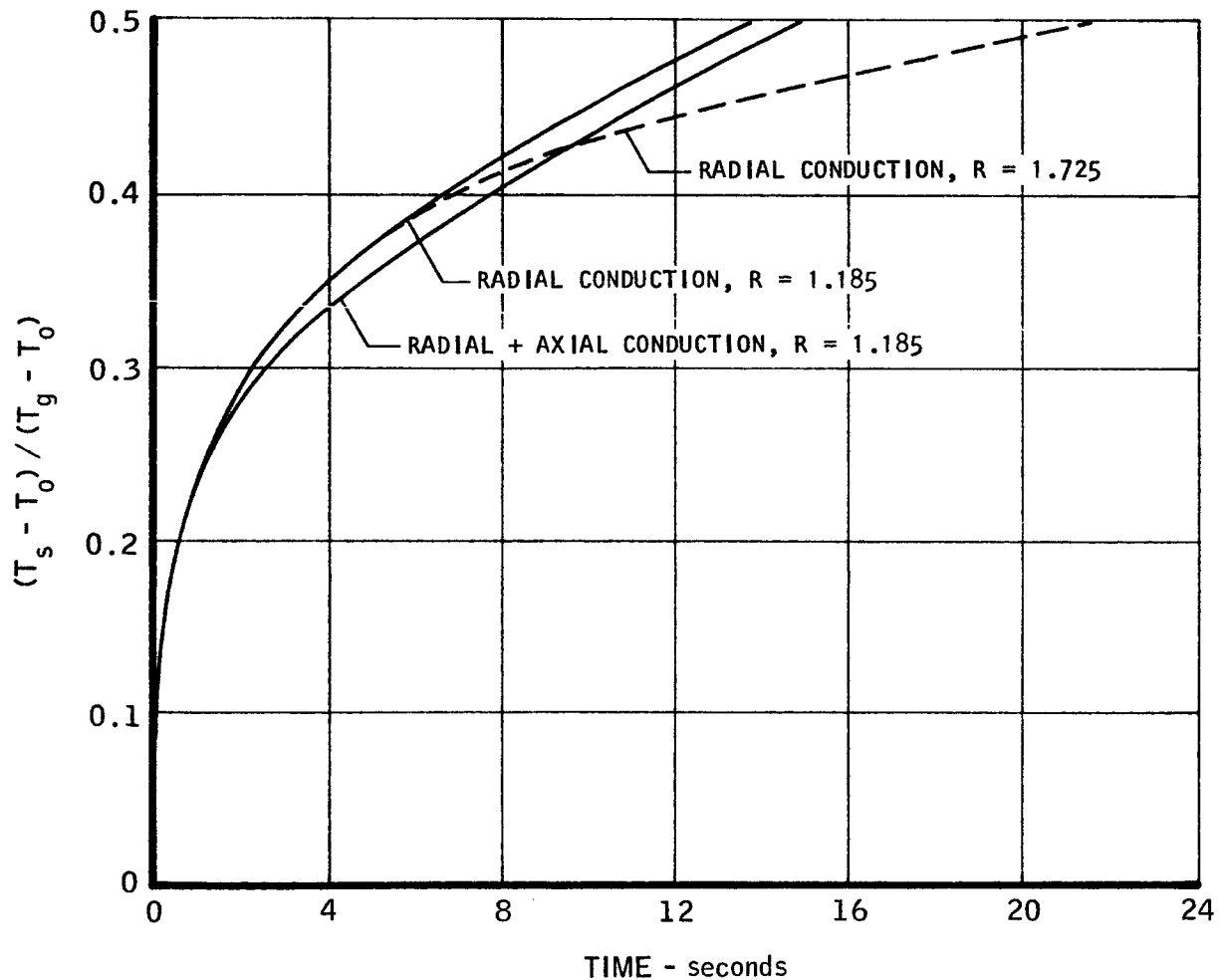
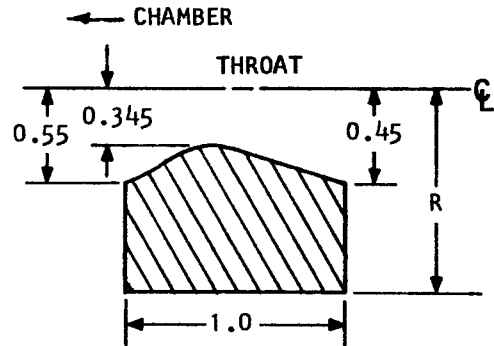
TIME FOR HEATED INSIDE SURFACE OF CYLINDER TO REACH $(T_s - T_0) / (T_g - T_0) = 0.7$



UNCLASSIFIED

TRANSIENT TEMPERATURE RESPONSE OF INNER SURFACE OF GRAPHITE THROAT INSERT

$$\begin{aligned} h_{\text{throat}} &= 800 \text{ Btu/ft}^2 \text{ hr } ^\circ\text{F} \\ K_{\text{throat}} &= 40 \text{ Btu/ft hr } ^\circ\text{F} \\ C &= 0.35 \text{ Btu/lb } ^\circ\text{F} \\ \rho &= 110 \text{ Lb cu ft} \end{aligned}$$

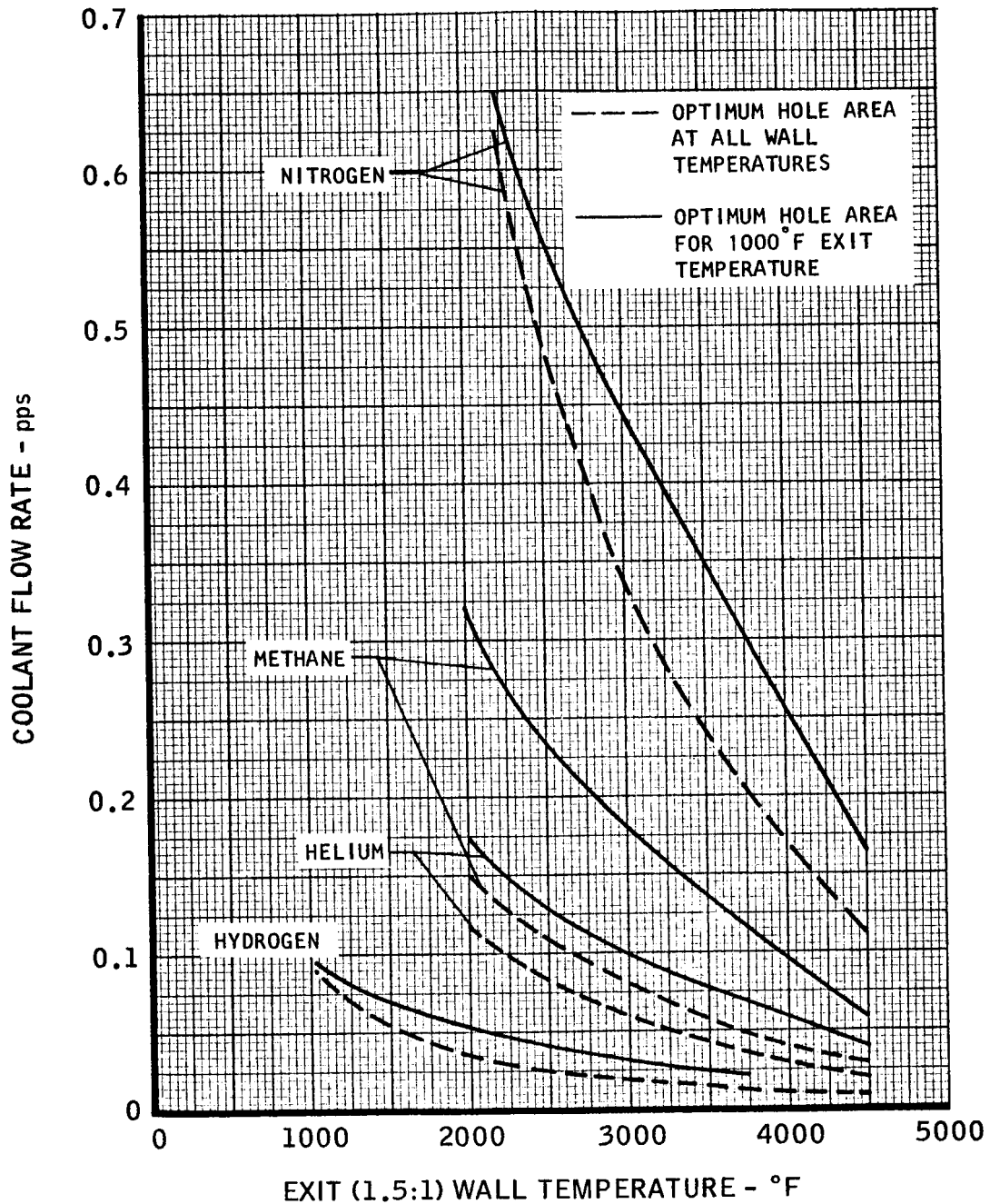


UNCLASSIFIED

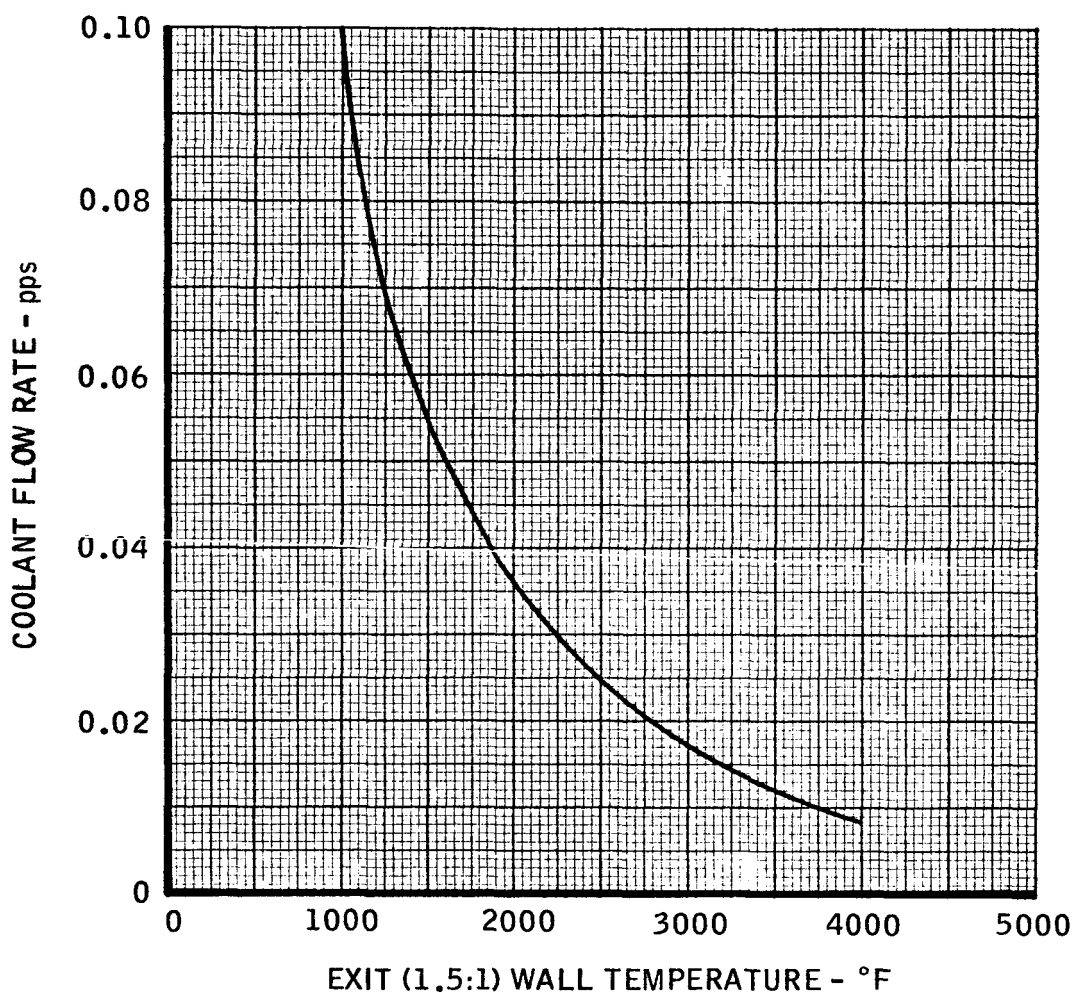
REPORT 6069

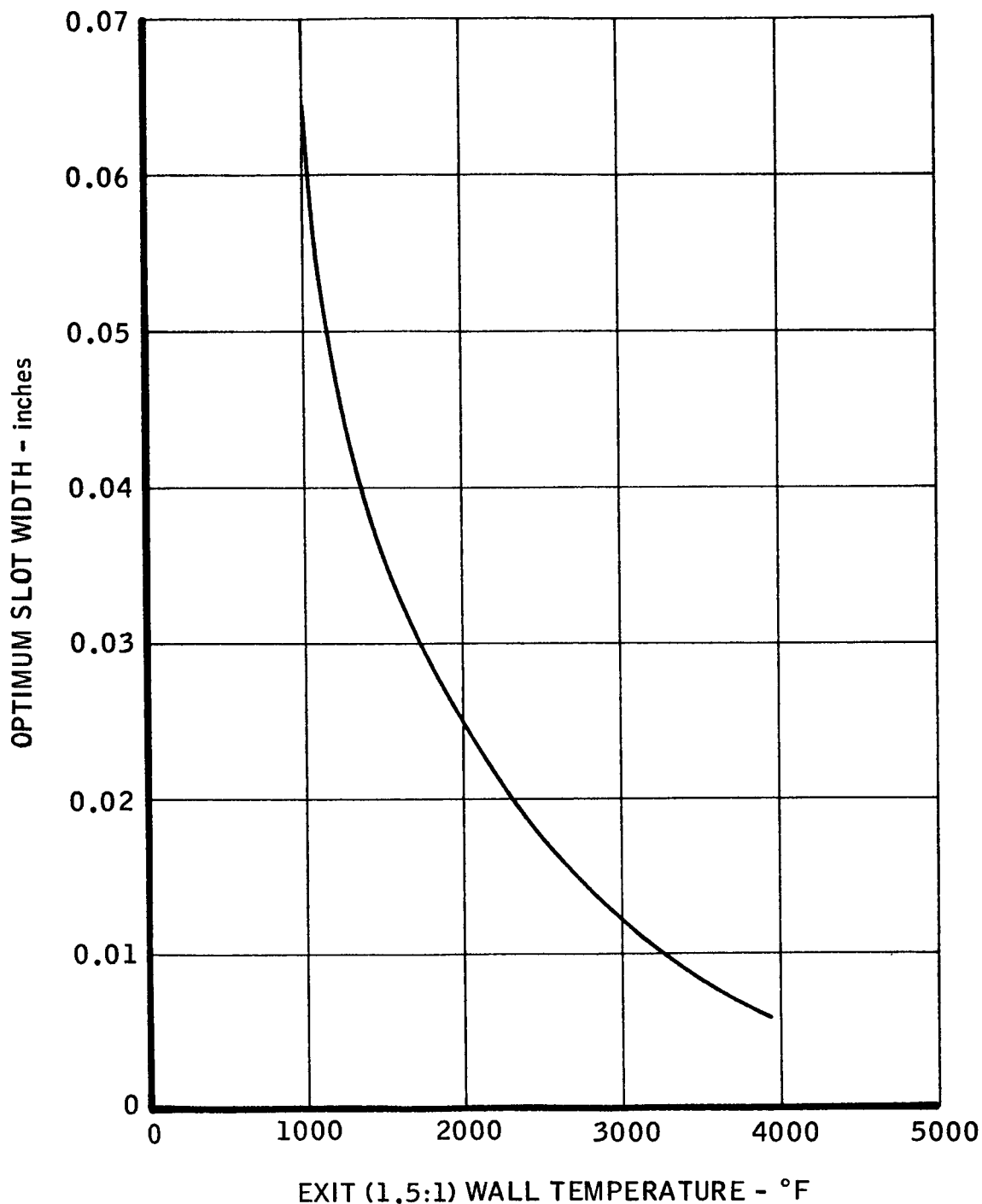
GASEOUS FILM COOLING REQUIREMENTS FOR STANDARD NOZZLE WITH TWO-ROW HOLE PATTERN AT 4:1

H_2 COOLANT; O_2/H_2 ; $P_0 = 100$ psia

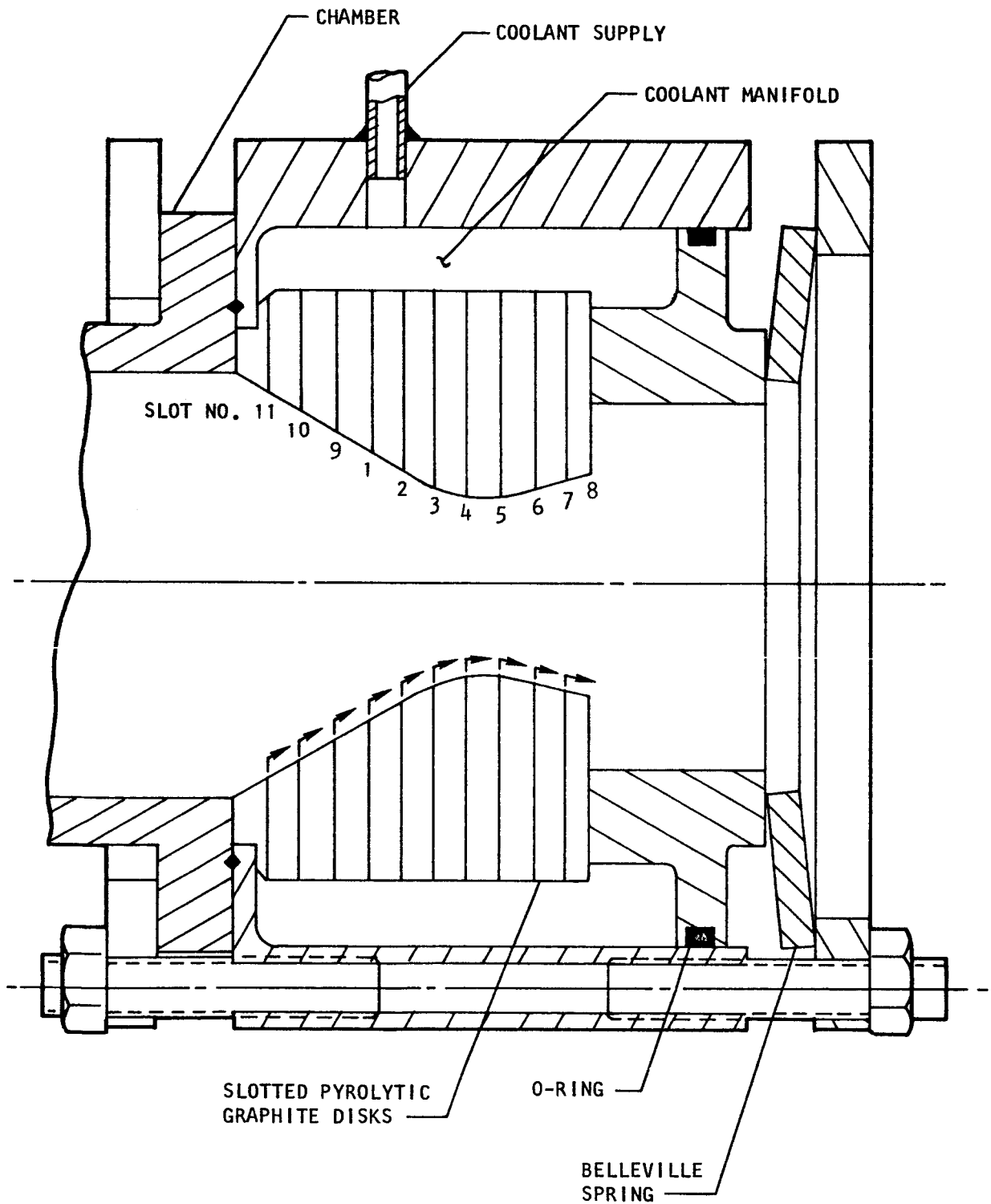


TMC A 673

GASEOUS FILM COOLING REQUIREMENTS FOR STANDARD NOZZLE
WITH OPTIMUM TANGENTIAL SLOT AT 5.38:1 H_2 COOLANT, O_2/H_2 ; $P_o = 100$ psia

OPTIMUM SLOT WIDTH FOR STANDARD NOZZLE
WITH TANGENTIAL SLOT AT 5.38:1 H_2 COOLANT, O_2/H_2 , $P_0 = 100$ psia

MULTISLOT, FILM COOLED PYROLYTIC GRAPHITE NOZZLE



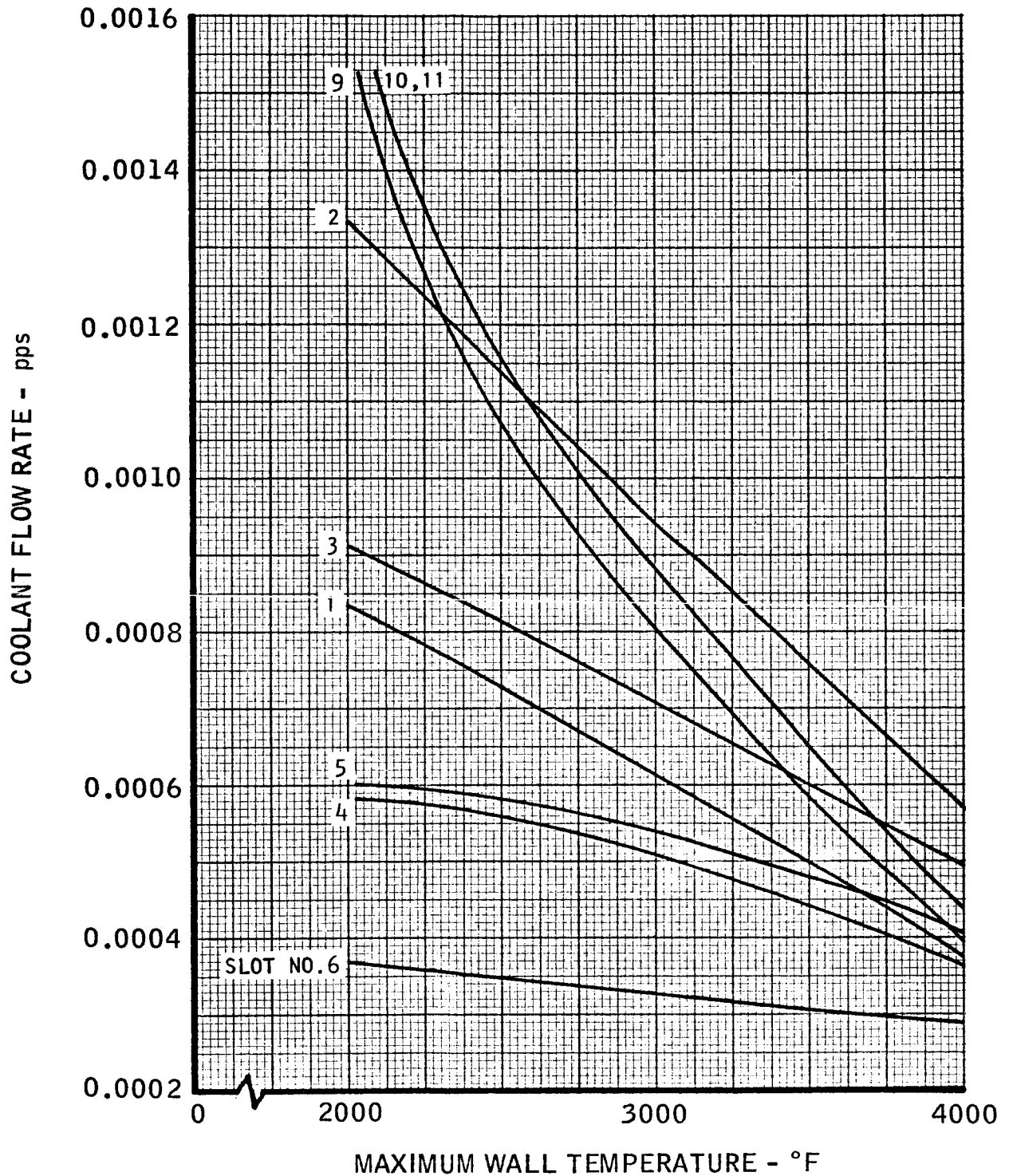
TMC A673



T3149-38
FIGURE 64. Insert Disk for Multislots, Film Cooled Pyrolytic Graphite Nozzle

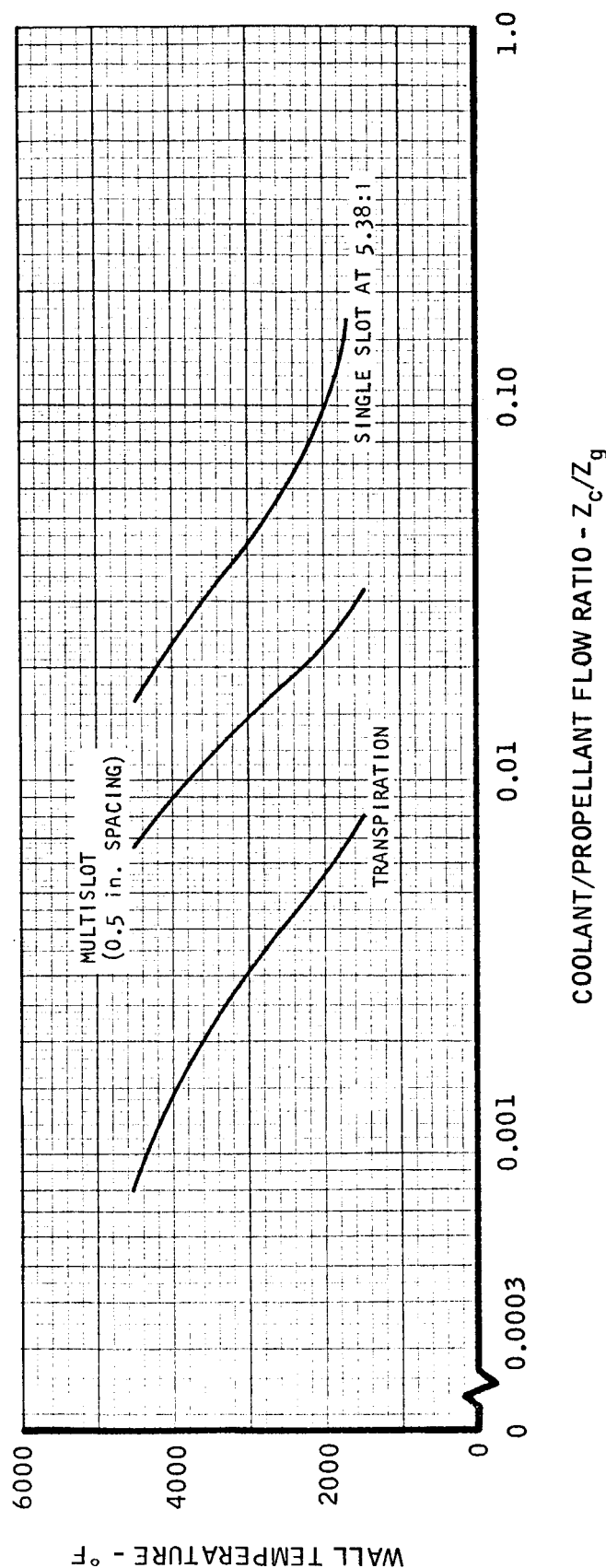
GASEOUS FILM COOLING FOR STANDARD NOZZLE WITH MULTISLOT COOLING

H_2 COOLANT, O_2/H_2 , $P_0 = 100$ psia



TMC A673

COMPARISON OF COOLING TECHNIQUES

 O_2/H_2 $D_* = 1.25 \text{ in.}, P_o = 100 \text{ psia}, T_g = 5210^\circ R$ COOLANT/PROPELLANT FLOW RATIO - Z_c/Z_g

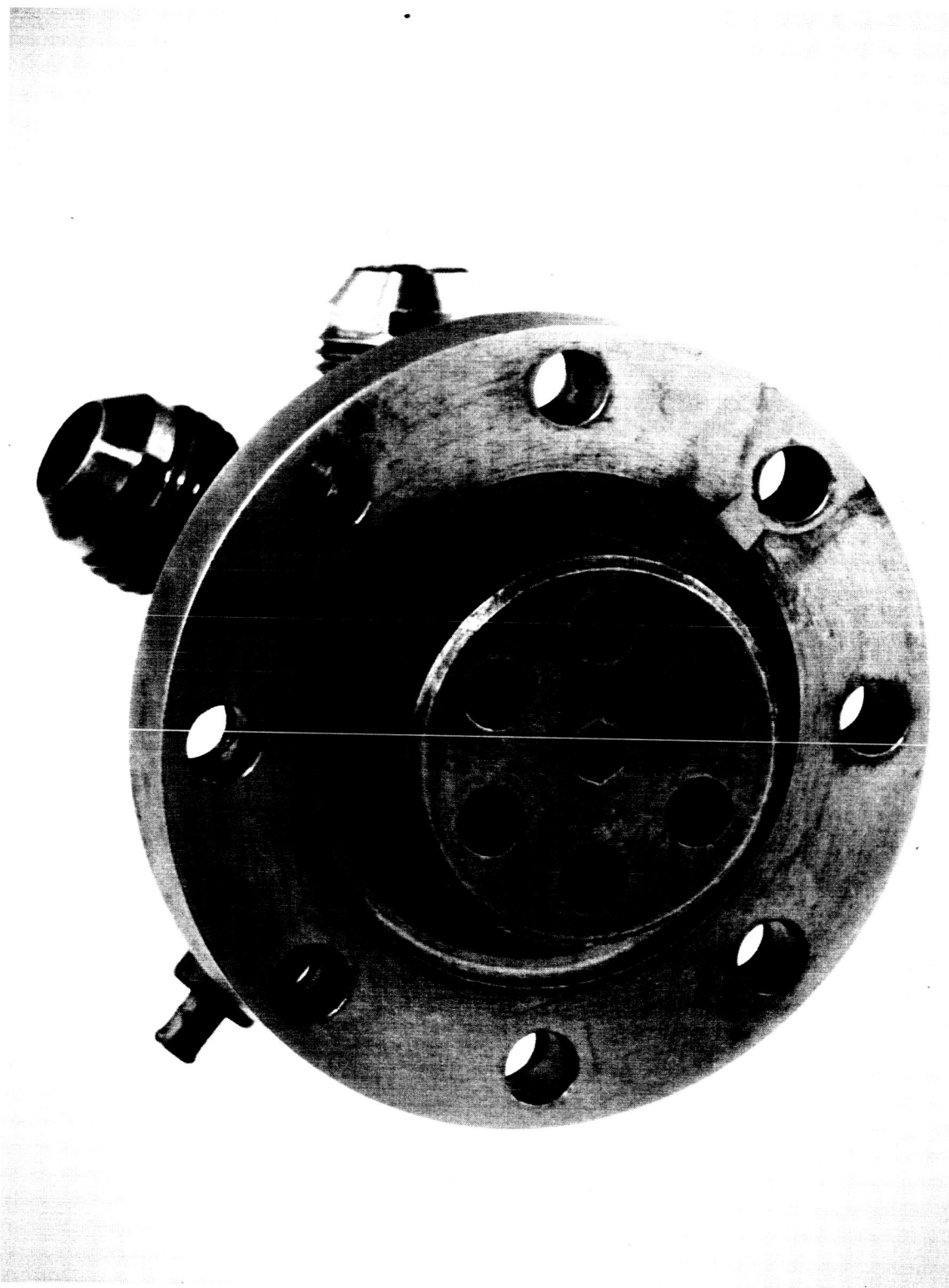


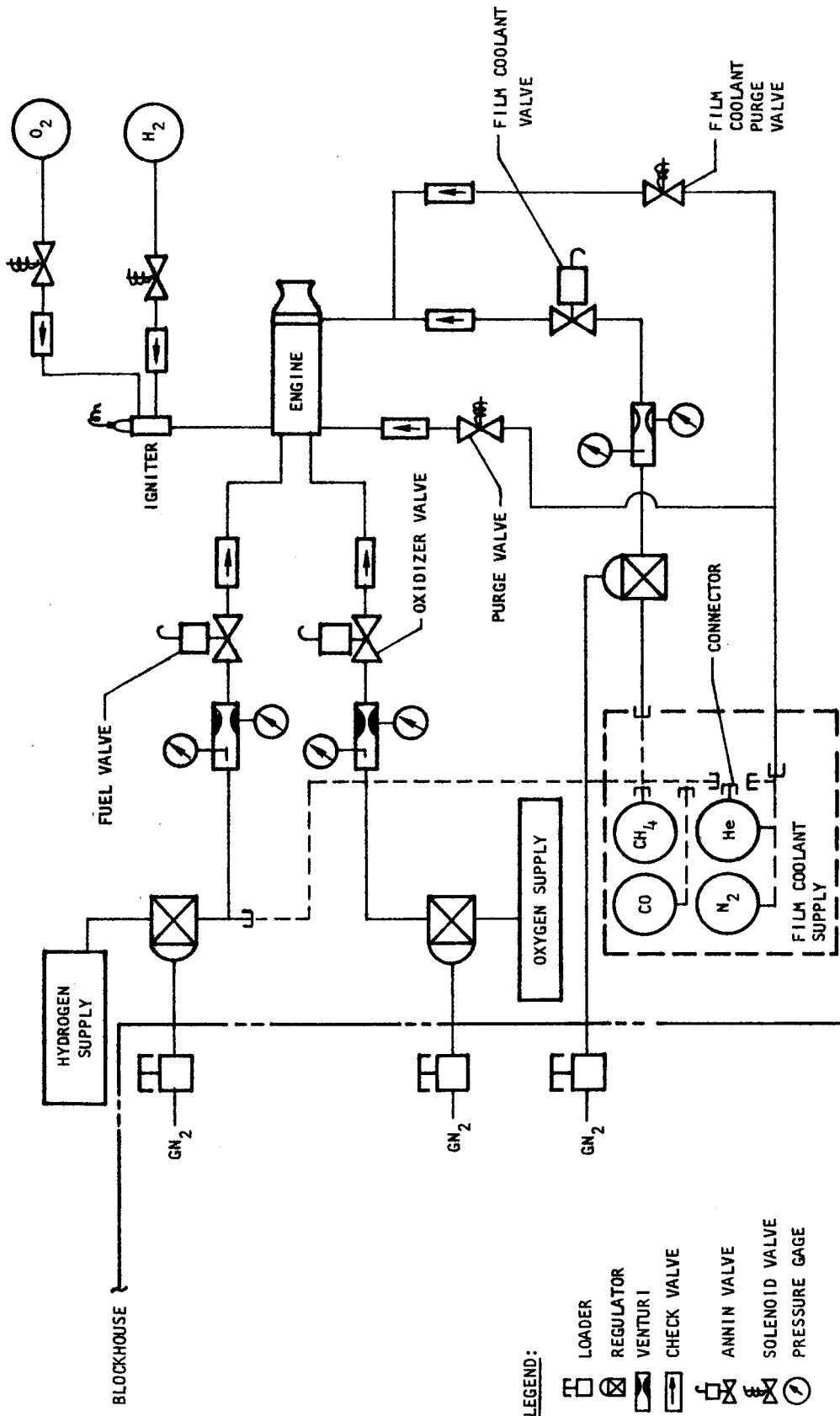
FIGURE 67. Saturn Model Engine Injector (Copper Injector)

T3149-19

UNCLASSIFIED

REPORT 6069

SCHEMATIC OF PROPELLANT FEED AND FILM COOLANT SYSTEM



TMC A 673

278-155 UNCLASSIFIED

FIGURE 68

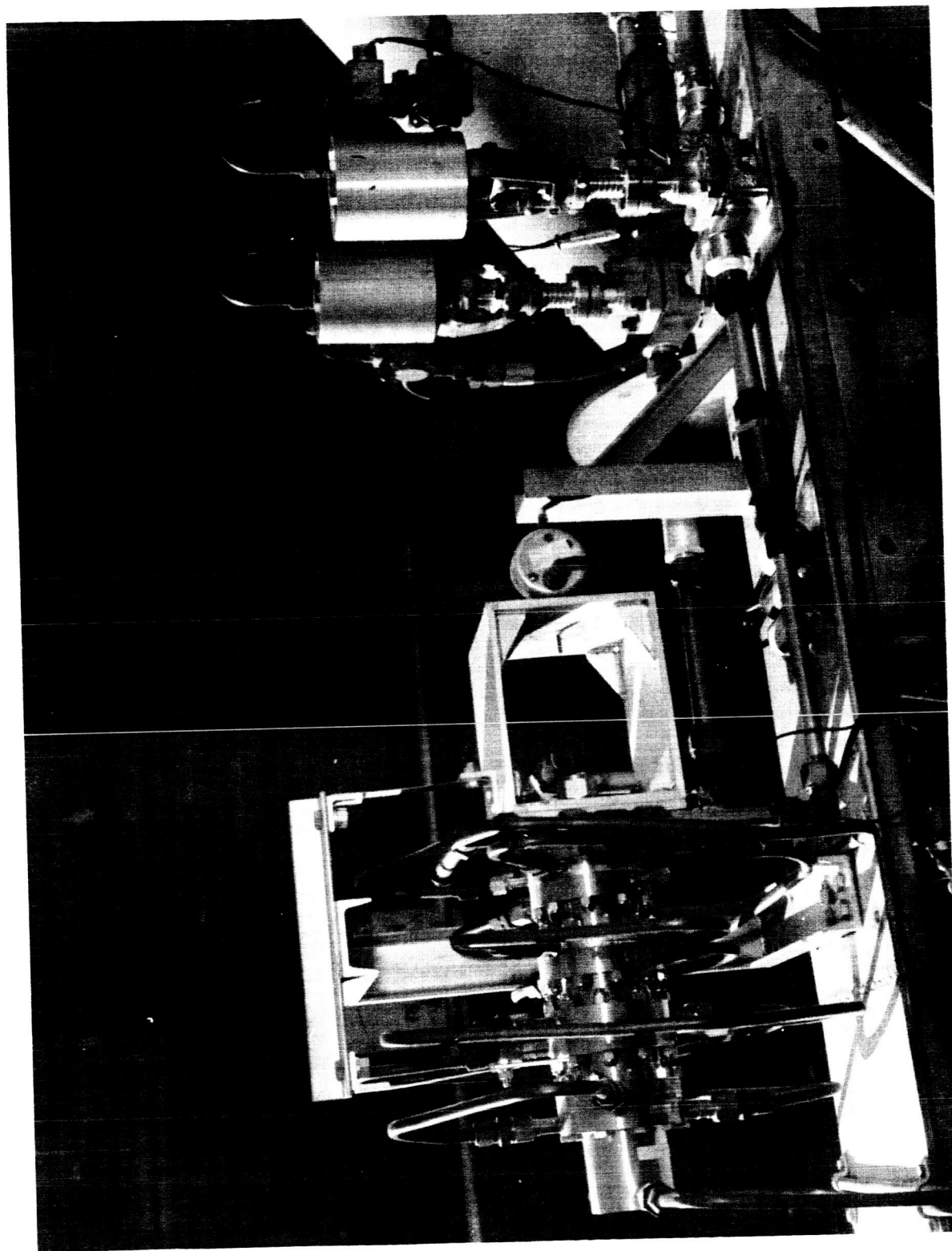


FIGURE 69. Astrosystems Engine Installed in ATL Pad B

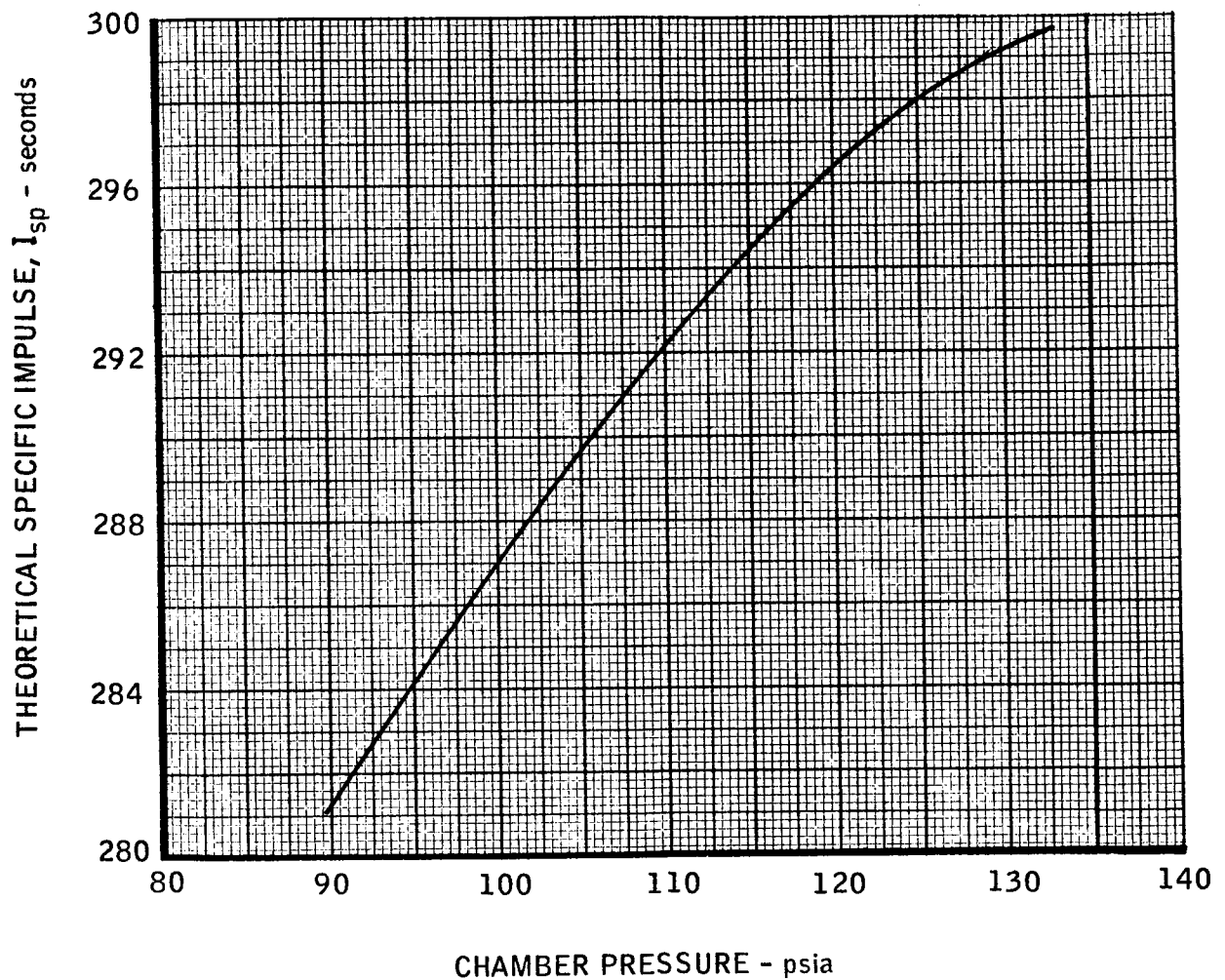
TP3149-3

UNCLASSIFIED

REPORT 6069

VARIATION OF THEORETICAL SPECIFIC IMPULSE WITH CHAMBER PRESSURE

GASEOUS O_2H_2 ; $O/F = 5.0$; $A_e/A_x = 1.5$
SHIFTING EQUILIBRIUM EXPANSION TO 14.3 psia

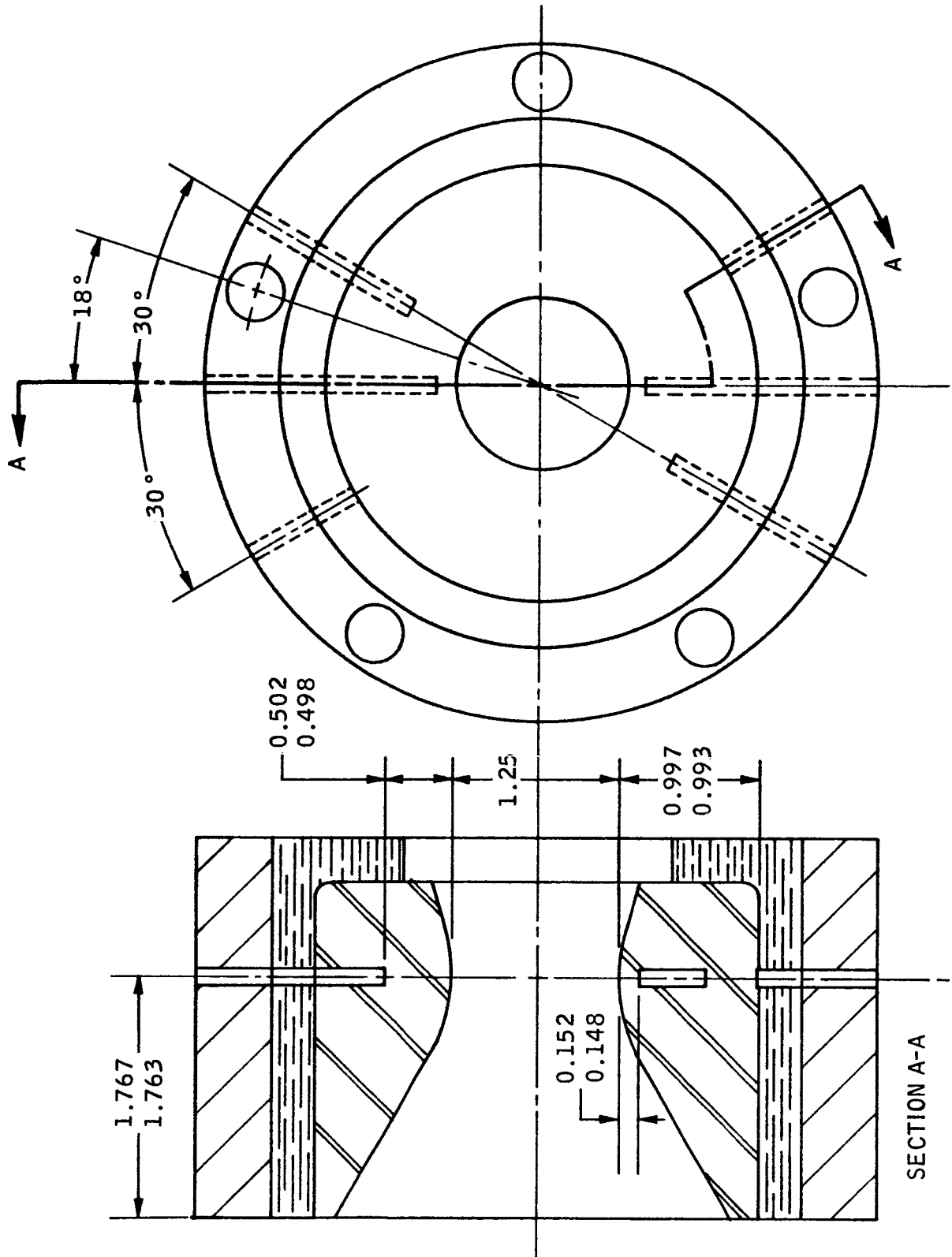


TMC A 673

UNCLASSIFIED

REPORT 6069

THERMOCOUPLE INSTALLATION IN GRAPHITE NOZZLE



TMC A 673

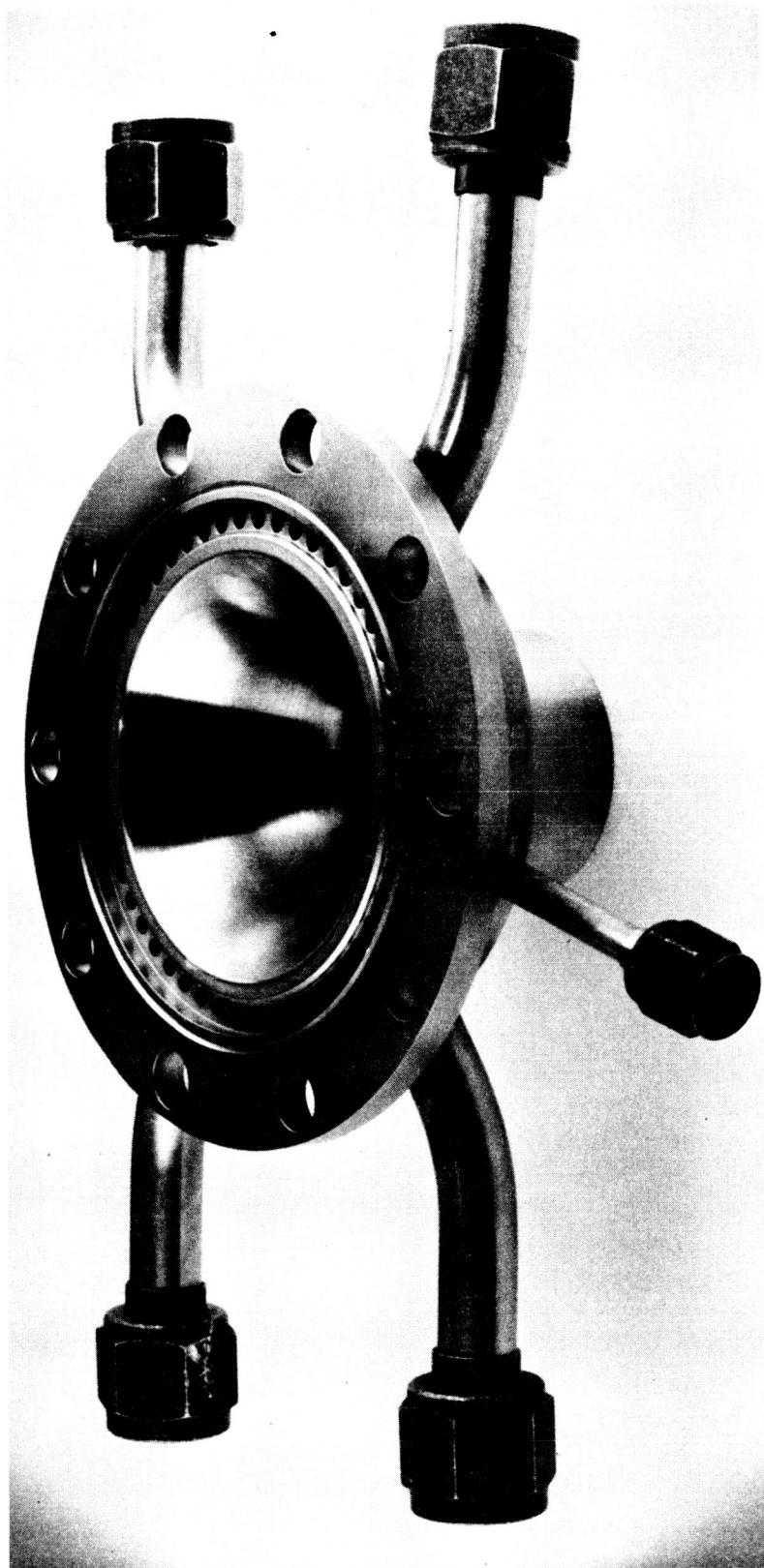


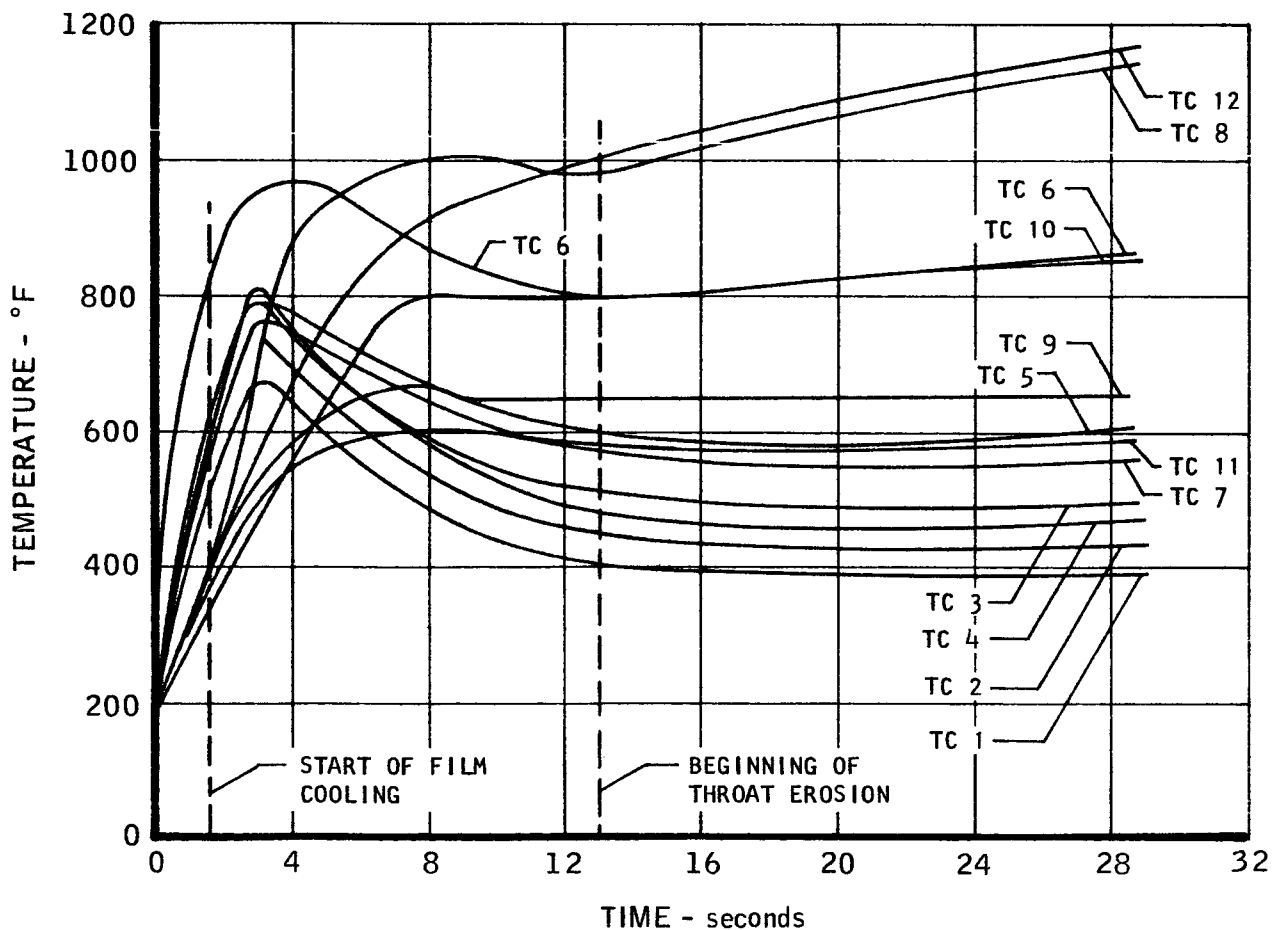
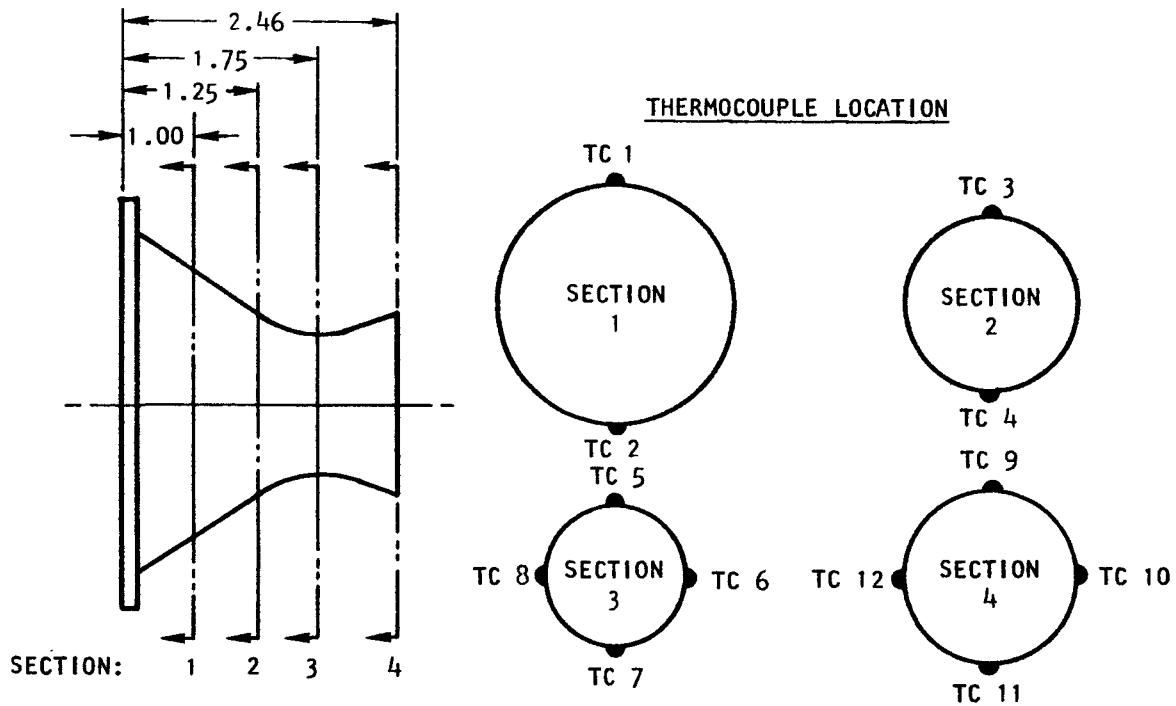
FIGURE 72. Film Cooled Slotted Steel Nozzle

T3149-8

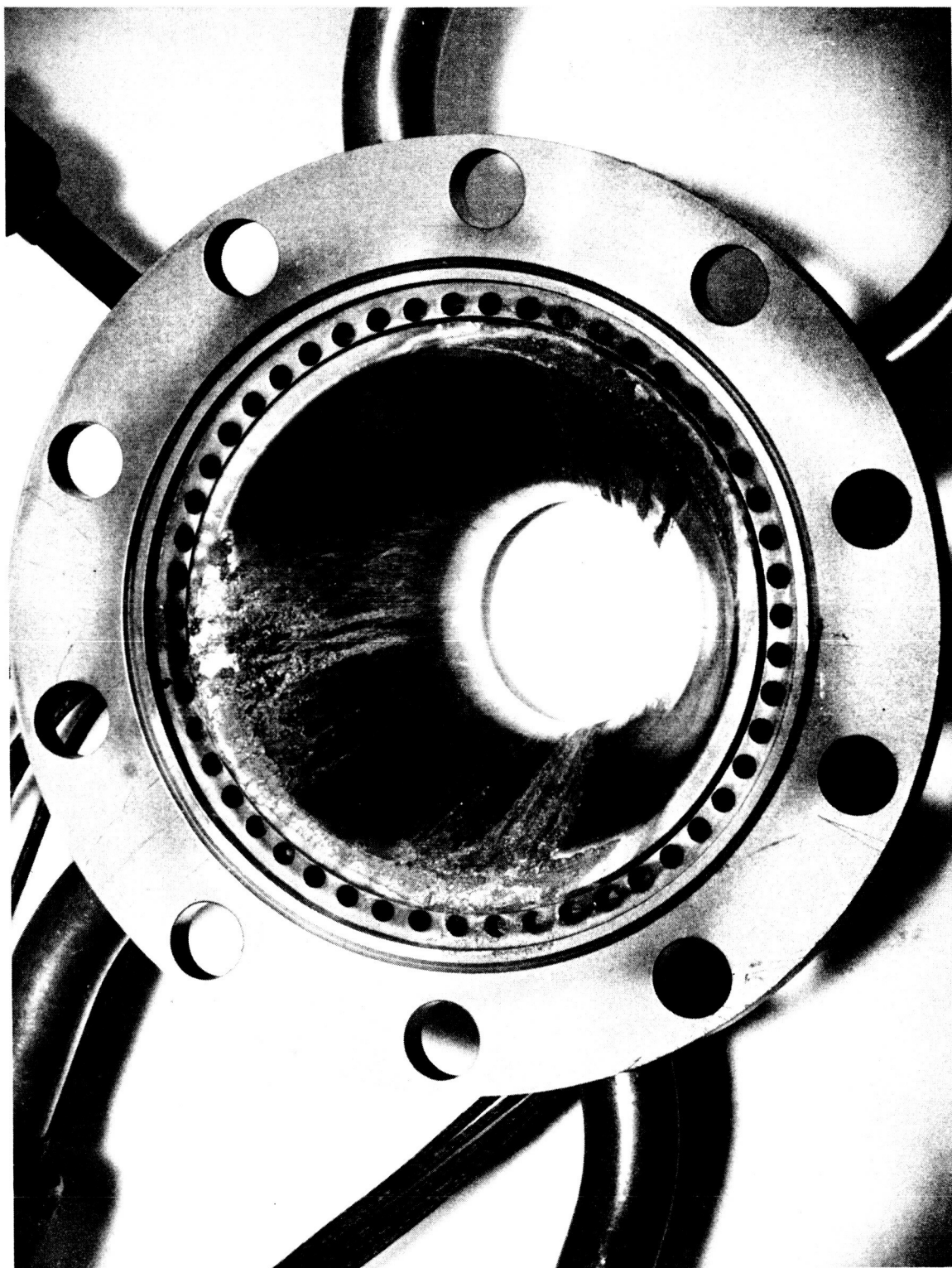
UNCLASSIFIED

REPORT 6069

VARIATION OF TEMPERATURE WITH TIME FOR SLOTTED STEEL NOZZLE WITH HYDROGEN FILM COOLING, RUN 24



TMC A 673



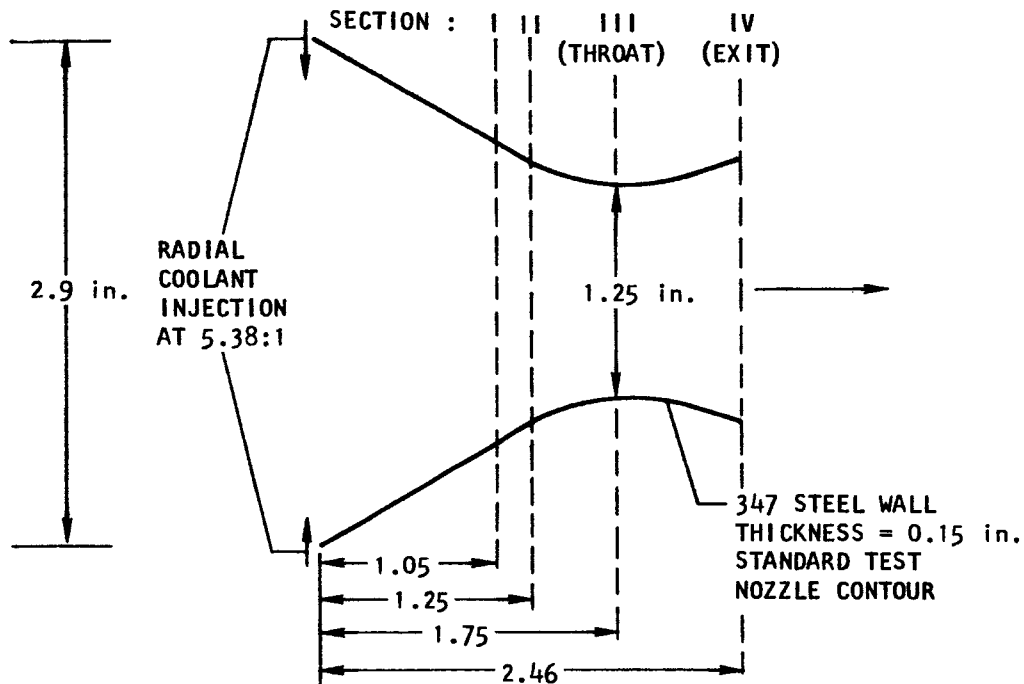
T3149-15

FIGURE 74. Burnout of Slotted Steel Nozzle with Hydrogen Film Cooling
at 0.098 pps Hydrogen Flow Rate

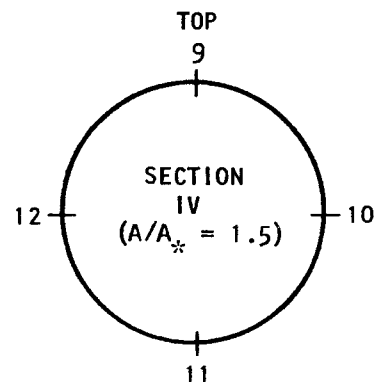
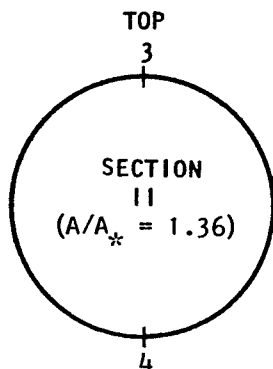
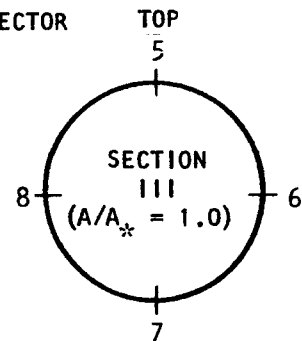
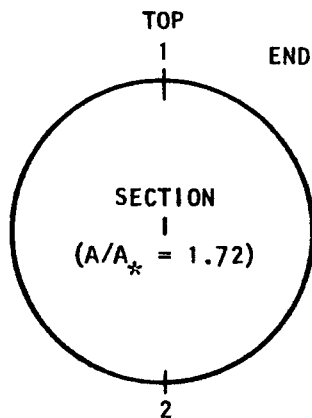
UNCLASSIFIED

REPORT 6069

THERMOCOUPLE LOCATIONS FOR RUNS 30 TO 33 COMBINED RADIATION/FILM COOLING

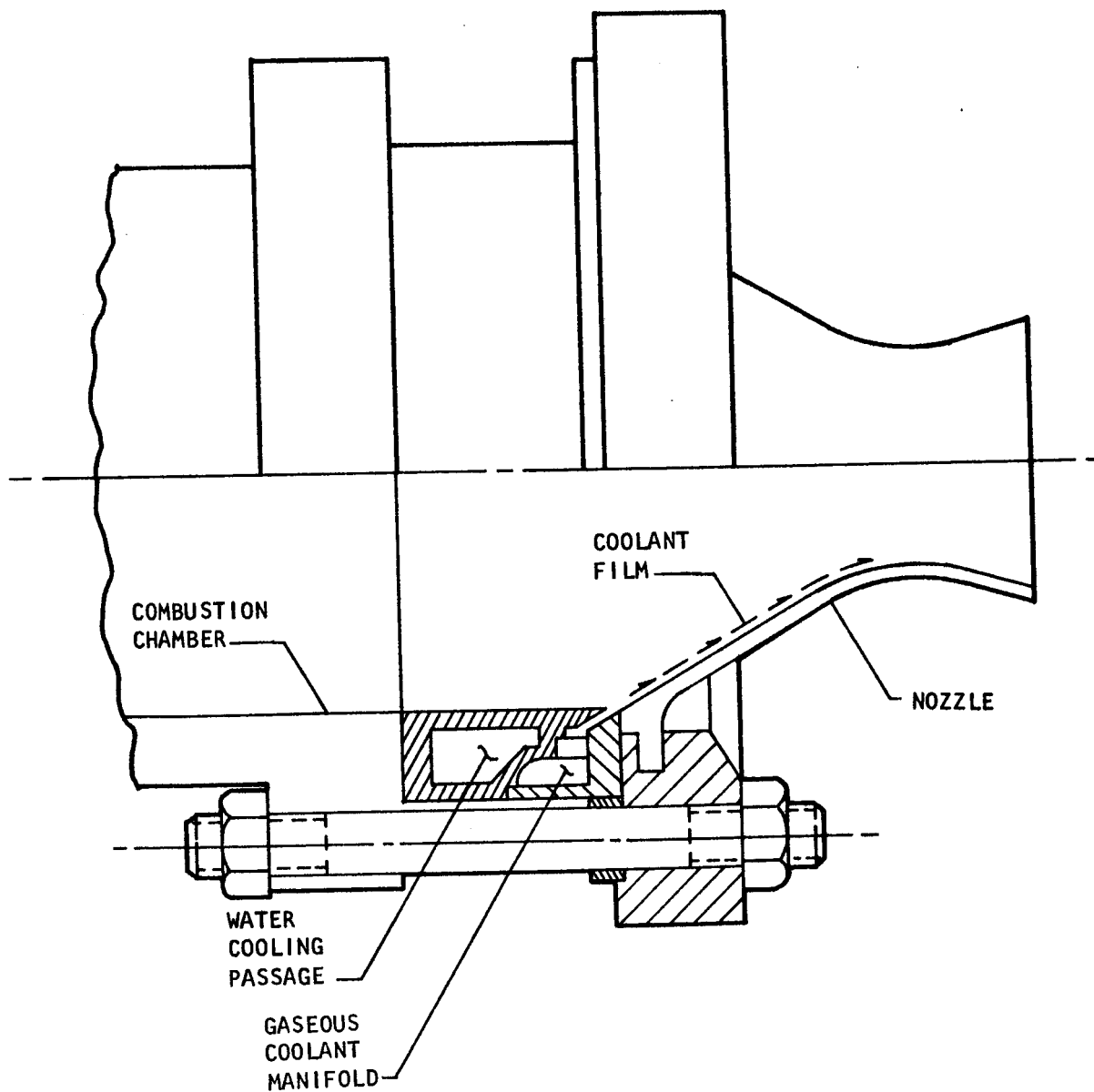


END VIEWS LOOKING TOWARD INJECTOR



TMC 673

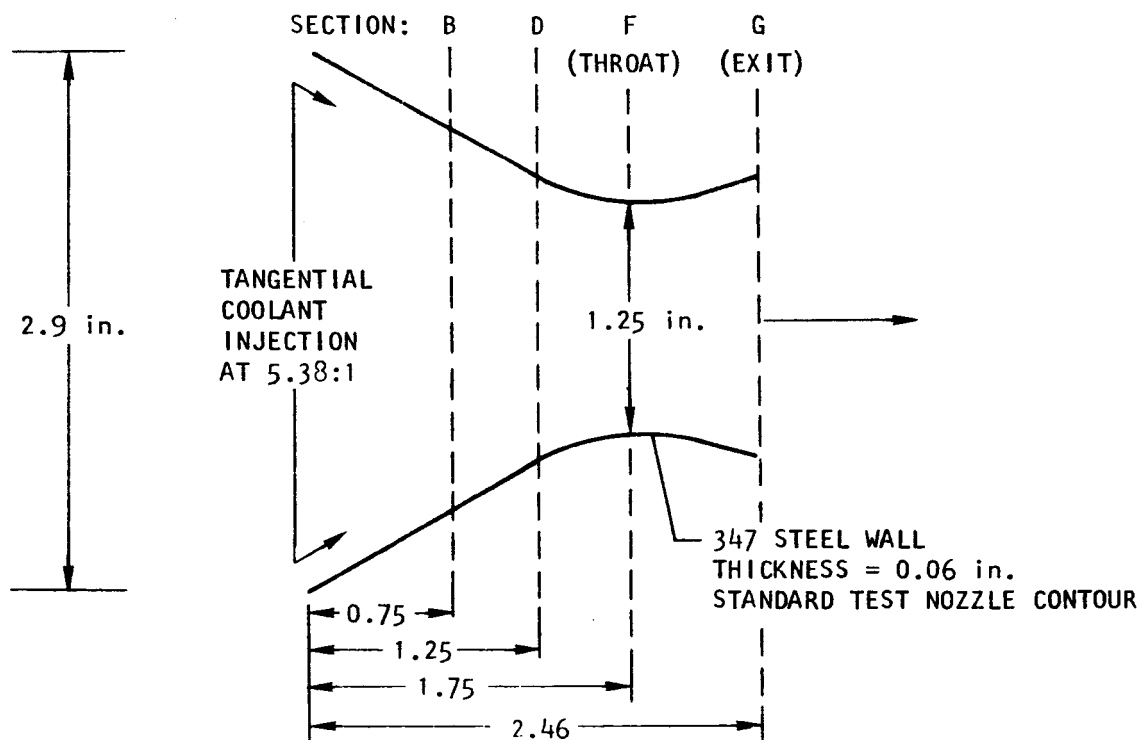
GASEOUS FILM COOLANT MANIFOLD USED FOR TANGENTIAL FILM INJECTION



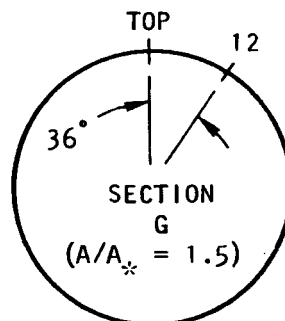
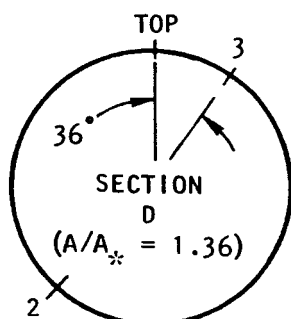
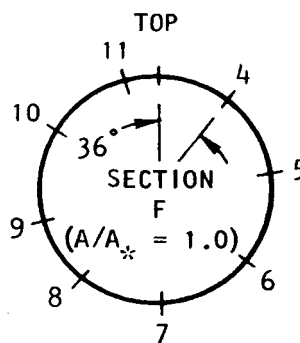
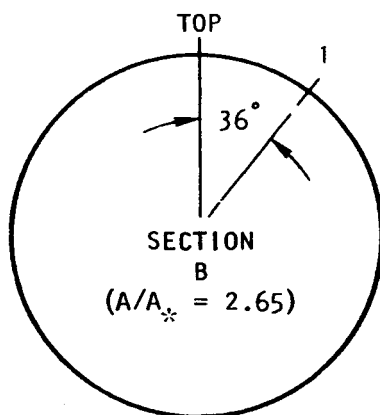
TMC A 673

UNCLASSIFIED

THERMOCOUPLE LOCATIONS FOR RUNS 43, 44, AND 58 COMBINED RADIATION/FILM COOLING

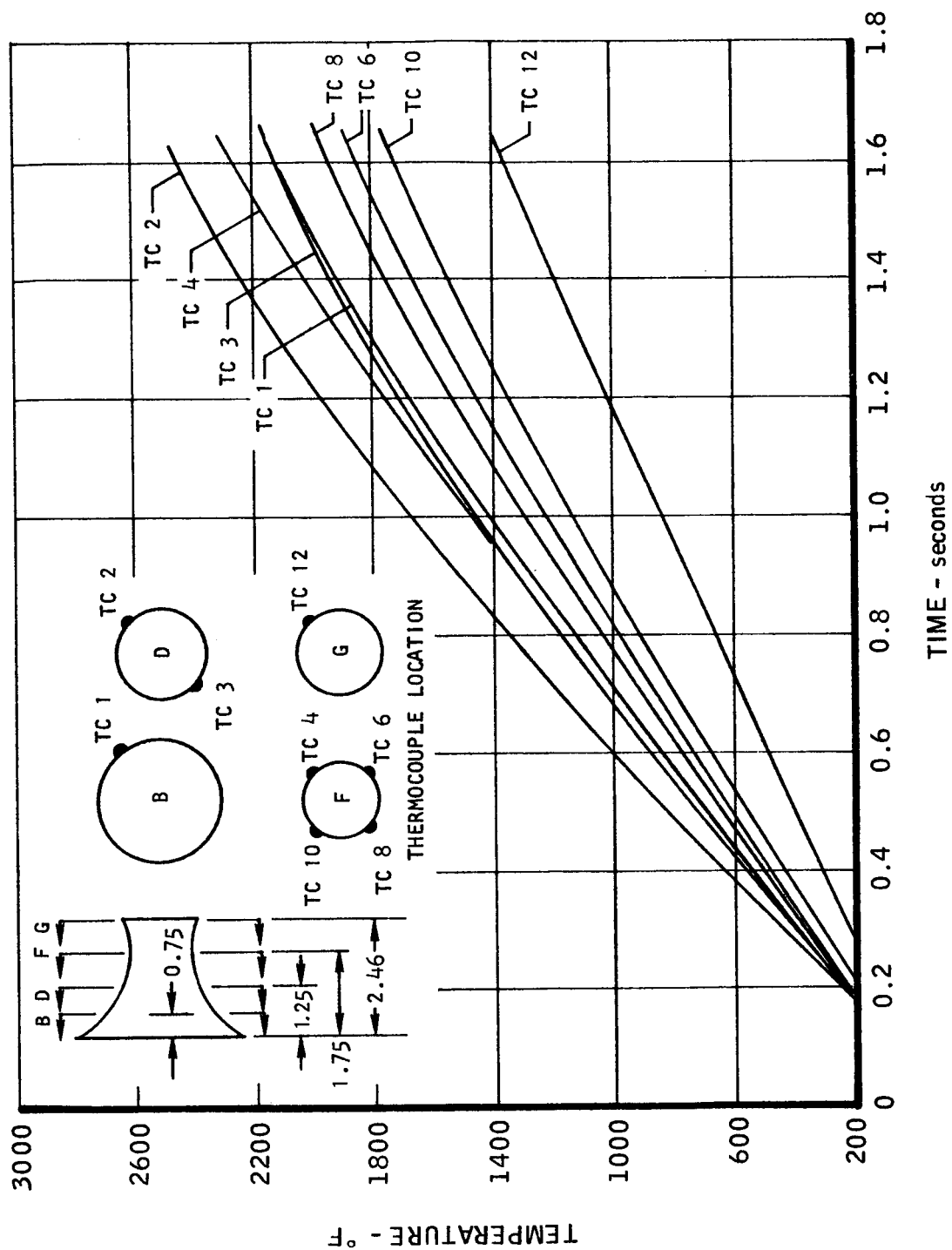


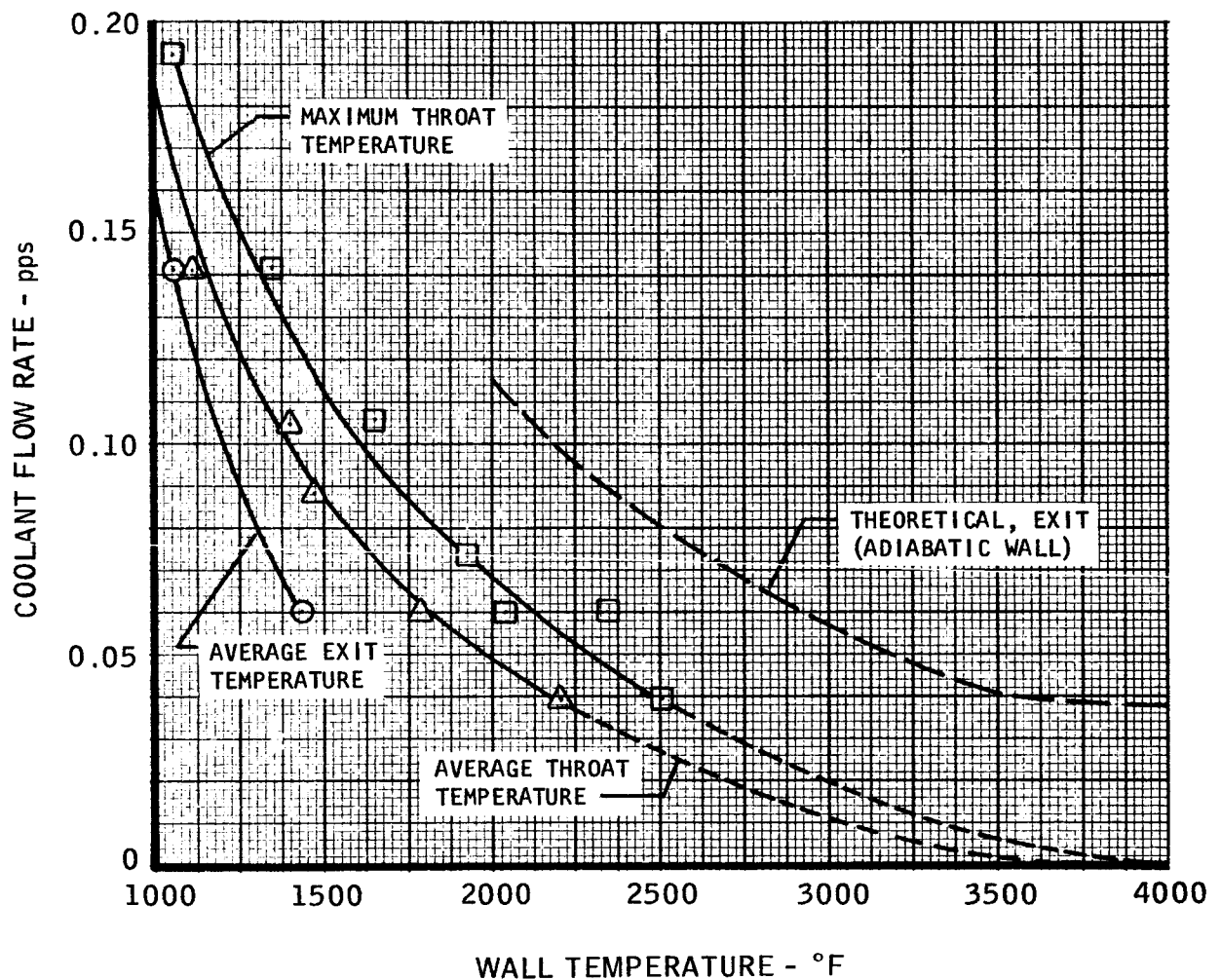
END VIEWS LOOKING TOWARD INJECTOR



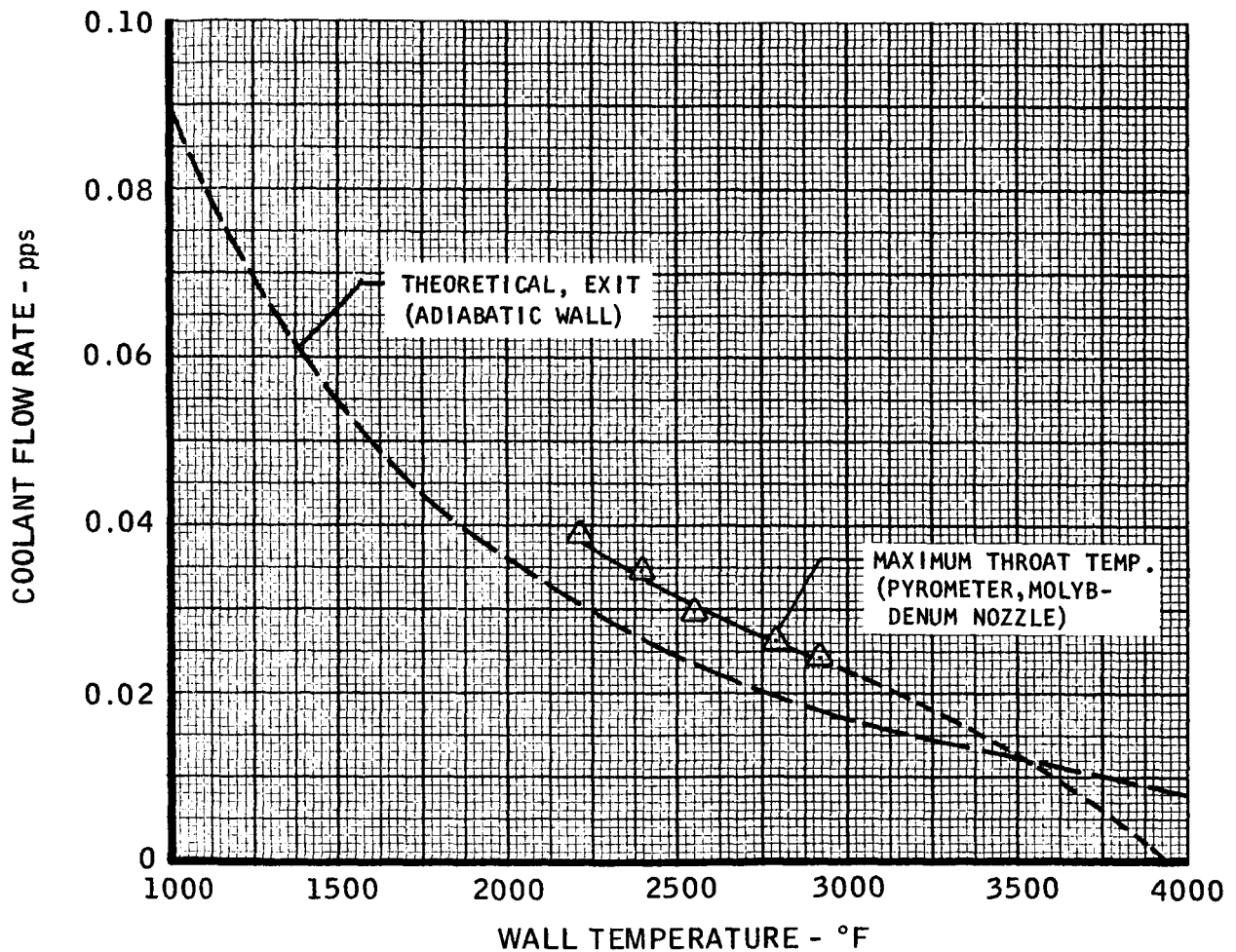
TMC A 673

VARIATION OF TEMPERATURE WITH TIME FOR UNCOOLED STEEL NOZZLE, RUN 51



VARIATION OF ANALYTICAL AND EXPERIMENTAL NOZZLE TEMPERATURES
WITH FLOW RATE
RADIATION / HELIUM FILM COOLING

TMC A 673

VARIATION OF ANALYTICAL AND EXPERIMENTAL NOZZLE TEMPERATURES
WITH FLOW RATE RADIATION / HYDROGEN FILM COOLING

TMC 673

UNCLASSIFIED

VARIATION OF SPECIFIC IMPULSE EFFICIENCY WITH FILM COOLANT FLOW RATE FOR HELIUM, HYDROGEN, AND METHANE

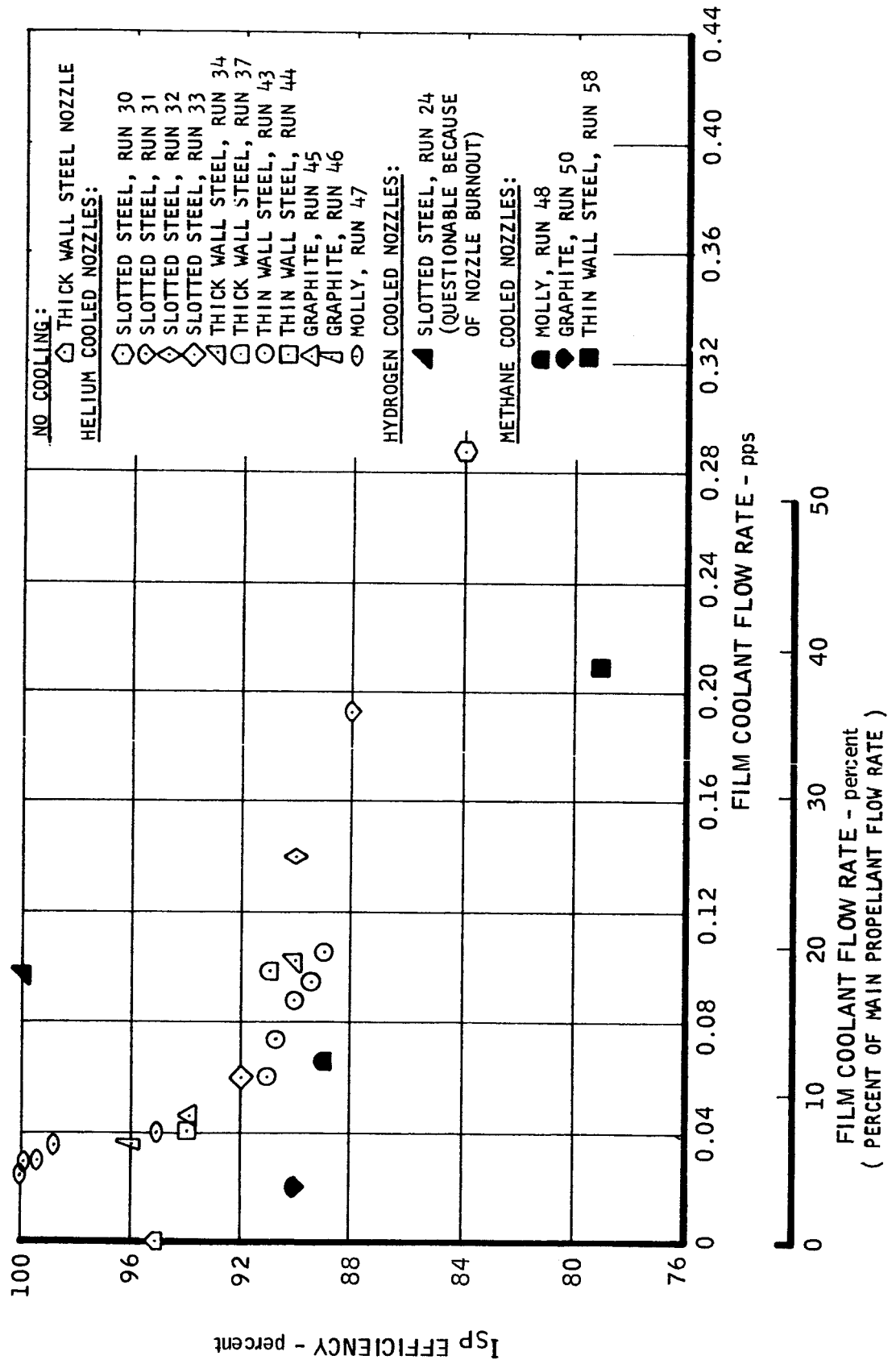
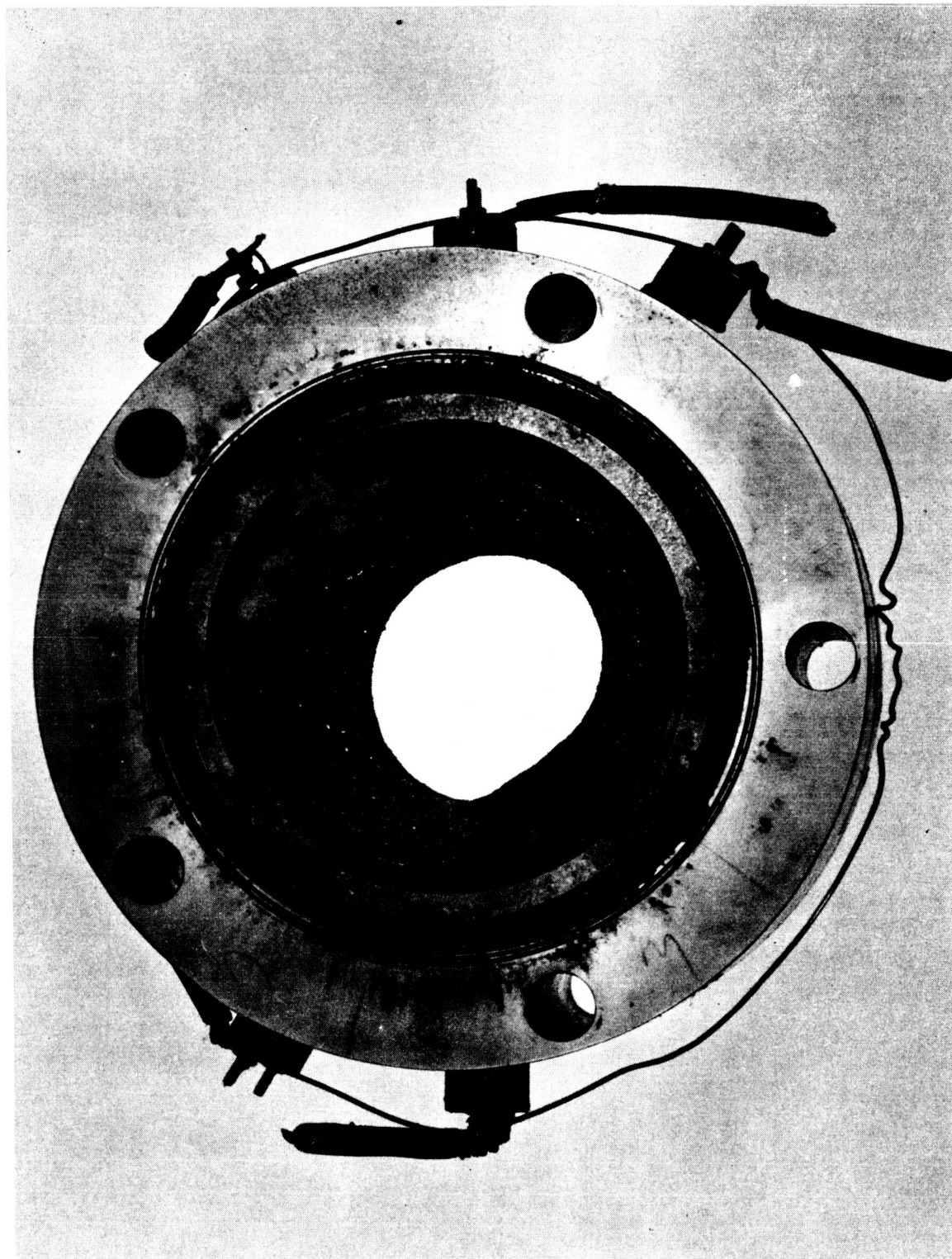


FIGURE 81

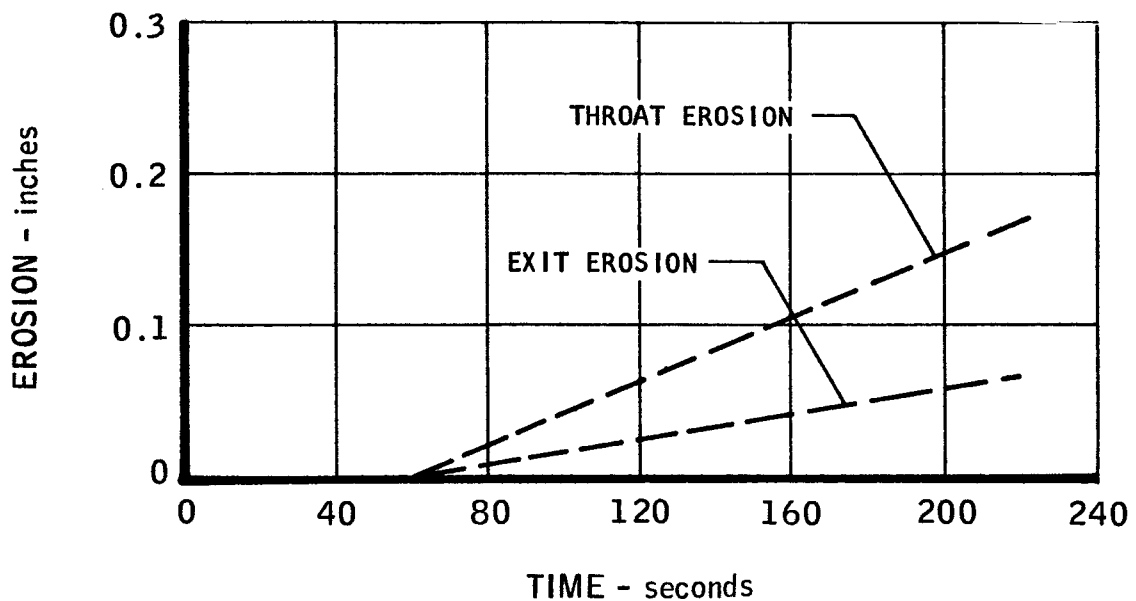
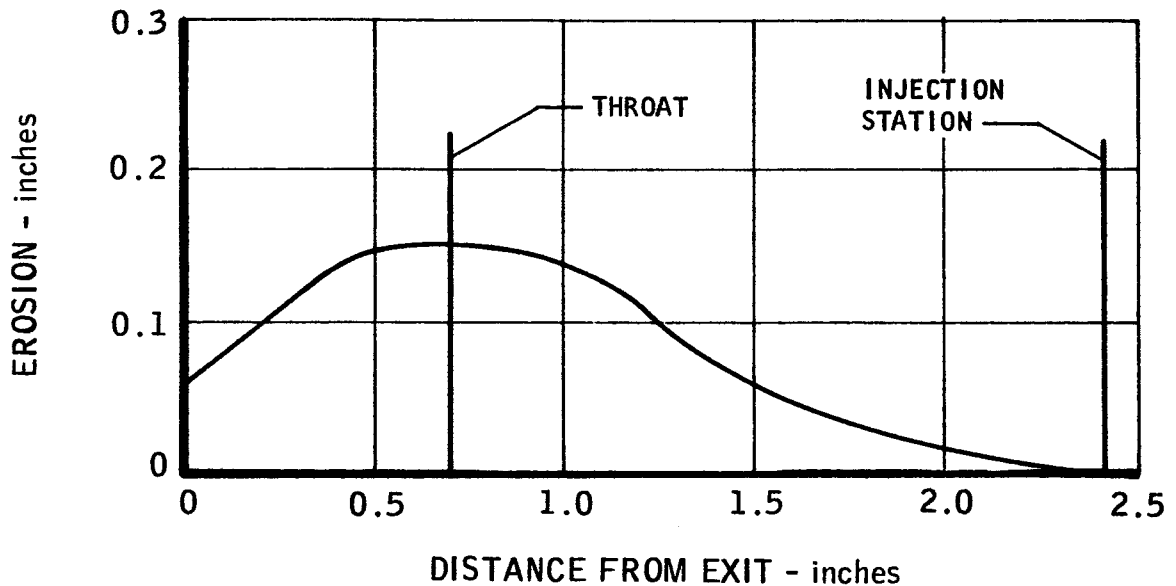


T3149-48

FIGURE 82. Graph-I-Tite G Nozzle after 203 seconds of Operation with Helium Film Cooling

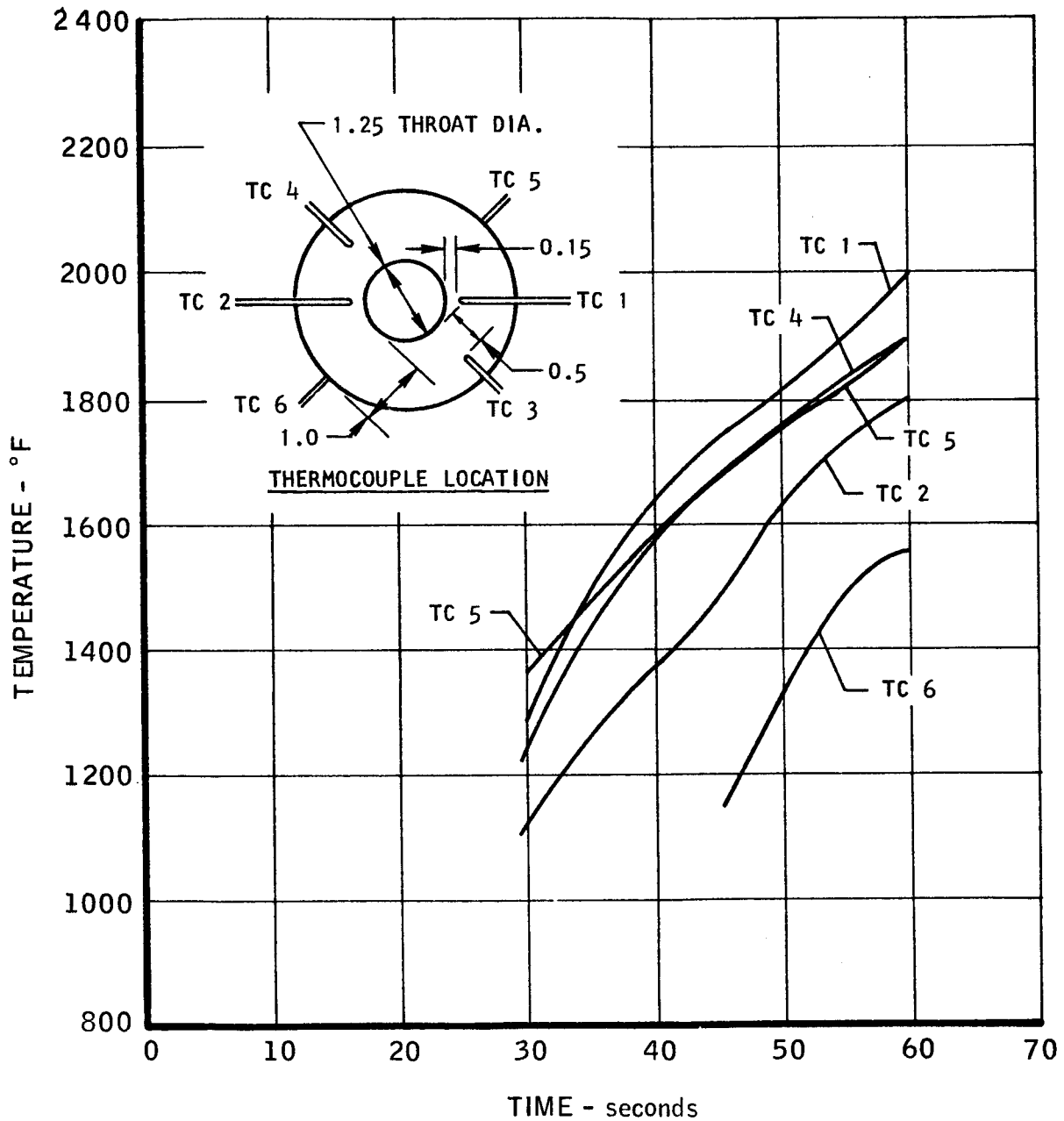
AVERAGE EROSION OF HELIUM FILM COOLED GRAPHITE NOZZLE AFTER RUNS 45 AND 46

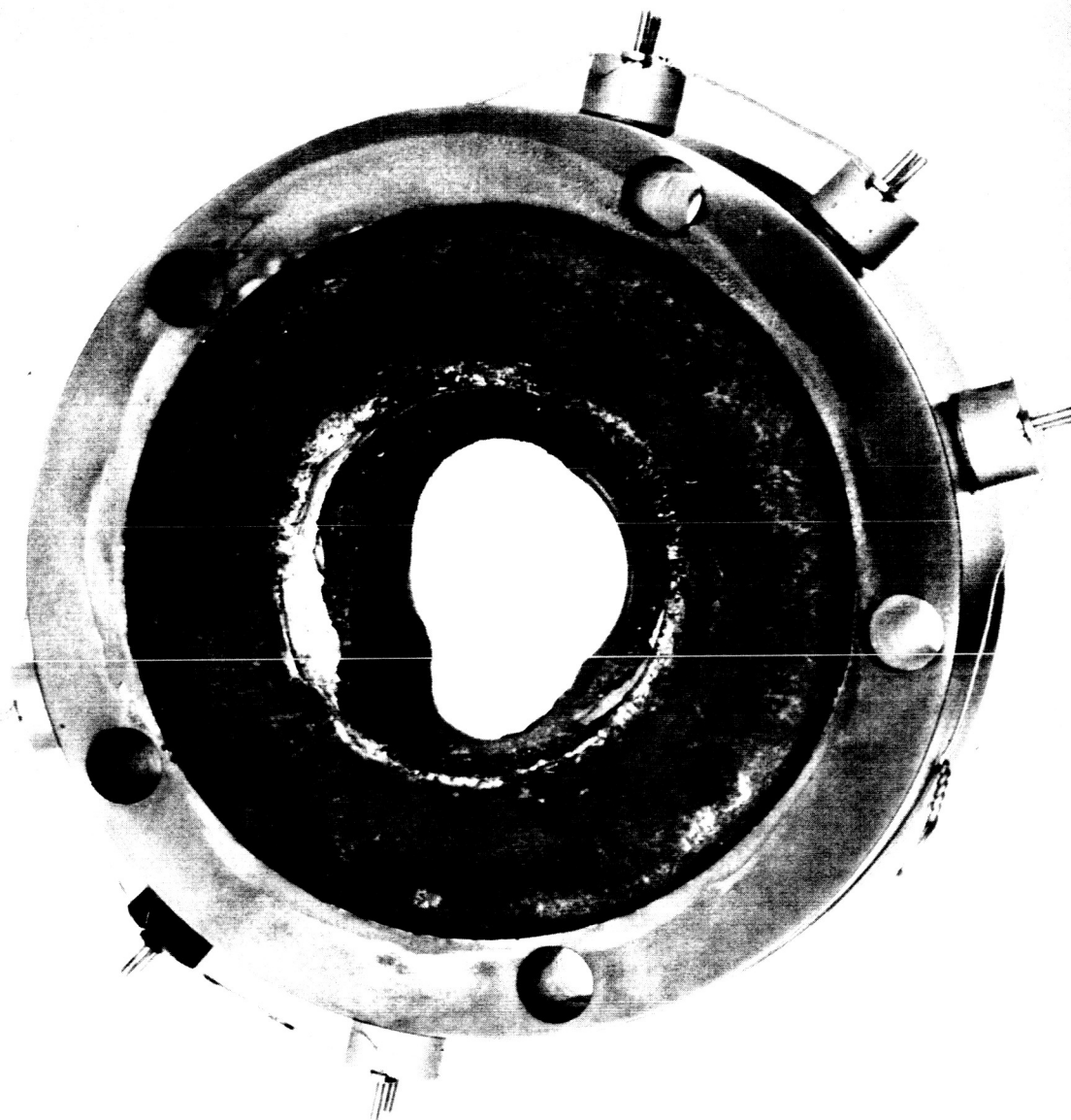
TOTAL DURATION 204 SECONDS



UNCLASSIFIED

VARIATION OF TEMPERATURE WITH TIME FOR HELIUM FILM COOLED GRAPH-ITITE G NOZZLE, RUN 45





T3149-59

FIGURE 85. Graph-I-Tite G Nozzle after 240 seconds of Operation with Methane Film Cooling

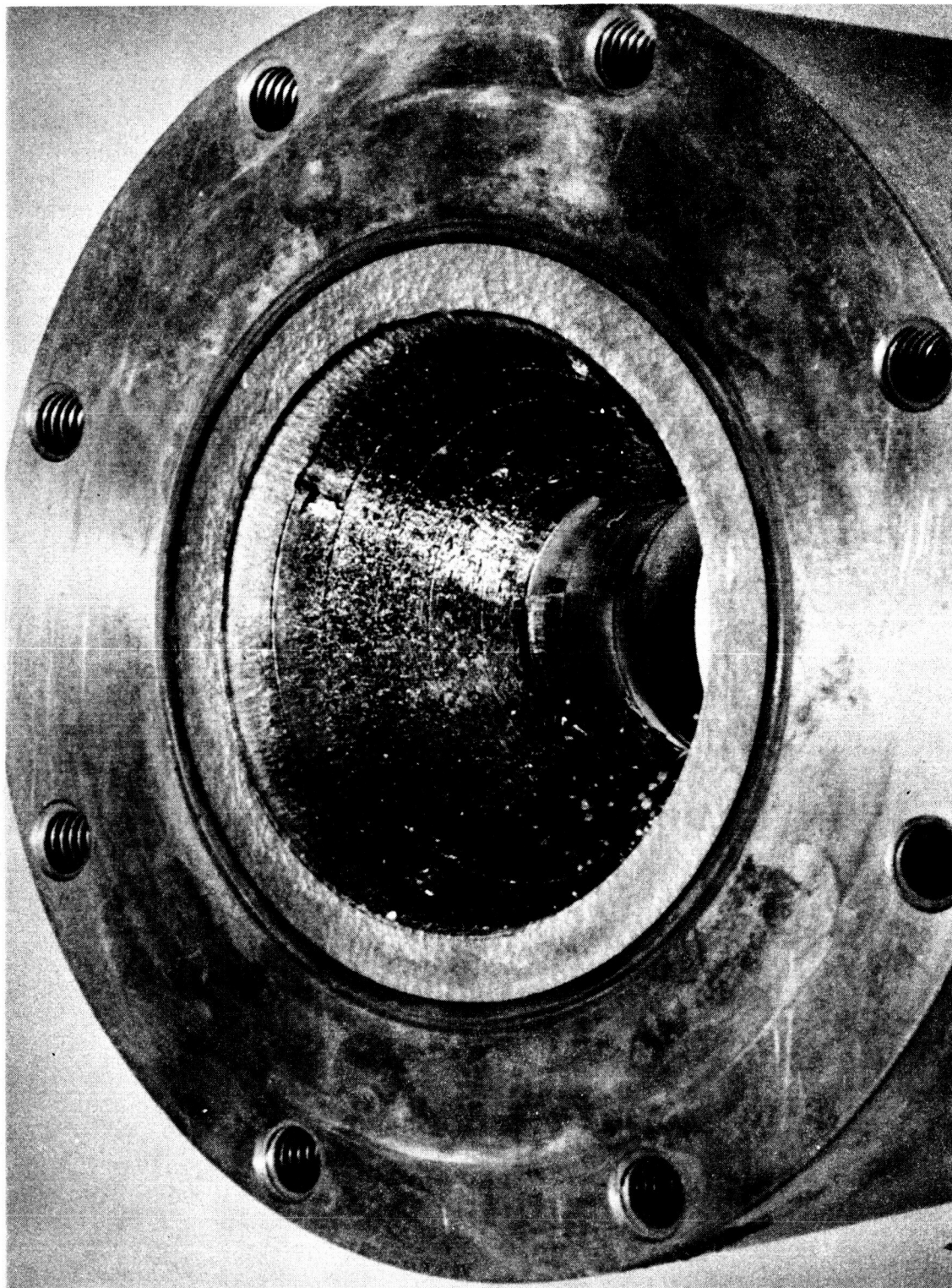
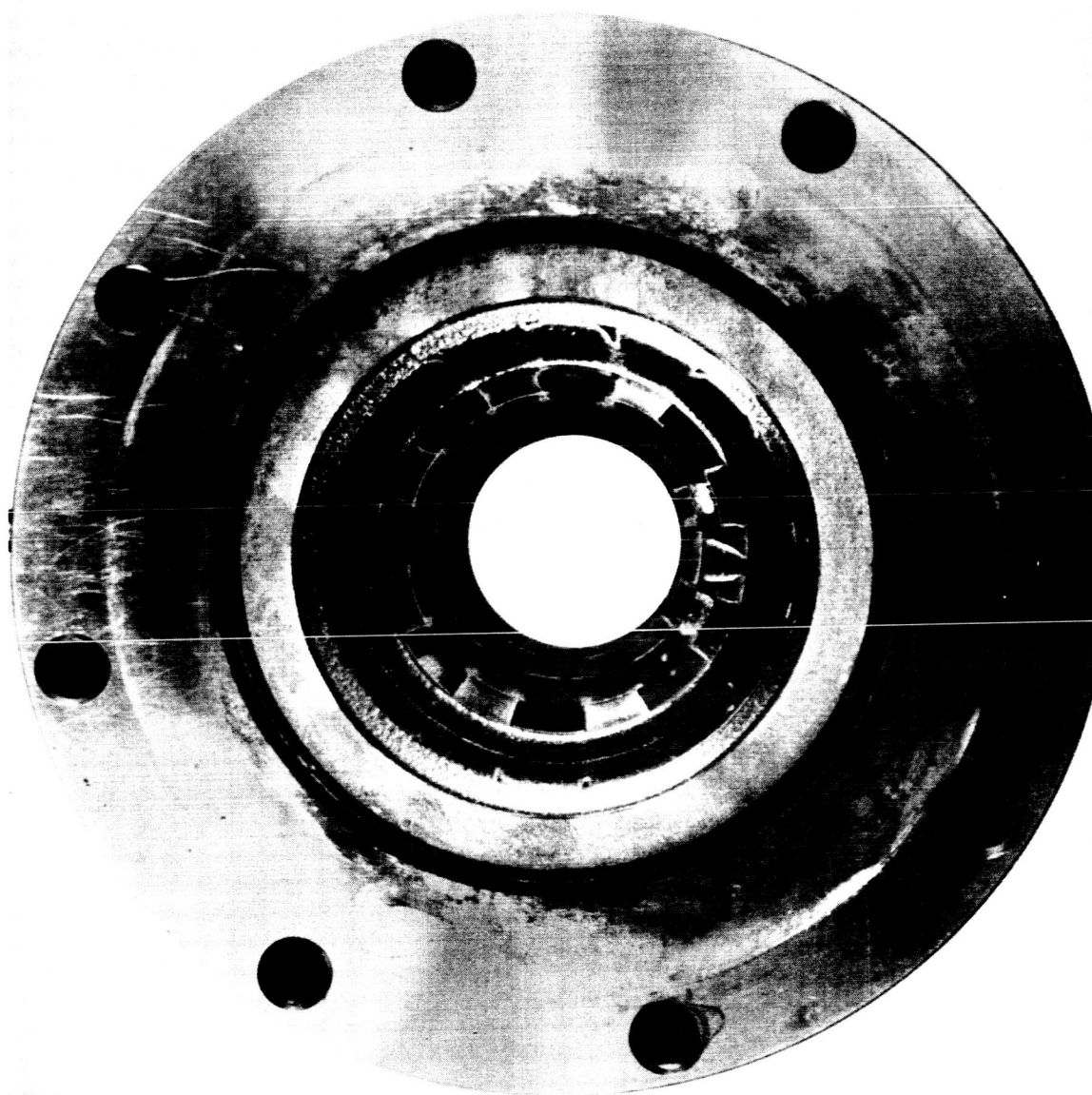


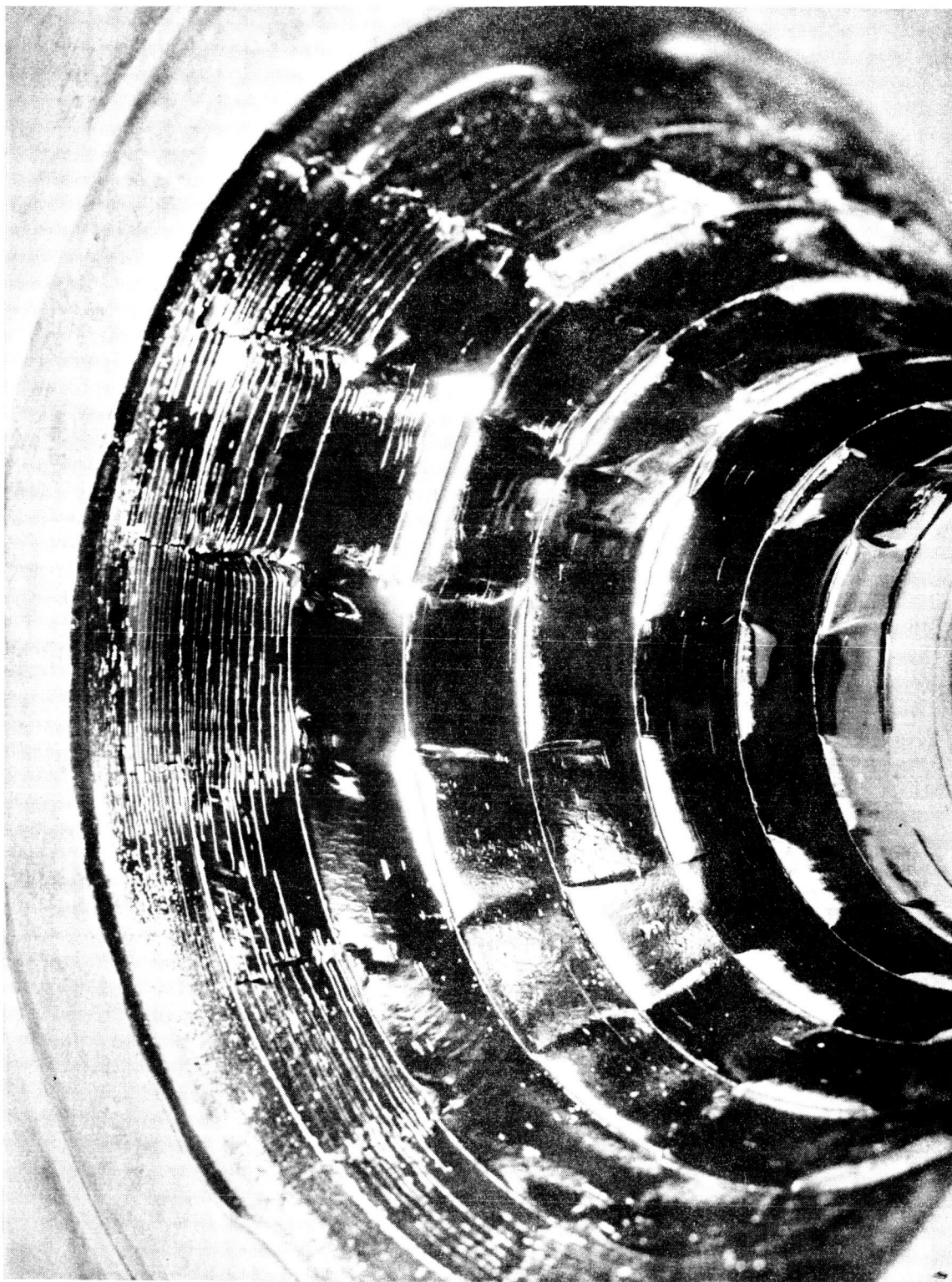
FIGURE 86. 180° Single Slot Pyrolytic Graphite Nozzle after 228 seconds of Operation with Methane Film Cooling

T3149-36



T3149-55

FIGURE 87. Multislot Pyrolytic Graphite Nozzle after 180 seconds of Operation with Methane Film Cooling



T3149-62

FIGURE 88. Multislotted Pyrolytic Graphite Nozzle after 247 seconds of Operation
with Carbon Monoxide Cooling

APPENDIX A

SUMMARY OF NOMENCLATURE

Symbol	Description	Units
$A_{1, 2, 3}$	Constants defined by Equations (10), (11), (12)	
$c_{1, 2, 3}$	Constants defined by Equations (4), (5), (6)	
c_{p_i}	Specific heat of i^{th} species	
c_p	Specific heat	
\bar{c}_p	Average specific heat	
C_m	Mass transfer multiple	
D_*	Throat diameter	
$E_{1, 2, 3}$	Activation energies defined by Equations (4), (5), (6)	Btu/lb-mole
f	Friction factor	
F	Bulk convection rate defined by Equation (13d)	lb-mole/in ² -sec
G	Mass flow rate	
h	Convective heat transfer coefficient, corrected for mass transfer effect	Btu/in ² -sec-°F
h_g	Uncorrected convective heat transfer coefficient	Btu/in ² -sec-°F
$\Delta H_{1, 2, 3}$	Heat of reaction of reactions 1, 2, 3	
k	Thermal conductivity	
k	Mass transfer coefficient	lb-mole/in ² -sec
\dot{k}	Mass transfer coefficient corrected for mass transfer effect	lb-mole/in ² -sec
$K_{e_{1, 2, 3}}$	Equilibrium constants defined by Equations (7), (8), (9)	
L	Efficiency factor for temperature rise of transpiration coolant from inlet to wall temperature	
L^*	Characteristic length	inches
\bar{M}	Molecular weight of stream \div molecular weight at wall	

APPENDIX A (Continued)

Symbol	Description	Units
N_i	Mass transfer rate of i^{th} species	lb-mole/in ² -sec
P	Pressure	atms
P_i	Partial pressure of i^{th} species	atms
Q_k	Conduction into wall	Btu/in ² -sec
$r_{1, 2, 3}$	Reaction rates of reactions 1, 2, 3	lb-mole/in ² -sec
r_e	Outside radius	
r_i	Inside radius	
R	Universal gas constant, 1.987	Btu/lb-mole-°R
Re	Radius ratio, r_e/r_i	
St_g	Stanton Number	
t	Time	
T	Temperature	°R
V	Combustion gas velocity	
x_i	Mole fraction of i^{th} species	
\dot{y}	Erosion rate	mils/sec
Z	Mass flow rate	lb/sec
α	Thermal diffusivity	
θ	Mass transfer correction factor defined by Equation (14)	
μ	Viscosity	
ρ	Density of graphite wall	
ρ	Density of combustion gas	
τ	Shear stress	
ϕ	Mass transfer correction factor defined in Equation (16)	

APPENDIX B

REACTION PHENOMENA AND KINETICS OF SOLID-GAS REACTIONS

B-I. SOLID GAS REACTIONS

A. General Discussion

When a gas and solid react, either gaseous or solid products (or both) are formed. Reactions involving solid products have been ignored in this first analytical treatment although it may be necessary to include them later. Where the products are gaseous, several gross steps are involved in the overall chemical attack:

1. Transfer of the reactants to the surface
2. Reaction at the surface
3. Transfer of the products from the surface
4. Transfer of the energy involved in the reaction to or from the surface

Each of these gross steps represents a resistance to the erosion, and under some conditions may be much slower than the other steps, thereby becoming the rate limiting step of the overall chemical erosion process. Furthermore, the overall reaction may possibly be described by a number of different models such as the following:

Model I - The solid sublimates and reacts in the vapor phase. Either the sublimation or the vapor reaction could be the rate limiting step.

Model II - A reactant molecule collides with an active site on the solid surface forming a chemisorbed product which is then desorbed. Either the impact (collision) step or the desorption step could be rate limiting.

Model III - The reacting gas is chemisorbed on the surface and then reacts with an adjacent site, or sites, to form chemisorbed products which are then desorbed. At least one site for each molecule of reactants and products will be involved. Any of the steps mentioned (i.e., chemisorption, surface reaction, or desorption) might be rate limiting.

APPENDIX B (Continued)

The following definitions are useful in understanding the above descriptions of the reaction models:

1. Adsorption - Attachment of molecules of a fluid to a solid surface

- a. Physical Adsorption

Weak forces between solid surface molecules and fluid molecules, similar to condensation. Amount adsorbed decreases rapidly with increased temperature.

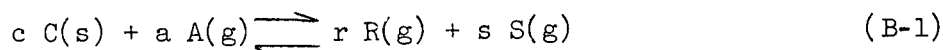
- b. Chemisorption

Strong forces similar to valence bonds between adsorbed fluid molecules and solid surface molecules. More important at higher temperatures than physical adsorption.

2. Desorption - Separation of molecules of a fluid from a solid surface involving breaking of adsorption bonds.

In addition, if a gaseous reactant is polyatomic, it may decompose in the gaseous phase and each of its decomposition products may react with the solid by one of the models just described. Thus, in any single system, chemical erosion may take place simultaneously by more than one model. Fortunately, one model is often dominant and an approximate solution can be obtained by considering a single step of that model as rate controlling.

If the reaction can be characterized by some limiting step in the model, a much simpler expression can be written for the reaction rate. Take for example the general equation



Rate expressions developed for this general reaction can be readily modified for reactions with two like product molecules or only one product molecule. Rate expressions for the above reaction resulting from several of the abovementioned models are developed below in the manner of Hougen and Watson (Reference 8), assuming that specie C is solid and species A, R and S are gaseous.

APPENDIX B (Continued)

B. Model I -- Sublimation Mechanism

1. Rate Limited by Homogeneous Reaction Step

The sublimation mechanism is possible even though the vapor pressure of the solid is very low. If the homogeneous (gas phase) reaction is the slowest step and mass transfer effects are not important (i.e., very fast), the overall reaction rate will be controlled by the rate of sublimation which is necessary to keep the gas saturated with the vapor of the solid wall. Therefore, the overall reaction rate will be proportional to the volume of gas flow per unit area of solid and the vapor pressure of the solid. Thus

$$r = C_i \bar{y}_s \frac{V}{A_s} = C_i \frac{(vp)_s}{P_T} \frac{V}{A_s} \quad (B-2)$$

Where

r = Reaction rate, moles of solid per unit area per unit time

C_i = Constants, where $i = 1, 2, 3, 4, \dots, n$

\bar{y}_s = Average mole fraction of sublimed solid in gas phase

V = Volumetric flow rate, unit volume per unit time

A_s = Area of solid

P_T = Total pressure

$(vp)_s$ = Vapor pressure of solid at temperature of solid surface

If the vapor pressure is found by the Clausius-Clapeyron equation,

$$(vp)_s = C_2 e^{\left(\frac{-\Delta H_{sub}}{RT_w} \right)} \quad (B-3)$$

the reaction rate can be written as

$$r = C_3 e^{\left(\frac{-\Delta H_{sub}}{RT_w} \right)} \frac{V}{P_T A_s} \quad (B-4)$$

APPENDIX B (Continued)

Where

ΔH_{sub} = Molal heat of sublimation

T_w = Absolute temperature of the surface

R = Universal gas constant

Important observations about this equation are that the rate of total mass depletion of a solid is independent of its area and is directly proportional to the volumetric flow rate. The same interpretation expressed differently is that the erosion rate in depth per unit time is (for a given volume of gas) inversely proportional to the exposed area.

2. Rate Limited by Sublimation Step

If the rate of the sublimation step is controlling and mass transfer rates are fast, thermochemical equilibrium between the sublimed solid and the combustion gas may be assumed in the gas phase. The rate of the forward reaction is then expressed as

$$r = k_{\text{sc}} - k'_{\text{sc}} a_w(C) = k_{\text{sc}} - k'_{\text{sc}} \frac{a_w(R) \cdot a_w(S)}{K_g a_w(A)} \quad (\text{B-5})$$

Where

$k_{\text{sc}}, k'_{\text{sc}}$ = Velocity constants for sublimation and condensation, respectively, of the solid (C(s) in Equation (B-1))

$a_w(A), a_w(R)$ = Activities in the gas phase at the wall (interface) of components A, R, etc.

K_g = Gas-phase-reaction equilibrium constant

$$K_g = \frac{a_w(R) \cdot a_w(S)}{a_w(C) \cdot a_w(A)} \quad (\text{B-6})$$

APPENDIX B (Continued)

In an ideal or near ideal system where the activities can be represented by the partial pressures, $P_w(A)$, $P_w(R)$, etc., of the gaseous components at the wall (interface), then

$$r = k_{sc} - k'_{sc} \frac{P_w(R) \cdot P_w(S)}{K_g P_w(A)} \quad (B-7)$$

When equilibrium between the solid and gas exists, $r = 0$, and $a_w(C) = (vp)_s = k_{sc}/k'_{sc}$ (for ideal gas). Thus

$$r = k_{sc} \left[1 - \frac{P_w(R) \cdot P_w(S)}{K_g P_w(A) \cdot (vp)_s} \right]$$

$$r = C_4 e^{-\frac{\Delta H_{sub}^\ddagger}{RT_w}} \left[1 - \frac{P_w(R) \cdot P_w(S)}{K_g P_w(A) \cdot (vp)_s} \right] \quad (B-8)$$

Where

ΔH_{sub}^\ddagger = Molal activation energy of sublimation

An important observation of this mechanism is that it indicates a zero order initial reaction (i.e., no products present) with respect to the gaseous reactant. That is, the initial reaction rate is independent of the reactant partial pressures.

C. Model II -- Impact Mechanism

If the reaction takes place by collision between gaseous reactant molecules and active sites on the solid surface, the forward reaction rate will be proportional to the activity (or partial pressure for ideal systems) of the reactant and the number of vacant (i.e., available) reactive sites on the surface. The reverse reaction will be proportional to the concentrations of adsorbed product molecules on the surface, and the net reaction rate can be written as

UNCLASSIFIED

REPORT 6069

APPENDIX B (Continued)

$$r = k P_w(A) \cdot c_V - k' c_R c_S \quad (B-9)$$

Where

c_R, c_S = Concentration of adsorbed R, S molecules per unit area

k, k' = Velocity constants of forward and reverse reactions, respectively

c_V = Concentration of vacant reactive sites per unit area

At equilibrium, $r = 0$, and

$$\frac{k}{k'} = \frac{c_R c_S}{P_w(A) \cdot c_V} = K'_e \quad (B-10)$$

So that

$$r = k \left[P_w(A) \cdot c_V - \frac{c_R c_S}{K'_e} \right] \quad (B-11)$$

where K'_e = Surface reaction equilibrium constant.

1. Rate Limited by Impact-Surface Reaction

If the impact-surface reaction is the limiting step, the concentrations of R and S on the surface can be approximated by adsorption-equilibrium values between the available sites on the surface and the gas at the surface, or

$$c_R = K_{aR} P_w(R) \cdot c_V \quad (B-12)$$

and

$$c_S = K_{aS} P_w(S) c_V \quad (B-13)$$

UNCLASSIFIED

UNCLASSIFIED

REPORT 6069

APPENDIX B (Continued)

Where K_{aR} , K_{aS} = Adsorption equilibrium constants for R and S, respectively.

Now

$$c_V = L - (c_R + c_S + c_I \dots) \quad (B-14)$$

Where

L = Total available sites per unit surface area

c_I = Sites occupied by inerts

Then

$$c_V = L - c_V(K_{aR} P_w(R) + K_{aS} P_w(S) + K_{aI} P_w(I) + \dots)$$

Where K_{aI} = Adsorption equilibrium constants for inerts I, and

$$c_V = \frac{L}{(1 + K_{aR} P_w(R) + K_{aS} P_w(S) + K_{aI} P_w(I) + \dots)} \quad (B-15)$$

Therefore

$$r = k \left[\frac{P_w(A) \cdot L}{(1 + K_{aR} P_w(R) + K_{aS} P_w(S) + K_{aI} P_w(I) + \dots)} - \frac{L^2 (K_{aR} K_{aS} P_w(R) \cdot P_w(S))}{K'_e (1 + K_{aR} P_w(R) + K_{aS} P_w(S) + K_{aI} P_w(I) + \dots)^2} \right]$$

Or

$$r = \frac{kL}{(1 + K_{aR} P_w(R) + K_{aS} P_w(S) + K_{aI} P_w(I) + \dots)} \left[P_w(A) - \frac{c_V K_{aR} K_{aS} P_w(R) P_w(S)}{K'_e} \right] \quad (B-16)$$

TMC A 673

UNCLASSIFIED

APPENDIX B (Continued)

Now at equilibrium, $r = 0$ and

$$\frac{K'_e}{c_V K_{aR} K_{aS}} = \frac{P_W(R) \cdot P_W(S)}{P_W(A)} = K_e \quad (B-17)$$

Where K_e = Thermodynamic chemical equilibrium constant. Therefore

$$r = \frac{kL}{(1 + K_{aR} P_W(R) + K_{aS} P_W(S) + K_{aI} P_W(I) + \dots)} \left[P_W(A) - \frac{P_W(R) \cdot P_W(S)}{K_e} \right]$$

$$r = \frac{C_5 L e^{-\frac{\Delta H^\ddagger}{RT_W}}}{(1 + K_{aR} P_W(R) + K_{aS} P_W(S) + K_{aI} P_W(I) + \dots)} \left[P_W(A) - \frac{P_W(R) \cdot P_W(S)}{K_e} \right] \quad (B-18)$$

Note that where only one molecule of A per site is involved, the reaction will be first order with respect to A. If two molecules of A reacted with each active site, the reaction would be second order with respect to A. The second order reaction is unlikely, since it implies simultaneous collision between two molecules and one site.

2. Rate Limited by Desorption Step

If the limiting step of the overall reaction is the desorption of one product, R, the rate equation becomes the rate of desorption of R, or

$$r = k'_{aR} c_R - k_{aR} P_W(R) c_V = k_{aR} \left(\frac{c_R}{K_{aR}} - P_W(R) \cdot c_V \right) \quad (B-19)$$

where

$$K_{aR} = \frac{k'_{aR}}{k_{aR}} \quad (B-20)$$

APPENDIX B (Continued)

and k_{aR} , k'_{aR} = Velocity constants for adsorption and desorption of R, respectively.

Now, c_R under these circumstances can be approximated by the surface reaction equilibrium value, or

$$c_R = \frac{K'_e c_V P_w(A)}{c_S} \quad (B-10a)$$

and

$$r = c_V k_{aR} \left[\frac{P_w(A) \cdot K'_e}{c_S K_{aR}} - P_w(R) \right] \quad (B-21)$$

At equilibrium

$$\frac{K'_e}{c_S K_{aR}} = \frac{P_w(R)}{P_w(A)} = \frac{K_e}{P_w(S)} \quad (B-22)$$

Therefore

$$r = c_V k_{aR} \left[\frac{P_w(A) \cdot K_e}{P_w(S)} - P_w(R) \right] \quad (B-23)$$

Substituting for c_V and since $k_{aR} = C_6 e^{\frac{\Delta H_{ar}^\ddagger}{RT_w}}$, from absolute reaction rate theory,

$$r = \frac{C_6 L e^{-\frac{\Delta H_{ar}^\ddagger}{RT_w}}}{(1 + K_{aR} K_e \frac{P_w(A)}{P_w(S)} + K_{aS} P_w(S) + K_{aI} P_w(I) + \dots)} \left[\frac{P_w(A) \cdot K_e}{P_w(S)} - P_w(R) \right] \quad (B-24)$$

Where ΔH_{ar}^\ddagger = Molal energy of activation for adsorption of R.

APPENDIX B (Continued)

Note that the forward reaction is first order with respect to (A) and inversely proportional to $P_w(S)$. The reverse reaction is first order with respect to $P_w(R)$.

D. Model III - Adsorption Mechanism

1. Rate Limited by Adsorption Step

When the limiting step in the overall reaction is the adsorption of A, the rate equation becomes

$$r = k_{aA} P_w(A) \cdot c_V - k'_{aA} c_A \quad (B-25)$$

At equilibrium

$$\frac{k_{aA}}{k'_{aA}} = \frac{c_A}{P_w(A) c_V} = K_{aA} \quad (B-26)$$

And

$$r = k_{aA} (P_w(A) c_V - \frac{c_A}{K_{aA}}) \quad (B-27)$$

Under the circumstances, c_A can be approximated by the equilibrium value from the surface reaction, or

$$c_A = \frac{c_S c_R}{c_V K'_e} \quad (B-28)$$

Therefore

$$r = k_{aA} (P_w(A) c_V - \frac{c_S c_R}{c_V K'_e K_{aA}}) \quad (B-29)$$

UNCLASSIFIED

REPORT 6069

APPENDIX B (Continued)

Substituting for c_R and c_S from Equations (B-12) and (B-13)

$$r = k_{aA} \left(P_w(A) c_V - \frac{c_V K_{aR} K_{aS} P_w(R) \cdot P_w(S)}{K'_e K_{aA}} \right) \quad (B-30)$$

At equilibrium

$$\frac{K_{aR} K_{aS}}{K'_e K_{aA}} = \frac{P_w(A)}{P_w(R) \cdot P_w(S)} = \frac{1}{K_e} \quad (B-31)$$

Therefore

$$r = k_{aA} c_V \left(P_w(A) - \frac{P_w(R) P_w(S)}{K_e} \right) \quad (B-32)$$

Now

$$c_V = L - (c_A + c_R + c_S + c_I + \dots) \quad (B-33)$$

Or

$$c_V = \frac{L}{\left(1 + K_{aA} \frac{P_w(R) \cdot P_w(S)}{K_e} + K_{aR} P_w(R) + K_{aS} P_w(S) + K_{aI} P_w(I) + \dots \right)} \quad (B-34)$$

Therefore

$$r = \frac{c_7 e^{\left(-\frac{\Delta H_{aA}^\ddagger}{RT_w} \right)} L \left(P_w(A) - \frac{P_w(R) \cdot P_w(S)}{K_e} \right)}{\left(1 + K_{aA} \frac{P_w(R) \cdot P_w(S)}{K_e} + K_{aR} P_w(R) + K_{aS} P_w(S) + K_{aI} P_w(I) + \dots \right)} \quad (B-35)$$

TMCA 673

UNCLASSIFIED

APPENDIX B (Continued)

2. Rate Limited by Surface Reaction Step

Development of the rate equation for an adsorption mechanism, when the surface reaction step is controlling (when the adsorbed reactant molecule reacts with the site to which it is attached) is completely analogous to the development of the rate expression for the impact mechanism, surface reaction controlling, except that the adsorption of Species A on the surface must be included in the equation for c_v , as in Equation (B-33), and in the equation for the net reaction rate, which becomes

$$r = k c_A c_v = k' c_R c_S \quad (B-36)$$

Where

$$K'_e = \frac{c_R c_S}{c_A} \quad (B-37)$$

The final rate equation becomes

$$r = \frac{C_0 L K_{aA} e^{-\frac{\Delta H^\ddagger}{RT_w}} (P_w(A) - \frac{P_w(R) \cdot P_w(S)}{K_e})}{(1 + K_{aA} P_w(A) + K_{aR} P_w(R) + K_{aS} P_w(S) + K_{aI} P_w(I) + \dots)} \quad (B-38)$$

For the case where the adsorbed reactant reacts with an adjacent vacant active site, the basic reaction rate equation becomes

$$r = k \frac{S}{L} c_A c_v - k' c_R c_S \quad (B-39)$$

Where S/L = Fraction of the total active sites which are immediately adjacent to any particular active site, S = Number of sites surrounding each individual site.

APPENDIX B (Continued)

Thus $\frac{S}{L} c_V$ represents the concentration of vacant sites adjacent to the site occupied by the reactant molecule. Now

$$K'_e = \frac{c_R c_S}{c_A c_V} \frac{L}{S} \quad (B-40)$$

And the final rate expression will become

$$r = \frac{C_9 L K_{aA} e^{-\frac{\Delta H^\ddagger}{RT_W}} \left(P_W(A) - \frac{P_W(R) \cdot P_W(S)}{K_e} \right)}{(1 + K_{aA} P_W(A) + K_{aR} P_W(R) + K_{aS} P_W(S) + K_{aI} P_W(I) + \dots)} \quad (B-41)$$

3. Rate Limited by Desorption Step

The development of the rate equation for the adsorption mechanism, product desorption controlling, is analogous to the development of the rate equation for the impact mechanism, product desorption controlling, except for accounting for the adsorption of Species A in the equation for c_V . The final equation becomes

$$r = \frac{C_{10} L K_{aA} e^{-\frac{\Delta H^\ddagger}{RT_W}} \left(\frac{P_W(A) \cdot K_e}{P_W(S)} - P_W(R) \right)}{(1 + K_{aA} P_W(A) + K_{aR} \frac{K_e P_W(A)}{P_W(S)} + K_{aS} P_W(S) + K_{aI} P_W(I) + \dots)} \quad (B-42)$$

E. Choice of Reaction Model

Choosing the exact mechanism for a particular reaction is not an easy task, especially if the many constants appearing in the reaction equations must be determined. An extensive and thorough research program is required. However, for engineering purposes, a satisfactory choice might be made from

APPENDIX B (Continued)

limited data by examining some of the differences between the equations. By comparing observed effects on the reaction rate caused by changes in some of the primary variables (e.g., temperature, pressure, composition) with changes predicted from each equation, some of the mechanisms can be eliminated. Sometimes the remaining possibilities do not differ much in the range of their intended use and the final choice is nearly academic when the equation is to be empirically fitted to experimental data.

With a suitable reaction rate equation chosen, the chemical erosion can then be determined from the concentrations of the gaseous constituents at the wall. These concentrations at the wall will depend upon the mass and heat transfer to and from the surface.

B-II. APPLICATION OF THE COMPUTER SOLUTION

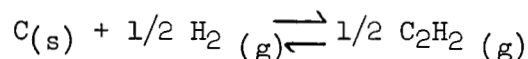
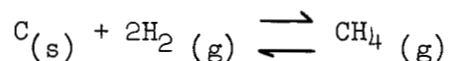
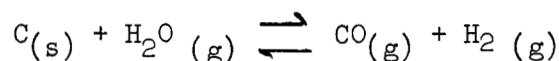
Ideally, a complete kinetic study of the gas-solid system in question would be available and kinetic equations for the conditions involved could be used in the program for predicting "from scratch" the chemical erosion rate. While this may be possible with one or two very common systems, it is not usual. For most systems, one or two more likely situations will exist. The first possibility will be that some kinetic information will be available but will be for conditions other than those to be considered. In this case one or two experimental data points of actual nozzle erosion may be sufficient to complete the picture.

Another problem exists when little or no kinetic information is available as may well be the case with advanced high energy propellant systems. If the reactions are few in number a few actual experimental data points may still be sufficient to permit an engineering analysis of the system.

When no information of any kind is available, the only alternative to a costly experimental program is to assume similarity to some system for which the necessary information is available. This approach certainly is better than a pure guess. No absolute values obtained would be reliable but predicted relative effects should be at least directionally correct.

B-III. CHEMICAL EROSION OF GRAPHITE BY MIXTURES OF HYDROGEN, WATER, CARBON MONOXIDE, METHANE, AND ACETYLENE

The chemical erosion of graphite by mixtures of hydrogen, water, carbon monoxide, methane, and acetylene can be described by the three reactions:



APPENDIX B (Continued)

First applications of the program will be with hydrogen rich fuel systems, the reactions between oxygen and C(s) being temporarily excluded. Other secondary reactions, such as reactions between products or dissociation of the various species might also have been included, but if the empirical constants in the rate equations are evaluated over the range of conditions for which they will be used, the secondary effects should be inherent. Of course, extrapolation to conditions not included in the empirical evaluations would be risky.

A choice of the best reaction mechanism for each reaction might be made by considering the various possibilities along with available data. All of the three reactions include graphite as a solid only. In considering the sublimation of graphite as a mechanism, note first that the apparent activation energy of any reaction under initial conditions with no products in significant quantities is the negative slope of the curve, $\ln r$ vs $1/T$, or where

$$\left. \begin{aligned} \frac{\partial \ln r}{\partial (1/T)} &= \Delta H_{app}^{\ddagger} \\ \Delta H_{app}^{\ddagger} &= \text{Apparent activation energy} \end{aligned} \right\} \quad (B-43)$$

For the sublimation mechanisms, Equations (B-4) and (B-8), reactions I(A) and I(B), $\Delta H_{app}^{\ddagger}$ should be the heat of sublimation or the activation energy of sublimation of graphite. Both of these quantities have been reported as $\sim 175,000$ Kcal/g-mole⁽¹⁵⁾. Since these values are almost twice the observed activation energies for any of the reactions at the observed temperatures, sublimation of graphite followed by gas phase reaction should be eliminated as a possible mechanism for the graphite reactions considered. This should not be interpreted to mean that sublimation can be ignored entirely. At higher temperatures, near the sublimation point, graphite vapor pressure will increase appreciably and sublimation must be considered in accounting for graphite losses under those conditions.

Of the remaining five possible mechanisms described previously, each of the rate equations includes a term in the denominator which reflects a reduction in reaction rate from coverage of part of the reaction sites by adsorbed species on the surface. While there are slight differences in the denominator terms of the rate equations, they have a common characteristic.

APPENDIX B (Continued)

Under conditions of high temperature and low or moderate pressures, such as the conditions pertinent to this study, adsorption is not favorable, and the denominator terms of all the rate equations approach unity. For the purposes of developing a calculation procedure, little loss in accuracy is risked by dropping the denominator terms of the reaction rate expressions. The respective rate equations simplify to the following forms.

Model IIA Impact Mechanism -- Reaction controlling

$$r = C_5 L e^{\left[\frac{-\Delta H^\ddagger}{RT_w} \right]} \left[P_w(A) - \frac{P_w(R) \cdot P_w(S)}{K_e} \right] \quad (B-44)$$

Model IIB Impact Mechanism -- Desorption of one product controlling

$$r = C_6 L e^{\left[\frac{-\Delta H_{aR}^\ddagger}{RT_w} \right]} \left[\frac{P_w(A) K_e}{P_w(S)} - P_w(R) \right] \quad (B-45)$$

Model IIIA Adsorption Mechanism -- Reactant adsorption controlling

$$r = C_7 L e^{\left[\frac{-\Delta H_{aA}^\ddagger}{RT_w} \right]} \left[P_w(A) - \frac{P_w(R) \cdot P_w(S)}{K_e} \right] \quad (B-46)$$

Model IIIB Adsorption Mechanism -- Surface reaction controlling

(1). Reaction with adsorbing site

$$r = C_8 L K_{aA} e^{\left[\frac{-\Delta H^\ddagger}{RT_w} \right]} \left[P_w(A) - \frac{P_w(R) \cdot P_w(S)}{K_e} \right] \quad (B-47)$$

APPENDIX B (Continued)

(2). Reaction with adjacent site

$$r = C_9 L K_{aA} e^{\left[\frac{-\Delta H^\ddagger}{RT_w} \right]} \left[P_w(A) - \frac{P_w(R) \cdot P_w(S)}{K_e} \right] \quad (B-48)$$

Model IIIC Adsorption Mechanism -- Reactant desorption controlling

$$r = C_{10} L e^{\left[\frac{-\Delta H_{aR}^\ddagger}{RT_w} \right]} \left[\frac{P_w(A) \cdot K_e}{P_w(S)} - P_w(R) \right] \quad (B-49)$$

Notice that simplification of the reaction rate expressions by dropping the denominator term leaves only two basic forms to choose from empirically. The reactions controlled by reactant adsorption or the surface reaction all fit to the general form

$$r = C_{11} e^{\left[\frac{-\Delta H_{app}^\ddagger}{RT_w} \right]} \left[P_w(A) - \frac{P_w(R) \cdot P_w(S)}{K_e} \right] \quad (B-50)$$

The reactions limited by product desorption all fit the general form

$$r = C_{12} e^{\left[\frac{-\Delta H_{aR}^\ddagger}{RT_w} \right]} \left[\frac{P_w(A) \cdot K_e}{P_w(S)} - P_w(R) \right] \quad (B-51)$$

where $C_{12} = C_{11} L$, and is constant when L , the total available reaction sites on the surface, does not change with reaction conditions. Under circumstances unfavorable to adsorption, the desorption rate of products should be appreciably higher and should not limit the reaction rate. This leaves the equation for reactant adsorption or surface reaction controlling as the most likely choice for this program.

UNCLASSIFIED

REPORT 6069

APPENDIX B (Continued)

The actual choice between the three possible mechanisms which can be approximated by this equation is academic since the application will depend on empirically determining the constants C_{12} and ΔH_{app}^\ddagger . Likewise when only one product results from the reaction the elimination of the product desorption controlling mechanism also becomes academic. Under these circumstances that rate expression becomes

$$r = C_{13} e^{\left[\frac{-\Delta H_{aR}^\ddagger}{RT_w} \right]} \left[P_w(A) \cdot K_e - P_w(R) \right]$$

which can be rearranged to

$$r = C_{13} e^{\left[\frac{-\Delta H_{aR}^\ddagger}{RT_w} \right]} \left[P_w(A) - \frac{P_w(R)}{K_e} \right] K_e \quad (B-52)$$

or

$$r = C_{14} e^{\left[\frac{-\Delta H_{aR}^\ddagger - \Delta H_R}{RT_w} \right]} \left[P_w(A) - \frac{P_w(R)}{K_e} \right] \quad (B-53)$$

and

$$r = C_{15} e^{\left[\frac{-\Delta H_{app}^\ddagger}{RT_w} \right]} \left[P_w(A) - \frac{P_w(R)}{K_e} \right] \quad (B-54)$$

This is the same form as that obtained for reactant absorption or surface reaction controlling where only one product results from the reaction.

APPENDIX B (Continued)

It must be acknowledged at this time that other variations of the mechanisms discussed so far are possible. We have only considered the two cases of one reactant molecule reacting with one surface molecule and yielding either one or two product molecules. Other distinct possibilities include reactions of one reactant molecule with two surface molecules to give either one or two reactant molecules. However, similar analyses can be done for these models just as have been done for those considered. Under conditions of unfavorable adsorption, these yield very similar rate equations. Thus for establishing calculation procedure, a general rate equation form can be written as

$$r = C_{16} e^{\left[\frac{-\Delta H_{app}^{\ddagger}}{RT_w} \right]} \left[\prod_{i=1}^n P(i)^{u(i)} - \frac{\prod_{i=1}^n P(i)^{v(i)}}{(K_e)^t} \right] \quad (B-55)$$

where i represents each of the n species involved in the reaction. The values of C_{16} , $\Delta H_{app}^{\ddagger}$, $u(i)$, and $v(i)$ must be determined empirically.

The reaction of water with carbon



has been studied by a number of investigators (References 10, 11, 12, 13, and 14). Nearly all have reported that the forward reaction is first order with respect to the water partial pressure except at pressures near complete vacuum. For this reason, a first order reaction model is chosen for the basis of the empirical equation.

Lacking enough data to evaluate $\Delta H_{app}^{\ddagger}$ for the H_2O-C reaction, it is necessary to rely on values reported by others. A variety of values have been reported ranging from 35 Kcal/mole to 90 Kcal/mole. Of these, the value of 60.3 Kcal/mole recently reported by Eyring and Blyholder (Reference 11) appeared most appropriate for the present purposes as well as representing an average value. The value of C_{16} is directly related to the type of graphite, the condition of the surface, and the structural orientation (as with pyrolytic graphite). This value is best determined experimentally if possible for the particular graphite in use.

APPENDIX B (Continued)

For this reason, the value of C_{16} for Reaction 1 was based on results from a Marquardt test of a free standing pyrolytic graphite motor. This test was described as Run No. 1 (Boron-pyrolloy chamber No. 1, Table VII, Marquardt Report 5907, 31 July 1962). For a first guess, a value of 2.99×10^{-3} for C_{16} was used in the program based on the data of Eyring and Blyholder (Reference 11). This value for C_{16} actually gave an erosion rate one or two orders of magnitude greater than that observed in the motor test, which involved erosion of the a-b plane of pyrolytic graphite for the free standing chamber. This was not too surprising since Eyring and Blyholder used a commercial graphite and there have been some indications that the a-b plane of pyrolytic graphite may be far less reactive than commercial graphites. The value of C_{16} was then reduced until the computer program predicted an erosion rate at the throat of 0.2 mils/second, as was observed during the motor tests.

Reactions 2 and 3, between hydrogen and the pyrolytic graphite wall, were also taken to be first order in the forward direction. The respective values of C_{16} for both reactions were then determined from the reported results of Rogers and Sesonske (Reference 16) who studied the kinetics of graphite-hydrogen-methane reactions above 1600°K. The results by Rogers and Sesonske were not applied directly because they considered only the reaction yielding methane even though at the higher temperatures used by them thermodynamic considerations favored the formation of acetylene rather than methane. For this program, a value of 5.12×10^{-5} for C_{16} was used initially for both reaction rate equations. The values of C_{16} for the two equations were then adjusted individually, by trial and error, to give combined calculated erosion rates from the two equations corresponding to rates reported by Rogers and Sesonske over the entire temperature range studied. First order reactions were used in both cases since others have reported some success with this approach even though Rogers and Sesonske did not concur. The value of ΔH^*_{app} was taken as 39000 Kcal/q mole for both reactions. The results of Rogers and Sesonske did not indicate any change in this value over the temperature range from 1600° to 3000°K so there was no basis for considering different values for the two equations.

The values of all empirically determined constants are included below. The table shows necessary substitutions into Equation (B-55) to obtain Equations (B-56), (B-57), and (B-58).

UNCLASSIFIED

REPORT 6069

APPENDIX B (Continued)

Values for Using Equation B-55

Constant	Reaction 1	Reaction 2	Reaction 3
C_{16} (Initial assumption)	$2.99 \times 10^3^*$	$5.12 \times 10^{-5**}$	$5.12 \times 10^{-5**}$
C_{16} (Final value)	3.2×10^{-2}	3.7×10^{-5}	7.4×10^{-5}
ΔH_{app}^\ddagger (Btu/lb mole)	108400	70000	70000
$\prod_{i=1}^n P(i)^{u(i)}$	P_{H_2O}	P_{H_2}	P_{H_2}
$\prod_{i=1}^n P(i)^{v(i)}$	$P_{CO} P_{H_2}$	$(P_{CH_4})^{1/2}$	$P_{C_2H_4}$
$(K_e)^{t***}$	K_{e1}	$(K_{e2})^{1/2}$	$(K_{e3})^2$

* From work of Eyring and Blyholder (Reference 11) with graphite at very low pressures.

** From work of Rogers and Sesonke (Reference 16) with graphite at 1600° to 3000°K.

*** K_{e1} , K_{e2} , and K_{e3} defined by Equations (B-7), (B-8), and (B-9) in the text.

FINAL EQUATIONS USED IN THE COMPUTER PROGRAM

Reaction 1

$$r_1 = 0.032 e^{\left[\frac{-108400}{RT_w} \right]} \left[P_{H_2O} - \frac{P_{CO} P_{H_2}}{K_{e1}} \right] \quad (B-56)$$

TMC A673

UNCLASSIFIED

APPENDIX B (Continued)

Reaction 2

$$r_2 = 0.000037 e^{\left[\frac{-70000}{RT_w} \right]} \left[P_{H_2} - \frac{(P_{CH_4})^{1/2}}{(K_{e2})^{1/2}} \right] \quad (B-57)$$

Reaction 3

$$r_3 = 0.000074 e^{\left[\frac{-70000}{RT_w} \right]} \left[P_{H_2} - \frac{P_{C_2H_2}}{(K_{e3})^2} \right] \quad (B-58)$$

The values of the constants in these equations should not be regarded as fixed. As more experimental data becomes available, adjustments can be made to improve their accuracy. However, for initial calculations of the effect of a transpiring coolant on the chemical erosion, they should be satisfactory, since the order of magnitude of the effects will be of primary interest.

B-IV. BIBLIOGRAPHY

1. Lewis, W. K., and K. C. Chang, Trans. A.I.ChE, 21, 127-136 (1928).
2. Ackermann, G., Forschungsheft, 382, 1-16 (1937).
3. Colburn, A. P., and T. B. Drew, Trans, A.I.ChE, 33, 197-212 (1937).
4. Mickley, H. S., R. C. Ross, A. L. Squyers, and W. E. Stewart, NACA TN-3208 (1954).
5. Bird, R. B., W. E. Stewart, E. N. Lightfoot, "Transport Phenomena", John Wiley & Sons, Inc., 2nd Printing, 1962.
6. Ibid, page 646
7. Ibid, 656-668
8. Hougen, O. A., and K. M. Watson, "Chemical Process Principles", Vol. III, pg 1063-1067, John Wiley & Sons, 7th Printing, 1959.

UNCLASSIFIED

APPENDIX B (Continued)

9. Eckert, E. R. G., and R. M. Drake, Jr., "Heat and Mass Transfer", McGraw-Hill, New York, 2nd Edition, Chapter 16 (1959).
10. Meyer, L., Trans., Faraday Soc., 37, 1154 (1915).
12. Binford, J. S., Jr., and H. Eyring, "Kinetics of Steam-Carbon Reaction", AD 294334, Tech. Note No. X11, August 1955, AF Contract AF 33(638)-20839, Chem Div., Univ. of Utah, Salt Lake City.
12. Sihvonen, V., Ann. Acad. Sci. Fenn., A34, No. 7 (1932).
13. Sihvonen, V., Ann. Acad. Sci. Fenn., A38, No. 2 (1933)
14. Strickland-Constable, R. F., Trans. Faraday Soc., 43, 769 (1947).
15. Honig, R. E., J. Chem. Phys., 22, 126 (1954).
16. Rogers & Sesonske, Los Alamos Sci. Lab. Report LAMS-2896, UC-4, Chemistry, TID-4500 (19th Ed.), August 1962.

TMC A673

UNCLASSIFIED

DISTRIBUTION

<u>Copy No.</u>	<u>Transmitted to</u>
1.	NASA Headquarters Washington, D. C. 20546 Attn.: Contracting Officer, BCA
2.	NASA Headquarters Washington, D. C. 20546 Attn.: Patent Office, AGP
3.	NASA Lewis Research Center 21000 Brookpark Road Cleveland, Ohio 44135 Attn.: Office of Technical Information
4.	NASA Lewis Research Center 21000 Brookpark Road Cleveland, Ohio 44135 Attn.: Contracting Officer
5.	NASA Lewis Research Center 21000 Brookpark Road Cleveland, Ohio 44135 Attn.: Patent Office
6.	NASA Marshall Space Flight Center Huntsville, Alabama 35812 Attn.: Office of Technical Information, M-MS-IPC
7.	NASA Marshall Space Flight Center Huntsville, Alabama 35812 Attn.: Contracting Officer, M-P & C-C
8.	NASA Marshall Space Flight Center Huntsville, Alabama 35812 Attn.: Patent Office, M-PAT
9.	NASA Western Operations Office 150 Pico Boulevard Santa Monica, California 90406 Attn.: Office of Technical Information
10.	NASA Western Operations Office 150 Pico Boulevard Santa Monica, California 90406 Attn.: Contracts Management Division

UNCLASSIFIED

REPORT 6069

DISTRIBUTION (Continued)

<u>Copy No.</u>	<u>Transmitted to</u>
11.	NASA Western Operations Office 150 Pico Boulevard Santa Monica, California 90406 Attn.: General Counsel for Patent Matters
12 to 15.	NASA Headquarters Washington 25, D. C. 20546 Attn.: Mr. Henry Burlage, Jr. Chief, Liquid Propulsion Systems, RPL
16.	NASA Headquarters Washington 25, D. C. 20546 Attn.: Mr. V. E. Jaramillo Advanced Manned Mission, MTC
17 to 41.	Scientific and Technical Information Facility P.O. Box 5700 Bethesda, Maryland 20014 Attn.: NASA Representative, Code CRT
42.	Jet Propulsion Laboratory 4800 Oak Grove Drive Pasadena, California 91103 Attn.: Mr. Bruce Johnson, Technical Manager
43, 44.	NASA Ames Research Center Moffett Field, California 94035 Attn.: Mr. Harold Hornby, Mission Analysis Division
45, 46.	NASA Goddard Space Flight Center Greenbelt, Maryland 20771 Attn.: M. L. Moseson, Code 623
47, 48.	Jet Propulsion Laboratory 4800 Oak Grove Avenue Pasadena, California 91103 Attn.: R. F. Rose, Propulsion Division, 38
49, 50.	NASA Langley Research Center Langley Station, Hampton, Virginia 23365 Attn.: F. L. Thompson, Director
51, 52.	NASA Lewis Research Center 21000 Brookpark Road Cleveland, Ohio 44135 Attn.: Dr. A. Silverstein, Director

TMC 673

UNCLASSIFIED

UNCLASSIFIED

DISTRIBUTION (Continued)

<u>Copy No.</u>	<u>Transmitted to</u>
53, 54.	NASA Marshall Space Flight Center Huntsville, Alabama 35812 Attn.: H. K. Weidner, Code R-P & VED
55, 56.	NASA Manned Spacecraft Center Houston, Texas 77001 Attn.: R. R. Gilruth, Director
57, 58.	NASA Western Operations Office 150 Pico Boulevard Santa Monica, California 90406 Attn.: R. W. Kamm, Director
59.	Advanced Research Products Agency Washington 25, D. C. Attn.: D. E. Mock
60.	Aeronautical Systems Division Air Force Systems Command Wright-Patterson Air Force Base Dayton, Ohio 45433 Attn.: D. L. Schmidt, Code ASRCNC-2
61.	Air Force Missile Development Center Holloman Air Force Base, New Mexico Attn.: Maj. R. E. Bracken, Code MDGRT
62.	Air Force Missile Test Center Patrick Air Force Base, Florida Attn.: L. J. Ullian
63.	Air Force Systems Command, Dyna-Soar Air Force Unit Post Office Los Angeles 45, California Attn.: Col. Clark, Technical Data Center
64.	Arnold Engineering Development Center Arnold Air Force Station Tullahoma, Tennessee Attn.: Dr. H. K. Doetsch
65.	Bureau of Naval Weapons Department of the Navy Washington 25, D. C. Attn.: J. Kay, Code RTMS-41

TMC A 673

UNCLASSIFIED

UNCLASSIFIED

REPORT 6069

DISTRIBUTION (Continued)

<u>Copy No.</u>	<u>Transmitted to</u>
66.	Defense Documentation Center Headquarters Cameron Station, Building 5 5010 Duke Street Alexandria, Virginia 22314 Attn.: TISIA
67.	Headquarters, U. S. Air Force Washington 25, D. C. Attn.: Col. C. K. Stambaugh Code AFRST
68.	Picatinny Arsenal Dover, New Jersey 07801 Attn.: I. Forsten, Chief, Liquid Propulsion Laboratory
69.	Rocket Research Laboratories Edwards Air Force Base Edwards, California 93523 Attn.: Col. Silk
70.	U. S. Atomic Energy Commission Box 62, Oak Ridge, Tennessee Attn.: Technical Information Services
71.	U. S. Army Missile Command Redstone Arsenal, Alabama 35809 Attn.: Dr. W. Wharton
72.	U. S. Naval Ordnance Test Station China Lake, California 93557 Attn.: Chief, Missile Propulsion Division, Code 451
73.	Chemical Propulsion Information Agency Johns Hopkins University, Applied Physics Laboratory 8621 Georgia Avenue Silver Spring, Maryland Attn.: N. Safeer
74.	Aerojet-General Corporation P. O. Box 296 Azusa, California Attn.: L. F. Kohrs

TWCA 673

UNCLASSIFIED

UNCLASSIFIED

DISTRIBUTION (Continued)

<u>Copy No.</u>	<u>Transmitted to</u>
75.	Aerojet-General Corporation P. O. Box 1947 Sacramento, California 95809 Attn.: Technical Library, Bldg. 2015, Dept. 2410, R. Stiff
76.	Aeronutronics, A Division of the Ford Motor Company Ford Road Newport Beach, California Attn.: D. A. Carrison
77.	Aerospace Corporation 2400 East El Segundo Blvd. P. O. Box 95085 Los Angeles, California 90045 Attn.: J. G. Wilder, Propulsion Dept., MS-2293
78.	Arthur D. Little, Inc. Acorn Park Cambridge 40, Massachusetts Attn.: A. C. Tobey
79.	Astropower, Inc., Subsidiary of Douglas Aircraft Company 2968 Randolph Avenue Costa Mesa, California Attn.: Dr. G. Moc, Director, Research
80.	Astrosystems, Inc. 1275 Bloomfield Avenue Caldwell Township, New Jersey Attn.: A. Mendenhall
81.	Atlantic Research Corporation Edsall Road and Shirley Highway Alexandria, Virginia Attn.: A. Scurlock
82.	Beech Aircraft Corporation Boulder Facility Box 631 Boulder, Colorado Attn.: J. H. Rodgers
83.	Bell Aerosystems Company P. O. Box 1 Buffalo 5, New York Attn.: W. M. Smith

TMC 673

UNCLASSIFIED

UNCLASSIFIED

REPORT 6069

DISTRIBUTION (Continued)

<u>Copy No.</u>	<u>Transmitted to</u>
84.	Bendix Systems Division Bendix Corporation Ann Arbor, Michigan Attn.: J. M. Brueger
85.	Boeing Company P. O. Box 3707 Seattle 24, Washington Attn.: J. D. Alexander
86.	Chrysler Corporation Missile Division Warren, Michigan Attn.: J. Gates
87.	Curtiss-Wright Corporation Wright-Aeronautical Division Wood-Ridge, New Jersey Attn.: G. Kelley
88.	Douglas Aircraft Company, Inc. Missile and Space Systems Division 3000 Ocean Park Boulevard Santa Monica, California 90406 Attn.: R. W. Hallet, Chief Eng. Adv. Space Tech.
89.	Fairchild Stratos Corporation Aircraft Missiles Division Hagerstown, Maryland Attn.: J. S. Kerr
90.	General Dynamics/Astronautics P. O. Box 1128 San Diego, California 92112 Attn.: F. Dore, Library & Info. Services (128-00)
91.	General Electric Company Re-entry Systems Department Box 8555 Philadelphia, Pennsylvania 19101 Attn.: F. E. Schultz
92.	General Electric Company Flight Propulsion Lab. Department Cincinnati 15, Ohio Attn.: D. Suichu

TMCA 673

UNCLASSIFIED

DISTRIBUTION (Continued)

<u>Copy No.</u>	<u>Transmitted to</u>
93.	Grumman Aircraft Engineering Corp. Bethpage, Long Island, New York Attn.: Joseph Gavin
94.	Kidde Aerospace Division Walter Kidde and Company, Inc. 675 Main Street Belleville 9, New Jersey Attn.: R. J. Hanville, Director of Research Engineering
95.	Lockheed California Company 10445 Glen Oaks Boulevard Pacoima, California Attn.: G. D. Brewer
96.	Lockheed Missiles and Space Company P. O. Box 504 Sunnyvale, California Attn.: Y. C. Lee, Power Systems R&D
97.	Lockheed Propulsion Company P. O. Box 111 Redlands, California Attn.: H. L. Thackwell
98.	Martin Division Martin-Marietta Corporation Baltimore 3, Maryland Attn.: John Calathes (3214)
99.	Martin Denver Division Martin-Marietta Corporation Denver, Colorado 80201 Attn.: J. D. Goodletter, Mail A-241
100.	McDonnell Aircraft Corporation P. O. Box 6101 Lambert Field, Missouri Attn.: R. A. Herzmark
101.	North American Aviation, Inc. Space and Information Systems Division Downey, California Attn.: H. Storms

UNCLASSIFIED

REPORT 6069

DISTRIBUTION (Continued)

<u>Copy No.</u>	<u>Transmitted to</u>
102.	Northrop Corporation 1001 East Broadway Hawthorne, California Attn.: W. E. Gasich
103.	Pratt & Whitney Aircraft Corp. Florida Research and Development Center P. O. Box 2691 West Palm Beach, Florida 33402 Attn.: R. J. Coar
104.	Radio Corporation of America Astro-Electronics Division Defense Electronics Products Princeton, New Jersey Attn.: S. Fairweather
105.	Reaction Motors Division Thiokol Chemical Corporation Denville, New Jersey 07832 Attn.: A. Sherman
106.	Republic Aviation Corporation Farmingdale, Long Island, New York Attn.: Dr. W. O'Donnell
107.	Rocketdyne Division of North American Aviation, Inc. 6633 Canoga Avenue Canoga Park, California 91304 Attn.: E. B. Monteath, Library Dept. 586-306
108.	Space-General Corporation 9200 Flair Avenue El Monte, California Attn.: C. E. Roth
109.	Space Technology Laboratories Subsidiary of Thompson-Ramo-Wooldridge P. O. Box 95001 Los Angeles 45, California Attn.: G. W. Elverum
110.	Stanford Research Institute 333 Ravenswood Avenue Menlo Park, California 94025 Attn.: T. Smith

TMC A 673

UNCLASSIFIED

UNCLASSIFIED

REPORT 6069

DISTRIBUTION (Continued)

<u>Copy No.</u>	<u>Transmitted to</u>
111.	TAPCO Division Thompson-Ramo-Wooldridge, Inc. 23555 Euclid Avenue Cleveland 17, Ohio
112.	Thiokol Chemical Corporation Redstone Division Huntsville, Alabama Attn.: J. Goodloe
113.	United Aircraft Corporation Research Laboratories 400 Main Street East Hartford, Connecticut 06108 Attn.: E. Martin
114.	United Technology Center 587 Methilda Avenue P. O. Box 358 Sunnyvale, California Attn.: B. Abelman
115.	Vought Aeronautics Box 5907 Dallas 22, Texas Attn.: W. C. Trent

TMC 673

UNCLASSIFIED